MODELING OF HYDRAULIC FRACTURING AND DESIGN OF ONLINE OPTIMAL PUMPING SCHEDULE FOR ENHANCED PRODUCTIVITY IN SHALE FORMATIONS

A Dissertation

by

PRASHANTH KUMAR SIDDHAMSHETTY

Submitted to the Office of Graduate and Professional Studies of
Texas A&M University
in partial fulfillment of the requirements for the degree of

DOCTOR OF PHILOSOPHY

Chair of Committee,	Joseph Sang-Il Kwon
Committee Members,	Costas Kravaris
	Mahmoud El-Halwagi
	Peter P. Valkó
Head of Department,	Arul Jayaraman

May 2020

Major Subject: Chemical Engineering

ABSTRACT

In hydraulic fracturing, the proppant-filled fracture length at the end of pumping strongly influences the fluid conductivity of natural oil and gas. Therefore, it is very important to regulate proppant bank height and suspended proppant concentration across the fracture to increase the recovery of shale hydrocarbon. From a control engineering viewpoint, hydraulic fracturing has been traditionally viewed as an open-loop problem. Well logs and mini-frac test results are interpreted prior to operation in order to obtain petrophysical and rock-mechanical properties of the formation. The operation is designed based on the properties and then is conducted accordingly. However, the open-loop operation may lead to poor performance if there are large disturbances and plant-model mismatch.

In this research, a model predictive control framework is developed for the design of pumping schedules to regulate the spatial variation of proppant concentration across the fracture at the end of pumping for both of conventional and unconventional reservoirs. To this end, we initially focus on the development of a first-principle model of hydraulic fracturing process to obtain fundamental understanding of the proppant bank formation mechanism and its relationship to manipulated input variables such as proppant concentration and flow rate of the injected fracturing fluids by considering a single fracture. Then, a model-based feedback controller is developed to achieve the uniform proppant bank height and suspended proppant concentration along the fracture at the end of pumping for both of conventional and unconventional reservoirs by explicitly taking into account the desired fracture geometry, type of the fracturing fluid injected, total amount of injected proppant, actuator limitations, and safety considerations.

Then, we extend this study to multi-stage hydraulic fracturing, where in each stage, multiple simultaneously propagating fractures are generated. In multi-stage hydraulic fracturing treatments, simultaneously propagating multiple fractures with close spacing often induce non-uniform fracture development due to “stress shadow effects”. In order to mitigate these undesired stress-shadow effects, we propose a model-based design technique by utilizing the limited entry design

technique to compute the flow rate of fracturing fluids and the perforation conditions which will promote equal distribution of fracturing fluids to achieve uniform growth of multiple fractures. Then, a model-based feedback controller is developed to achieve a uniform proppant bank height in simultaneously propagating multiple fractures at the end of pumping by handling the undesired stress-shadow effects using the optimal perforation conditions.

In hydraulic fracturing, higher fracturing fluid injection rates can trigger increased stress, thereby creating more microseismic events; particularly, simultaneously occurring multiple microseismic events can reduce measurement errors. This suggests a new state and output estimation scheme that utilizes the dependence between the fracturing fluid injection rate (i.e., manipulated input) and measurement errors. Motivated by this, we improve our control framework for measurement uncertainty reduction while achieving the original control task of proppant bank height control in hydraulic fracturing. Specifically, the developed model-based feedback control system regulates the uniformity of proppant bank height along the fracture length and achieve accurate state and output estimation by manipulating the fracturing fluid pumping schedule that includes the fracturing fluid injection rate and proppant concentration at the wellbore.

In some of the unconventional reservoirs, natural fractures (discontinuities in shale rock formations) are commonly observed using advanced fracture diagnostic techniques such as microseismic monitoring, core samples and outcrops. In naturally fractured unconventional reservoirs, naturally present fractures will interact with hydraulic fractures and divert fracture propagation. Because of complex fracture growth, the ultimate goal of hydraulic fracturing operation in naturally fractured unconventional reservoirs should be changed from achieving a desired fracture geometry to maximizing the total fracture surface area (TFSA) for given fracturing resources, as it will allow more drainage area available for oil recovery. To further consider the interaction between hydraulic fractures and natural fractures, we develop a model-based pumping schedule that maximizes the TFSA by utilizing a recently developed unconventional complex fracture propagation model called Mangrove describing complex fracture networks in naturally fractured unconventional reservoirs.

ACKNOWLEDGMENTS

I would like to sincerely thank my advisor, Dr. Joseph Kwon, for his guidance and encouragement throughout my study at Texas A&M University. He provided me tremendous support both in professional and personal life. Also, I would like to deeply thank Dr. Peter P. Valkó, a member of my committee, for valuable discussions and guidance, especially in the field of hydraulic fracturing. I would like also to thank my dissertation committee: Dr. Costas Kravaris, Dr. Mahmoud El-Halwagi, and Dr. Peter P. Valkó for their insightful comments and encouragement to widen my research from various perspectives.

I would like to thank Dr. Kan Wu and her lab members who collaborated with us on various studies. I also thank Dr. Rashid Hasan for his guidance on Hilcorp company project on wellhead burning. I appreciate all my lab colleagues, Seeyub Yang, Kaiyu Cao, Yuchan Ahn, Parth Bhandakkar, Harwinder Singh Sidhu, Abhinav Narasingam, Dongheon Lee, Hyun-Kyu Choi, Niranjan Arvind Sitapure, Mohammed Saad Faizan Bangi, and Bhavana Bhadriraju Venkata Naga Sai for their help in my research. I would also like to thank all the staff in the chemical engineering department for helping promptly whenever required and providing a hasslefree work environment.

Finally, I am grateful to my family and friends. Words cannot possibly describe the sacrifices they have made for me or the support they have given.

CONTRIBUTORS AND FUNDING SOURCES

This work was supervised by a dissertation committee consisting of Dr. Joseph Kwon (chair), Dr. Costas Kravaris and Dr. Mahmoud El-Halwagi of the Artie McFerrin Department of Chemical Engineering, and Dr. Peter P. Valkó of the Department of Petroleum Engineering.

All work for the dissertation was completed by the student with certain computational contributions made by various members of Dr. Joseph Kwon' lab; the students are either explicitly mentioned in the thesis and/or in papers that were published or that will be published in the future. Some of the modeling contributions have been made by Dr. Peter P. Valkó's lab and Dr. Kan Wu's lab of the Department of Petroleum Engineering at Texas A&M University; their names are mentioned in the thesis or in papers that were published or will be published in the future.

This work was made possible in part by the startup fund awarded to Dr. Joseph Kwon by the Artie McFerrin Department of Chemical Engineering at Texas A&M University. This work was also made possible by financial support from the National Science Foundation (CBET-1804407).

TABLE OF CONTENTS

Page

ABSTRACT ii

ACKNOWLEDGMENTS iv

CONTRIBUTORS AND FUNDING SOURCES v

TABLE OF CONTENTS vi

LIST OF FIGURES x

LIST OF TABLES xvi

1. INTRODUCTION 1

    1.1 Hydraulic fracturing 1
    1.2 Background and challenges 2
        1.2.1 Pumping schedules for hydraulic fracturing treatment 2
        1.2.2 Multi-stage hydraulic fracturing 5
        1.2.3 Microseismic measurement uncertainty 6
        1.2.4 Naturally fractured unconventional reservoirs 6
    1.3 Research objectives 7
    1.4 Dissertation layout 8

2. MODELING OF HYDRAULIC FRACTURING AND DESIGN OF AN OPEN-LOOP OPTIMAL PUMPING SCHEDULE TO ACHIEVE A UNIFORM PROPPANT CONCENTRATION LEVEL IN CONVENTIONAL RESERVOIRS 10

    2.1 Introduction 10
    2.2 Dynamic modeling of hydraulic fracturing processes 11
        2.2.1 Modeling of fracture propagation 11
            2.2.1.1 Fluid momentum (lubrication theory) 11
            2.2.1.2 Rock deformation (elasticity equation) 12
            2.2.1.3 The conservation of local fluid mass 13
            2.2.1.4 Carter's fluid leak-off model 13
        2.2.2 Modeling of proppant transport 14
            2.2.2.1 Proppant advection 14
            2.2.2.2 Proppant settling 14
    2.3 Numerical simulation 15
        2.3.1 Numerical solution procedure 16

2.4 Design of optimal pumping schedule 17
2.4.1 Unified fracture design 17
2.4.2 Optimal pumping schedule 19
2.5 Simulation results 23
2.6 Conclusions 32

3. DESIGN OF ONLINE PUMPING SCHEDULES TO ACHIEVE UNIFORM PROPPANT CONCENTRATION IN CONVENTIONAL OIL RESERVOIRS 35

3.1 Introduction 35
3.2 Dynamic modeling of hydraulic fracturing processes 35
3.3 Open-loop pumping schedule 36
3.4 Model predictive control for hydraulic fracturing systems 37
3.4.1 Unified fracture design 38
3.4.2 System Identification 39
3.4.3 State estimator design using Kalman filter 40
3.4.4 Pumping schedule formulation using model predictive controller 41
3.5 Closed-loop simulation results 44
3.6 Novelty of the proposed method 50
3.7 Conclusions 51

4. FEEDBACK CONTROL OF PROPPANT BANK HEIGHTS DURING HYDRAULIC FRACTURING FOR ENHANCED PRODUCTIVITY IN SHALE FORMATIONS 54

4.1 Introduction 54
4.2 Dynamic modeling of hydraulic fracturing processes 56
4.2.1 Modeling of fracture propagation 56
4.2.2 Modeling of proppant transport 56
4.2.2.1 Proppant advection 57
4.2.2.2 Proppant settling 57
4.2.3 Proppant bank formation 58
4.3 Numerical simulation 59
4.3.1 Challenges in numerical simulations 59
4.3.2 Meshing Strategy 60
4.3.3 Numerical solution procedure 61
4.4 Computation of optimal fracture configuration in unconventional reservoirs 62
4.4.1 Section-based optimization method 62
4.4.2 Calculation of the optimal well-fracture configuration using the section-based optimization method 68
4.4.3 Treatment targets 69
4.5 Model predictive control for hydraulic fracturing processes 69
4.5.1 Development of reduced-order model 70
4.5.2 Kalman filter design 71
4.5.3 Design of model-based feedback controller 72
4.6 Closed-loop simulation results under model-based feedback controller 74
4.7 Conclusions 77

5. OPTIMIZATION OF SIMULTANEOUSLY PROPAGATING MULTIPLE FRACTURES IN HYDRAULIC FRACTURING TO ACHIEVE UNIFORM GROWTH USING DATA-BASED MODEL REDUCTION 79

5.1 Introduction 79
5.2 A dynamic model of simultaneously propagating multiple fractures 81
5.2.1 Rock deformation 82
5.2.2 Fluid flow 83
5.2.3 Development of reduced-order models 86
5.2.4 Validation of ROMs 88
5.3 Model-based design technique to achieve uniform fracture growth 90
5.3.1 Optimal perforation conditions 91
5.4 A case study for three fractures propagating simultaneously 93
5.4.1 Non-uniform fracture growth (Base case) 93
5.4.2 Uniform fracture growth using the proposed model-based design technique . 94
5.5 Conclusions 98

6. MODELING AND CONTROL OF PROPPANT DISTRIBUTION OF MULTI-STAGE HYDRAULIC FRACTURING IN HORIZONTAL WELLS 102

6.1 Introduction 102
6.2 Dynamic modeling of simultaneously propagating multiple fractures 104
6.2.1 Modeling of proppant transport 104
6.2.2 Modeling of proppant settling and proppant resuspending 105
6.3 Optimal fracture geometry in unconventional reservoirs 106
6.4 Model predictive control for hydraulic fracturing processes 107
6.4.1 Development of reduced-order models 108
6.4.2 Kalman filter design 109
6.4.3 Model-based feedback control formulation 110
6.5 A case study for three fractures propagating simultaneously 112
6.5.1 Non-uniform fracture growth (Base case) 112
6.5.2 Closed-loop simulation results under the proposed model-based feedback controller 113
6.6 Conclusions 116

7. SIMULTANEOUS MEASUREMENT UNCERTAINTY REDUCTION AND PROPPANT BANK HEIGHT CONTROL OF HYDRAULIC FRACTURING 119

7.1 Introduction 119
7.2 Problem statement 121
7.3 Modeling of hydraulic fracturing 123
7.4 Optimal configuration of fractures and wells in unconventional oil and gas reservoirs 124
7.5 Model-based control systems for simultaneous uncertainty reduction and set-point tracking in hydraulic fracturing 125
7.5.1 Development of ROM 125
7.5.2 Uncertainty reduction 127

7.5.3 MPC formulations 128
7.6 Closed-loop simulation results under the proposed MPC 130
7.7 Conclusions 135

8. ENHANCING TOTAL FRACTURE SURFACE AREA IN NATURALLY FRACTURED UNCONVENTIONAL RESERVOIRS VIA MODEL PREDICTIVE CONTROL 143

8.1 Introduction 143
8.2 High-fidelity model formulation using Mangrove 146
8.2.1 Overview of the UFM 146
8.2.1.1 Fluid Flow equations 146
8.2.1.2 Hydraulic and natural fractures interaction 149
8.2.1.3 Stress shadow effects 149
8.2.2 Reservoir Simulator 150
8.3 Sensitivity analysis of complex fracture growth in naturally fractured reservoirs 151
8.3.1 Effect of natural fracture distribution on TFSA 151
8.3.1.1 Effect of natural fracture orientation on TFSA 151
8.3.1.2 Effect of natural fracture length on TFSA 154
8.3.1.3 Effect of natural fracture spacing on TFSA 155
8.3.2 Effect of pumping schedule on TFSA 158
8.4 Background on pumping schedule design techniques 160
8.5 Handling computational requirement in control of hydraulic fracturing processes 162
8.6 Model-based feedback control system for enhancing TFSA in naturally fractured unconventional reservoirs 166
8.7 Closed-loop simulation results under the proposed MPC 167
8.8 Conclusions 171

9. SUMMARY AND FUTURE WORK 174

9.1 Summary 174
9.2 Future work 176

REFERENCES 178

LIST OF FIGURES

FIGURE Page

1.1 Illustration of multi-stage hydraulic fracturing operation in a horizontal wellbore. ... 2

1.2 Illustration of three stages in hydraulic fracturing. ... 3

2.1 The PKN fracture model [1, 2]. ... 12

2.2 Schematic flow diagram of the numerical simulator. ... 17

2.3 (a) proppant pumping schedule, and (b) practically-feasible target concentration profile. ... 21

2.4 Flowchart for the optimal pumping schedule design procedure. ... 24

2.5 Spatiotemporal evolution of the fracture width. ... 26

2.6 The evolution of the fracture width at the wellbore with time. ... 27

2.7 Spatial proppant concentration profiles obtained at the end of pumping for different constant-concentration pumping schedules. ... 28

2.8 Practically-feasible target concentration (bold line) that minimizes the error from the ideal target concentration. ... 29

2.9 Pumping schedules generated using the proposed design technique and Nolte's method. ... 30

2.10 Spatial proppant concentration profile obtained at the end of pumping using the generated pumping schedule. ... 31

2.11 Spatial proppant concentration profiles obtained at the end of pumping for different f_a values. ... 32

2.12 Spatial proppant concentration profiles obtained at the end of pumping using the proposed method and Nolte's pumping schedule. ... 33

2.13 Proppant bank height along the fracture length at the end of pumping. ... 34

3.1 Comparison of spatial proppant concentration profiles obtained at the end of pumping under different pumping schedules. ... 37

3.2 Comparison between the true values and the estimates of proppant concentration at 6 different locations. 43

3.3 Closed-loop operation of hydraulic fracturing under MPC. 44

3.4 Spatial proppant concentration profiles obtained at the end of pumping under MPC and by Nolte's pumping schedule. 46

3.5 Comparison of the pumping schedule generated under MPC with Nolte's pumping schedule. 47

3.6 Spatial proppant bank height profile obtained at the end of pumping. 48

3.7 Spatial proppant concentration profiles obtained at the end of pumping under MPC when there is a plant-model mismatch in Young's modulus with 90% and 110% of its nominal value. 49

3.8 Variations in the proppant pumping schedule when there is a disturbance introduced to the 5^{th} substage of the pumping schedule. 50

3.9 Spatial proppant concentration profiles obtained at the end of pumping under MPC when there is a disturbance introduced to the 5^{th} substage of the pumping schedule. . 51

3.10 Spatial proppant concentration profiles obtained at the end of pumping under MPC with different number of substages considered in the pumping schedule design. 52

3.11 Spatial proppant concentration profiles obtained at the end of pumping under MPC with different numbers of spatial locations considered in the cost function. 53

4.1 Growth and propagation of proppant bank during hydraulic fracturing. 60

4.2 Illustration of the proposed re-meshing strategy. 61

4.3 Schematic flow diagram of the proposed closed-loop operation of hydraulic fracturing processes. 62

4.4 Illustration of a section for the case of two wells ($n_c = 2$) and eight fractures per well ($n_r = 8$). 64

4.5 Illustration of a subsection (the drainage area of a single fracture). 65

4.6 Contour plot of the $J_{D,f}$ obtained by solving the eigenvalue problem, Eq. (4.9), for different A_r and I_x values. 67

4.7 Comparison between the true values and the estimates of average fracture width, fracture width at the wellbore, and fracture length. 72

4.8 Average fracture width during the hydraulic fracturing process under MPC. 75

4.9 Optimal pumping schedule generated under MPC to obtain the required average fracture width at the end of pumping. 76

4.10 Spatial profile of proppant bank height obtained at the end of pumping under the MPC. 77

5.1 Boundary elements on a fracture of interest [3]. 83

5.2 Illustration of the distribution of fracturing fluids into each fracture and the pressure drops due to wellbore friction, perforation friction and fracture propagation [4]. 84

5.3 Comparison of the pressure drop profiles due to fracture propagation, $\Delta p_{fp,i}$, obtained at three different spatial locations ($z = 30$ m, $z = 60$ m, and $z = 90$ m) from the high-fidelity process model and the linear time-invariant state space model. 89

5.4 Comparison of the pressure drop profiles from the wellbore heel to three different spatial locations ($z = 30$ m, $z = 60$ m, and $z = 90$ m) in fractures, $\Delta p_i(z,t)$, from the high-fidelity process model and the integrated ROM for $n_p = 20$ and $d_p = 0.015$ m. 90

5.5 Comparison of the pressure drop profiles from the wellbore heel to three different spatial locations ($z = 30$ m, $z = 60$ m, and $z = 90$ m) in fractures, $\Delta p_i(z,t)$, from the high-fidelity process model and the integrated ROM for $n_p = 12$ and $d_p = 0.00762$ m. 91

5.6 Fracture length and width distributions obtained at the end of pumping for the base case. 95

5.7 The pressure at three different locations in multiple fractures during the hydraulic fracturing process for the base case with a constant flow rate. 96

5.8 Percentage of the total fracturing fluid volume distributed into each fracture at the end of pumping for the base case. 97

5.9 Pumping schedule of fracturing fluids using the proposed model-based design technique to achieve uniform pressure at different locations in multiple fractures with time. 98

5.10 The pressures at three different locations in multiple fractures during the hydraulic fracturing process after applying the flow rate of fracturing fluids and perforation conditions using the proposed model-based design technique. 99

5.11 Fracture length and width distributions obtained at the end of pumping using the proposed model-based design technique. 100

5.12 Percentage of the total fracturing fluid volume distributed into each fracture at the end of pumping for the base case and for the one with the proposed model-based design technique. 101

6.1 Comparison between the true values and the estimates of average width profiles of simultaneously propagating multiple fractures. 110

6.2 Fracture length and width distributions in multiple fractures obtained at the end of pumping for the base case. 113

6.3 Spatial proppant bank height profiles of the simultaneously propagating three fractures obtained at the end of pumping for the base case. 114

6.4 Percentage of the total fracturing fluid volume distributed into each fracture at the end of pumping under the optimal perforation conditions. 115

6.5 Average width profiles of simultaneously propagating multiple fractures during hydraulic fracturing under the proposed controller. 116

6.6 Optimal pumping schedules generated under the proposed controller. 117

6.7 Spatial proppant bank height profiles of the simultaneously propagating three fractures obtained at the end of pumping. 118

7.1 Schematic of how MSM works. 120

7.2 Comparison between the true values and the estimates of average fracture width and fracture length. 126

7.3 Schematic of the proposed closed-loop operation. 130

7.4 The fixed pumping schedule used in the first case. 132

7.5 Average fracture width profile under the fixed pumping schedule. 133

7.6 Trace of output error covariance under the fixed pumping schedule. 134

7.7 Average fracture width profile under the fixed pumping schedule compared to its target. 135

7.8 Average fracture width profile under the proposed MPC. 136

7.9 Pumping schedule computed by the proposed MPC. 137

7.10 Trace of output error covariance under the proposed MPC. 138

7.11 Proppant bank height at the end of the hydraulic fracturing process under the fixed pumping schedule. 139

7.12 Average fracture width profile under the proposed MPC compared to its target. 139

7.13 Proppant bank height at the end of the hydraulic fracturing process under the proposed MPC. 140

7.14 Pumping schedule computed by the proposed MPC after extending simulation time. 140

7.15 Average fracture width profile under the proposed MPC after extending simulation time. 141

7.16 Average fracture width profile under the fixed pumping schedule after extending simulation time. 141

7.17 Average fracture width profile under the proposed MPC when there is a plant-model mismatch in the Young's modulus with 110% of its nominal value. 142

8.1 Possible scenarios when a hydraulic fracture interacts with a natural fracture. 144

8.2 Schematic showing a hydraulic fracture approaching a natural fracture. 153

8.3 Fracture network at the end of hydraulic fracturing operation for four different relative angles between hydraulic fractures and natural fractures. 154

8.4 Comparison of TFSA for four different relative angles between hydraulic fractures and natural fractures. 155

8.5 Fracture network at the end of hydraulic fracturing operation for two different natural fracture length distributions. 156

8.6 Comparison of TFSA for two different natural fracture length distributions. 157

8.7 Fracture network at the end of hydraulic fracturing operation for two different natural fracture spacing distributions. 158

8.8 Comparison of TFSA for two different natural fracture spacing distributions. 159

8.9 Pumping Schedules used for sensitivity analysis. 161

8.10 Comparison of TFSA for three cases with different pumping schedules. 162

8.11 Cumulative oil production over time for three cases with different pumping schedules. 163

8.12 Comparison between the true values and the estimates of TFSA for a given pumping schedule. 164

8.13 Validation of ROM by comparing it with high fidelity model for a given pumping schedule. 165

8.14 Fracture geometry at the end of hydraulic fracturing operation under the proposed MPC. 168

8.15 Pumping schedule obtained under the proposed MPC. 169

8.16 Nolte's pumping schedule with input constraints being considered. 170

8.17 Pumping schedule obtained by the method proposed by Siddhamshetty et al. [5]. 171

8.18 Comparison of TFSA under the proposed MPC, Nolte's and Siddhamshetty et al. [5] pumping schedules. 172

8.19 Comparison of cumulative oil production under the proposed MPC, Nolte's and Siddhamshetty et al. [5] pumping schedules. 173

8.20 Comparison of oil production rates under the proposed MPC, Nolte's and Siddhamshetty et al. [5] pumping schedules. 173

LIST OF TABLES

TABLE Page

2.1 Model parameters used for the simulation. 25

3.1 Cost function values under MPC with different number of substages considered in the pumping schedule design. 47

3.2 Cost function values under MPC with different number of spatial locations considered in the cost function. 48

3.3 The computation time to solve the optimization problem, Eq. (3.8), at each sampling time. 53

4.1 Optimal number of fractures per well n_r, penetration ratio I_x, overall dimensionless productivity J_D, individual well productivity $J_{D,well}$, fracture half-length x_f and separation distance d_{sep} for fixed number of wells, n_c 68

4.2 Model parameters used in the high-fidelity model simulation. 75

5.1 Model parameters used for the base case simulation. 94

5.2 Fracture length and average width at the end of pumping using the proposed model-based design technique. 98

5.3 Fracture length and average width at the end of pumping for a constant flow rate using the proposed model-based design technique. 99

5.4 Maximum deviation between the fracture lengths when there is plant-model mismatch in the Young's modulus. 100

8.1 Model parameters used for sensitivity studies. 152

8.2 Natural fracture distribution with different relative angles. 152

8.3 Natural fracture distribution with different lengths. 156

8.4 Natural fracture distribution with different spacing values. 157

8.5 Reservoir properties used for the oil production simulation. 160

8.6 TFSA and cumulative oil production for three cases with different pumping schedules. 160

8.7 Natural fracture distribution used in the closed-loop simulation. 168

8.8 TFSA, cumulative oil production and NPV of oil produced under the proposed MPC, Nolte's and Siddhamshetty et al. [5] pumping schedules. 169

8.9 Computational time required to solve the optimization problem, Eq. (8.13), at each pumping stage. 170

1. INTRODUCTION

1.1 Hydraulic fracturing

Typically, the term shale gas refers to natural gas trapped in rock of low porosity (2% or less) and ultra-low permeability (0.01 to 0.0001 md or even less) [6]. Because of the low permeability (interconnected spaces between the rocks) of the shale formations, if a well were drilled into such a rock, the production rate would be so low that extracting gas from such a well would be considered to be economically infeasible. The shale boom in the U.S. has been triggered by directional drilling [7] and hydraulic fracturing [8] technologies. As a result, the total natural gas reserves in the U.S. was about 175 trillion cubic feet (tcf) in 1998, but after about 250 tcf of production over the next 11 years, the total gas reserves increased to 285 tcf [6].

One of most commonly used completion techniques in unconventional reservoirs for horizontal wells is the plug-and-perforation completion technique. Using this technique, multiple isolated fracturing stages are created along the horizontal wellbore from the wellbore toe to the heel, where each stage consists of three to six perforation clusters with spacing of 10 to 30 m (Fig. 1.1). Each perforation cluster will create a single dominant fracture to connect the wellbore to the rock formation; typically 6 to 20 perforations are created per cluster, and the cluster length is between 0.5 and 1 m [9]. Specifically, hydraulic fracturing treatment starts with perforation, in which stage, explosions along the wellbore are used to create initial fracture paths at spaced intervals along the well (Fig. 1.2). A viscous fluid is pumped inside the wellbore, inducing a steep rise in the pressure level which eventually leads to the initiation of fractures at the perforated sites. A clean fluid (called pad) is usually pumped first to initiate the fracture opening for the introduction of the subsequent fracturing fluid. Then, proppant (sand) particles are injected in the form of a suspension at a sufficiently high pressure and flow rate for further fracture propagation. The suspended proppant travels into the fracture along the fluid as the fracture propagates. The treatment usually takes place on a time-scale of tens of minutes to a few hours, depending on the fracture size and mass of prop-

pant to be injected. After pumping is stopped and the remaining fluid leaks off to the reservoir, the natural stress by the formation closes the fracture, trapping the proppant inside the fracture walls. The trapped proppant will form a conductive packed conduit that helps extracting the oil and gas inside the reservoir more effectively, and the large amount of leak-off fluid enhances the permeability of the stimulated volume of the formation. After generating simultaneously growing multiple fractures with a stage, another plug-and-perforation gun can be used to work on the next stage.

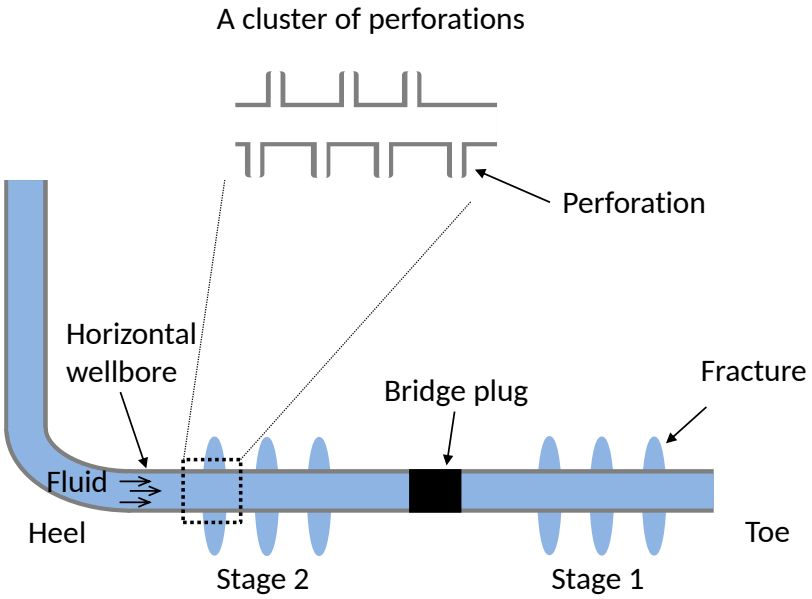

Figure 1.1: Illustration of multi-stage hydraulic fracturing operation in a horizontal wellbore.

1.2 Background and challenges

1.2.1 Pumping schedules for hydraulic fracturing treatment

There have been many efforts by researchers using optimization techniques to determine the number of fracturing stages, the distance between adjacent stages, and the total amount of the fracturing fluid to be introduced and its injection rate for well completions. For a given amount of proppant, a unified fracture design (UFD) that provides the practically optimal design has been ad-

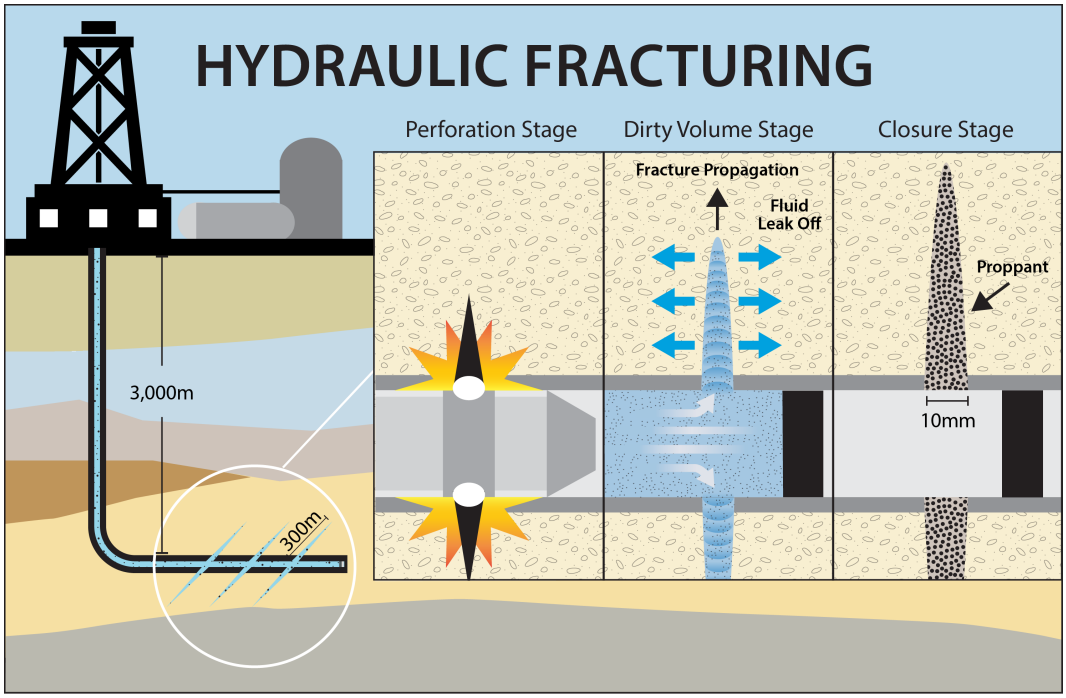

Figure 1.2: Illustration of three stages in hydraulic fracturing.

dressed for conventional (high-permeability) oil and gas reservoirs [10, 11, 12], and the approach has been recently extended to unconventional (low-permeability) resources [13]. By taking into account reservoir properties, design objectives, and design constraints, the maximization of net present value (NPV) was presented in [14, 15, 16]. Additionally, optimization techniques have been applied to a variety of applications such as resource scheduling [17], field development under uncertainty [18], automated history matching of reservoir parameters [19], optimal well location and spacing [20], production parameter settings [21, 22, 23, 24, 25], and optimization of the displacement efficiency or recover factor [26, 27].

To produce a fracture with desired features determined by the aforementioned optimization-base approaches and to have a desired distribution of proppant across the fracture at the end of pumping, it is also important to develop a technique to generate an optimal pumping schedule. One of the most commonly used approaches for generating the pumping schedule is developed by Nolte [28]. He provided a pumping schedule based on the following assumptions: 1) no proppant settling, 2) pumping schedule in the pre-defined form as a power-law, 3) the final fluid efficiency

is known a priori, and 4) a constant leak-off coefficient is considered. The approach is based on the conservation of fluid volume, particularly estimating the amount of fluid that leaks off during the hydraulic fracturing treatment, and the approach is not tied to a particular fracture geometry. Hence, this pumping schedule can be applied to a variety of fracture models, however it notably underestimates the pad size, which causes premature tip screen-out leading to a shorter propped fracture length than which is required to maximize the productivity of a stimulated well.

Another alternative to generate an optimal pumping schedule is to develop a pumping schedule generator that uses a detailed forward numerical simulator. The forward simulator requires an initial pumping schedule to run a simulation in the beginning, which is normally obtained by dividing the pumping schedule into multiple constant-concentration sub-stages. As the simulation proceeds, based on the obtained forward simulation results, proppant concentration of the sub-stages in the pumping schedule is iteratively adjusted until the desired fracture geometry and fracture conductivity are achieved. Typically, this type of approaches requires many iterations, and thus, it is a highly computationally expensive task. For example, Gu and Desroches [29] used a proppant transport model to solve an inverse problem to generate a pumping schedule iteratively. In the inverse problem, the desired fracture geometry and spatial proppant concentration at the end of pumping are the inputs, whereas the duration and proppant concentration of each stage in the pumping schedule are the outputs to be determined iteratively. Because of the iterative nature of this scheme, we can obtain the results with good accuracy but the computational requirement is significant. In an effort to develop a pumping schedule which is more accurate than Nolte [28], but at the same time, less computationally challenging than the iterative procedure described by Gu and Desroches [29], a new pumping schedule generation technique was proposed by Dontsov and Peirce [30]. However, they did not consider the explicit dependence of fracture propagation on proppant concentration level by assuming that the proppant particles have a weak impact on the fracture propagation. The accuracy of this method deteriorates for high concentration levels, which limits the applicability of the method to relatively low concentration levels where the viscosity (thereby, the fracture propagation) does not change much with proppant concentration.

The aforementioned pumping schedules viewed hydraulic fracturing processes as an open-loop problem, which may lead to poor process performance if there are large disturbances and plant-model mismatch. Over the last ten years, the oil and gas production industries have applied model predictive control (MPC) theory to drilling processes to enhance pressure control flexibility and process safety [31, 32, 33, 34, 35, 36, 37, 38, 39, 40, 41, 42], however its application to hydraulic fracturing, particularly in the context of regulating the proppant distribution across the fracture, has not received much attention because of the following reasons: (1) limited access to real-time measurements, (2) presence of uncertainties in the measurement data, and (3) large computational requirements due to dynamic simulation of multiple highly-coupled PDEs defined over a time-dependent spatial domain. While some attempts to employ model-based control schemes have been made by [43, 44], these studies did not explicitly take into account practical considerations such as the desired fracture geometry, optimality and safety considerations, and uniformity in final proppant distribution across the fracture.

1.2.2 Multi-stage hydraulic fracturing

In multi-stage hydraulic fracturing treatments, simultaneously propagating multiple fractures with close spacing often induce non-uniform fracture development, resulting in one or two dominant fractures due to the uneven distribution of fracturing fluids [45, 46]. Miller et al. [47] analyzed the production log data obtained by applying state-of-the art diagnostic technologies to multiple basins; the conclusion was that one third of all perforation clusters contribute to two thirds of gas production, and approximately another one third of the clusters are ineffective and do not contribute to production. One underlying reason for this uneven distribution is the non-uniformity of reservoir properties such as spatial heterogeneity in the in-situ stress along the well [48, 49]. Another contributing factor for the uneven distribution is the well-known phenomenon called "stress-shadowing" [50, 51, 52]. In general, fracturing fluids are distributed to multiple fractures inversely proportional to their flow resistances, which is a function of perforation friction, wellbore friction, and fracture propagation. The problem with stress-shadow effects is that it exerts extra compressional stresses on the interior fractures and increases the flow resistance within interior fractures,

resulting in fluid diverting into the exterior fractures. Therefore, to achieve uniform growth of simultaneously propagating multiple fractures and facilitate more fracturing fluids entering into the interior fractures, stress-shadow effects should be balanced or mitigated.

1.2.3 Microseismic measurement uncertainty

In hydraulic fracturing, among a variety of available measurement technologies, microseismic monitoring (MSM) is the most commonly used one to determine the geometry and location of created hydraulic fractures because it provides the most comprehensive picture of hydraulic fracture growth [53, 54, 55]. In general, the measurement uncertainty associated with geophones in MSM technique is very high due to the remote nature of hydraulic fracturing taking place in an underground environment. Using these measurements with high uncertainty may lead to incorrect state and output estimation and thereby to a poor controller performance. However, unlike other industrial applications, in hydraulic fracturing the occurrence of measurement depends on the fracturing fluid injection rate at the wellbore [53]. More microseismic events can take place due to increased stress triggered by higher fracturing fluid injection rates. Therefore, creating more microseismic events can reduce measurement errors using MSM. Considering the inaccurate nature of the microseismic sensors, it is very important to accurately estimate states and unmeasurable output variables during the hydraulic fracturing process by taking advantage of the relationship between the fracturing fluid injection rate and measurement noise covariance in MSM technique.

1.2.4 Naturally fractured unconventional reservoirs

Field observations using advanced fracture diagnostic techniques of outcrops, core samples, and image logs show that discontinuities in shale such as natural fractures are commonly presented in unconventional reservoirs, acting as planes of weakness that divert hydraulic fracture propagation and generate complex fracture geometry [56, 57]. Natural fractures will interact with the hydraulic fractures and consequentially affect fracture fluid flow and proppant transport, which is critical for predicting the ultimate fracture geometry [58, 59]. The complex fracture geometry plays an important role in affecting well performance in unconventional oil and gas reservoirs.

Therefore, it is very important to consider the interactions with natural fractures to optimize hydraulic fracturing treatment in naturally fractured unconventional reservoirs.

1.3 Research objectives

The primary objective of this dissertation is to develop a model predictive control framework for the design of a pumping schedule to regulate the spatial variation of proppant concentration/ proppant bank height across the fracture at the end of pumping for conventional and unconventional reservoirs. The unifying theme is to develop a first-principle model of hydraulic fracturing process and to design a control framework to optimize the fracture geometry for enhanced productivity from shale formations. The specific objectives of this dissertation are to:

1. Develop a first-principle model of hydraulic fracturing process to obtain fundamental understanding of the proppant bank formation mechanism and its relationship to manipulated input variables such as the proppant concentration and flow rate of the injected fracturing fluids.

2. Design a model-based feedback controller to achieve the uniform proppant bank height and suspended proppant concentration along the fracture at the end of pumping for both of conventional and unconventional reservoirs by explicitly taking into account the desired fracture geometry, type of the fracturing fluid injected, total amount of injected proppant, actuator limitations, and safety considerations.

3. Study the physical mechanisms of simultaneously propagating multiple fractures and develop a model-based feedback controller to achieve a uniform proppant bank height by handling undesired stress-shadow effects.

4. Study the effect of microseismic measurement uncertainty on the performance of the proppant bank control in the hydraulic fracturing process and improve the control framework by taking advantage of the relationship between the fracturing fluid injection rate and the measurement noise covariance in MSM technique.

5. Analyze the interaction of hydraulic fractures with natural fractures and develop a model-based pumping schedule to maximize the total fracture surface area (TFSA) in naturally fractured unconventional reservoirs.

1.4 Dissertation layout

Following this chapter, Chapter 2 describes the development of a dynamic hydraulic fracturing model for the simulation of proppant transport, fracture propagation and proppant settling by considering single fracture propagation. Using this model, we then present a novel design framework for developing an optimal and practical pumping schedule in open-loop to achieve a uniform proppant concentration across fracture at the end of pumping. Finally, we apply the generated pumping schedule to the high-fidelity hydraulic fracturing model, and the performance is compared with Nolte's pumping schedule.

In Chapter 3, using the model developed in Chapter 2 for single fracture propagation, we design an online pumping schedule to achieve a uniform proppant concentration in conventional oil reservoirs by explicitly taking into account the desired fracture geometry, type of the fracturing fluid injected, total amount of injected proppant, actuator limitations, and safety considerations.

In Chapter 4, we improve the model developed in Chapter 2 for unconventional reservoirs to describe the dominant proppant settling behavior during hydraulic fracturing by considering single fracture propagation. Then, we design a real-time model-based feedback control system to compute an optimal pumping schedule leading to a uniform proppant bank height along the targeted fracture length for enhanced productivity.

We extend this study to multi-stage hydraulic fracturing in Chapter 5. First, we present a dynamic model of hydraulic fracturing process to describe stress-shadow effects in simultaneously propagating multiple fractures. Then, we design a model-based design technique that computes the flow rate of fracturing fluids and perforation conditions to achieve uniform growth of simultaneously propagating multiple fractures by explicitly handling stress-shadow effects.

In chapter 6, we incorporate the proppant transport model into the dynamic model of hydraulic fracturing process to describe stress-shadow effects in simultaneously propagating multiple frac-

tures. Then, we design a real-time model-based feedback control system to compute online fracturing fluid pumping schedules to generate a uniform proppant bank height in simultaneously propagating multiple fractures.

Chapter 7 presents the effect of microseismic measurement uncertainty on the developed proppant bank control in Chapter 4. Using the the relationship between the fracturing fluid injection rate and the measurement noise covariance in MSM technique, we then improve the model-based feedback control system to regulate the uniformity of the proppant bank height along the fracture length and achieve accurate state and output estimation.

Chapter 8 primarily studies the interaction between hydraulic fractures and natural fractures to optimize hydraulic fracturing treatments in naturally fractured unconventional reservoirs. We propose a model-based feedback control system to determine the fracturing fluid pumping schedule that maximizes the TFSA, which will lead to an enhanced oil production rate from naturally fractured unconventional reservoirs. We demonstrate that by using the proposed control scheme, the TFSA can be greatly enhanced which will lead to an oil production rate greater than those of the existing pumping schedules which were developed without considering natural fractures.

2. MODELING OF HYDRAULIC FRACTURING AND DESIGN OF AN OPEN-LOOP OPTIMAL PUMPING SCHEDULE TO ACHIEVE A UNIFORM PROPPANT CONCENTRATION LEVEL IN CONVENTIONAL RESERVOIRS*

2.1 Introduction

In this chapter, we propose a theoretical framework to provide an open-loop practical pumping schedule. Unlike other pumping schedules [28, 29, 30], the proposed pumping schedule design technique explicitly takes into account the practical constraints such as the limit on the change of proppant concentration between pumping stages and the desired fracture geometry that has to be satisfied at the end of pumping to maximize the productivity of a stimulated well for a given amount of proppant particles. More importantly, motivated by many studies devoted to proppant transport [60, 61, 62, 63, 64, 65], the proposed pumping schedule design technique directly incorporates the effect of proppant concentration on the fracturing fluid viscosity.

This chapter is organized as follows: First, we present a dynamic model of hydraulic fracturing by taking into account elasticity theory, mass balance on local fluid, lubrication equation, pressure-width relationship, leak-off model and Stokes' law. Then, a simulator is developed to describe the spatiotemporal evolution of fracture geometries, suspended proppant concentration and proppant bank formation across the fracture, effectively handling the computational requirement attributed to coupling of multiple equations over the time-dependent spatial domain. Using the developed simulator, we propose a new methodological framework to design the optimal pumping schedule that can incorporate practical constraints while achieving a uniform proppant concentration level across the fracture at the end of pumping. Lastly, we present a series of results that demonstrate the performance of the generated pumping schedule compared to one of the most widely used pumping schedules, proposed by Nolte [28].

*Reprinted with permission from "Optimal pumping schedule design to achieve a uniform proppant concentration level in hydraulic fracturing" by Yang et al., 2017. *Computers & Chemical Engineering*, 101, 138-147, Copyright 2017 by Elsevier.

2.2 Dynamic modeling of hydraulic fracturing processes

In this work, a hydraulic fracturing process is characterized by the following two sub-processes: (1) fracture propagation, and (2) proppant transport.

2.2.1 Modeling of fracture propagation

The fracture propagation is modeled based on the following standard assumptions: (1) in ultra-low permeability formations, the fracture length is greater than its height; hence, the fracture propagation is described by using the Perkins, Kern, and Nordgren (PKN) model (Fig. 2.1), and the fluid pressure along the vertical direction is constant; (2) the fracture is confined within a single horizontal rock layer (with a constant height) as the formation layers above and below have sufficiently large stresses that the fracture cannot grow to the neighboring rock layers; (3) the rock properties such as Young's modulus and Poisson ratio remain constant with respect to time and space, and the fracturing fluid is assumed to be incompressible; and (4) because the fracture length is much greater than its width, the fracture propagation and proppant advection in the width direction are neglected. Since the bi-wing PKN model is mirror symmetric, we focus on the modeling of the one-wing fracture as presented in Fig. 2.1.

The PKN model is often used when the fracture length is significantly larger than the height and the height can be considered constant along the fracture. It results in an elliptical cross-sectional area available for flow. In this model, please note that the fracture shape is rectangular and the fracture cross-sectional area is elliptical.

2.2.1.1 Fluid momentum (lubrication theory)

The coordinate axes are defined as follows: x is the spatial coordinate in the fracture propagation direction and z is the spatial coordinate in the vertical direction. Thus, the unit vectors aligned with the x and z axes are denoted by $\hat{x}$ and $\hat{z}$, respectively. The flow of the fracturing slurry is assumed to be steady and fully developed, and it is driven by a sustained pressure gradient, $-\frac{dP}{dx}\hat{x}$, assuming no pressure gradient along the z-coordinate. Additionally, assuming that neither external forces nor instantaneous acceleration affecting the flow, the local flow rate into the horizontal

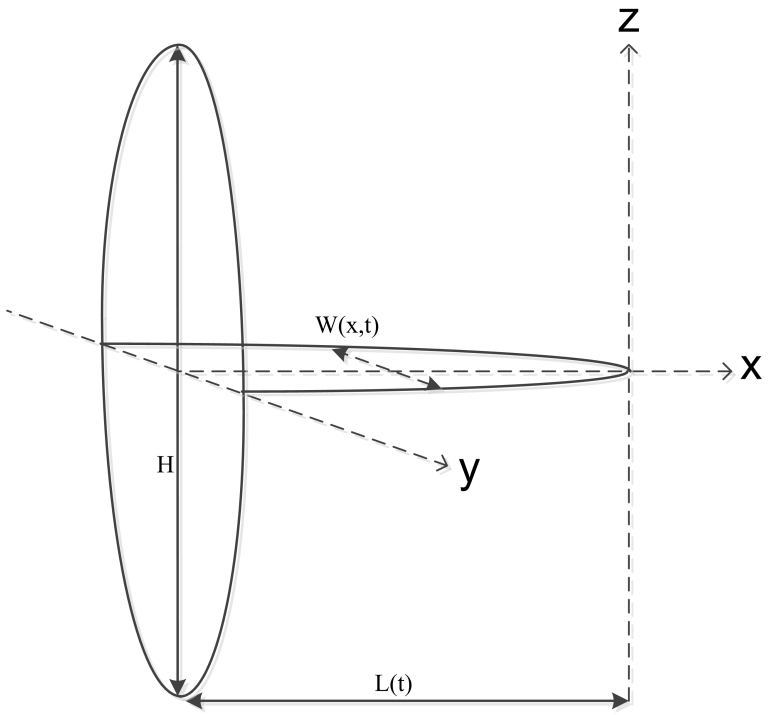

Figure 2.1: The PKN fracture model [1, 2].

direction, Q_x, for a Newtonian fluid is obtained by integrating the superficial fluid velocity into the horizontal direction, $V(x)\hat{x}$, over the cross-sectional area of an elliptic fracture, dA, which is presented below [2, 8]:

$$Q_x = \oint_{ellipse} V(x)dA = -\frac{\pi H W^3}{64\mu}\frac{dP}{dx} \tag{2.1}$$

where P is the net pressure that only depends on the x-coordinate, μ is the fracturing fluid viscosity, H is the fracture height and W is the fracture width.

2.2.1.2 Rock deformation (elasticity equation)

For a crack under constant normal pressure, the fracture shape is elliptical as presented in Fig. 2.1. The relationship between the maximum fracture width (i.e., the minor axis of the ellipse) and the net pressure loaded by fracturing fluids is given by the following equation [66, 67]:

$$W = \frac{2PH\,(1-\nu^2)}{E} \tag{2.2}$$

where ν is Poisson ratio of the formation and E is Young's modulus of the formation.

2.2.1.3 *The conservation of local fluid mass*

The local mass conservation of an incompressible fluid inside the fracture along the horizontal direction is given by [2]:

$$\frac{\partial A}{\partial t} + \frac{\partial Q_x}{\partial x} + HU = 0 \tag{2.3}$$

where $A = \pi W H/4$ is the cross-sectional area of the elliptic fracture [2], t is the elapsed time since the hydraulic fracturing process was initiated, and U is the rate of fluid leak-off into the formation. The two boundary conditions and an initial condition for Eq. (2.3) are formulated as follows:

$$Q_x(0,t) = Q_0 \quad \text{and} \quad W(L(t),t) = 0 \tag{2.4a}$$

$$W(x,0) = 0 \tag{2.4b}$$

where Q_0 is the injection rate of fracturing fluids at the wellbore (i.e., the manipulated input) and $L(t)$ is the fracture length. Substituting Eqs. (2.1) and (2.2) into Eq. (2.3) will generate the following nonlinear parabolic PDE model with the moving boundary:

$$\frac{\pi H}{4}\frac{\partial W}{\partial t} - \frac{\pi E}{128\mu(1-\nu^2)}\left[3W^2\Big(\frac{\partial W}{\partial x}\Big)^2 + W^3\frac{\partial^2 W}{\partial x^2}\right] + HU = 0 \tag{2.5}$$

2.2.1.4 *Carter's fluid leak-off model*

The model that describes the rate of fluid leak-off into the rock formation per unit height in the direction orthogonal to the elliptic fracture plane during the fracture propagation is presented as follow [8, 68]:

$$U = \frac{2C_{leak}}{\sqrt{t-\tau(x)}} \tag{2.6}$$

where C_{leak} is the overall fluid leak-off coefficient, and $\tau(x)$ is the time at which the fracture propagation has arrived at the location x for the first time.

2.2.2 Modeling of proppant transport

In this work, the modeling of proppant transport in both the horizontal and vertical directions is considered. In the horizontal direction, it is assumed that the injected proppant will travel at the fracturing fluid's velocity while in the vertical direction, the suspended proppant is assumed to have a settling velocity relative to the fracturing fluid due to the gravitational force.

2.2.2.1 Proppant advection

The advection of suspended proppant can be expressed by the following equation:

$$\frac{d\,(WC)}{dt} + \Delta \cdot (WCV_p) = 0 \tag{2.7}$$

$$C(0,t) = C_0(t) \quad \text{and} \quad C(x,0) = 0 \tag{2.8}$$

where C is the proppant volumetric concentration, $C_0(t)$ is the volumetric concentration of proppant injected at the wellbore, and V_p is the velocity with which the proppant particles are advected. Proppant particles are assumed to be sufficiently large so that the diffusive flux is neglected while the convective flux is considered. Therefore, the diffusive flux is neglected compared to convective flux. The interactions between the individual proppant particles are assumed to be negligible because of the low proppant concentration, and the drag and gravitational forces acting on proppant particles are considered. The relationship between the velocity of an individual proppant particle, V_p, the velocity of the fluid, V, and gravitational settling, V_s, is given by [69]:

$$V_p = V - (1 - C)V_s \tag{2.9}$$

2.2.2.2 Proppant settling

The gravity-induced proppant settling velocity in a slurry, V_s, is computed by [60],

$$V_s = \frac{(1-C)^2}{10^{1.82C}} \frac{(\rho_{sd} - \rho_f)\, g d^2}{18\mu} \tag{2.10}$$

where ρ_{sd} is the proppant particle density, ρ_f is the pure fluid density, g is the gravitational acceleration constant, d is the proppant diameter, and μ is the fracture fluid viscosity where its relationship with C can be modeled through the following empirical expression [70]:

$$\mu(C) = \mu_0 \left(1 - \frac{C}{C_{\max}}\right)^{-\alpha} \tag{2.11}$$

where μ_0 is the pure fluid viscosity, α is an exponent in the range of 1.2 to 1.8, and $C_{\max}$ is the theoretical maximum concentration, which is determined by $C_{\max} = (1-\phi)\,\rho_{sd}$ where ϕ is the proppant bank porosity. The particles settle out of the flow to the fracture bottom and forms a proppant bank. The evolution of proppant bank height, δ, by the settling flux at the boundary is described by [43, 71],

$$(1-\phi)\frac{d\,(\delta W)}{dt} = C V_s W \tag{2.12}$$

The proppant bank is initially of vanishing thickness $(\delta(x,0) = 0)$. Because of the dilute suspension, the proppant bank height will remain much smaller than the fracture height ($\delta \ll H$) unless the hydraulic fracturing operation continuous for a long period of time.

In order to describe the spatiotemporal evolution of important variables in hydraulic fracturing, there are challenges associated with coupling of nonlinear dynamic equations defined over the time-dependent spatial domain. For example, (1) rock deformation, fluid flow, and proppant transport are described by a set of highly coupled nonlinear equations; (2) leak-off rate has to be determined via iterations; (3) considering proppant settling and advection requires fine meshes; (4) the spatial domain changes with time; and (5) the number of discretized nonlinear algebraic equations to be solved for accurate solutions grows with time, significantly increasing the computational requirements [72, 73, 74, 75, 76, 77].

2.3 Numerical simulation

Motivated by these challenges, a novel numerical scheme is developed for efficiently solving these equations defined over the time-dependent spatial domain. In order to capture the detailed process dynamics of the system that has a boundary condition associated with the time-dependent

spatial domain, a fixed-mesh strategy is selected. Additionally, the size of integration time step is adopted on the basis of Courant-Friedrichs-Lewy (CFL) condition to handle the computational requirement effectively.

2.3.1 Numerical solution procedure

The steps of the proposed numerical algorithm are explained below:

1. At time step t_k, the fracture length, $L(t_{k+1})$, is obtained by elongating the fracture tip by Δx.

2. The coupled equations of lubrication theory and elasticity equations (Eqs. (2.1)–(2.6)) are solved to calculate the fracture width, $W(x, t_{k+1})$, net pressure, $P(x, t_{k+1})$, flow rate, $Q(x, t_{k+1})$, and the fluid velocity field, $V(x, t_{k+1})$.

3. Calculate $\tau(x_{k+1})$ in Eq. (2.5) iteratively by repeating Steps 2 and 3.

4. Advection and proppant settling equations (Eqs. (2.7)–(2.12)) are solved using the proppant solver with the updated fluid velocity field, $V(x, t_{k+1})$, to obtain suspended proppant concentration, $C(x, t_{k+1})$, settling velocity, $V_s(x, t_{k+1})$, and proppant bank height, $\delta(x, t_{k+1})$, across the fracture.

5. The time interval Δt_k is determined. For computational efficiency, the size of a numerical integration time step can be adapted based on the CFL condition.

6. Set $k \leftarrow k + 1$ and go to Step 1.

The schematic diagram of the above numerical algorithm is shown in Fig. 2.2. In this work, the fracture width changes more rapidly near the fracture tip compared to that near the wellbore, which provides room for improvement in the computational efficiency by increasing Δt near the wellbore according to the CFL condition. This technique has been widely accepted to improve the computational efficiency [78].

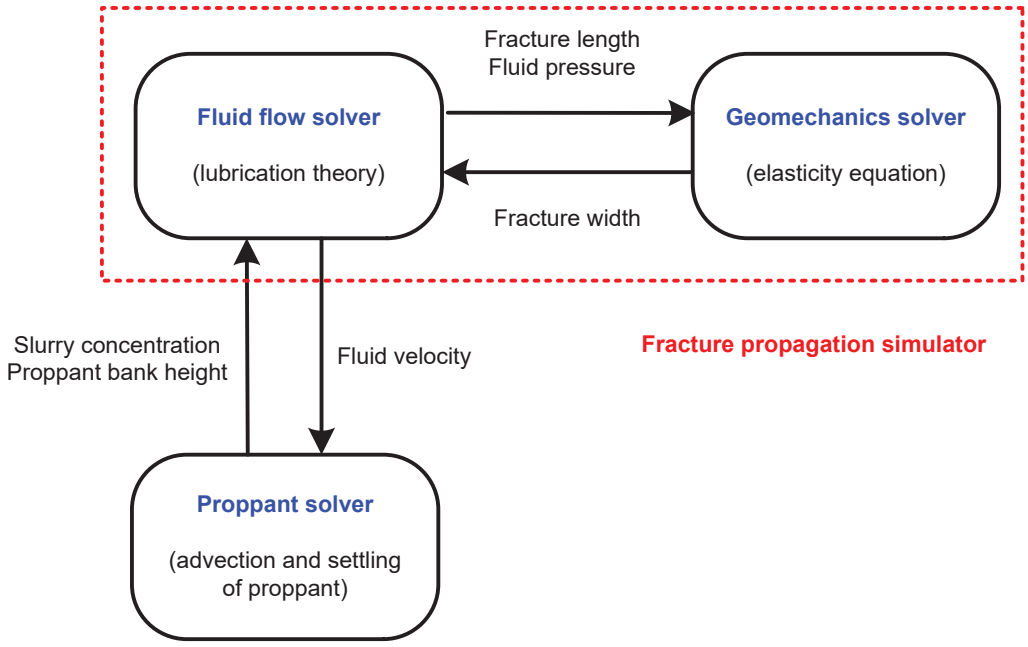

Figure 2.2: Schematic flow diagram of the numerical simulator.

2.4 Design of optimal pumping schedule

In hydraulic fracturing, the same propped volume may lead to different fracture productivity. For example, in a high-permeability formation, a wide and short fracture is preferred while in a low-permeability formation a narrow and long fracture is preferred [10]. Therefore, producing fractures with desired width and length are essential for productivity improvement, which can be explicitly considered through the UFD scheme explained in the following section.

2.4.1 Unified fracture design

UFD is an offline optimization-based technique to find a set of optimal values for the fracture width and length that maximizes the productivity of a stimulated well. For a given mass of proppant, M_{prop} (equivalently, for a given propped volume $V_{\text{p}} = M_{\text{prop}}/((1-\phi)\,\rho_{sd})$), to be injected to a reservoir well with a volume V_{r} and of a formation permeability k, there exists the optimal fracture conductivity C_{fd} at which the productivity index J_{D} becomes maximum. For the optimal C_{fd} value, a set of corresponding values for the fracture length and width is determined, which has to be satisfied at the end of pumping [11, 12]. More specifically, the steps for the UFD scheme are

as follow:

1. Determine the amount of proppant to be injected, M_{prop} (or equivalently, V_{p}).

2. Calculate the proppant number, N_{p}, which is given by the following expression:

$$N_{\text{p}} = \frac{2k_{\text{f}}V_{\text{p}}}{kV_{\text{r}}} \tag{2.13}$$

   where k_{f} is the fracture permeability which depends on the type of the proppant.

3. Determine the optimal fracture conductivity, C_{fd}, from the proppant number, N_{p} (please refer to Figs. 2 and 3 in [11]).

4. Calculate the optimal fracture length and width through the following formula:

$$L_{\text{opt}} = \left(\frac{k_{\text{f}}V_{\text{p}}}{2C_{\text{fd}}kh}\right)^{0.5} \quad \text{and} \quad W_{\text{opt}} = \left(\frac{C_{\text{fd}}kV_{\text{p}}}{2k_{\text{f}}h}\right)^{0.5} \tag{2.14}$$

When the generated fractures are being closed because of the surrounding natural stress after the pumping is stopped, which is known as fracture closure, the fracture width will decrease and eventually reach the optimal fracture width, W_{opt}, while the fracture length will remain identical. Therefore, the desired fracture length, L_{opt}, and fracture width, W_{opt}, have to be satisfied at the end of hydraulic fracturing treatment to achieve maximum productivity of a stimulated well.

Additionally, it is also very important to achieve a uniform proppant concentration level across the fracture at the end of pumping for effective extraction of oil and gas inside the reservoir. One of the most commonly used pumping schedules is developed by Nolte [28] where he provides a power-law type pumping schedule $\phi(t)$, which is formulated as follows:

$$\phi(t) = \begin{cases} \phi_d \left(\frac{t-t_p}{t_e-t_p}\right)^{\epsilon} & \text{for } t \geq t_p \\ 0 & \text{for } t < t_p \end{cases} \tag{2.15}$$

where ϕ_d is the target concentration, $\epsilon = (1-\eta)\,/\,(f_a+\eta)$ is an exponent calculated based on

the proppant mass balance equation for a given efficiency η, t_e is the total pumping time, f_a is the aggressiveness of the pad selection (total amount of pad) and $t_p = f_a \epsilon t_e$ is the time at which proppant injection is started. The amount of pad to be injected will depend on the value of f_a. For example, if $f_a > 1$, the pad amount will be higher than required (called conservative pumping schedules), while if $f_a < 1$, the pad amount to be injected will be less than required (called aggressive pumping schedules).

Another approach is proposed by Gu and Desroches [29], which suggests using an iterative scheme together with a detailed forward simulator to solve an inverse problem. One additional effort has been made by Dontsov and Peirce [30] based on the assumption that the proppant particles have a weak impact on the fracture propagation to generate a pumping schedule which is more accurate than Nolte [28] and less computationally challenging than Gu and Desroches [29]. However, the accuracy of this method deteriorates for high concentration levels, which limit its applicability to low proppant concentration regimes. We want to note that, none of these three pumping schedules explicitly consider the practical constraints for the design of optimal pumping schedules, which has motivated the design of the following pumping schedule.

2.4.2 Optimal pumping schedule

In this section, we introduce a novel methodology to design a practical yet optimal pumping schedule to achieve a uniform proppant concentration level across the fracture at the end of pumping. We consider the practical constraints such as the limit on the change of proppant concentration between pumping stages and the optimal fracture geometries which have to be satisfied at the end of pumping. The proposed methodology consists of two parts, (A) and (B). Part A is to achieve the desired fracture geometry at the end of pumping, which is described below:

1. Select the amount of proppant to be injected, M_{prop}.

2. Obtain the optimal fracture length, L_{opt}, and width, W_{opt}, from UFD.

3. Provide an initial guess for the fracture width at the **e**nd **o**f **p**umping, W_{eop}, which should be greater than the optimal fracture width ($W_{\text{eop}} > W_{\text{opt}}$).

4. Calculate the average viscosity, μ_{avg}, using the following equation:

$$\mu_{\text{avg}} = \frac{\mu(0) + \mu(C_{\text{target}})}{2} \tag{2.16}$$

where $\mu(0)$ and $\mu(C_{\text{target}})$ are the viscosity of the fluid at $C = 0$ (i.e. no proppant) and $C = C_{\text{target}}$ (i.e. target concentration at the end of pumping), respectively. C_{target} can be obtained through the following formula:

$$C_{\text{target}} = \frac{M_{\text{prop}}}{L_{\text{opt}} W_{\text{eop}} H} \tag{2.17}$$

5. Fix the flow rate, Q_0, and run the forward simulator by using μ_{avg} to obtain the total treatment time, t_e, pad time, $t_p = f_a \epsilon t_e$, and the fracture width at the end of pumping, W_{eop}, to reach L_{opt} at the end of pumping.

6. Using the updated W_{eop}, repeat Steps 4 to 5 until the simulation result converges.

After determining the pad and total treatment times (t_p and t_e), we focus on designing a practical pumping schedule to achieve a uniform proppant concentration level across the fracture at the end of pumping (Part B). The main idea of Part B of the proposed methodology for the pumping schedule design is the following: The target concentration profile can be approximated by linear combinations of multiple spatial concentration profiles, each of which is generated using the constant-concentration pumping schedules with the viscosity at the average concentration level. As a result, a practically-feasible target concentration profile is obtained (see Fig. 2.3.b). By assuming that there is no fluid backmixing, the amount of proppant particles injected between t_i and t_{i+1} in the pumping schedule (the area in red on Fig. 2.3.a) with the fixed proppant concentration $\phi_{\text{stage,i}}$ will be identical to the amount of proppant particles located between $x_{\text{stage,i}}$ and $x_{\text{stage,i+1}}$ (the area in red on Fig. 2.3.b) at the end of pumping. It will lead to an inverse problem which can be solved for the duration of each stage in the pumping schedule. The concentration unit used in this work is 1 pound of proppant added to the gallon of fluid (ppga), which is not a standard concentration def-

inition in chemical engineering, but it is popular in petroleum engineering. The detailed procedure for Part B of the proposed pumping schedule design technique to achieve a uniform concentration level is described below:

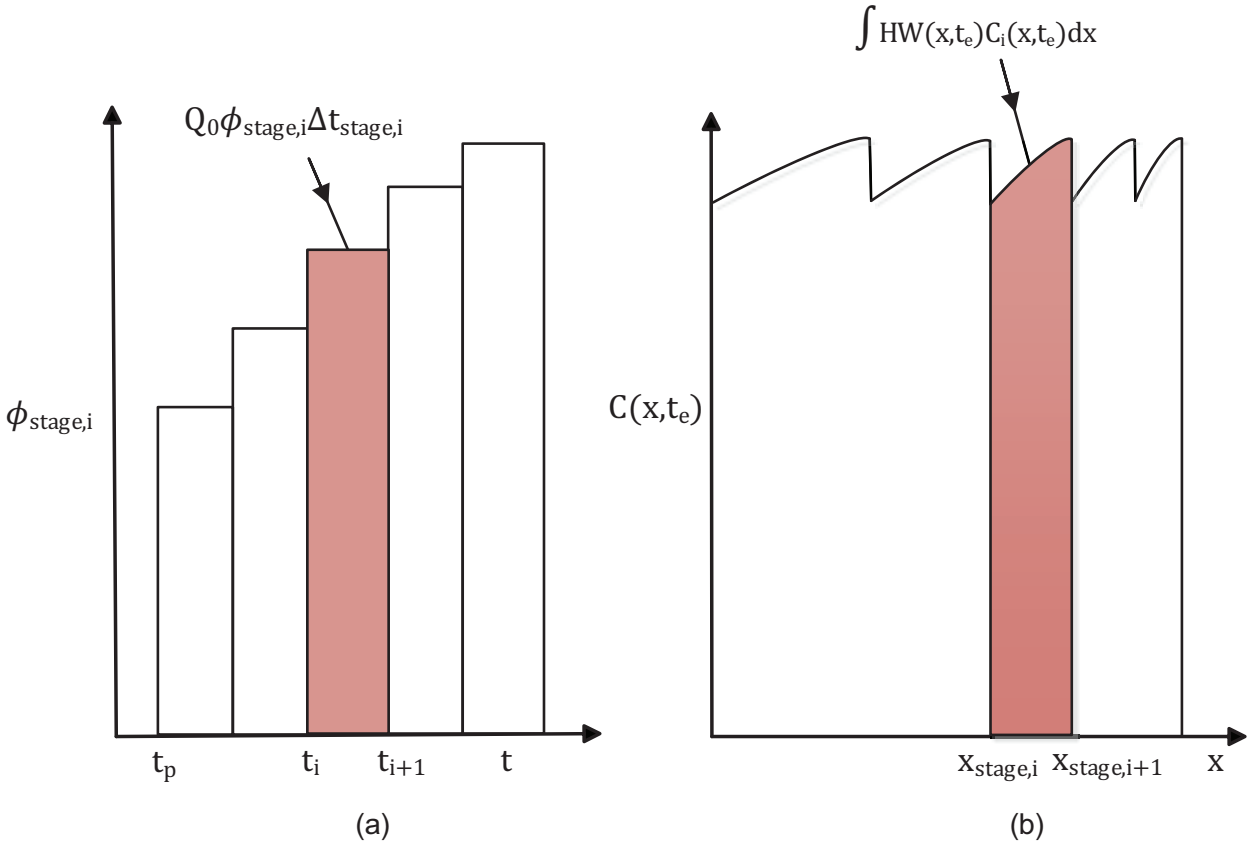

Figure 2.3: (a) proppant pumping schedule, and (b) practically-feasible target concentration profile.

1. For the fixed flow rate, Q_0, and pad time, t_p, run multiple forward simulations with constant-concentration pumping schedules, $\phi_{\text{stage,i}}(t) = i$, where $i \in \{1, 2, 3, ...\}$ in ppga.

2. For each constant-concentration pumping schedule, $\phi_{\text{stage,i}}$, obtain the corresponding spatial proppant concentration profiles at the end of pumping, $C_i(x, t_e)$.

3. Find the following piecewise practically-feasible target concentration profile

$$C(x,t_e)=\begin{cases} C_1(x,t_e) & \text{if } 0\le x<x_{\text{stage,1}} \\ C_2(x,t_e) & \text{if } x_{\text{stage,1}}\le x<x_{\text{stage,2}} \\ \vdots & \\ C_{\text{n}}(x,t_e) & \text{if } x_{\text{stage,n}-1}\le x<x_{\text{stage,n}}=L_{\text{opt}} \end{cases} \tag{2.18}$$

where $x_{\text{stage,1}},...,x_{\text{stage,n}}$ should be determined to minimize $\left(C(x,t_e)-C_{\text{target}}\right)^2$ where C_{target} is the ideal target concentration.

4. With identified $x_{\text{stage,i}}$ and $x_{\text{stage,i+1}}$, determine the time interval, $\Delta t_{\text{stage,i}}$, of the corresponding stage i, by solving the following inverse problem based on a mass balance equation on proppant:

$$Q_0\times\phi_{\text{stage,i}}\times\Delta t_{\text{stage,i}}=\int_{x_{\text{stage,i}}}^{x_{\text{stage,i+1}}}HW(x,t_e)C_{\text{i}}(x,t_e)dx \tag{2.19}$$

The generated pumping schedule uses the average viscosity to consider the effect of proppant particles on fracture propagation. We can further improve the performance of the generated pumping schedule by iteratively adjusting the pad time, t_p, and the total treatment time, t_e, from the simulation results. A flowchart for the proposed methodological framework to design an optimal pumping schedule is presented in Fig. 2.4.

Remark 1. *The plant-model mismatch and the uncertainties in process model parameters (fracture height and leak-off coefficient) can be an issue in implementing the proposed pumping schedule, which can be handled through the design of a feedback control system that uses a set of real-time measurements as a feedback from the system. In practice, we have very limited access to real-time measurements such as the fracture width at the wellbore and the fracture length.*

Remark 2. *The whole problem of pumping schedule design can be formulated as an optimization*

problem including the practical considerations such as the amount of proppant to be injected, limit on the range of proppant concentration inside the fracture, optimal fracture geometry as constraints. To avoid a high computational requirement, a reduced-order model can be derived to describe the spatiotemporal evolution of the important variables of the hydraulic fracturing process.

Remark 3. *The operation of hydraulic fracturing can be viewed as a 'batch' process. A system identification method can be applied to obtain, for example, a state-space model, which will be used within the optimization problem that can be solved to obtain an optimal pumping schedule.*

2.5 Simulation results

In this section, we initially obtained the optimal fracture geometry using the UFD scheme which will maximize the productivity of a stimulated well for a given amount of proppant particles. Then, we applied the proposed methodology for the design of an optimal yet practical pumping schedule to achieve a uniform proppant concentration level across the fracture at the end of the pumping. The values of the model parameters used in our simulations are listed in Table 2.1. Specifically, we injected a total amount of $48000\ \mathrm{kg}$ proppant over the entire hydraulic fracturing treatment. For this fixed amount, we obtained the corresponding optimal fracture length $L_{\mathrm{opt}} = 135\ \mathrm{m}$ and width $W_{\mathrm{opt}} = 5.4\ \mathrm{mm}$ as per Steps 1-2 in Part A of the proposed methodology, which are used as constraints that have to be satisfied at the end of pumping.

To achieve the above optimal fracture geometry, we subsequently followed Steps 3-6 in Part A of the proposed methodology. In particular, we used a constant flow rate of $Q_0 = 0.03\ \mathrm{m}^3/\mathrm{s}$ throughout the entire hydraulic fracturing treatment. With this flow rate, the simulation was carried out to determine the total treatment time, t_e, pad time, t_p, and fracture width at the end of pumping, W_{eop}, in order to reach the desired fracture length of $L_{\mathrm{opt}} = 135\ \mathrm{m}$. The spatiotemporal evolution of the fracture width and length is shown in Fig. 2.5. It is observed that the growth rate of the fracture width is initially very high, but it slows down with time, while the fracture length grows steadily with a constant flow rate. Additionally, Fig. 2.6 shows how the fracture width changes

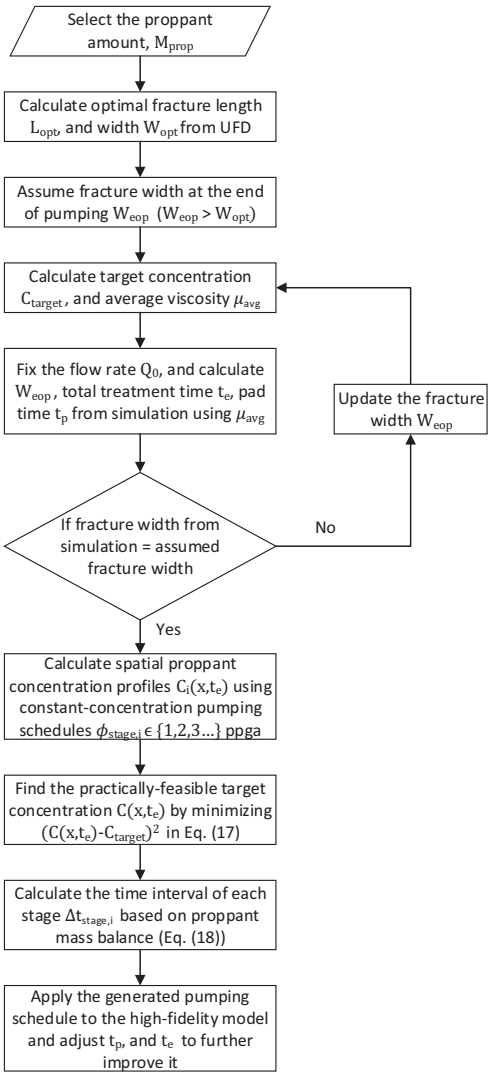

Figure 2.4: Flowchart for the optimal pumping schedule design procedure.

with time at the wellbore. Both Figs. 2.5 and 2.6 clearly indicate that the system never reaches steady-state.

We now continue with the design of the optimal pumping schedule as per Steps 1-4 in Part B of the proposed methodology using the calculated average viscosity, total treatment time, t_e, and pad time, t_p. With the average viscosity and developed dynamic model, we executed a total of 6 forward simulations using the constant-concentration pumping schedules: 4, 5, 6, 7, 8, 9 ppga. The difference between the values are selected to account for a limit on the change of proppant concen-

Parameter	Symbol	Value
Leak-off coefficient	C_{leak}	$6.3 \times 10^{-5}\ \text{m/s}^{1/2}$
Maximum concentration	$C_{\max}$	0.64
Young's modulus	E	$0.5 \times 10^{10}\ \text{Pa}$
Proppant permeability	k_{f}	$60000\ \text{mD}$
Formation permeability	k_{r}	$1.5\ \text{mD}$
Vertical Fracture height	H	$20\ \text{m}$
Proppant particle density	ρ_{sd}	$2648\ \text{kg/m}^3$
Pure fluid density	ρ_f	$1000\ \text{kg/m}^3$
Fracture fluid viscosity	μ	$0.56\ \text{Pa} \cdot \text{s}$
Poisson ratio of formation	ν	0.2

Table 2.1: Model parameters used for the simulation.

tration between pumping stages, which is 1 ppga/stage. For each constant-concentration pumping schedule, the spatial proppant concentration distribution along the fracture at the end of pumping is obtained, and they are plotted altogether in Fig. 2.7 with the ideal target concentration, C_{target}. It is observed that due to leak-off of the fluid mixture, proppant concentration level increases along the fracture length. Motivated by this, a practically-feasible target concentration was obtained by linear combinations of the generated spatial concentration profiles as shown in Fig. 2.8. Then, we applied mass balance, Eq. (2.19), to each piece of the practically-feasible target concentration profile to determine the duration of the corresponding constant-concentration stage in the pumping schedule. The generated pumping schedule, which is based on the average viscosity, was applied to the high-fidelity model, and t_e and t_p are adjusted to improve its performance, which is presented in Fig. 2.9. As a result, the spatial proppant concentration obtained at the end of pumping is presented in Fig. 2.10 along with ideal target concentration. The difference between the two profiles increases along the fracture and it reaches maximum particularly at the fracture tip, which is attributed to the extra time during which more leak-off can take place.

We also studied the effect of f_a to the spatial concentration profile at the end of pumping. The value of f_a will affect the total amount of pad to be injected. Pumping the sufficient amount of pad to create the fracture with the selected length, L_{opt}, is important. An ideal schedule for a

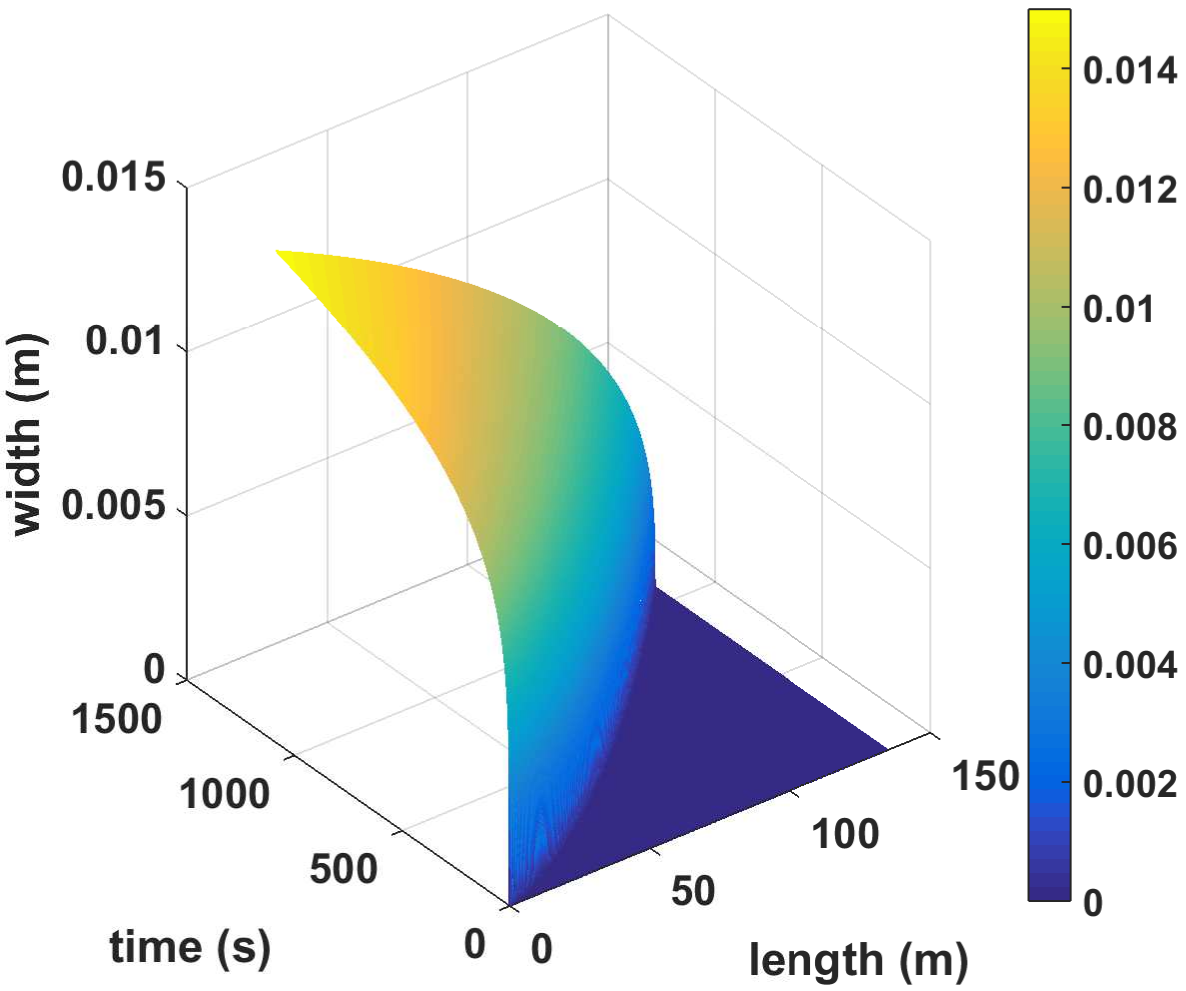

Figure 2.5: Spatiotemporal evolution of the fracture width.

fracture treatment is the one where the pumping stops as soon as the proppant front reaches the fracture tip at the specified fracture length, L_{opt}, to prevent a premature tip screenout behavior. To study the effect of f_a, we carried out the simulations with the high-fidelity model for the proposed pumping schedule with three different f_a values ($f_a = 0.3$, 0.6 and 0.9), which will directly affect the pumping schedule through $t_p = f_a \epsilon t_e$. The spatial proppant concentrations at the end of pumping for different f_a values are shown in Fig. 2.11. It is observed that for $f_a = 0.9$, the spatial concentration profile at the end of pumping is close to the target concentration but the propped

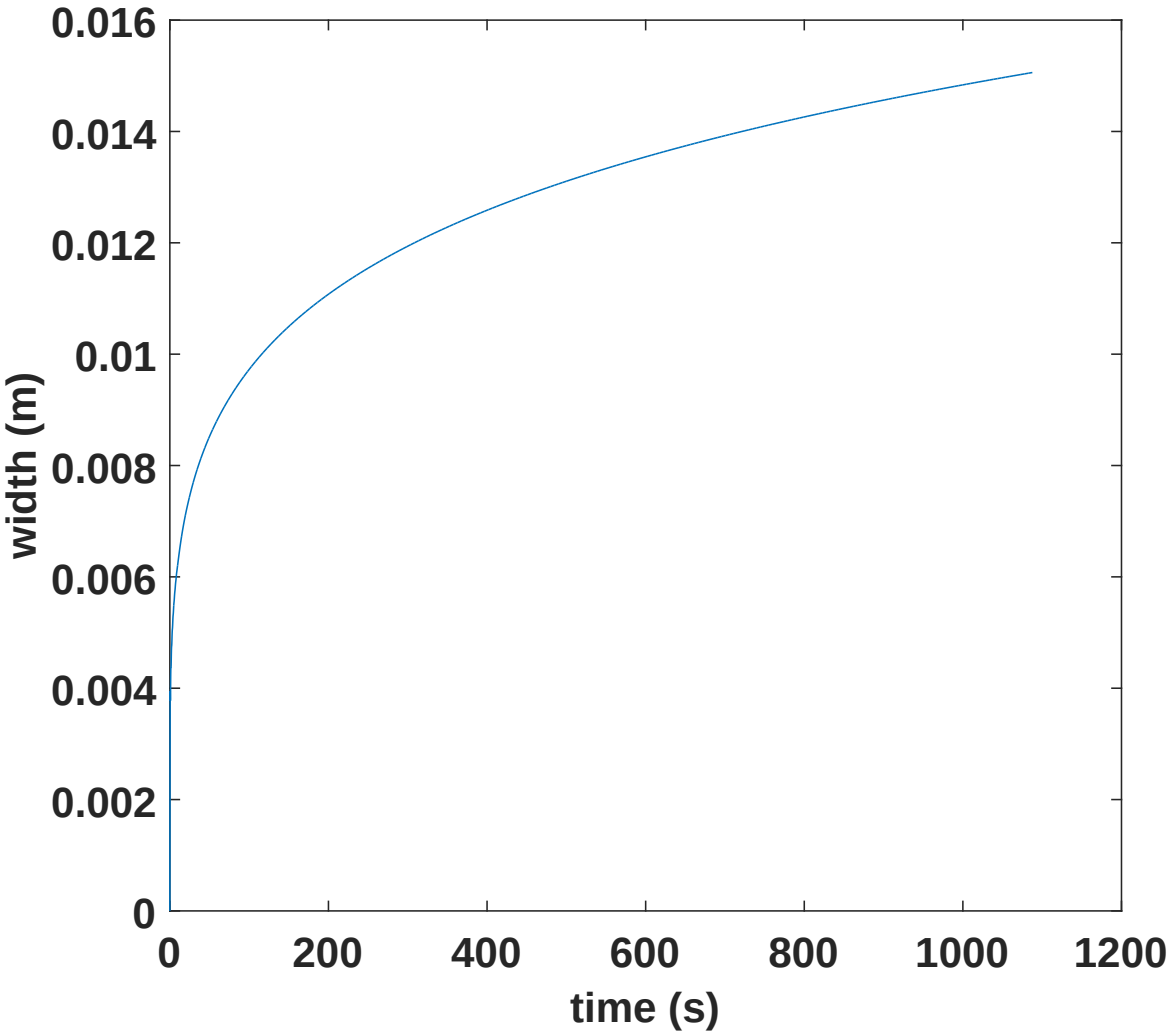

Figure 2.6: The evolution of the fracture width at the wellbore with time.

length is short. In this case, the amount of pad injected is more than required, leaving a large, unpropped region near the fracture tip. On the other hand, for $f_a = 0.3$, the concentration profile deviates from the target, particularly at the fracture tip. However, it produces a longer propped fracture length as the pad size is close to the ideal amount. Therefore, depending on the f_a value, the generated pumping schedule can create a fracture with the desired propped length and the spatial proppant concentration profile at the end of pumping.

After the role of f_a on pad size is investigated, we compare the proposed pumping schedule

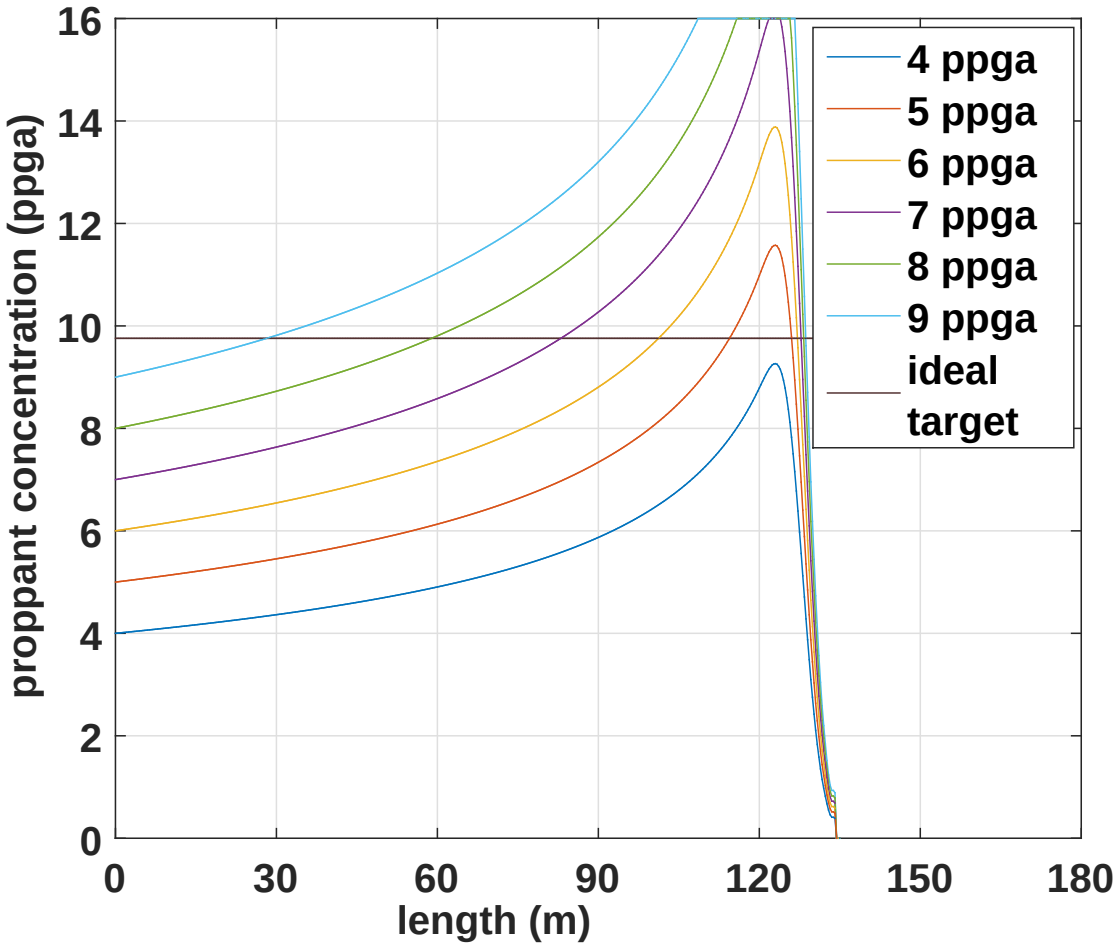

Figure 2.7: Spatial proppant concentration profiles obtained at the end of pumping for different constant-concentration pumping schedules.

with Nolte's pumping schedule [28]. The spatial proppant concentration profiles obtained from the proposed method and Nolte's pumping schedule are shown in Fig. 2.12. It can be observed that the spatial concentration obtained at the end of pumping using the proposed method is closer to the target concentration compared to that of Nolte's pumping schedule. Fig. 2.9 compares the pumping schedules of the two methods. It is observed that the schedule generated using the proposed method introduces proppant very aggressively in the beginning and levels off to Nolte's pumping schedule. The total treatment time is similar in the both schedules. Therefore, we can view the generated pumping schedule as the projection of Nolte's pumping schedule onto the feasible space

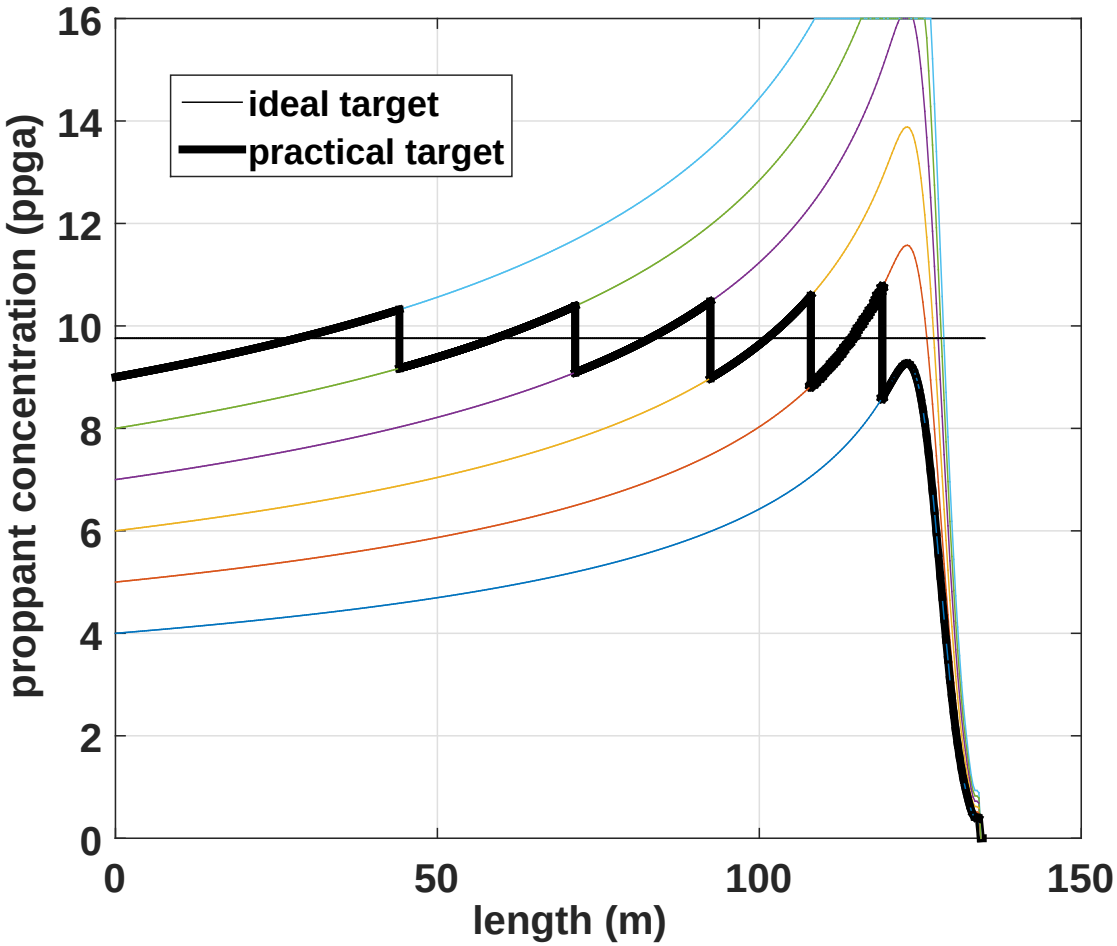

Figure 2.8: Practically-feasible target concentration (bold line) that minimizes the error from the ideal target concentration.

constructed by considering operational constraints to achieve a uniform concentration level at the end of pumping across the fracture.

Specifically, the developed dynamic model is used to describe the spatiotemporal evolution of proppant settling because of gravity and thereby proppant bank formation using the proposed pumping schedule design technique. Fig. 2.13 shows the proppant bank height at the end of pumping. It is observed that the maximum proppant bank height is only 0.2% of the total fracture height, and it decrease along the fracture. Under the operating condition of interest, the degree of proppant bank formation is negligible, which is attributed to the high flow rate and high viscosity

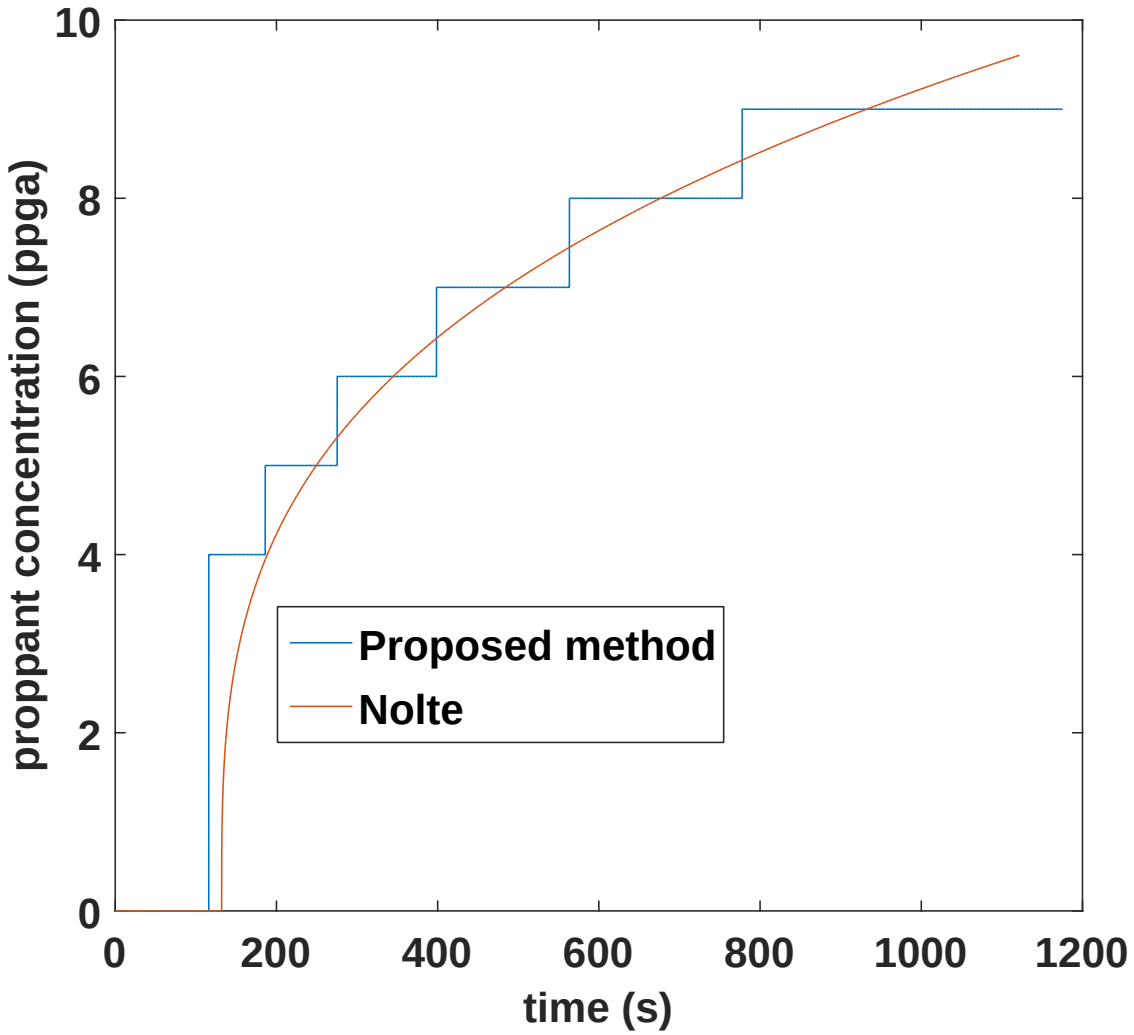

Figure 2.9: Pumping schedules generated using the proposed design technique and Nolte's method.

of the fluid mixture which prevents fast proppant settling. Therefore, the effect of proppant settling is not explicitly considered in the design of proppant pumping schedules.

Overall, the proposed methodological framework will offer a systematic approach for the design of pumping schedule to achieve a uniform proppant concentration level across the fracture at the end of pumping by directly taking into account the effect of proppant concentration to the fluid viscosity. Therefore, it can be applied to a broad range of proppant concentrations while the schedule developed by Dontsov and Peirce [30] is limited to low concentrations where the concentration

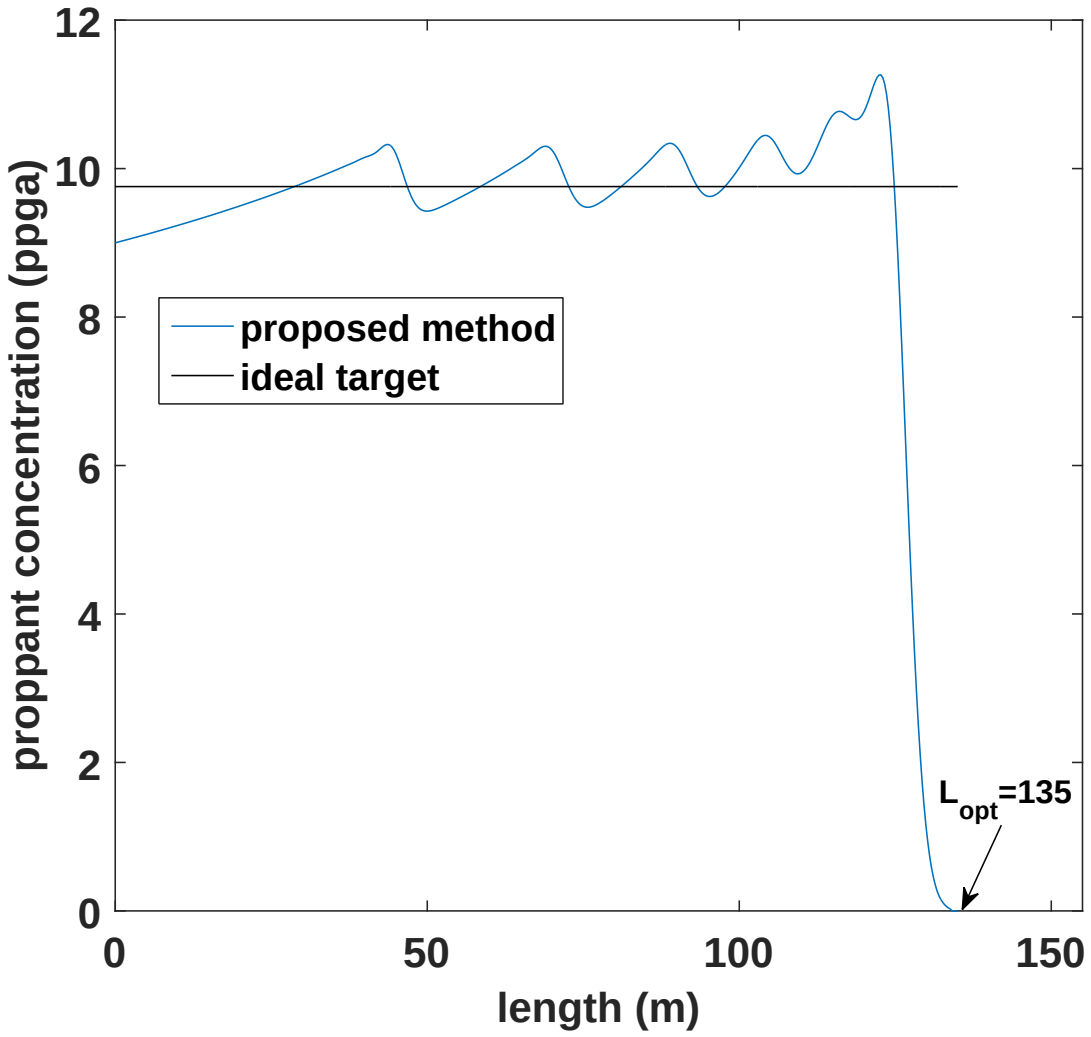

Figure 2.10: Spatial proppant concentration profile obtained at the end of pumping using the generated pumping schedule.

dependence of viscosity can be negligible. Furthermore, it requires fewer iterations compared to Gu and Desroches [29], which used a proppant transport model to solve an inverse problem iteratively, because we start with a guided initial guess (i.e. pumping schedule). Last but not least, the generated pumping schedule is more practical compared to other pumping schedules as it directly considers operating constraints such as the limit on the change of proppant concentration between pumping stages and the desired fracture geometry that maximizes the productivity of a stimulated well for a given amount of proppant.

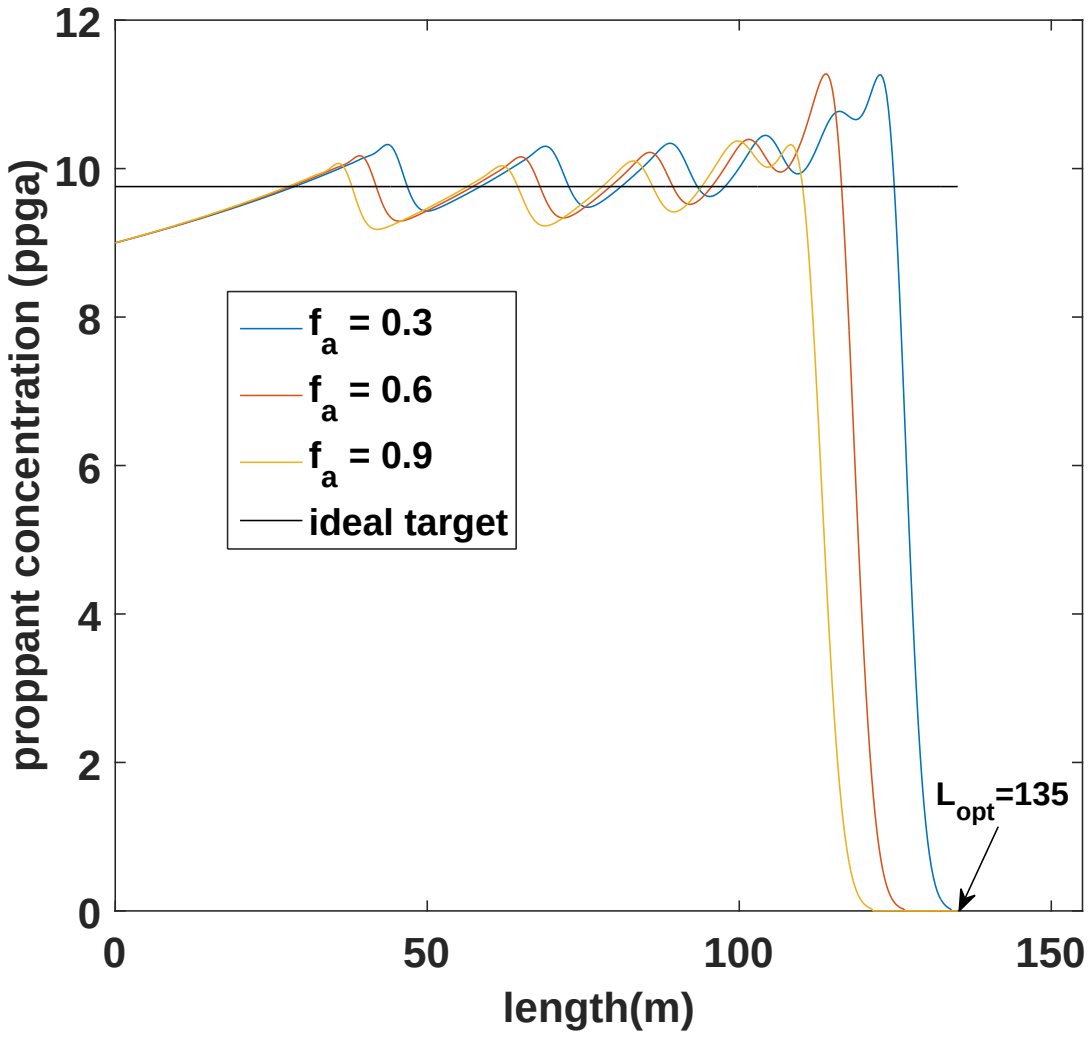

Figure 2.11: Spatial proppant concentration profiles obtained at the end of pumping for different f_a values.

2.6 Conclusions

In this work, we developed a dynamic hydraulic fracturing model for the simulation of proppant transport, fracture propagation and proppant settling. Using the developed dynamic model, we proposed a new methodological framework for the design of an optimal and practical proppant pumping schedule to achieve a uniform proppant concentration level across the fracture at the end of pumping. First, the effect of proppant particles on fracture propagation was approximated by us-

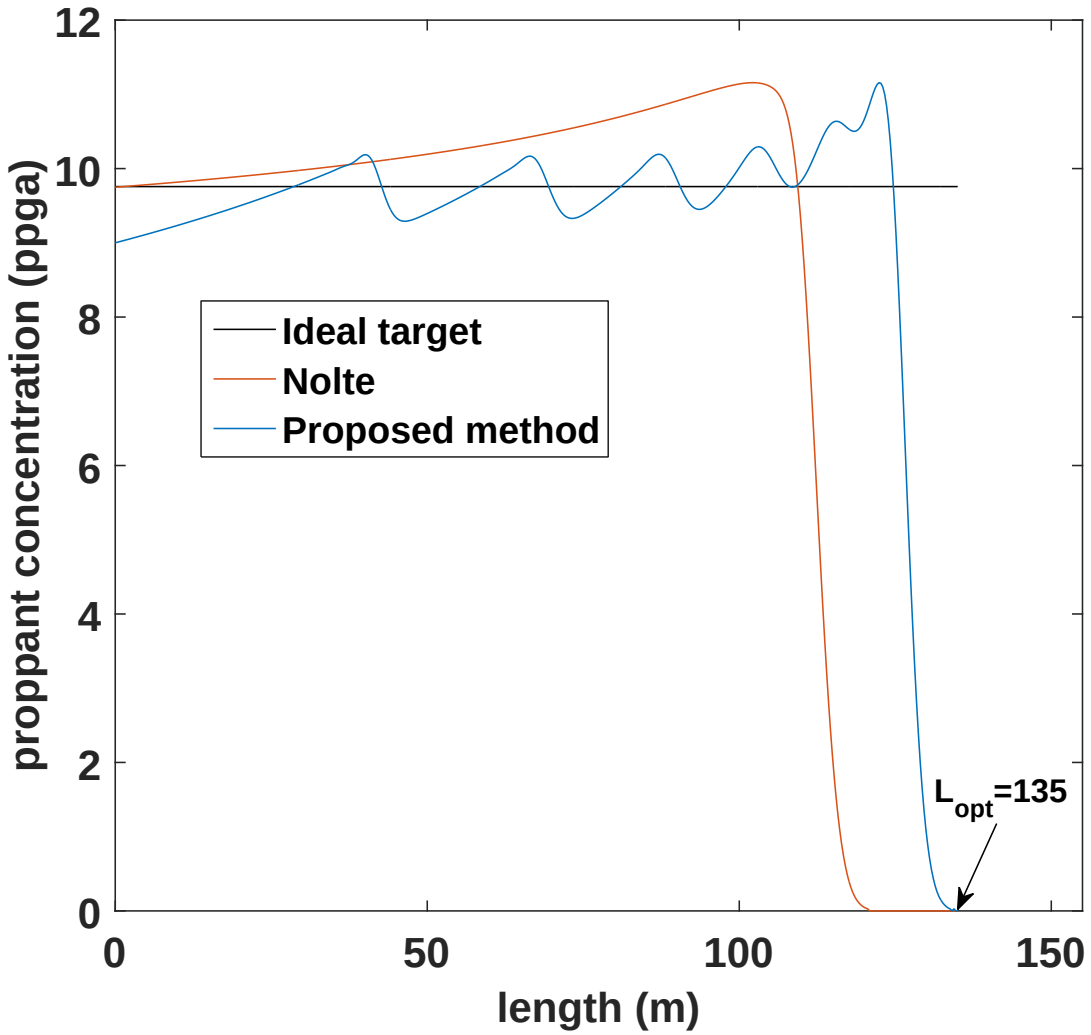

Figure 2.12: Spatial proppant concentration profiles obtained at the end of pumping using the proposed method and Nolte's pumping schedule.

ing the viscosity at the average proppant concentration level during the entire hydraulic fracturing treatment. With the average viscosity, a set of multiple spatial concentration profiles was generated by using the developed dynamic model with different constant-concentration pumping schedules. Second, the target concentration was approximated by linear combinations of the generated spatial concentration profiles to obtain the practically-feasible target concentration profile. Third, mass balance was then applied to calculate the time interval of each pumping stage with constant proppant concentration in the pumping schedule. The generated pumping schedule was applied to the

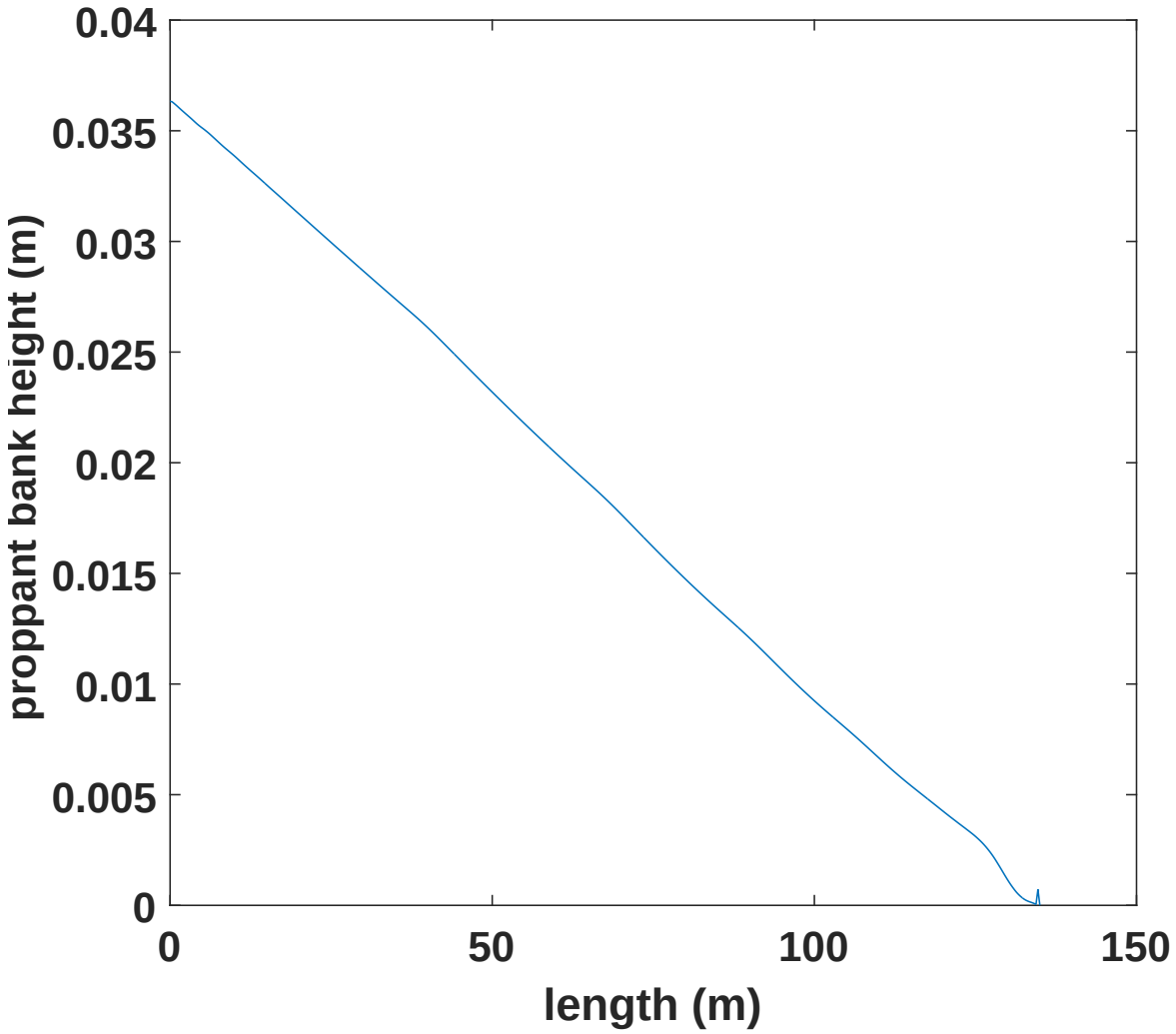

Figure 2.13: Proppant bank height along the fracture length at the end of pumping.

high-fidelity model, and the obtained spatial concentration profile at the end of pumping was very close to the target concentration, compared to Nolte's pumping schedule, which is one of the most commonly used pumping schedules. Therefore, the proposed methodology was able to generate an optimal pumping schedule with a small computational requirement, while taking into account practical constraints such as the limit on the change of proppant concentration between pumping stages and the desired fracture geometry that has to be satisfied at the end of pumping to maximize the productivity of a stimulated well for a given amount of proppant particles.

3. DESIGN OF ONLINE PUMPING SCHEDULES TO ACHIEVE UNIFORM PROPPANT CONCENTRATION IN CONVENTIONAL OIL RESERVOIRS*

3.1 Introduction

In Chapter 2, we presented a novel design framework for developing an optimal and practical pumping schedule. However, we viewed hydraulic fracturing processes as an open-loop problem, which has motivated this work that considers the closed-loop operation of a hydraulic fracturing process utilizing the available real-time measurements as feedback to adjust the pumping schedule online. We focus on the development of a model predictive control framework to regulate the spatial variation of proppant concentration across the fracture at the end of pumping. Unlike other pumping schedules [28, 29, 30, 79], the proposed control framework will generate an optimal pumping schedule by utilizing the real-time measurements to estimate unmeasurable states as well as considering the fact that a pumping schedule consists of multiple substages where the concentration can vary and the desired fracture geometry that has to be satisfied at the end of pumping.

This chapter is organized as follows: First, available open-loop pumping schedule design techniques are presented. Next, a reduced-order model is developed using the simulator results, based on which a Kalman filter is designed to estimate unmeasurable states such as the proppant concentration inside the fracture. Lastly, a model predictive controller that uses the available state estimates is designed to achieve uniform proppant concentration across the fracture at the end of pumping.

3.2 Dynamic modeling of hydraulic fracturing processes

The dynamic model presented in Section 2.1 is used to simulate hydraulic fracturing process.

*Reprinted with permission from "Modeling of hydraulic fracturing and designing of online pumping schedules to achieve uniform proppant concentration in conventional oil reservoirs" by Siddhamshetty et al., 2018. *Computers & Chemical Engineering*, 114, 306-317, Copyright 2018 by Elsevier.

3.3 Open-loop pumping schedule

In hydraulic fracturing, it is very important to achieve uniform proppant concentration across the fracture at the end of pumping for effective extraction of oil and gas inside the reservoir. One of the most commonly used pumping schedules is developed by Nolte [28] where he provided a power-law type pumping schedule $C_0(t)$, which is formulated as follows:

$$C_0(t) = \begin{cases} C_{target} \left(\frac{t - t_p}{t_e - t_p} \right)^{\epsilon} & \text{for } t \geq t_p \\ 0 & \text{for } t < t_p \end{cases} \tag{3.1}$$

where C_{target} is the target concentration, $\epsilon = (1 - \eta) \,/\, (1 + \eta)$ is an exponent calculated based on the proppant volume balance for a given efficiency η, t_e is the total pumping time, and $t_p = \epsilon t_e$ is the time at which proppant injection is started.

Fig. 3.1 shows the obtained spatial proppant concentration profile using multiple pumping schedules along with the target concentration profile. In this case, we injected a total amount of 48000 kg proppant over the entire hydraulic fracturing treatment. For this amount of proppant, the optimal fracture length calculated using UFD is 135 m, which will be discussed later in Section 3.4.1. The concentration unit used in this work is 1 pound of proppant added to the gallon of fluid (ppga), which is not a standard concentration unit in chemical engineering, but it is popular in petroleum engineering. First, it was observed that the constant-concentration pumping schedule was not able to achieve uniform proppant concentration. This is due to the leak-off of the fracturing fluid during the hydraulic fracturing operation, which will increase the proppant concentration along the fracture length. Second, Nolte's pumping schedule was able to generate uniform proppant concentration near the wellbore, but the discrepancy from the target concentration increases with the fracture, leading to a short propped length compared to the target length of 135 m. This is because the predefined formula did not estimate the leak-off amount accurately, due to the process-model mismatch, leading to the early termination of the hydraulic fracturing process.

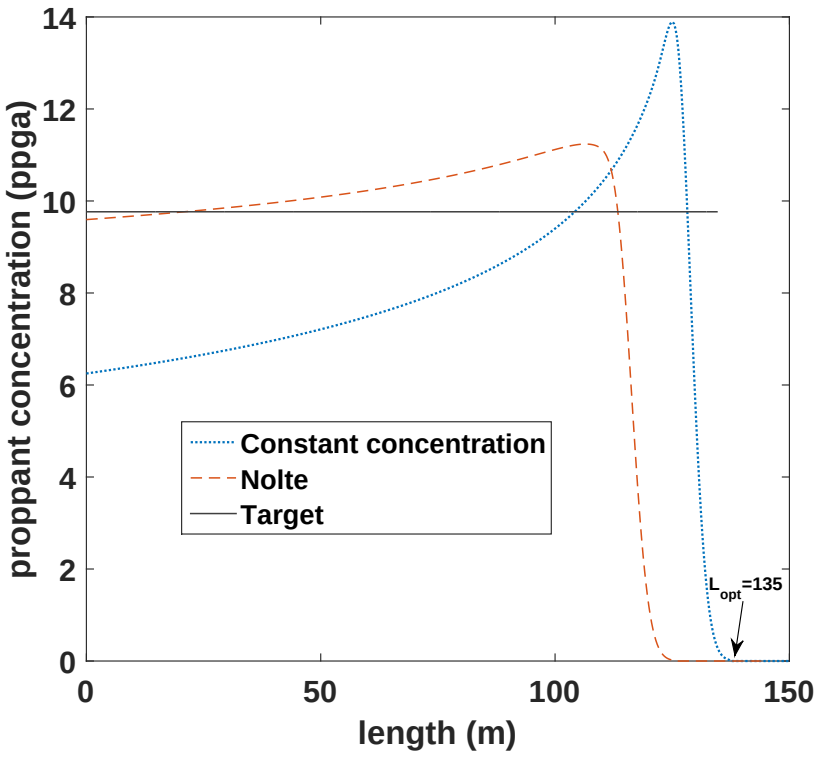

Figure 3.1: Comparison of spatial proppant concentration profiles obtained at the end of pumping under different pumping schedules.

Additionally, there are other pumping schedules proposed by Gu et al. and Dontsov et al. [29, 30] where the former is computationally expensive while the application of the latter is limited to low proppant concentration. It is important to point out that the above-mentioned pumping schedule design techniques viewed the hydraulic fracturing operation as an open-loop problem, which may lead to poor performance if there is a plant-model mismatch and uncertainties in the process model parameters. Motivated by these considerations, in this work, we focus on the development of a control strategy that is able to regulate the spatial variation of proppant concentration across the fracture at the end of pumping, which will be further discussed in the following section.

3.4 Model predictive control for hydraulic fracturing systems

In this section, we first use the multivariable output error state-space (MOESP) algorithm to regress a linear time-invariant state-space model of the hydraulic fracturing process using the simulation results from the high-fidelity model. Typically, a set of real-time measurements readily avail-

able from the hydraulic fracturing system is limited to the wellbore pressure and microseismic data [80], which will be further analyzed to determine the fracture width at the wellbore (through the elasticity equation, Eq. (2.2)) and the fracture length, respectively. Based on the developed time-invariant state-space model, we will design a Kalman filter that uses the real-time measurements to estimate unmeasurable states such as the proppant concentration across the fracture. Then, we will present a model predictive control formulation that will compute a proppant pumping schedule to achieve uniform proppant concentration across the fracture at the end of pumping while explicitly taking into account practical, safety, and optimality considerations.

3.4.1 Unified fracture design

In hydraulic fracturing, depending on the geological condition of the rock formation, the same propped volume may lead to different fracture productivity. For example, in a high-permeability formation, a wide and short fracture is preferred while in a low-permeability formation, a narrow and long fracture is preferred [10]. Therefore, producing fractures with the desired width and length is essential for the high productivity of a stimulated well, which can be achieved through an optimization-based technique called UFD.

The UFD scheme is an offline technique that calculates a set of optimal values for the fracture width and length that maximizes the productivity index J_D when the amount of the proppant to be injected, the proppant permeability, the reservoir permeability, the pay-zone thickness, and the dimension of the fracture drainage volume are available [11, 12, 81]. The steps for the UFD scheme are briefly presented below:

1. For the amount of proppant to be injected, M_{prop}, calculate the proppant number, N_{p}, through the following expression:
$$N_p = \frac{2k_f M_{prop}}{(1-\phi)\,\rho_{sd} k V_r} \tag{3.2}$$
where k_f is the proppant permeability, and V_{r} is the reservoir volume.

2. Determine the optimal fracture conductivity, C_{fd}, which depends on the proppant number, N_p (please refer to Figs. 2 and 3 in [11]).

3. Calculate the optimal fracture length and width through the following formula:

$$L_{opt} = \left(\frac{k_f M_{\text{prop}}}{2C_{fd} k H \left(1-\phi\right) \rho_{sd}} \right)^{0.5} \quad \text{and} \quad W_{opt} = \left(\frac{C_{fd} k M_{\text{prop}}}{2k_f H \left(1-\phi\right) \rho_{sd}} \right)^{0.5} \tag{3.3}$$

When the pumping is stopped, the suspended proppant will be settled and the natural stress imposed by the surrounding rock formation will close the fracture opening all the way to the area already occupied by the proppant. Therefore, it is very important for the desired fracture length, L_{opt}, and width, W_{opt}, to be satisfied at the end of pumping to achieve the maximum productivity of a stimulated well, which will be introduced to the MPC formulation as a terminal constraint (Section 3.4.4). Additionally, a target concentration is calculated as follows:

$$C_{target} = \frac{M_{prop}}{H L_{opt} W_{opt}} \tag{3.4}$$

3.4.2 System Identification

Due to the infinite-dimensional nature of the models of Eqs. (2.1)–(2.12), they cannot be directly used for the purpose of controller design. While there are a variety of linear [82, 83, 84] and nonlinear [85, 86, 87, 88] model order-reduction techniques available, in this work, we developed a reduced-order model by applying the MOESP algorithm to regress a linear time-invariant state-space model of the hydraulic fracturing process, which is presented in the following form:

$$x(t_{k+1}) = Ax(t_k) + Bu(t_k) \tag{3.5a}$$

$$y(t_k) = Hx(t_k) \tag{3.5b}$$

where $y(t_k) = [W_0(t_k), L(t_k), C(x_1, t_k), C(x_2, t_k), C(x_3, t_k), C(x_4, t_k), C(x_5, t_k), C(x_6, t_k)]^{\mathrm{T}}$ denotes the vector of output variables, $W_0(t_k)$ is the fracture width at the wellbore, $L(t_k)$ is the fracture length, $C(x_1, t_k), ..., C(x_6, t_k)$ are the proppant concentration at 6 different locations across the fracture, and $u(t_k) = [C_0(t_k), C_0(t_k - \theta_{x_1}), C_0(t_k - \theta_{x_2}), C_0(t_k - \theta_{x_3}), C_0(t_k - \theta_{x_4}), C_0(t_k -$

$\theta_{x_5}), C_0(t_k - \theta_{x_6})]^{\mathrm{T}}$ is the inlet concentration at the wellbore (i.e, the manipulated input variable), and θ_{x_i} is the input time-delay due to the time required for the proppant to travel from the wellbore to a particular location x_i. We want to note that the model identification is performed once and offline using the data obtained from the high-fidelity process model or field experiments.

In the hydraulic fracturing system, the available real-time measurements are limited to the fracture width near the wellbore and fracture length. This leaves many important state variables, including the proppant concentration across the fracture, to be estimated through the design of a Kalman filter, which will be discussed in the following section.

Remark 4. *The linear discrete-time state space model is good for the purpose of this study. Specifically, we varied the input profile so that we can cover the entire range of operating conditions that are being considered in the field. As the reviewer mentioned, nonlinear MPC will definitely help because the governing equation is indeed a nonlinear parabolic PDE with the moving boundary. Recently, we have developed a local model order-reduction technique which will generate a nonlinear reduced-order model. Nonlinear MPC theory will be applied to this reduced-order model.*

3.4.3 State estimator design using Kalman filter

The process and measurement noise is added to the reduced-order model presented in Eq. (3.5) as follows:

$$x(t_{k+1}) = Ax(t_k) + Bu(t_k - \theta) + w(t_k) \tag{3.6a}$$

$$y(t_k) = Hx(t_k) + v(t_k) \tag{3.6b}$$

where w is the process noise which is assumed to be drawn from a zero mean multivariate normal distribution with covariance Q, and v is the measurement noise which is assumed to be zero mean gaussian white noise with covariance R.

The algorithm works in a two-step process: prediction and measurement update. Combining the prediction and measurement update steps, the Kalman filter equations are presented in the

following form:

$$\hat{x}(t_{k+1}) = A\hat{x}(t_k) + Bu(t_k - \theta) + M(t_k)(y_m(t_k) - \hat{y}(t_k)) \tag{3.7a}$$

$$M(t_k) = P(t_k)H^T(R(t_k) + HP(t_k)H^T)^{-1} \tag{3.7b}$$

$$P(t_{k+1}) = (I - M(t_k)H)P(t_k) \tag{3.7c}$$

where the operator $\hat{(\cdot)}$ is used to denote the estimated variables, $M(t_k)$ is the Kalman filter gain, and $P(t_k)$ denotes the covariance of the state estimation error.

Fig. 3.2 shows the comparison between the estimated and actual concentration profiles at 6 different locations. It can be observed that the state estimates of the proppant concentration at specific locations across the fracture quickly converge to the true values obtained from the high-fidelity model. In all instances, the effect of the measurement noise, often found in experimental readings, is simulated by introducing white noise with a fixed variance.

3.4.4 Pumping schedule formulation using model predictive controller

Within this regard, a novel model predictive control scheme is formulated for the design of a single-input multi-output feedback control system with the objective of minimizing the squared deviation of the proppant concentration across the fracture from the target concentration. The proposed control scheme is formulated in the following form:

$$\min_{C_{stage,k},\ldots,C_{stage,10}} \quad \sum_{i=1}^{6}(\hat{C}_i(t_f) - C_{target})^2 \tag{3.8a}$$

$$\text{s.t.} \quad \text{Kalman filter, Eq. (3.7)} \tag{3.8b}$$

$$\hat{W}_0(t_k) = W_0(t_k), \qquad \hat{L}(t_k) = L(t_k) \tag{3.8c}$$

$$C_{min} \leq \hat{C}_i(t_k + j\Delta) \leq C_{max} \tag{3.8d}$$

$$j = 0, \ldots, 10 - k \tag{3.8e}$$

$$C_{stage,k-1+m} \leq C_{stage,k+m} \leq C_{stage,k-1+m} + 4\ (ppga) \tag{3.8f}$$

$$m = 1, \ldots, 10 - k \tag{3.8g}$$

$$2Q_0\Delta\left(\sum_{k=1}^{10} C_{stage,k}\right) = M_{prop} \tag{3.8h}$$

$$\hat{L}(t_f) = L_{opt}, \qquad \hat{W}_0(t_f) \geq W_{opt} \tag{3.8i}$$

where t_f is the total treatment time, Δ is the sampling time, t_k is the current time, $\hat{C}_i(t_k)$ is the predicted proppant concentration inside the fracture at a specific location where $i = 1, \ldots, 6$, $W(t_k)$ and $L(t_k)$ are the measurements of the fracture width at the wellbore and fracture length at the k^{th} sampling time, which are the only measurable outputs in real-time with accuracy, and $C_{stage,k}$ is the inlet proppant concentration (i.e., manipulated inputs) of the k^{th} substage, which corresponds to $t \in [t_k, t_k + \Delta)$, which can be computed by solving Eq. (3.8) with a shrinking prediction horizon $N_p = t_f - t_k$. The schematic diagram of the closed-loop operation of hydraulic fracturing is presented in Fig. 3.3.

In the optimization problem of Eq. (3.8), the cost function of Eq. (3.8a) describes the squared variation of the proppant concentration at 6 different locations across the fracture at the end of pumping. A Kalman filter of Eq. (3.7) is used to predict the dynamic behavior of the proppant concentration at 6 spatial locations across the fracture as well as the fracture width at the wellbore and fracture length. The Kalman filter is initialized at every sampling time t_k utilizing the

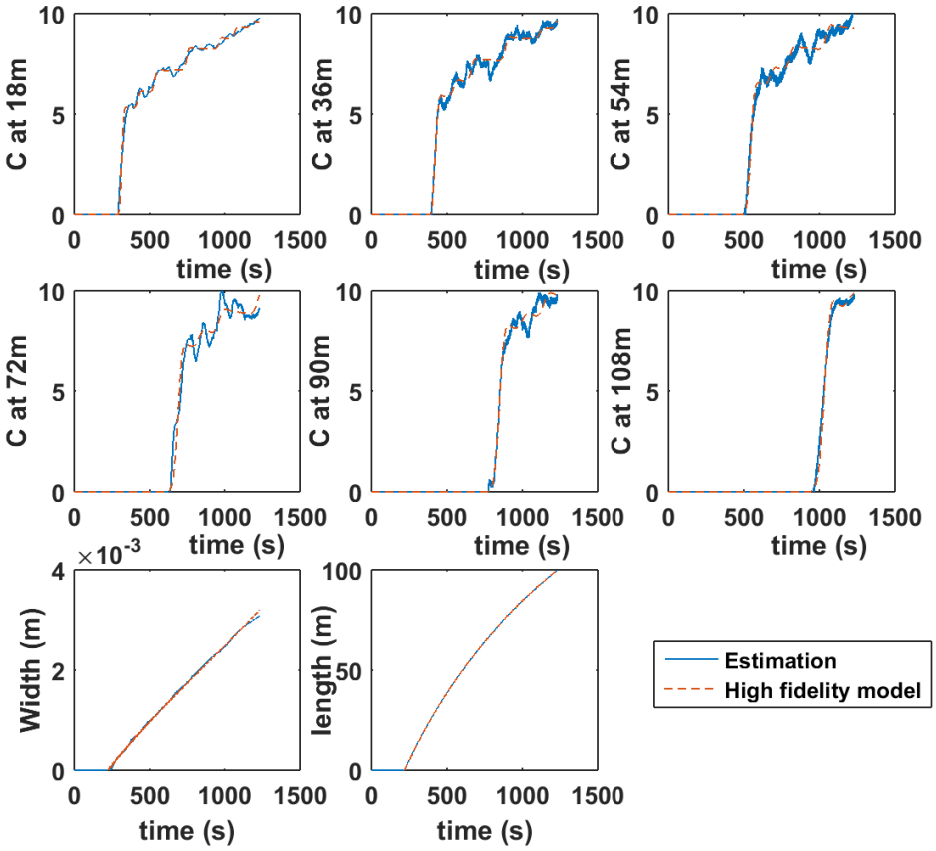

Figure 3.2: Comparison between the true values and the estimates of proppant concentration at 6 different locations.

real-time measurement of fracture width at the wellbore and fracture length, which is described by Eq. (3.8c). The constraint of Eq. (3.8d) imposes the limits on the state variables to avoid premature termination of the hydraulic fracturing process. The constraint of Eq. (3.8f) implies that the proppant concentration will be increased monotonically, but the increase should not be more than 4 ppga. The constraint of Eq. (3.8h) describes the amount of proppant to be injected over the entire hydraulic fracturing process. The optimal fracture geometry calculated by UFD will be employed through the terminal constraint of Eq. (3.8i).

Remark 5. *The real-time measurements readily available online from the hydraulic fracturing process are the fracture width at the wellbore (using the wellbore pressure data) and the fracture length (using the microseismic data). Without any human interaction, the data are processed auto-*

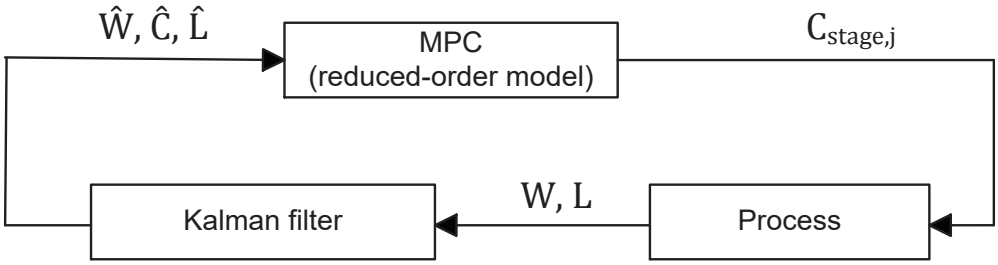

Figure 3.3: Closed-loop operation of hydraulic fracturing under MPC.

matically and provided almost in real-time. In particular, the microseismic data usually contains more measurement noise, because the geospones (i.e., sensors) are located on the surface while the event takes place at 10,000 ft below the surface. To handle this measurement noise, a geophysicist or other trained expert can review the data as they arrive and remove unrealistic samples before sending out final results at the expense of time delay in the measurement.

3.5 Closed-loop simulation results

In this section, we demonstrated the feasibility of the proposed control framework for the regulation of proppant concentration in hydraulic fracturing at the end of pumping. The dynamic model developed in Section 3.2 was utilized to simulate the hydraulic fracturing process. The values of the process model parameters used in our simulations are listed in Table 2.1. Specifically, we injected a total amount of 48000 kg proppant over the entire hydraulic fracturing treatment. For this fixed amount, we obtained the corresponding optimal fracture length $L_{\text{opt}} = 135$ m and width $W_{\text{opt}} = 5.4$ mm from UFD, which were introduced as a constraint (Eq. (3.8i)) in the MPC formulation that has to be satisfied at the end of pumping. These values were also used to calculate the target proppant concentration at the end of pumping, $C_{target} = 10$ ppga. Throughout the entire hydraulic fracturing treatment, we used constant flow rate of $Q_0 = 0.03$ m^3/s. The pad time, t_p, was fixed to be 220 s in order to reach the desired fracture length of $L_{\text{opt}} = 135$ m without tip screen-out (i.e., premature termination of the hydraulic fracturing process). The Kalman filter and feedback control system were initialized after the injection of pad (i.e., $t_k \geq t_p$). In the closed-loop simulation, Δ and t_f were chosen to be 100 s and 1220 s, respectively. The proppant pumping

schedule was divided into 10 substages and the duration of each substage was identical to the sampling time Δ. We assumed that at the beginning of each substage, the real-time measurements of $W_0(t_k)$ and $L(t_k)$ are available, which are used to compute estimates of $\hat{C}_i$ via the Kalman filter, and it is the time at which the controller is called [53]. The developed Kalman filter was used in the optimization problem to predict the process behavior by handling the process and measurement noise. The first step of solution, $C_{stage,k}$, obtained by solving the optimization problem over a prediction horizon length of N_p was applied to the dynamic model in a sample-and-hold fashion, and this procedure was repeated at every sampling time until the end of treatment.

The proposed control framework was applied to the high-fidelity model, and the generated spatial proppant concentration at the end of pumping is presented in Fig. 3.4. Compared to Nolte's pumping schedule, the generated proppant concentration from the proposed control framework was closer to the target concentration, and it was able to achieve the desired fracture length, $135\ \mathrm{m}$, while Nolte's pumping schedule was not able to make it because of the early-termination. Fig. 3.5 compares the pumping schedule obtained from the proposed control framework and Nolte's pumping schedule. It is observed that the treatment time as well as the overall trend of pumping schedules of the both pumping schedules is similar. Additionally, we want to note that the generated pumping schedule under MPC is less aggressive in a sense that more proppant was injected at a later time stage, compared to that of Nolte's pumping schedule. This is because the generated pumping schedule is the projection of Nolte's pumping schedule onto the feasible space constructed by considering operational constraints to achieve uniform concentration at the end of pumping across the fracture.

Additionally, the developed dynamic model was used to describe the spatiotemporal evolution of proppant bank height formed by gravity-induced proppant settling. Fig. 3.6 shows that the proppant bank height at the end of pumping is at most 0.23% of the total fracture height, and it further decreases along the fracture. This is because under the current operating condition, the high flow rate and high viscosity of the fluid mixture prevent fast proppant settling. Therefore, the effect of proppant settling is not explicitly considered in the design of proppant pumping schedules.

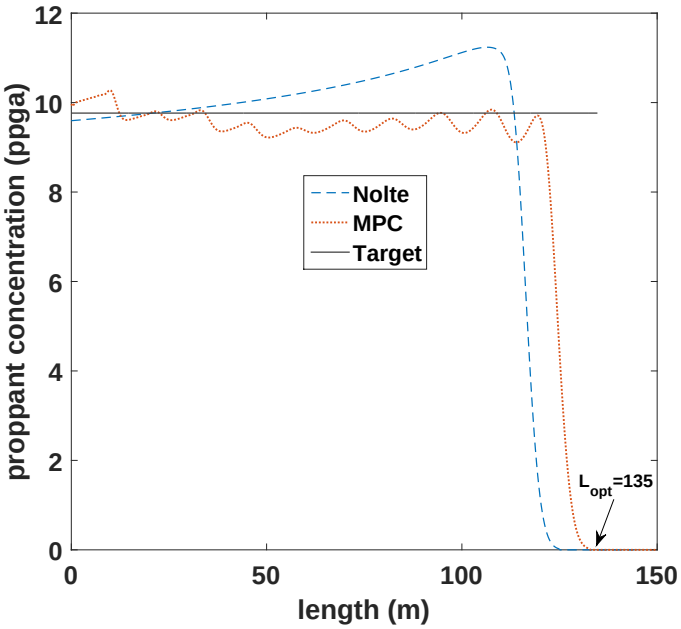

Figure 3.4: Spatial proppant concentration profiles obtained at the end of pumping under MPC and by Nolte's pumping schedule.

We also studied the effect of a plant-model mismatch in Young's modulus, E, by performing the closed-loop simulations with 90% and 110% of its nominal value. The obtained spatial proppant concentration profiles at the end of pumping are shown in Fig. 3.7 along with the case when there is no mismatch in E. The proposed control framework was not able to handle the mismatch in E due to the weak relationship between the proppant concentration at the wellbore (i.e., manipulated input) and the measurable outputs such as the fracture width at the wellbore and fracture length. More specifically, the undesired effect in the fracture width and length, directly caused by the mismatch in E, was not able to be compensated for by adjusting the proppant concentration at the wellbore.

Then, we studied the ability of the closed-loop system to reject disturbance introduced to a particular substage of the proppant pumping schedule. Specifically, we perturbed the optimal proppant concentration of the 5^{th} substage by -10%. Fig. 3.8 shows how the proposed control system responded to the disturbance, which is compared with the case when there is no disturbance. Once the disturbance introduced to the inlet concentration at the 5^{th} substage was detected, the controller took a prompt action by increasing the proppant concentration of the subsequent substages to in-

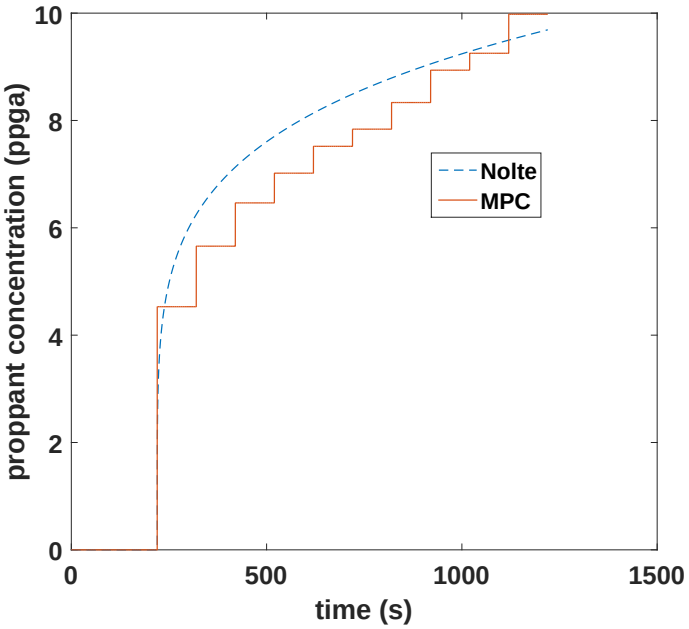

Figure 3.5: Comparison of the pumping schedule generated under MPC with Nolte's pumping schedule.

ject the required total proppant amount of $48000\ \mathrm{kg}$ by the end of pumping while at the same time attempting to achieve uniform concentration. Fig. 3.9 shows the resulting spatial proppant concentration at the end of pumping. The proposed feedback control system was able to minimize the undesired effect attributed to the disturbance introduced to the 5^{th} substage, eventually leading to the production of the final concentration close to the target concentration. Because of the unsteady state operation of the hydraulic fracturing process, some deviations from the target concentration still persist at some locations that were directly influenced by the disturbance.

No. of substages	Cost function
6	0.819
8	0.175
10	0.099

Table 3.1: Cost function values under MPC with different number of substages considered in the pumping schedule design.

After investigating the performance of controller to eliminate the plant-model mismatch and

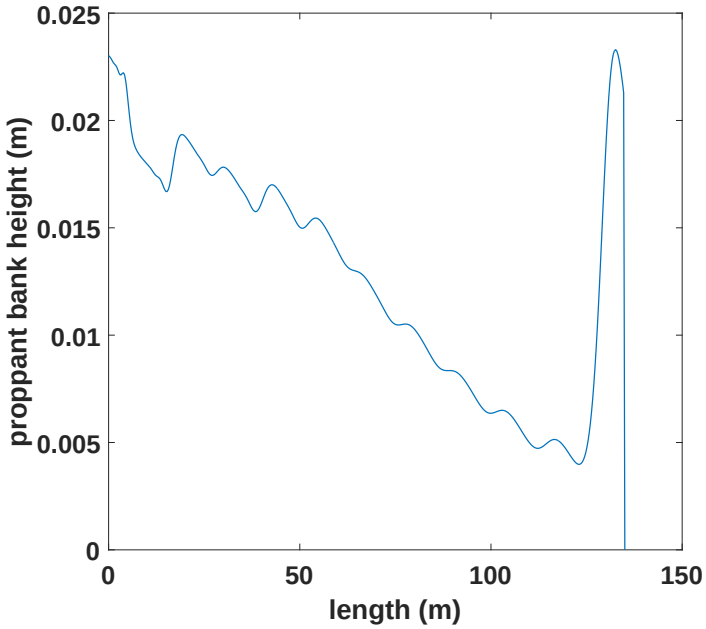

Figure 3.6: Spatial proppant bank height profile obtained at the end of pumping.

disturbances, we varied the number of proppant pumping substages while maintaining the number of spatial locations across the fracture at which we want to achieve uniform proppant concentration. Specifically, the control objective was to minimize the squared deviation of the proppant concentration from the target concentration across the 6 spatial locations. It was observed from Table 3.1 that the value of the cost function decreased with the number of pumping substages. The spatial concentration profiles obtained from the three cases at the end of pumping are compared in Fig. 3.10.

No. of locations	Cost function
4	0.239
5	0.118
6	0.099

Table 3.2: Cost function values under MPC with different number of spatial locations considered in the cost function.

On the other hand, using a pumping schedule with 10 substages, we then varied the number of spatial locations at which we want to achieve uniform proppant concentration. In Table 3.2, it is

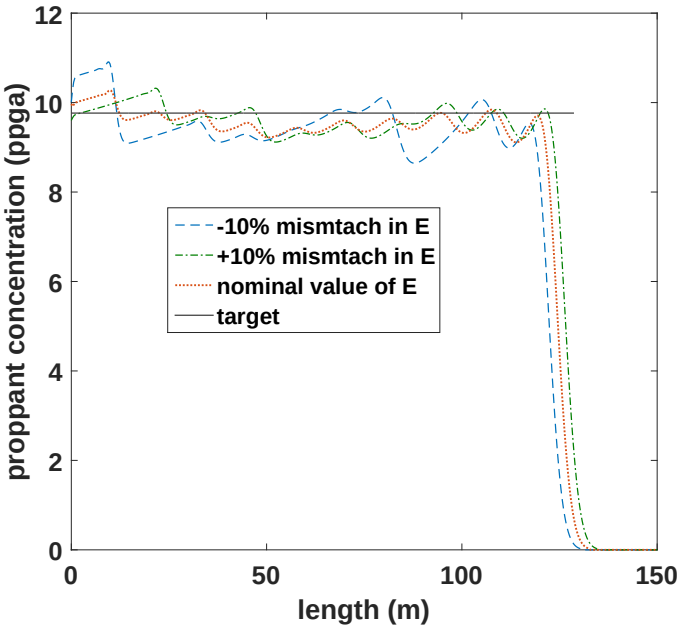

Figure 3.7: Spatial proppant concentration profiles obtained at the end of pumping under MPC when there is a plant-model mismatch in Young's modulus with 90% and 110% of its nominal value.

shown that the value of the cost function decreased with the number of spatial locations considered in the cost function. The spatial concentration profiles obtained at the end of pumping from the three cases are compared in Fig. 3.11.

The proposed control scheme was solved with a shrinking horizon fashion. Due to the use of linear reduced-order models, we were able to reduce the computational requirement significantly. The computation time to solve the optimization problem, Eq. (3.8), at each sampling time is given in Table 3.3. Please note all the calculations were performed using MATLAB on a Dell workstation, powered by Intel(R) Core(TM) i7-4790 CPU@3.60GHz, running the Windows 8 operating system.

According to the foregoing analysis, we can conclude that a pumping schedule that consists of 10 substages and attempts to achieve uniform proppant concentration over 6 locations will generate the spatial proppant concentration profile, which is closer to the target concentration than any other pumping schedules, across the fracture at the end of pumping.

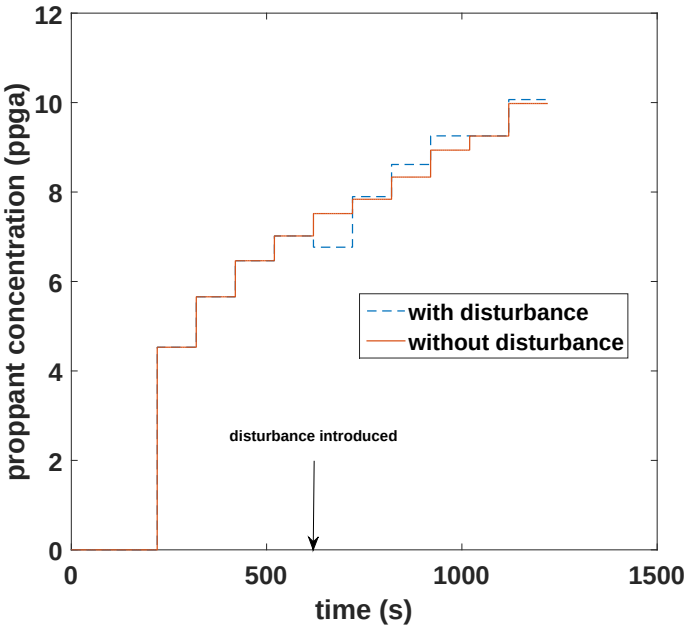

Figure 3.8: Variations in the proppant pumping schedule when there is a disturbance introduced to the 5^{th} substage of the pumping schedule.

3.6 Novelty of the proposed method

The proposed control framework will offer a systematic approach for the design of an optimal pumping schedule to achieve uniform proppant concentration across the fracture at the end of pumping. The novelty of the proposed method is as follows: First, the proposed method considers the influence of proppant transport on fracture propagation by directly taking into account the effect of proppant concentration to the fluid viscosity. Therefore, it can be applied to a broad range of proppant concentration while the proppant schedule developed by Dontsov and Peirce [30] is limited to low concentration where the concentration dependence of viscosity can be negligible. Second, a Kalman filter is used to estimate the unmeasurable states such as proppant concentration inside the fracture, and thus, we can regulate the unmeasurable states. Third, a reduced-order model is used to reduce the computational requirement, while Gu and Desroches [29] used a detailed forward model to solve an inverse problem iteratively. Fourth, the generated optimal pumping schedule is more practical compared to other pumping schedules as it is designed based on optimality and safety considerations such as (1) the fact that a pumping schedule consists of mul-

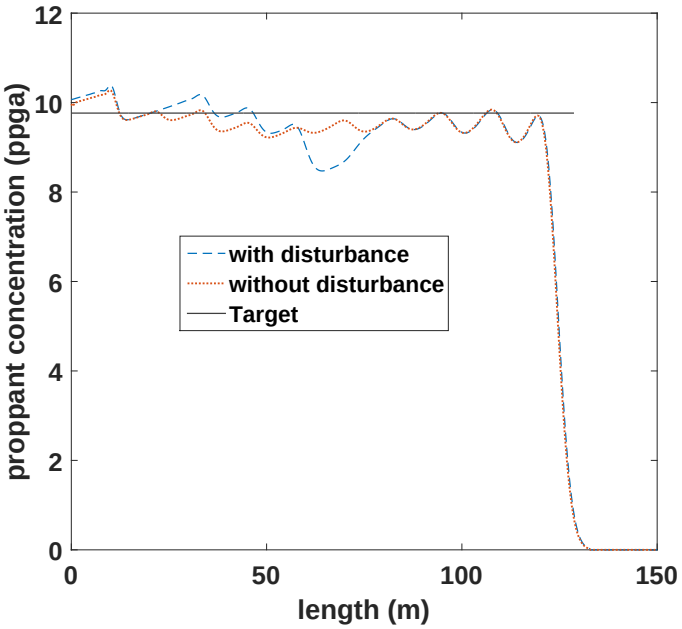

Figure 3.9: Spatial proppant concentration profiles obtained at the end of pumping under MPC when there is a disturbance introduced to the 5^{th} substage of the pumping schedule.

tiple substages where the concentration can vary, (2) the desired fracture geometry that maximizes the productivity of a stimulated well for a given amount of proppant to be injected, and (3) the state and input constraints to avoid premature termination of the hydraulic fracturing process.

3.7 Conclusions

In this work, we developed a control framework that generates an optimal pumping schedule to achieve uniform proppant concentration across the fracture at the end of pumping. Initially, we developed a first-principles model for the hydraulic fracturing process. Second, a novel numerical scheme was developed to deal with the high computational requirement caused by coupling of multiple PDEs defined over a time-dependent spatial domain. Third, a reduced-order model was constructed by using these simulation results, and a Kalman filter was designed to effectively estimate important variables that are not measurable in real-time. Lastly, MPC theory was applied for the design of the feedback control system to achieve uniform proppant concentration across the fracture at the end of pumping. The generated pumping schedule using the proposed control scheme was able to produce uniform concentration at the end of pumping which was closer to the

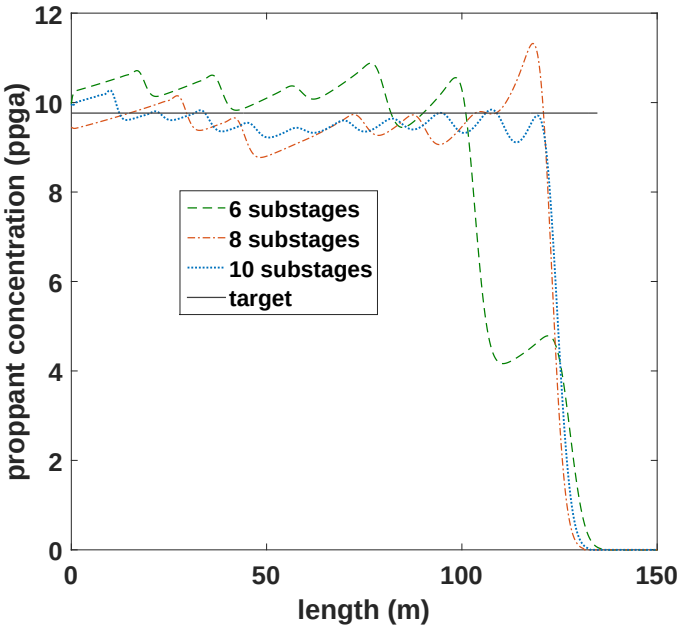

Figure 3.10: Spatial proppant concentration profiles obtained at the end of pumping under MPC with different number of substages considered in the pumping schedule design.

target concentration, compared to Nolte's pumping schedule, which is one of the most commonly used pumping schedules. Furthermore, the proposed methodology was able to generate an online pumping schedule with a reasonable computational requirement while explicitly taking into account practical, safety, and optimality considerations. The performance of the proposed control scheme was evaluated with respect to the use of different numbers of substages and spatial locations considered in the pumping schedule formulation.

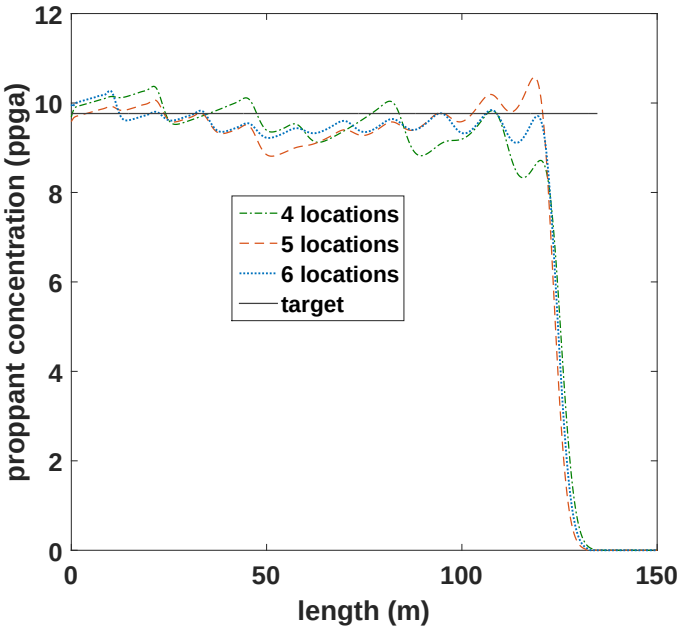

Figure 3.11: Spatial proppant concentration profiles obtained at the end of pumping under MPC with different numbers of spatial locations considered in the cost function.

k^{th} sampling time	Computation time (seconds)
1	64.39
2	36.48
3	32.49
4	22.11
5	17.28
6	10.37
7	6.43
8	2.83
9	0.64
10	0.23

Table 3.3: The computation time to solve the optimization problem, Eq. (3.8), at each sampling time.

4. FEEDBACK CONTROL OF PROPPANT BANK HEIGHTS DURING HYDRAULIC FRACTURING FOR ENHANCED PRODUCTIVITY IN SHALE FORMATIONS*

4.1 Introduction

In Chapter 3, we presented a control framework that generates an optimal pumping schedule to achieve uniform proppant concentration across the fracture at the end of pumping in conventional oil reservoirs. In conventional oil reservoirs, high-viscosity fracturing fluids ensure that most of the proppant remains in suspension during the treatment and the closure process. Thus, it is sufficient to regulate the suspended proppant concentration along the fracture at the end of pumping. In contrast, in unconventional reservoirs, predominantly low-viscosity ("slick-water") fluids are used and the proppant settles quickly forming a proppant bank. The proppant bank will continue to grow until it reaches the equilibrium height; a state when the rate of proppant washout on top of proppant banks due to the shear force is equal to the rate of bank formation via proppant settling. Thereafter, the injected proppant particles will flow over the top of the equilibrium-height proppant bank and travel farther to find a location at which the proppant bank has not reached the equilibrium height yet. This proppant transport behavior has been known for a long time [89, 90, 91, 92, 93] but has become dominant only recently, due to the widespread use of slick-water as fracturing fluids. We are not aware of incorporating it into the controller design.

Over the last two decades, the oil and gas industry has employed optimization techniques for a variety of purposes such as determining optimal well location and spacing of fracture stages [20, 94, 95], field development under uncertainty [18], resource scheduling [17, 96], maximization of net present value [14, 15], optimization of water management in shale oil and gas production process [97, 98, 99, 100], shale oil and gas supply chain optimization [101, 102], history matching of reservoir parameters [19, 103, 104, 105, 106, 107], and development of well and reservoir simulators [23, 24, 25, 108]. Specifically, for a given amount of proppant to be injected, a unified

*Reprinted with permission from "Feedback control of proppant bank heights during hydraulic fracturing for enhanced productivity in shale formations" by Siddhamshetty et al., 2018. *AIChE Journal*, 64, 1638-1650, Copyright 2018 by John Wiley and Sons.

fracture design (UFD) that provides the optimal fracture geometry was proposed for conventional oil and gas reservoirs to maximize well performance [10], and recently, the approach has been further extended to unconventional (low-permeability) resources [13]. However, in practice, while planning for hydraulic fracturing in unconventional reservoirs, very limited information is available. In fact, the enhanced formation permeability of the stimulated volume is created during the fracturing process and hence cannot be measured beforehand. Therefore, the usual combination of sophisticated reservoir simulations and computationally extensive nonlinear optimization algorithms [109, 110, 111, 112] might be difficult to justify at the planning stage. Motivated by these considerations, recently, Liu and Valkó [113] proposed a section-based optimization method to maximize the dimensionless productivity index (PI) assuming constant pressure at the wellbore and infinite conductivity fracture (i.e., zero pressure drop in the fracture during the production stage). In this approach, there is no need to know the enhanced permeability to be established, if one can assume that the selected total amount of fracturing materials is already enough to stimulate the available formation volume and within it, uniform enhanced permeability will be established. The approach converts a fixed amount of proppant into a total length of infinite conductivity fractures that in turn is used as an overall constraint to find the three decision variables: number of wells, number of fractures per well and fracture half-length. To make the optimum unique, one may need additional constraints on the admissible range of fracture half-lengths accounting for additional (non-fracturing related) costs.

Motivated by these considerations, we focus on the development of a high-fidelity process model to obtain a fundamental understanding of the proppant bank formation mechanism and its relationship to manipulated input variables such as proppant concentration and flow rate of the injected fracturing fluids. To deal with large computational requirements due to dynamic simulation of highly-coupled PDEs defined over a time-dependent spatial domain, a reduced-order model is developed by applying the multi-variable output error state-space algorithm to the data obtained from the high-fidelity process model. The obtained reduced-order model is used to design a Kalman filter to estimate the unmeasurable states in real-time and handle the presence of uncer-

tainties in the measurement data. Then, we develop a model-based feedback controller to minimize the spatial variation of proppant bank heights along the fracture at the end of pumping by taking into account (a) actuator limitations that the pumping schedule consists of multiple pumping stages where the flow rate and the proppant concentration can be varied, (b) state constraints to prevent premature termination of the process, and (c) the desired propped fracture geometry maximizing the overall productivity of the wells producing from the section.

This chapter is organized as follows: First, we improve the high-fidelity process model of hydraulic fracturing process presented in Chapter 2 by considering the dominant proppant bank formation process. Then, a periodic remeshing strategy is proposed to effectively handle the computational requirement attributed to the solving a system of multiple PDEs defined over the time-dependent spatial domain. The optimal fracture geometry is obtained by applying a section-based optimization method to the considered ultra-low permeability reservoir. Next, a data-based linear approximate model is constructed using the high-fidelity simulation data to design a Kalman filter that estimates unmeasurable states. Lastly, a model-based feedback controller is developed to achieve the uniform proppant bank height along the fracture at the end of pumping.

4.2 Dynamic modeling of hydraulic fracturing processes

In this work, a hydraulic fracturing process is characterized by the following three sub-processes: (1) fracture propagation, (2) proppant transport, and (3) proppant bank formation.

4.2.1 Modeling of fracture propagation

The fracture propagation model is presented in Section 2.1.1.

4.2.2 Modeling of proppant transport

In this work, the modeling of proppant transport in both the horizontal and vertical directions is considered. In the horizontal direction, it is assumed that the injected proppant will travel at the fracturing fluid's velocity while in the vertical direction, the suspended proppant is assumed to have a settling velocity relative to the fracturing fluid due to the gravitational force.

4.2.2.1 *Proppant advection*

The proppant particles are assumed to be sufficiently large so that the diffusive flux is neglected while the convective flux is considered. The interactions between the individual proppant particles are assumed to be negligible because of the low suspended proppant concentration in unconventional reservoirs, while the drag and gravitational forces acting on the proppant particles are considered. All the proppant particles are assumed to be uniform in size and they are uniformly distributed along the vertical direction. Based on these assumptions, the advection of suspended proppant can be described by the following equation:

$$\frac{\partial (WC)}{\partial t} + \nabla \cdot (WCV_p) = 0 \tag{4.1}$$

$$C(0,t) = C_0(t) \quad \text{and} \quad C(x,0) = 0 \tag{4.2}$$

where ∇ is the vector differential operator, C is the suspended proppant concentration, and $C_0(t)$ is the inlet proppant concentration at the wellbore (i.e., the manipulated input). The net velocity of proppant particles, V_p, is obtained by taking into account the superficial fluid velocity into the horizontal direction, V, and the gravitational settling velocity, V_s, which is given by [69]:

$$V_p = V - (1 - C)V_s \tag{4.3}$$

4.2.2.2 *Proppant settling*

The gravity-induced proppant settling velocity in the fracturing fluid, V_s, is computed by [60]:

$$V_s = \frac{(1-C)^2}{10^{1.82C}} \frac{(\rho_{sd} - \rho_f)\, g d^2}{18\mu} \tag{4.4}$$

where ρ_{sd} is the proppant particle density, ρ_f is the pure fluid density, g is the gravitational acceleration constant, and d is the proppant diameter. The relationship between the fracturing fluid viscosity, μ, and the suspended proppant concentration, C, can be described through the following

empirical model [70]:

$$\mu(C) = \mu_0 \left(1 - \frac{C}{C_{\max}}\right)^{-\alpha} \tag{4.5}$$

where μ_0 is the pure fluid viscosity at $C = 0$, α is an exponent in the range of 1.2 to 1.8, and $C_{\max}$ is the theoretical maximum concentration, which is determined by $C_{\max} = (1 - \phi)\, \rho_{sd}$ where ϕ is the proppant bank porosity.

Even though the fracture propagation is considered only along the horizontal direction only (1-D), the proppant transport into the vertical as well as the horizontal direction is considered in V_p. Such a simplified model is sufficient for the purpose of the present study where we want to regulate the proppant bank with equilibrium heights along the horizontal direction.

4.2.3 Proppant bank formation

In unconventional reservoirs, due to the use of low-viscosity fracturing fluids, the amount of proppant settled during the hydraulic fracturing process is significant. The settled proppant forms a proppant bank (solid lines in Fig. 4.1; proppant bank growth is indicated with an arrow). Specifically, the evolution of proppant bank height, δ, via the proppant settling is described by [43, 71]:

$$(1 - \phi)\frac{d\,(\delta W)}{dt} = C V_s W, \qquad \delta(x, 0) = 0 \tag{4.6}$$

where the proppant bank is initially of a vanishing thickness. The proppant bank will grow to the equilibrium height, h_{eq}; namely, the state when the rate of proppant washout on top of the proppant bank due to the shear force is equal to the rate of bank formation via proppant settling. The equilibrium proppant bank height is determined by the suspended proppant concentration and

the flow rate of fracturing fluids as follows [64, 91]:

$$h_{eq} = H - Wc_1 R_f^{m_1} R_p^{m_2} \tag{4.7a}$$

$$c_1 = -2.3 \times 10^{-4} ln(R_G) + 2.92 \times 10^{-3} \tag{4.7b}$$

$$m_1 = 1.2 - 1.26 \times 10^{-3} \lambda^{-0.428} (15.2 - ln(R_G)) \tag{4.7c}$$

$$m_2 = -0.0172 ln(R_G) - 0.12 \tag{4.7d}$$

$$R_f = \frac{q_{f,flux} h_s}{\mu} \quad \text{and} \quad R_p = \frac{q_{p,flux} h_s}{\mu} \tag{4.7e}$$

$$R_G = \frac{\rho_f (\rho_p - \rho_f) g d^3}{\mu^2} \tag{4.7f}$$

$$\lambda = \frac{\mu \,/\, \rho_f}{W^{1.5} \sqrt{g}} \tag{4.7g}$$

where R_f, R_p, and R_G are the fluid, proppant, and gravity Reynolds numbers, respectively, λ is the gravity Reynolds number for the fluid, $q_{f,flux}$ and $q_{p,flux}$ are the fluid and proppant mass flux in the fracturing fluid, respectively, c_1, m_1, and m_2 are the coefficients in Eq. (4.7a) and they are given by Eqs. (4.7b)–(4.7d), respectively, and h_s is the height of the free cross-sectional area ($h_s = H - h_{eq}$). Once the proppant bank height at a location reaches the equilibrium value, the injected proppant particles will flow over the top of the proppant bank and travel farther to find a location available for proppant settling. The above model is an empirical model and its validity over limited operating conditions is described in [64, 91]

4.3 Numerical simulation

4.3.1 Challenges in numerical simulations

In order to describe the spatiotemporal evolution of key variables in hydraulic fracturing such as $Q_x(x,t)$, $\delta(x,t)$, $W(x,t)$, $U(x,t)$, $C(x,t)$, $V(x,t)$, there are challenges associated with the numerical simulation of high-fidelity process models. For example, (1) fracture propagation, rock deformation, fluid flow and proppant transport are described by a system of nonlinear dynamic PDEs; (2) considering the proppant settling and advection requires fine meshes; (3) the spatial domain changes with time, and the boundary of spatial domains is a part of the solution to be

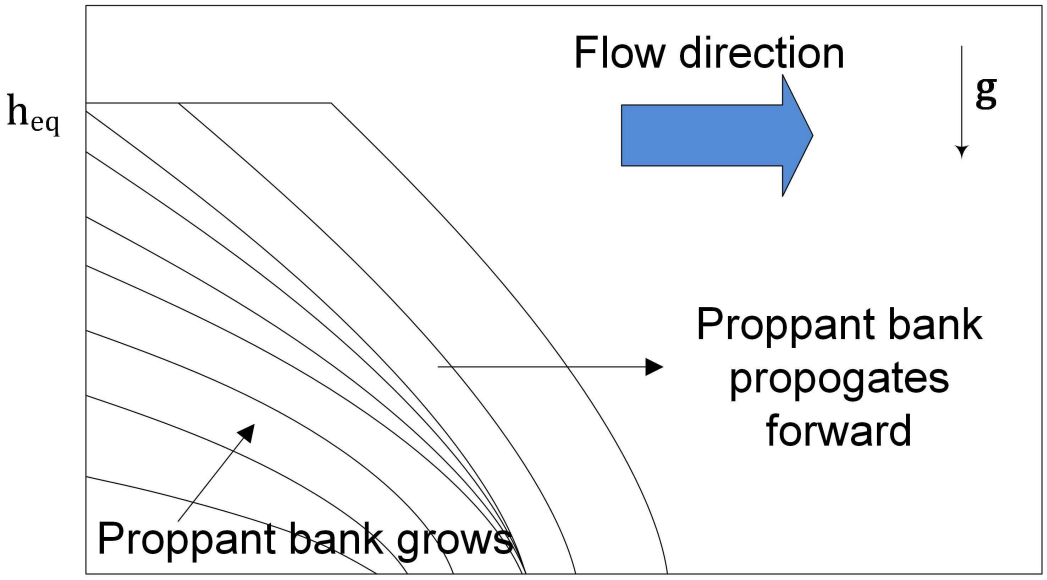

Figure 4.1: Growth and propagation of proppant bank during hydraulic fracturing.

determined; and (4) because of the time-dependent spatial domain, the number of equations to be solved grows with time, significantly increasing the computational requirements [72, 73, 74, 75, 76, 77].

4.3.2 Meshing Strategy

Since we assume that the fluid pressure along the vertical direction is constant, no mesh element is generated in the z-direction. However, to model the time-dependent spatial domain in the x-direction, the number of mesh elements has to grow with time. For fracture propagation, the rate of change of several process variables including the fracture width, net pressure, and the flow rate of fracturing fluids at the wellbore decreases with time, while the rate of change of the same variables remain significant near the fracture tip. Motivated by this observation, we propose a periodic remeshing strategy that combines multiple mesh elements near the wellbore when the rate of change of variables becomes insignificant. Suppose Δx is the fixed mesh size and the time step required to grow the spatial domain from $x = k\Delta x$ to $x = (k+1)\,\Delta x$ is dt_k. Please note that dt_k is a part of the solution to be determined and it grows with time. Specifically, when the total number of mesh elements exceeds a pre-specified value, N_{ps}, the first N_m mesh elements from the wellbore are combined to form a larger mesh element of size $N_m \Delta x$. The proposed

remeshing strategy is illustrated in Fig. 4.2, where $N_{ps} = 50$ and $N_m = 5$. For example, when the number of mesh elements reaches 50, the first 5 mesh elements from the wellbore, 1^{st} to 5^{th}, are combined into a larger mesh element of size $5\Delta x$ and the mesh element indices are renumbered with the combined mesh element being 1^{st}. Then, at the 55^{th} propagation step, the number of mesh elements of size Δx, excluding the 1^{st} mesh element of size $5\Delta x$, again exceeds 50. Therefore, the first 5 mesh elements, 2^{nd} to 6^{th}, are combined into a larger mesh element of size $5\Delta x$ and the mesh element indices are renumbered with the combined mesh element being 2^{nd}. In practice, from the high-fidelity simulation data, we can get some educated initial values for N_{ps} and N_m. Then, we will gradually increase them until we lose the model accuracy significantly. The remeshing process continues until the simulation ends. During the remeshing process, the process variables are adapted so that the conservation of mass and energy holds. Specifically, the fracture width, suspended proppant concentration, and proppant bank height values of the new mesh element are updated by taking the average value of the same variables in the old mesh elements. Even though we did not search extensively for the optimal values for N_{ps} and N_m, by applying the proposed remeshing strategy with $N_{ps} = 50$ and $N_m = 5$, an accurate full-order solution of the PDE system was obtained at less than 5% of the original computation time.

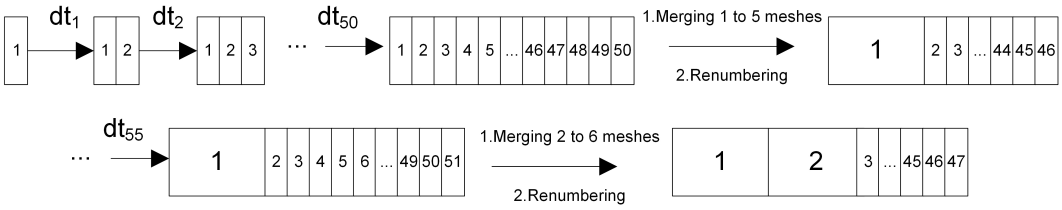

Figure 4.2: Illustration of the proposed re-meshing strategy.

4.3.3 Numerical solution procedure

By employing the proposed remeshing strategy, the steps of the proposed numerical algorithm are presented below:

1. At time step t_k, the fracture length $L(t_k)$ is extended by Δx.

2. For fracture propagation, Eqs. (2.1)–(2.6) are solved iteratively to calculate $W(x, t_{k+1})$, $P(x, t_{k+1})$, $Q_x(x, t_{k+1})$, $V_p(x, t_{k+1})$, and dt_k.

3. For proppant transport, Eqs. (4.1)–(4.7) are solved with the updated $V_p(x, t_{k+1})$, to obtain $C(x, t_{k+1})$, $V_s(x, t_{k+1})$, $\delta(x, t_{k+1})$, and $\mu(x, t_{k+1})$.

4. If $\delta(x, t_{k+1})$ reaches h_{eq}, then the location is no longer available for proppant settling, and the injected proppant will travel farther to find a location available for proppant settling.

5. The mesh elements are combined and the process variables are updated as described in the preceding section.

6. Set $k \leftarrow k + 1$ and go to Step 1.

The schematic diagram of the above numerical algorithm is shown in Fig. 4.3.

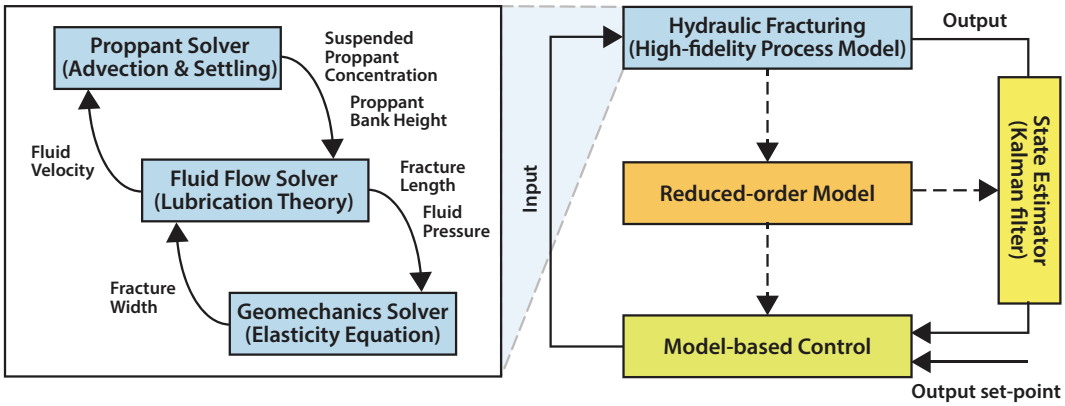

Figure 4.3: Schematic flow diagram of the proposed closed-loop operation of hydraulic fracturing processes.

4.4 Computation of optimal fracture configuration in unconventional reservoirs

4.4.1 Section-based optimization method

At this point, we intend to employ a section-based optimization method, developed by Liu and Valkó [113], to find the optimum number of wells, number of fractures per well and fracture half-length, x_f, that maximize the overall dimensionless PI subject to fixed fracturing resources.

The section-based optimization is performed for planning the development of an unconventional reservoir with multi-stage fractured horizontal wells in a large square drainage area that we call a section (Fig. 4.4). The section is evenly divided into multiple subsections such that there are n_c wells and n_r fractures per well. section illustrates the case of two wells ($n_c = 2$) and eight fractures per well ($n_r = 8$) in a section. An individual subsection is considered as the drainage area of a single fracture (Fig. 4.5), and all the subsections in one column represent a single horizontal well. In this approach, there is no need to know the actual value of the enhanced permeability to be established, because it is assumed that the created fractures will be of infinite conductivity [114]. In addition, it is assumed that the selected total amount of fracturing materials is already enough to ensure that the stimulated volume will cover the whole section in which a uniform enhanced permeability will be established. Specifically, it is implicitly assumed that permeability enhancement is primarily caused by the injected fluid that is already fixed, by fixing the total amount of proppant. The approach converts the fixed amount of proppant into a fixed total fracture length that in turn is used as an overall constraint to find the three decision variables: number of wells, number of fractures per well and fracture half-length. Reservoir fluid properties, such as the formation volume factor B, which is the ratio of the volume of oil and gas at reservoir in-situ conditions to that at standard surface conditions, and the oil viscosity μ_{oil} are also considered constant. Based on the assumptions, the productivity of a section is expressed as follows:

$$J = \frac{2\pi kH}{B\mu_{oil}} n_f J_{D,f}(A_r, I_x) \tag{4.8}$$

where $n_f = n_c n_r$ is the total number of fractures in the section, and $J_{D,f}$ is the dimensionless PI for each fracture (i.e., a subsection), which is a function of aspect ratio, $A_r = x_e/y_e$, and penetration ratio, $I_x = x_f/x_e$, of a subsection, where x_e and y_e are the half-width and half-length of the subsection (Fig. 4.5). Specifically, $J_{D,f}$ is given by $J_{D,f}(A_r, I_x) = 2\lambda_0/\pi$, where λ_0 is the

first positive eigenvalue of the following eigenvalue problem:

$$\frac{\partial^2 \phi_0}{\partial x^2} + \frac{\partial^2 \phi_0}{\partial y^2} = -\lambda_0 \phi_0 \tag{4.9}$$

with zero Neumann boundary conditions along the perimeter of the subsection, and zero Dirichlet condition along the fracture, which is presented in Fig. 4.5. The eigenvalue problem, Eq. (4.9), is solved numerically with the finite element method (FEM) combined with Richardson extrapolation [115]. Fig. 4.6 shows the contour plot of the dimensionless PI per fracture, $J_{D,f}$, which is obtained by solving the eigenvalue problem for different A_r and I_x values. The figure shows that a very small difference in I_x (equivalently, the propped fracture length) may lead to a huge difference in the productivity index. More details regarding this approach can be found in [113].

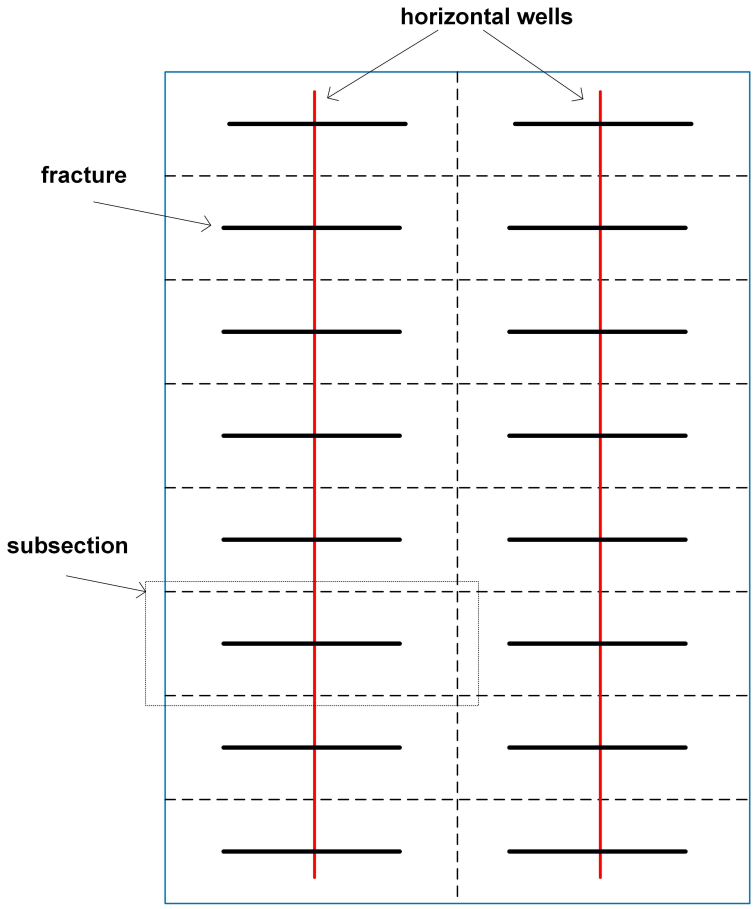

Figure 4.4: Illustration of a section for the case of two wells ($n_c = 2$) and eight fractures per well ($n_r = 8$).

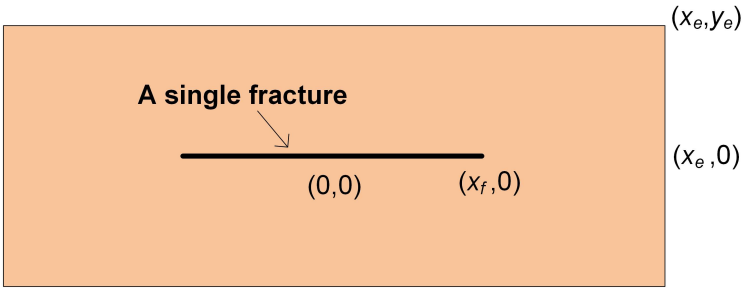

Figure 4.5: Illustration of a subsection (the drainage area of a single fracture).

Remark 6. *One of the important results of our study is that - under the assumptions made - the optimal number of man-made propped fractures is on the order of ten, not hundred or more. In section, possible re-opened natural fractures are not shown. In this work, the continuum model is used to describe the formation, therefore the stimulated reservoir volume has no discrete fractures, only an enhanced permeability. Another important result of this study is that we do not need to know the actual value of the enhanced permeability for determining the optimum development parameters (well spacing, fracture spacing and fracture half-length) as far as we can consider the man-made fractures having infinite conductivity.*

The optimization problem to maximize the overall dimensionless PI, J_D, using the section-based optimization method is formulated as follows:

$$\max_{n_r,n_c} \quad J_D = n_r n_c J_{D,f}(A_r, I_x) \tag{4.10a}$$

$$\text{s.t.} \quad J_{D,f} \text{ from the eigenvalue problem, Eq. (4.9)} \tag{4.10b}$$

$$A_r = \frac{n_r}{n_c}, \qquad I_x = \frac{l_{fD}}{n_r} \tag{4.10c}$$

$$l_{fD} = \frac{l_f}{\sqrt{A_s}}, \qquad l_f = \frac{M_{prop}}{\rho_{sd} W_{opt} H_r} \tag{4.10d}$$

$$0 < x_f \leq x_{f,max} \tag{4.10e}$$

$$x_e - x_f \geq 0.5 d_{sep,min} \tag{4.10f}$$

$$x_f = \frac{l_f}{2 n_r n_c} \tag{4.10g}$$

$$x_e = \frac{x_f}{I_x}, \qquad y_e = \frac{x_e}{A_r} \tag{4.10h}$$

where l_f is the total fracture length (sum of $2x_f$ over the entire subsections) to be created in the section, expressing the available fracturing resources. The dimensionless total fracture length l_{fD} is the total fracture length divided by the section side length, A_s is the square drainage area of the section, M_{prop} is the total amount of proppant to be injected, W_{opt} is the average propped fracture width, H_r is the reservoir thickness, n_c and n_r are the number of wells per section and number of fractures per well, respectively. The smallest distance between the tips of two fractures created from neighboring wells is called the separation distance d_{sep}. In the maximization problem, Eq. (4.10), there are only two decision variables (n_c and n_r). The objective function, Eq. (4.10a), is the dimensionless PI for the section. The dimensionless PI for one fracture, $J_{D,f}$, is calculated by solving the eigenvalue problem given in Eq. (4.10b) using the dimensions of the subsection obtained from Eq. (4.10h). The aspect ratio, A_r, and penetration ratio, I_x, of a subsection are obtained using Eq. (4.10c). Once M_{prop}, W_{opt}, ρ_{sd}, H_r, and A_s are available, the total fracture length to be created in the section, l_f, is obtained using Eq. (4.10d). Since we use the concept of infinite conductivity fracture, the W_{opt} average propped fracture width is not the result of the optimization, rather an input, providing the minimum required propped width of a fracture to be considered a propped fracture at all (often taken as three times the proppant grain diameter). There are two constraints. The constraint, Eq. (4.10e), imposes the limit $x_{f,max}$ on the fracture half-length. It is a crucial parameter, representing the current level of fracturing technology in the given unconventional formation, meaning that fractures can be routinely and reliably created and propped up to this half-length. In the current problem we use $x_{f,max} = 122$ m [116]. The other constraint, Eq. (4.10f), requires that there should be at least $d_{sep,min}$ separation distance between the tips of two fractures created from neighboring wells to avoid fracture overlapping [117]. In this work, we consider $d_{sep,min} = 25$ m. In the maximization problem, Eq. (4.10), the essential part of the work is done by computing the objective function, that is the first eigenvalue. There is no need for sophisticated optimization algorithms, because the two essential decision variables (n_c, n_r) are positive integer values and the whole problem can be solved conveniently by nested enumeration, that is fixing the number of wells n_c, and solving for the sub-optimal n_r. The final

choice regarding the number of wells (n_c) will be made inspecting the sub-optima.

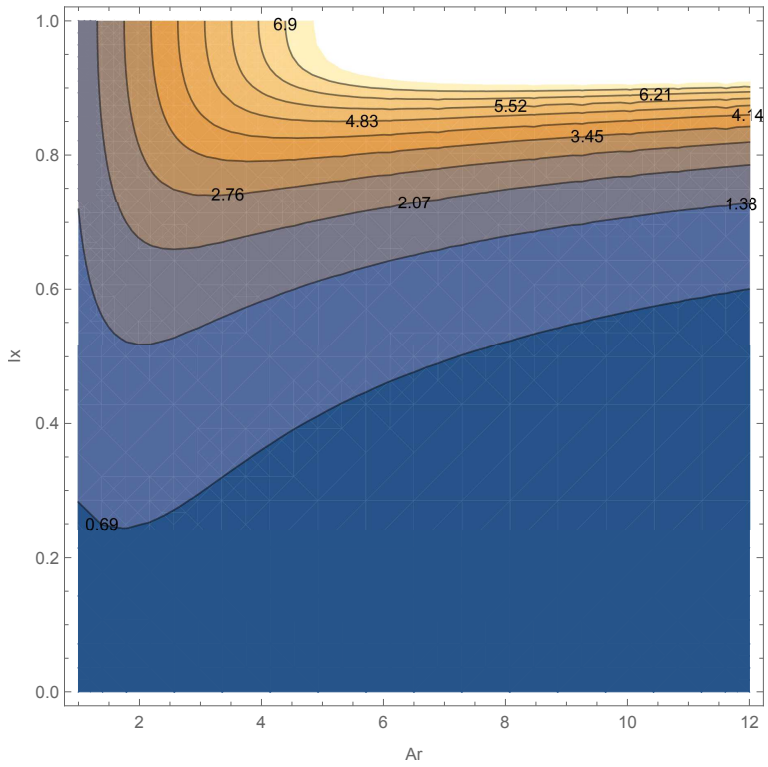

Figure 4.6: Contour plot of the $J_{D,f}$ obtained by solving the eigenvalue problem, Eq. (4.9), for different A_r and I_x values.

Remark 7. *In this work, we optimize the development plan for a section, considering only the most important development parameters (well spacing, fracture spacing and fracture half-length). This is why we call it section-based optimization, to distinguish it from other types of optimization. Specifically, enumeration is a legitimate optimization method for discrete variable optimization problems. For instance, "Branch and bound" is nothing else but a clever enumeration scheme.*

Remark 8. *In many shale developments, the overwhelming part of the capital investment is spent on fracturing. For example, according to a recent study [118], completion cost was* 67% *of the total well and facilities cost in the Midland Wolfcamp play. The completion cost could be further decomposed into 3 main components: a) pumping -* 42%*, b) completion fluids including flow back disposal -* 30%*, c) proppants -* 28%*. However, it is clear that in a given play the pumping and*

fluid costs are essentially proportional to the amount of proppant used. Therefore, the decisive element in the total development cost is the amount of proppant. This is one of the distinctive characteristics of unconventional field development.

4.4.2 Calculation of the optimal well-fracture configuration using the section-based optimization method

In the following, we assumed the total amount of proppant for the section is $M_{prop} = 3.96 \times 10^7$ kg [119]. Then, we computed the total fracture length in a section, $l_f = 79,248$ m, by substituting $W_{avg} = 2.9$ mm and $H_r = 60$ m for Eq. (4.10d) [119, 120]. In Table 4.1, we present (n_c, n_r) pairs that maximize J_D for the different number of wells, n_c. It is apparent that for the low number of wells, the constraint Eq. (4.10e) is the limiting factor and the overall J_D increases rapidly with allowing more wells. When the number of wells is more than 5, the constraint Eq. (4.10f) becomes active and the objective function grows in small increments. In this region, the individual well productivity decreases as more wells are drilled (diminishing returns). It is quite obvious even without further economic calculations, that in this situation $n_c = 6$ wells should be drilled. Once the decision is made, the other variables follow: $n_r = 55$ fractures should be placed in each well with the propped half-length $x_f = 120$ m. Each fracture should be propped with $M_{prop,frac} = 72 \times 10^3$ kg proppant.

n_c	n_r	I_x	J_D	$J_{D,well}$	x_f (meters)	d_{sep} (meters)
4	83	0.593	137	34	119	164
5	66	0.746	474	95	120	82
6	55	0.895	2227	371	120	28
7	56	0.879	2293	328	101	28
8	57	0.863	2363	295	87	27
9	58	0.849	2437	271	76	27
10	59	0.835	2513	251	67	27

Table 4.1: Optimal number of fractures per well n_r, penetration ratio I_x, overall dimensionless productivity J_D, individual well productivity $J_{D,well}$, fracture half-length x_f and separation distance d_{sep} for fixed number of wells, n_c.

4.4.3 Treatment targets

The previous results also show that propped fracture half-length is critical in unconventional reservoirs. A mere $10\ \mathrm{m}$ deficit with respect to the optimal fracture half-length may cause loss of half of the productivity. As we already discussed, with the low-viscosity fracturing fluid, the proppant settles quickly and forms a proppant bank with an equilibrium height, h_{eq}, at which the rate of proppant bank formation via proppant settling is equal to that of the proppant washout on top of the bank due to the shear force. Once the equilibrium height is reached, the injected proppant particles will flow over the top of the proppant bank and travel farther to find a location at which the proppant bank height is below its equilibrium value. Because of this proppant transport mechanism, the proppant bank with an equilibrium height will gradually grow along the fracture (in the x-direction). By assuming that the proppant bank will cover the entire optimal fracture half-length, x_f, with the equilibrium height at the end of pumping, we can calculate the desired average fracture width, $W_{avg,target}$, as follows:

$$W_{avg,target} = \frac{M_{prop,frac}}{2\rho_p h_{eq} x_f (1-\phi)} \tag{4.11}$$

where the equilibrium proppant bank height is $h_{eq} = 54\ \mathrm{m}$. In our case, the calculated target fracture width at the end of pumping is $W_{avg,target} = 5.37\ \mathrm{mm}$. In the following section, we will focus on the development of a model-based feedback controller that aims to achieve the targeted length and width for the developing proppant bank.

4.5 Model predictive control for hydraulic fracturing processes

In this section, we first construct a linear time-invariant approximate model from the high-fidelity simulation data. The real-time measurements readily available from the hydraulic fracturing process are the fracture width at the wellbore (using the wellbore pressure data) and the fracture length (using the microseismic data) [53]. Utilizing these available measurements and the obtained linear approximate model, we will design a Kalman filter to estimate the average fracture width. Then, we design a model-based feedback controller that will compute the optimal prop-

pant pumping schedule (i.e., the flow rate and proppant concentration of the fracturing fluids at the wellbore) to achieve the desired average fracture width at the end of pumping, which will lead to the proppant bank height with a desired value along the fracture while accounting for actuator limitations, state constraints for process safety, and economic considerations.

4.5.1 Development of reduced-order model

Due to the infinite-dimensional nature of the high-fidelity process model of Eqs. (2.1)–(2.7) and Eqs. (4.1)–(4.7), a reduced-order model is required for the purpose of state estimator and model-based feedback controller designs. First, a series of step inputs are applied to the high-fidelity process model to generate input/output data. Then, the multi-variable output error state-space (MOESP) algorithm is used to obtain a linear time-invariant state-space model of the hydraulic fracturing process, which is presented in the following form:

$$x(t_{k+1}) = Ax(t_k) + Bu(t_k) \tag{4.12a}$$

$$y(t_k) = Hx(t_k) \tag{4.12b}$$

where $u(t_k) = [Q_{x0}(t_k), C_0(t_k)]^{\mathrm{T}}$ is the flow rate and proppant concentration of the fracturing fluid at the wellbore (i.e, the manipulated input variables) and $y(t_k) = [W_{avg}(t_k), W_0(t_k), L(t_k)]^{\mathrm{T}}$ denotes the vector of output variables where $W_{avg}(t_k)$ is the average fracture width, $W_0(t_k)$ is the fracture width at the wellbore, and $L(t_k)$ is the fracture length. In practice, the available real-time measurements are limited to the fracture width near the wellbore and the fracture length. This leaves the average fracture width to be estimated through a Kalman filter, which will be discussed in the following section.

4.5.2 Kalman filter design

The process and measurement noise is added to the reduced-order model presented in Eq. (4.12) as follows:

$$x(t_{k+1}) = Ax(t_k) + Bu(t_k) + w(t_k) \tag{4.13a}$$

$$y(t_k) = Hx(t_k) + v(t_k) \tag{4.13b}$$

where w is the process noise and v represents the measurement noise. Both w and v are assumed to be drawn from a zero mean Gaussian distribution with covariances Q and R, respectively.

$$w(t_k) \sim N(0, Q) \tag{4.14a}$$

$$v(t_k) \sim N(0, R) \tag{4.14b}$$

The Kalman filter is a two-step process: prediction and measurement update. Combining the prediction and measurement update steps, the Kalman filter equations are presented in the following form:

$$\hat{x}(t_{k+1}) = A\hat{x}(t_k) + Bu(t_k) + M(t_k)(y_m(t_k) - \hat{y}(t_k)) \tag{4.15a}$$

$$M(t_k) = P(t_k)H^T(R(t_k) + HP(t_k)H^T)^{-1} \tag{4.15b}$$

$$P(t_{k+1}) = (I - M(t_k)H)P(t_k) \tag{4.15c}$$

where the notation $\hat{(\cdot)}$ denotes the estimated variables, $M(t_k)$ is the Kalman filter gain, $P(t_k)$ denotes the covariance of the state estimation error, and $y_m(t_k) = [W_0(t_k), L(t_k)]^{\mathrm{T}}$ are the available real-time measurements, the fracture width at the wellbore and the fracture length.

Fig. 4.7 shows the comparison between the estimated and the actual average fracture width with time. It is observed that the estimated average fracture width quickly converges to the true value obtained from the high-fidelity process model. The effect of the measurement noise, which

is often found in experimental readings, is simulated by introducing white noise with a zero mean Gaussian distribution.

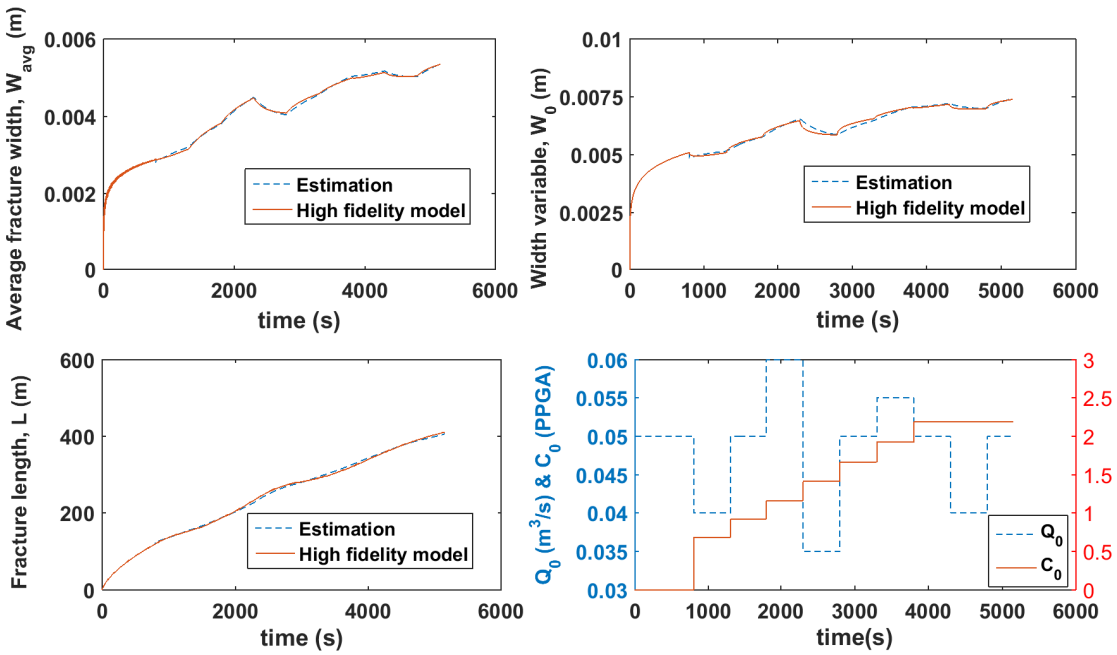

Figure 4.7: Comparison between the true values and the estimates of average fracture width, fracture width at the wellbore, and fracture length.

4.5.3 Design of model-based feedback controller

Within this regard, a novel model-based feedback control system is designed to minimize the squared deviation of the average fracture width at the end of pumping from its set-point value. The proposed model-based feedback controller is formulated in the following form:

$$\min_{\substack{C_{stage,k},\ldots,C_{stage,9}\\ Q_{stage,k},\ldots,Q_{stage,9}}} \quad (\hat{W}_{avg}(t_f) - W_{avg,target})^2 \tag{4.16a}$$

$$\text{s.t.} \quad \text{Kalman filter, Eq. (4.15)} \tag{4.16b}$$

$$\hat{W}_0(t_k) = W_0(t_k), \qquad \hat{L}(t_k) = L(t_k) \tag{4.16c}$$

$$C_{stage,k-1+m} \leq C_{stage,k+m} \leq 2 \text{ PPGA} \tag{4.16d}$$

$$Q_{min} \leq Q_{stage,k+m} \leq Q_{max} \tag{4.16e}$$

$$m = 1, \ldots, 9-k \tag{4.16f}$$

$$\Delta \left(\sum_{k=1}^{9} 2 Q_{stage,k} C_{stage,k} \right) = M_{prop,frac} \tag{4.16g}$$

where $W_{avg,target}$ is the set-point value for the average fracture width at the end of pumping, $\hat{W}_{avg}(t_k)$ is the predicted average fracture width obtained via Eq. (4.15), t_f is the total process operation time, Δ is the sampling time, which is also the duration of each pumping stage, t_k is the current time, $W_0(t_k)$ and $L(t_k)$ are the measurements of the fracture width at the wellbore and the fracture length, respectively, at the k^{th} sampling time, which corresponds to $t \in [t_k, t_k + \Delta)$, and $C_{stage,k}$ and $Q_{stage,k}$ are the inlet proppant concentration and the inlet flow rate of the k^{th} pumping stage, respectively, which are to be determined by solving Eq. (4.16) with a shrinking prediction horizon $N_p = t_f - t_k$. The schematic diagram of the closed-loop operation of the hydraulic fracturing process under the proposed model-based feedback controller is presented in pfd3.

In the optimization problem of Eq. (4.16), the cost function of Eq. (4.16a) describes the squared variation of the predicted average fracture width from the set-point value at the end of pumping. The real-time measurements of the fracture width at the wellbore and the fracture length are available at each sampling time, which is described by Eq. (4.16c), and are used to initialize Kalman filter of Eq. (4.15) to predict the average fracture width trajectory. The constraint of Eq. (4.16d) implies that the proppant concentration will be increased monotonically, and the maximum injected proppant concentration is less than 2 PPGA. The constraint of Eq. (4.16e) imposes the limits

on the flow rate of fracturing fluids at the wellbore. The constraint of Eq. (4.16g) describes the amount of proppant to be injected to a single fracture over the entire hydraulic fracturing process. A constrained optimization algorithm will be utilized to solve Eq. (4.16).

4.6 Closed-loop simulation results under model-based feedback controller

In this section, we applied the proposed model-based feedback controller for the regulation of the average fracture width to achieve the optimal propped fracture geometry at the end of pumping in unconventional reservoirs. The dynamic high-fidelity process model described earlier, was utilized to simulate the hydraulic fracturing process. The values of the model parameters used in the high-fidelity process model are provided in Table 4.2. This model is initially used for generating input/output data for developing a linear approximate model for Kalman filter and model-based feedback controller designs. To achieve the uniform equilibrium proppant bank height, h_{eq}, over the optimal fracture half-length, $x_f = 120$ m, the set-point value for the average fracture width that has to be satisfied at the end of pumping is $W_{avg,target} = 5.37$ mm. For the simulations, the pad time, t_p, was fixed to be 800 s in order to avoid premature termination of the hydraulic fracturing process before the fracture tip reaches the desired fracture half-length of $x_f = 120\ m$. At $t = t_p$, the feedback control system and the Kalman filter were initialized. In the closed-loop simulations, Δ and t_f were chosen to be 500 s and 5300 s, respectively. The proppant pumping schedule was divided into 9 pumping stages and the duration of each pumping stage was 500 s, which was equal to the sampling time Δ. The real-time measurements of the fracture width at the wellbore, $W_0(t_k)$, and the fracture length, $L(t_k)$, were assumed to be available at the beginning of each pumping stage, which were then used to estimate the average fracture width, $\hat{W}_{avg}$, via the Kalman filter. The developed Kalman filter was used within the optimization problem to predict the unmeasurable process variable by handling the process and measurement noise. The first step of solution, $C_{stage,k}$ & $Q_{stage,k}$, obtained by solving the optimization problem over a prediction horizon length of N_p was applied to the high-fidelity process model in a sample-and-hold fashion, and this procedure was repeated at every sampling time until the end of the process.

The proposed model-based feedback controller was applied to the high-fidelity process model

Parameter	Symbol	Value
Leak-off coefficient	C_{leak}	6×10^{-5} m/s$^{1/2}$
Young's modulus	E	0.3×10^{10} Pa
Poisson ratio of formation	ν	0.2
Reservoir thickness	H_r	60 m
Proppant particle density	ρ_{sd}	2648 kg/m^3
Fracture height	H	60 m
Pure fluid density	ρ_f	1000 kg/m^3
Fracturing fluid viscosity	μ	0.005 Pa $\cdot$ s
Proppant bank porosity during hydraulic fracturing	ϕ	0.61
Square drainage area of a section	A_s	2.59×10^6 m^2

Table 4.2: Model parameters used in the high-fidelity model simulation.

of the hydraulic fracturing process. The average fracture width during the hydraulic fracturing operation is presented in Fig. 4.8, where it is shown that the average fracture width at the end of pumping is very close to the set-point value. Fig. 4.9 shows the optimal pumping schedule computed by the proposed model-based feedback controller.

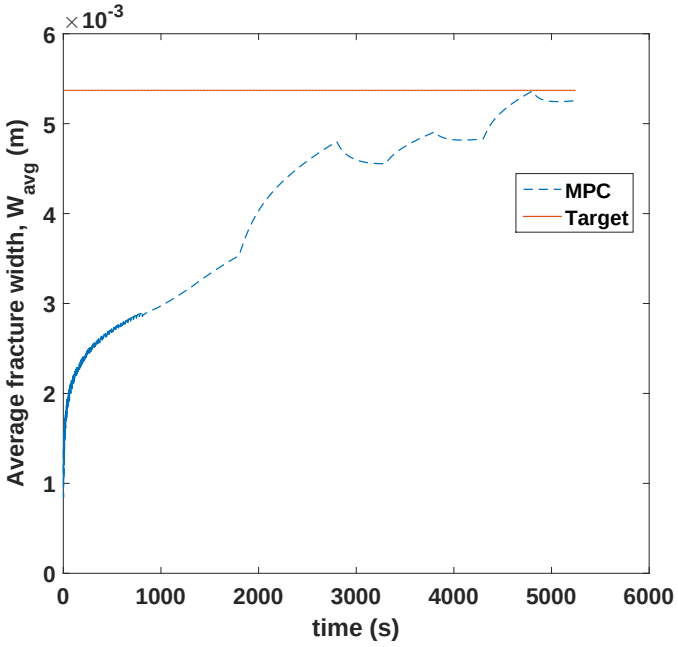

Figure 4.8: Average fracture width during the hydraulic fracturing process under MPC.

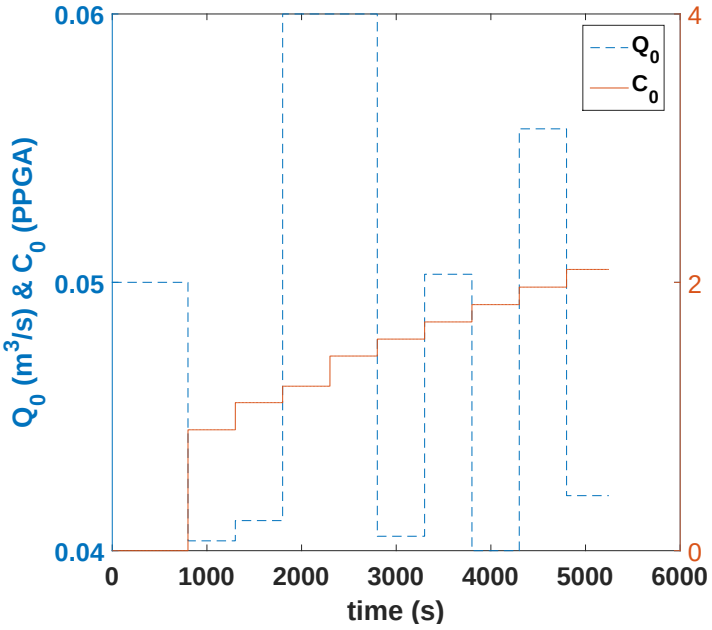

Figure 4.9: Optimal pumping schedule generated under MPC to obtain the required average fracture width at the end of pumping.

As we regulate the average fracture width at the end of pumping to the set-point value, for the given amount of proppant to be injected, the proppant bank height along the fracture with the optimal half-length, x_f, is uniform with the equilibrium value as shown in Fig. 4.10. At the end of pumping, some amount of proppant (900 kg) still remains in suspension. We can assume that in the following shut-in period it will quickly join the bank.

Remark 9. *In order to inject the required amount of proppant, the fracture had to propagate to* 400 m*, while the propped length was developing to* 120 m *only. The unpropped part of the fracture will eventually close when the fluid leaks-off. From the viewpoint of this optimization approach, the propagation and then closure of the unpropped fracture is just part of the creation of the stimulated volume. In the so called far-wellbore region, a gradual transition from dominant fracture into fracture network is anticipated [121], and the actual non-propped length can be much less.*

Remark 10. *We model the proppant bank development during pumping. Once in-situ stress starts to act on the bank directly (i.e., during fracture closure), the fracture width will somewhat decrease*

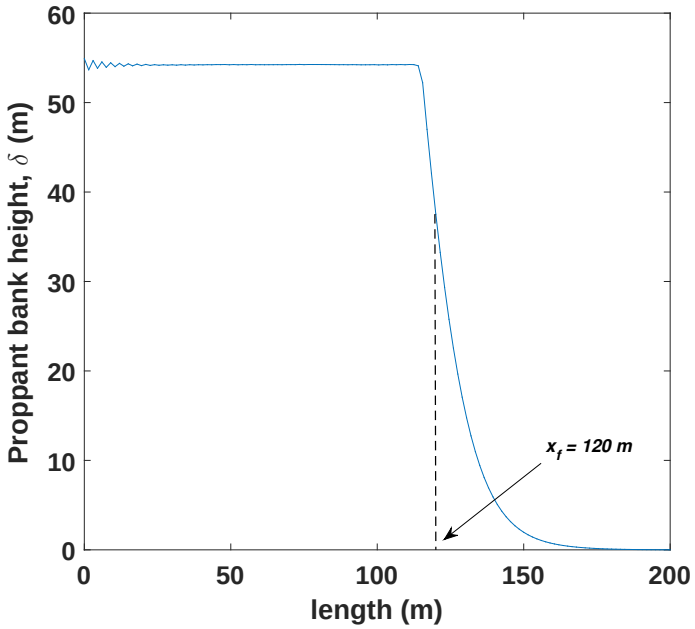

Figure 4.10: Spatial profile of proppant bank height obtained at the end of pumping under the MPC.

(to the W_{opt}), and the proppant bank height, h_{eq}, will somewhat increase, providing full coverage of the reservoir thickness, H_r.

4.7 Conclusions

In this work, we developed a model-based feedback control system that computes an optimal pumping schedule to achieve the proppant bank with a uniform height over the optimal fracture length at the end of pumping. First, we developed the high-fidelity process model of hydraulic fracturing processes to describe the formation of a proppant bank with the equilibrium height. Second, a novel remeshing strategy was developed to efficiently solve the high-fidelity process model. Third, a section-based optimization method was employed to determine the optimal well-fracture configuration, maximizing the overall productivity achievable from a given amount of proppant to be injected. Fourth, using the data generated from the high-fidelity process model of the hydraulic fracture propagation and proppant transport, a reduced-order model was constructed, and a Kalman filter was designed to effectively estimate average fracture width. Lastly, MPC theory was applied for the design of a real-time model-based feedback control system. The proposed methodology

was able to generate an online pumping schedule leading to a uniform proppant bank height along the targeted length while explicitly taking into account actuator limitations, state constraints for process safety, and economic considerations.

5. OPTIMIZATION OF SIMULTANEOUSLY PROPAGATING MULTIPLE FRACTURES IN HYDRAULIC FRACTURING TO ACHIEVE UNIFORM GROWTH USING DATA-BASED MODEL REDUCTION*

5.1 Introduction

In previous chapters 3 and 4, we improved the well performance via the regulation of the uniformity of proppant bank heights and suspended proppant concentration inside the fracture via real-time model-based feedback control of hydraulic fracturing; however, in these work, only a single fracture was considered.

In multi-stage hydraulic fracturing treatments, simultaneously propagating multiple fractures with close spacing often induces non-uniform fracture development, resulting in one or two dominant fractures due to the uneven distribution of fracturing fluids [45, 46]. Miller et al. [47] analyzed the production log data obtained by applying state-of-the art diagnostic technologies to multiple basins; the conclusion was that one third of all perforation clusters contribute to two thirds of gas production, and approximately another one third of the clusters are ineffective and do not contribute to production. One underlying reason for this uneven distribution is the non-uniformity of reservoir properties such as spatial heterogeneity in the in-situ stress along the well [48, 49]. Another contributing factor for the uneven distribution is the well-known phenomenon called "stress-shadowing" [50, 51, 52]. In general, fracturing fluids are distributed to multiple fractures inversely proportional to their flow resistances, which is a function of perforation friction, wellbore friction, and fracture propagation. The problem with stress-shadow effects is that it exerts extra compressional stresses on the interior fractures and increases the flow resistance within interior fractures, resulting in fluid diverting into the exterior fractures. Therefore, to achieve uniform growth of simultaneously propagating multiple fractures and facilitate more fracturing fluids entering into the interior fractures, stress-shadow effects should be balanced or mitigated.

*Reprinted with permission from "Optimization of simultaneously propagating multiple fractures in hydraulic fracturing to achieve uniform growth using data-based model reduction" by Siddhamshetty et al., 2018. *Chemical Engineering Research and Design*, 136, 675-686, Copyright 2018 by Elsevier.

In this regard, several hydraulic fracture simulators have been developed to describe stress-shadow effects in simultaneously propagating multiple fractures, and some of them were used to find the operating conditions for the production of uniform multiple hydraulic fractures. To name a few, Lecampion and Desroches [9] and Wu et al. [122] used the limited entry design technique which is manipulating the pressure drop in each perforation cluster by varying the diameter of perforations and the number of perforations in hydraulic fracture simulator; therefore, they were able to achieve uniform growth of simultaneously propagating multiple fractures by mitigating stress-shadow effects exerted by multiple fractures in a stage. Varying the perforation friction in order to improve uniform distribution of fracturing fluids among multiple fractures is similar to flow distribution in manifolds, where the uniformity of flow rates among the parallel tubes is achieved by varying the fluid pressures inside the entrance and discharge headers [123]. Peirce and Bunger [124] used a new hydraulic fracturing model to investigate the potential to minimize stress-shadow effects for uniform growth of simultaneously propagating multiple fractures by adjusting the location of the perforation clusters. Typically, the high-fidelity hydraulic fracture simulators used in these studies require several days, and sometimes over one week, to compute the growth of simultaneously propagating multiple fractures at real reservoir length and time scales. Hence, optimization of hydraulic fracturing design or computation of the optimal perforation conditions, which may often require hundreds or thousands of simulation runs, were not practically viable; in these directions, very limited efforts have been made by selecting a few important parameters via sensitivity analysis [122, 125] or based on first principles [126].

Recently, a few new model order-reduction techniques were developed to deal with large computational requirements arising from moving boundary problems like hydraulic fracturing [84, 88, 127]. However, these approaches are not directly applicable to simultaneously propagating multiple fractures, because (1) they were focused on a single fracture and (2) they did not directly take into account the pressure drop due to perforation friction, wellbore friction, and fracture propagation; which are important factors that determines the distribution of fracturing fluids into multiple fractures. Analytical models are widely used to calculate the pressure drop due to

perforation friction and wellbore friction [3, 128, 129]. However, it is important to note that the flow resistance associated with the fracture propagation is difficult to be modeled by an analytical expression because of stress-shadow effects. Therefore, in this work, we focus on the development of a new model order-reduction technique by integrating the analytical models to calculate the pressure drop due to perforation friction and wellbore friction and a data-based reduced-order model (ROM) that accounts for the pressure drop along the fractures due to stress-shadow effects. Then, we propose a model-based design technique by utilizing the integrated ROM and the limited entry design technique to compute the flow rate of fracturing fluids and the perforation conditions which will drive the system to achieve uniform growth of simultaneously propagating multiple fractures by promoting equal distribution of fracturing fluids into multiple fractures while mitigating the undesired stress-shadow effects.

This chapter is organized as follows: First, a dynamic model of simultaneously propagating multiple fractures is presented by coupling fluid flow and rock mechanics. Then, an integrated ROM is developed by combining the analytical models and a data-based model to predict the flow resistance in each fracture. Next, a model-based design technique is presented utilizing the developed integrated ROM and the limited entry design technique for even distribution of fracturing fluids into multiple fractures. Simulation results are presented to demonstrate that the proposed method is able to achieve a uniform fracture length at the end of pumping by handling the undesired stress-shadow effects.

5.2 A dynamic model of simultaneously propagating multiple fractures

A dynamic model of simultaneously propagating multiple fractures will be presented in this section. The model is proposed by Wu and Olson [3] based on the following assumptions: (1) all the fractures are confined in the pay layer as the formation layers above and below have sufficiently large stresses such that the fractures cannot grow to the neighboring rock layers; (2) proppant transport within the fractures is not considered; (3) fractures can be non-planar, but must be vertical.

5.2.1 Rock deformation

The elastic rock-deformation theory is typically used to solve for displacement discontinuities. Specifically, shear displacement discontinuities induce non-planar fracture propagation in fracture-length direction, D_s, normal displacement discontinuity, D_n, and displacement discontinuity in vertical direction, D_2. Since it is very hard to obtain analytical solutions for displacement discontinuities, numerical solutions are usually used to solve for displacement discontinuities. Recently [130] proposed a simplified 3D displacement discontinuity method to determine fracture opening and shearing (normal displacement discontinuity and shear displacement discontinuity) for vertical fractures ($D_2 = 0$) which provides a solution with the same accuracy at a much lower computational cost relative to the full 3D displacement discontinuity method [131, 132]. Additionally, the simplified method considers the nonlocal 3D stress interactions (stress-shadow effects) between multiple fractures. Using the simplified method, the normal displacement discontinuities, D_n^p, and shear displacement discontinuities, D_s^p, at each fracture element p are obtained by solving a linear system of equations given below:

$$\sigma_s^p = \sum_{q=1}^{M} A_{s,s}^{pq} D_s^p + \sum_{q=1}^{M} A_{s,n}^{pq} D_n^p \tag{5.1a}$$

$$\sigma_n^p = \sum_{q=1}^{M} A_{n,s}^{pq} D_s^p + \sum_{q=1}^{M} A_{n,n}^{pq} D_n^p \tag{5.1b}$$

where p and q represent fracture elements (Fig. 5.1), M is the total number of elements, σ_s^p and σ_n^p are the traction boundary conditions, which are provided by a fluid-flow model that computes the pressure drop along the fracture propagation direction, $A_{n,s}^{pq}$ is the elastic-influence coefficient matrix representing the normal stress at element p induced by a shear displacement discontinuity at element q, $A_{n,n}^{pq}$ gives the normal stress at element p because of normal displacement discontinuity at element q, $A_{s,s}^{pq}$ gives the shear stress at element p induced by a shear displacement discontinuity at element q, and $A_{s,n}^{pq}$ gives the shear stress at element p because of normal displacement discontinuity at element q. The traction boundary conditions are given below:

$$\sigma_n^p = p_i^p - \sigma_n^{remote,p} \tag{5.2a}$$

$$\sigma_s^p = \sigma_s^{local,p} - \sigma_s^{remote,p} \tag{5.2b}$$

where superscript p represents the fracture element, σ_n^p and σ_s^p are the net normal stress and shear stress acting on element p, respectively, p_i^p is the internal fluid pressure at element p, $\sigma_s^{local,p}$ is the locally applied shear traction on element p, and $\sigma_n^{remote,p}$ and $\sigma_s^{remote,p}$ are the normal stress and shear stress acting on element p due to remote boundary conditions, which can be calculated using the minimum and maximum horizontal stresses in rock formation, $S_{h,min}$ and $S_{h,max}$, respectively, and orientation of the fracture.

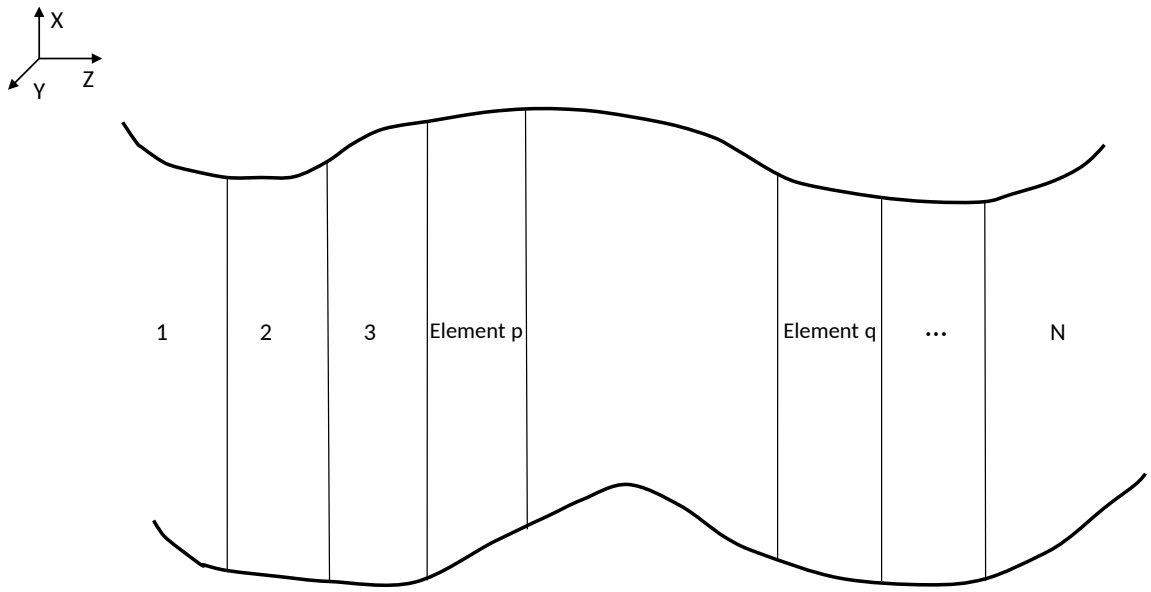

Figure 5.1: Boundary elements on a fracture of interest [3].

5.2.2 Fluid flow

For multiple fracture treatments, unlike single fracture treatments, the amount of fracturing fluids flows into each fracture through the horizontal wellbore is not known a priori. The fluid flow

can be considered analogous to the electric circuit network, where flow rate into each fracture and pressure are similar to current and voltage, respectively. Based on this analogy, Kirchoff's first and second laws can be applied to calculate the distribution of fracturing fluids into multiple fractures [133, 134, 135]. In this regard, once the total volumetric flow rate, Q_T, is specified, the flow rate of fracturing fluids into each fracture, Q_i, is determined by the interplay among the wellbore friction, perforation friction, and fluid pressure within the fractures. By ignoring the amount of fracturing fluids stored in the wellbore in the beginning of operation, the flow rate at the wellbore should be equal to the sum of the flow rates of fracturing fluids at each fracture as given below (Fig. 5.2):

$$Q_T = \sum_{i=1}^{N} Q_i \tag{5.3}$$

where N is the total number of fractures.

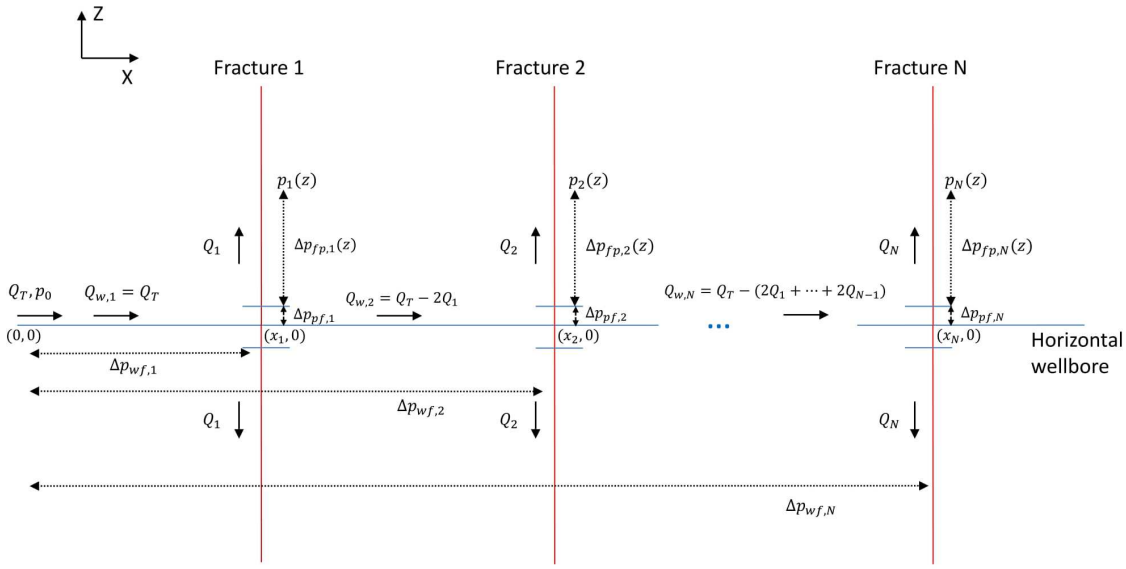

Figure 5.2: Illustration of the distribution of fracturing fluids into each fracture and the pressure drops due to wellbore friction, perforation friction and fracture propagation [4].

Kirchoff's second law describes the continuity of pressure along the wellbore (Fig. 5.2), where

the pressure at the wellbore heel is equal to the sum of pressure drops due to wellbore friction, perforation friction, fracture propagation, and the pressure in an element of a fracture, which is expressed as follows [135]:

$$p_o = \Delta p_{wf,i} + \Delta p_{pf,i} + \Delta p_{fp,i}(z) + p_i(z) \tag{5.4}$$

where subscript i denotes the fracture number, $z \in [0, L_i(t)]$ is the spatial coordinate of fracture i, where $L_i(t)$ is the length of fracture i at time t in the fracture propagation direction, p_o is the total pressure at the wellbore heel, $\Delta p_{wf,i}$ is the pressure drop due to wellbore friction, $\Delta p_{pf,i}$ is the pressure drop due to perforation friction, $\Delta p_{fp,i}(z)$ is the pressure drop due to fracture propagation from the fracture initiation ($z = 0$) to the fracture element at z, and $p_i(z)$ is the pressure at z in fracture i. The pressure drop due to wellbore friction, $\Delta p_{wf,i}$, is given by [129]:

$$\Delta p_{wf,i} = 2^{(3n'+2)} \pi^{-n'} k' \left(\frac{1+3n'}{n'} \right)^{n'} D^{-(3n'+1)} \sum_{l=1}^{i} (x_l - x_{l-1}) Q_{w,l} \tag{5.5a}$$

$$Q_{w,l} = Q_T - \sum_{k=1}^{l-1} 2Q_k \tag{5.5b}$$

$$Q_{w,l} = Q_T \qquad at\ l = 1 \tag{5.5c}$$

where x is the spatial coordinate in the horizontal wellbore direction, n' and k' are the fluid power-law index and consistency index, respectively, D is the diameter of the horizontal wellbore, and $Q_{w,l}$ is the flow rate in the horizontal wellbore between two neighboring fractures (Fig. 5.2). The pressure drop due to perforation friction, $\Delta p_{pf,i}$, is proportional to the square of flow rate and estimated by Elbel et al. [135] in the following form:

$$\Delta p_{pf,i} = \frac{0.807 \rho_s}{n_p^2 d_p^4 K_d^2} Q_i^2 \tag{5.6}$$

where ρ_s is the density of slurry, n_p is the number of perforations in a cluster, d_p is the diameter of the perforations, and K_d is a dimensionless discharge coefficient. Assuming fracture geometry has

two parallel and smooth surfaces with constant height, the pressure drop due to fracturing fluids inside fracture is given by the following simplified Navier-Stokes equation [129]:

$$\frac{\partial p_i}{\partial z} = 2^{(n'+1)} k' \left(\frac{1+2n'}{n'} \right)^{n'} H^{-n'} w^{-(2n'+1)} Q_i^{n'} \tag{5.7}$$

where H is the fracture height, and w is the fracture width.

It is important to note that the pressure drops due to wellbore and perforation frictions are directly available from Eqs. (5.5)–(5.6); however, the pressure drop due to fracture propagation accounting for stress-shadow effects requires the numerical calculation of Eqs. (5.1), (5.2) and (5.7), which is in general a computationally expensive task.

5.2.3 Development of reduced-order models

The distribution of fracturing fluids into multiple fractures depends on the pressure drop associated with wellbore friction, perforation friction, and fracture propagation. However, due to the large computational requirement of the high-fidelity process model, Eqs. (5.1)-(5.7), presented in the previous section, it cannot be directly used in an optimization problem for the computation of the optimal perforation conditions. Therefore, it is necessary to develop a computationally efficient ROM. The pressure drops associated with the wellbore friction and the perforation friction depend on the spacing between fractures, and the number and diameter of perforations in a cluster, respectively. Therefore, rather than generating a large data set that will cover the entire operating conditions with respect to fracturing spacing, the number of perforations, and the diameter of perforations in a cluster, it would be more accurate and computationally efficient to directly use the analytical expressions, Eqs. (5.5)–(5.6), to estimate pressure drops due to wellbore friction and perforation friction. However, estimating the pressure drop associated with fracture propagation is a computationally expensive task because of stress-shadow effects, so we can instead develop a data-based ROM using the data generated from the high-fidelity process model for fixed fracture spacing, the number of perforations, and the diameter of perforations in a cluster.

To develop such a data-based ROM, we can apply a series of step inputs (flow rates at the well-

bore) to the high-fidelity process model by fixing the fracture spacing, the number of perforations and the diameter of perforations in a cluster to generate input/output data. Then, the multi-variable output error state-space (MOESP) algorithm is used to obtain a linear time-invariant state-space model, which is presented in the following form:

$$\underbrace{\begin{bmatrix} x_1(t_{k+1}) \\ \vdots \\ \vdots \\ \vdots \\ \vdots \\ \vdots \\ \vdots \\ x_n(t_{k+1}) \end{bmatrix}}_{X(t_{k+1})} = A \underbrace{\begin{bmatrix} x_1(t_k) \\ \vdots \\ \vdots \\ \vdots \\ \vdots \\ \vdots \\ \vdots \\ x_n(t_k) \end{bmatrix}}_{X(t_k)} + B \underbrace{\begin{bmatrix} Q_1(t_k - \theta_1(z_1)) \\ \vdots \\ Q_N(t_k - \theta_N(z_1)) \\ Q_1(t_k - \theta_1(z_2)) \\ \vdots \\ Q_N(t_k - \theta_N(z_2)) \\ Q_1(t_k - \theta_1(z_3)) \\ \vdots \\ Q_N(t_k - \theta_N(z_3)) \end{bmatrix}}_{U(t_k)} \tag{5.8}$$

$$\underbrace{\begin{bmatrix} \Delta p_{fp,1}(z_1, t_k) \\ \vdots \\ \Delta p_{fp,N}(z_1, t_k) \\ \Delta p_{fp,1}(z_2, t_k) \\ \vdots \\ \Delta p_{fp,N}(z_2, t_k) \\ \Delta p_{fp,1}(z_3, t_k) \\ \vdots \\ \Delta p_{fp,N}(z_3, t_k) \end{bmatrix}}_{Y(t_k)} = C \underbrace{\begin{bmatrix} x_1(t_k) \\ \vdots \\ \vdots \\ \vdots \\ \vdots \\ \vdots \\ \vdots \\ x_n(t_k) \end{bmatrix}}_{X(t_k)} \tag{5.9}$$

where $U(t_k)$ denotes the vector of input variables where $Q_i(t_k)$ is the effective volumetric flow rate in fracture i, $\theta_i(z_1)$, $\theta_i(z_2)$, and $\theta_i(z_3)$ are input time-delays in fracture i due to the travel time from

the wellbore to 3 different locations along the fracture, z_1, z_2, and z_3, respectively, $Y(t_k)$ denotes the vector of output variables where $\Delta p_{fp,i}(z_1, t_k)$ is the pressure drop between $z = 0$ and $z = z_1$ in fracture i, N is the total number of fractures created in a stage, $X(t_k)$ represents the n-dimensional state vector, and $A \in \mathbb{R}^{\mathrm{n}\times\mathrm{n}}$, $B \in \mathbb{R}^{\mathrm{n}\times 3\mathrm{N}}$, and $C \in \mathbb{R}^{3\mathrm{N}\times\mathrm{n}}$ are the system matrices which are estimated via MOESP algorithm utilizing the input and output data, U and Y, respectively.

By combining Eqs. (5.5)-(5.6) and (5.8)-(5.9) to estimate the pressure drop due to wellbore friction, perforation friction, and fracture propagation accounting for stress-shadow effects, the following integrated ROM will be used to compute the pressure at $z = z_j$ in fracture i, $p_i(z_j, t_k)$:

$$\Delta p_i(z_j, t_k) = \Delta p_{wf,i}(t_k) + \Delta p_{pf,i}(t_k) + \Delta p_{fp,i}(z_j, t_k) \tag{5.10a}$$

$$p_i(z_j, t_k) = p_o(t_k) - \Delta p_i(z_j, t_k) \tag{5.10b}$$

where $p_o(t_k)$ is the total pressure at the wellbore heel, which can be changed by manipulating the total flow rate, $Q_T(t)$, and $\Delta p_i(z_j, t_k)$ is the pressure drop from the wellbore heel at $(x, z) = (0, 0)$ to a location at $z = z_j$ in fracture i associated with the wellbore friction, perforation friction, and fracture propagation.

Fig. 5.3 compares the high-fidelity model and the data-based ROM with respect to the pressure drop profiles due to fracture propagation accounting for stress-shadow effects from the fracture initiation ($z = 0$) to 3 different locations along the fracture propagation direction ($z = 30$, 60 and $90\ m$), where we observed that the two models in very good agreement at all times. It is important to note that even though Eq. (5.10) is of the same form to Eq. (5.4), the required computational cost is a small fraction relative to that of Eq. (5.4).

Remark 11. *In addition to the MOESP algorithm employed in this work, there are a variety of linear [82, 83, 84] and nonlinear [77, 85, 86, 87, 88] model order-reduction techniques available.*

5.2.4 Validation of ROMs

In this subsection, we validated the integrated ROM developed in the previous subsection. The high-fidelity simulation data, which is required to develop a linear time-invariant state-space model

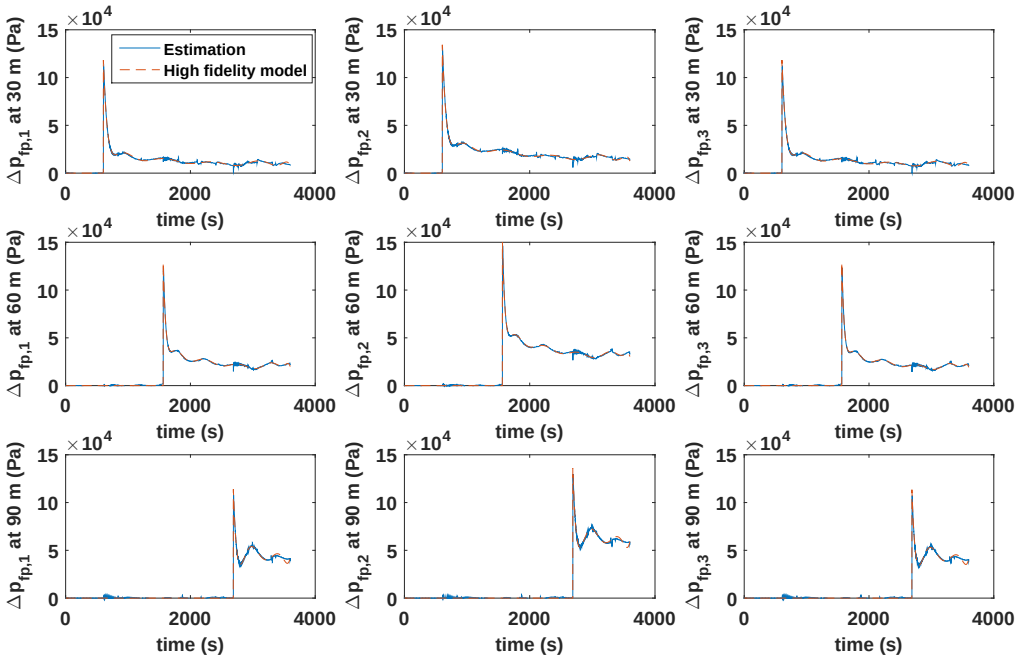

Figure 5.3: Comparison of the pressure drop profiles due to fracture propagation, $\Delta p_{fp,i}$, obtained at three different spatial locations ($z = 30$ m, $z = 60$ m, and $z = 90$ m) from the high-fidelity process model and the linear time-invariant state space model.

to describe the pressure drop due to fracture propagation accounting for stress-shadow effects, is generated for a specific set of the number of perforations ($n_p = 15$) and the diameter of perforations ($d_p = 0.0089$ m) in a cluster. It is important to note that the range of n_p and d_p used as a common practice in the actual field are $n_p = \{12, 13, \ldots, 20\}$ and $d_P = [0.00762, 0.015]$, respectively [122]. In order to validate the integrated ROM at different operating conditions, two particular operating conditions are considered, ($n_p = 20$ and $d_p = 0.015$ m) and ($n_p = 12$ and $d_p = 0.00762$ m), where the former is a set of lower bound and the latter is a set of upper bound values for the number and diameter of perforations in a cluster. In Figs. 5.4 and 5.5, the pressure drops at various locations across the fracture from the wellbore heel, $\Delta p_i(z_j, t_k)$, were compared betwe en the integrated ROM and the high-fidelity process model, which shows that the integrated ROM can be used to compute the pressure and the pressure drops, Eq. (5.10), for any n_p and d_p.

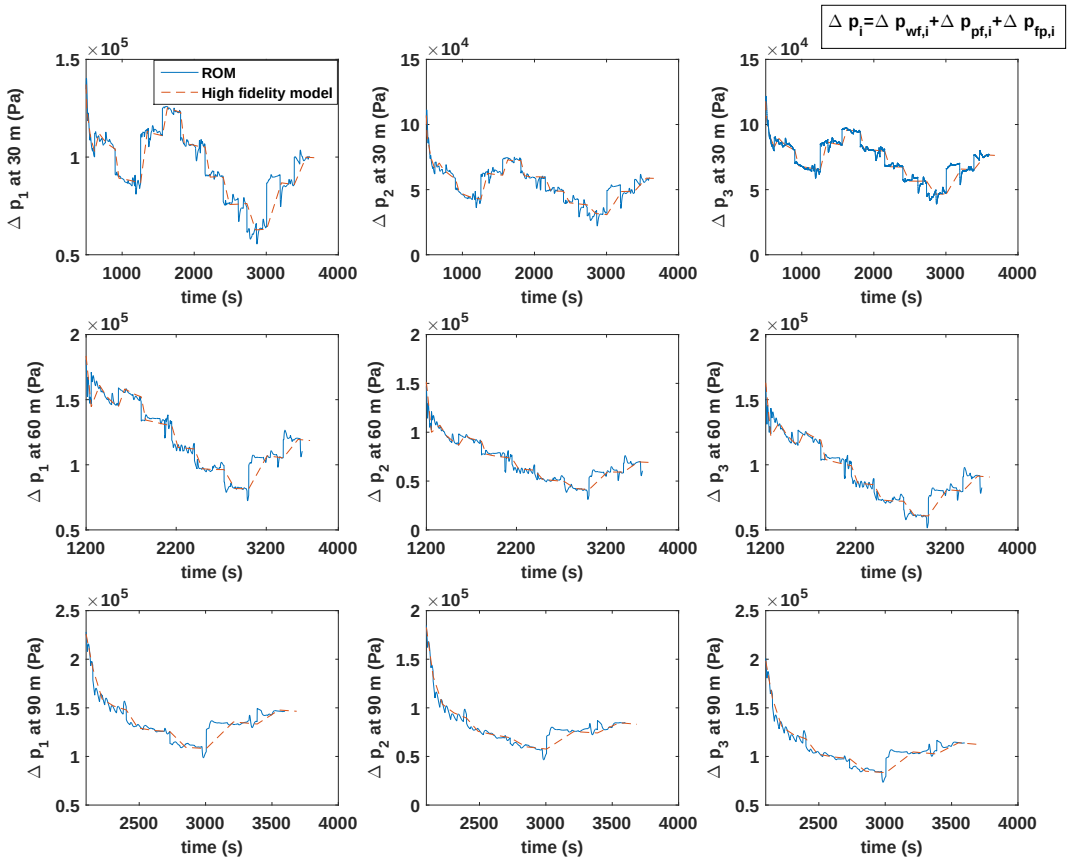

Figure 5.4: Comparison of the pressure drop profiles from the wellbore heel to three different spatial locations ($z = 30$ m, $z = 60$ m, and $z = 90$ m) in fractures, $\Delta p_i(z,t)$, from the high-fidelity process model and the integrated ROM for $n_p = 20$ and $d_p = 0.015$ m.

5.3 Model-based design technique to achieve uniform fracture growth

For multiple fracture treatments, the flow rate of fracturing fluids into each fracture, Q_i, is determined based on the pressure drop due to wellbore friction, perforation friction, and fracture propagation. By achieving uniform pressure drop in each fracture, we can promote the equal distribution of fracturing fluids into multiple fractures which will result in a uniform fracture length at the end of pumping. Specifically, we consider one of the widely used multiple hydraulic fracturing techniques in the field called the limited entry design technique to manipulate the pressure drop in each perforation cluster by varying the diameter of perforations, the number of perforations, and the flow rate at the wellbore to mitigate stress-shadow effects. Utilizing the developed integrated ROM that combines the analytical models and a data-based model to predict the flow resistance in

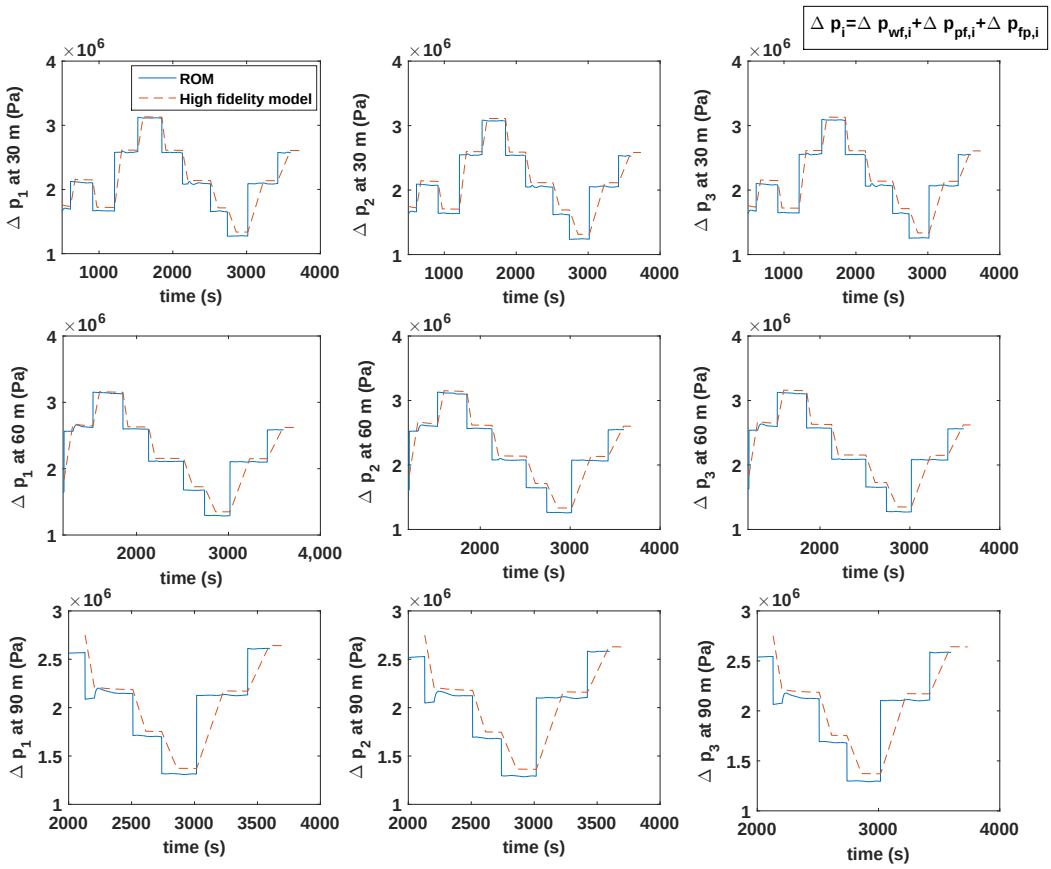

Figure 5.5: Comparison of the pressure drop profiles from the wellbore heel to three different spatial locations ($z = 30$ m, $z = 60$ m, and $z = 90$ m) in fractures, $\Delta p_i(z,t)$, from the high-fidelity process model and the integrated ROM for $n_p = 12$ and $d_p = 0.00762$ m.

each fracture, we present a model-based design technique for equal distribution of fracturing fluids into multiple fractures, resulting in uniform growth of multiple fractures at the end of pumping.

5.3.1 Optimal perforation conditions

In this subsection, a model-based design technique is presented to minimize the squared deviation of pressures at three different locations (z_1, z_2 and z_3) along the propagation direction in multiple fractures ($i = 1, ..., N$), which is formulated in the following form:

$$\min_{\substack{Q_{T,1},\ldots,Q_{T,12}\\ n_p\\ d_p}} \quad \sum_{j=1}^{3}\sum_{i=1}^{N}\sum_{m=1,m\neq i}^{N}\frac{1}{2}\left[p_i(z_j,t_k)-p_m(z_j,t_k)\right]^2 \tag{5.11a}$$

s.t.
$$p_i(z_j,t_k) = p_o(t_k) - \Delta p_{wf,i}(t_k) - \Delta p_{pf,i}(t_k) - \Delta p_{fp,i}(z_j,t_k) \tag{5.11b}$$

$$\Delta p_{wf,i}(t_k) = 2^{(3n'+2)}\pi^{-n'}k'\left(\frac{1+3n'}{n'}\right)^{n'} D^{-(3n'+1)}\sum_{l=1}^{i}(x_l - x_{l-1})Q_{w,l}(t_k) \tag{5.11c}$$

$$\Delta p_{pf,i}(t_k) = \frac{0.807\rho_s}{n_p^2 d_p^4 K_d^2}Q_{i,k}^2 \tag{5.11d}$$

$$X(t_{k+1}) = AX(t_k) + BU(t_k) \tag{5.11e}$$

$$Y(t_k) = CX(t_k) \tag{5.11f}$$

$$Q_{T,k} = \sum_{i=1}^{N} Q_{i,k} \tag{5.11g}$$

$$Q_{min} \leq Q_{T,k} \leq Q_{max} \qquad k = 1,\ldots,12 \tag{5.11h}$$

$$n_{p,min} \leq n_p \leq n_{p,max} \tag{5.11i}$$

$$d_{p,min} \leq d_p \leq d_{p,max} \tag{5.11j}$$

where the total treatment time t_f is divided into 12 stages with a time period of Δ, $Q_{T,k}$ and $Q_{i,k}$ are the flow rates at the wellbore and in fracture i, respectively, for $t \in [t_k, t_k + \Delta)$, n_p is the number of perforations in a cluster, d_p is the diameter of perforations, Q_{min} and Q_{max} are the lower and upper bounds on the flow rate at the wellbore, and N is the total number of fractures created in a stage.

In the optimization problem of Eq. (5.11), the cost function of Eq. (5.11a) describes the squared variation of pressures at three different locations in multiple fractures with time. The pressure at a particular location in fracture i is given by Eq. (5.11b). Specifically, the pressure drop due to wellbore friction and perforation friction are estimated using Eqs. (5.11c) and (5.11d), respectively, and the pressure drop due to fracture propagation by taking into account of stress-shadow effects

is estimated using the data-based model, Eqs. (5.11e) and (5.11f). The constraint of Eq. (5.11g) describes that the total flow rate of fracturing fluids at the wellbore is equal to the sum of the flow rates of fracturing fluids at each fracture. The distribution of total flow rate at the wellbore, $Q_{T,k}$, into each fracture, $Q_{i,k}$, at time t_k is estimated by using the pressure drops due to wellbore friction, perforation friction and fracture propagation at time t_{k-1} ($\Delta p_{wf,i}(t_{k-1})$, $\Delta p_{pf,i}(t_{k-1})$, and $\Delta p_{fp,i}(z, t_{k-1})$). The constraint of Eq. (5.11h) imposes the limits on the flow rate of fracturing fluids at the wellbore to account for pumping capacity. The constraints of Eq. (5.11i) and Eq. (5.11j) impose the limits on the number of perforations and the diameter of perforations in a cluster, respectively, to incorporate the common practice in the actual oil and gas field. In this work, we specifically used the uniform limited entry design technique, where all clusters have the same number and diameter of perforations, which is taken into account by using one set of variables, n_p and d_p, over the entire perforations.

5.4 A case study for three fractures propagating simultaneously

In this section, we first present a base case where the multiple fractures grow unevenly, and we apply the proposed model-based design technique to achieve a uniform length at the end of pumping. For all the cases, we considered three simultaneously propagating fractures per a single stage. The values of the model parameters used in the high-fidelity process model are provided in Table 5.1, which were selected broadly to resemble an actual shale gas development field case.

5.4.1 Non-uniform fracture growth (Base case)

In the base case, we considered a constant rate of $0.16\ \mathrm{m}^3/\mathrm{s}$ to inject fracturing fluids, the number of perforations per cluster of n_p = 20, and the diameter of the perforations of d_p = 0.015 m. The fracture geometry and width profile of the base case at the end of pumping are shown in Fig. 5.6. The exterior fractures are developed more at the expense of the interior fracture, and the width of the interior fracture is greatly restricted. Fracturing fluids tend to flow along the path with least resistance, minimizing the energy consumption of the entire physical process. The stress-shadow effects exert additional compression on the interior fracture and increases the

Parameter	Symbol	Value
Fracture spacing	X_{sep}	29.3 m
Young's modulus	E	0.2×10^{10} Pa
Poisson ratio of formation	ν	0.2
Density of slurry	ρ_s	1110 kg/m^3
Fracture height	H	60 m
Fracturing fluid power law index	n'	1
Fracturing fluid consistency index	k'	0.01 Pa $\cdot$ s
Horizontal wellbore diameter	D	0.1 m
Distance from horizontal wellbore heel to the first fracture in each stage	x_1	268 m
Dimensionless discharge coefficient	K_d	0.89
Minimum horizontal stress	$S_{h,min}$	6.95×10^7 Pa
Maximum horizontal stress	$S_{h,max}$	7.16×10^7 Pa

Table 5.1: Model parameters used for the base case simulation.

flow resistance because of reduced width as shown in Fig. 5.7, resulting in fluid diverting into the exterior fractures. As shown in Fig. 5.8, around 91% of the total fracturing fluid volume enters the exterior fractures, while only 9% of the total fracturing fluid volume was received by the interior fracture. The difference between the two exterior fractures is due to the wellbore friction. The pressure drop due to wellbore friction is proportional to the distance between the wellbore heel and fracture location, which causes the fracture close to the wellbore heel receives more fracturing fluids. The non-uniform fracture growth in simultaneously propagating multiple fractures will result in poor production of natural oil and gas resources from shale formations.

5.4.2 Uniform fracture growth using the proposed model-based design technique

In this subsection, we applied the proposed model-based design technique to achieve a uniform fracture length at the end of pumping. In the proposed design technique, we considered the limited entry design technique to manipulate the pressure drop in perforation clusters by changing the perforation conditions (n_p and d_p) and the flow rate at the wellbore to balance the additional compression caused by stress-shadow effects. The dynamic model described in Section 5.2 was utilized to generate input/output data for developing a linear approximate model to estimate the pressure drop due to fracture propagation, accounting for stress-shadow effects. By combining the data-based model for the pressure drop due to fracture propagation with analytical models for the

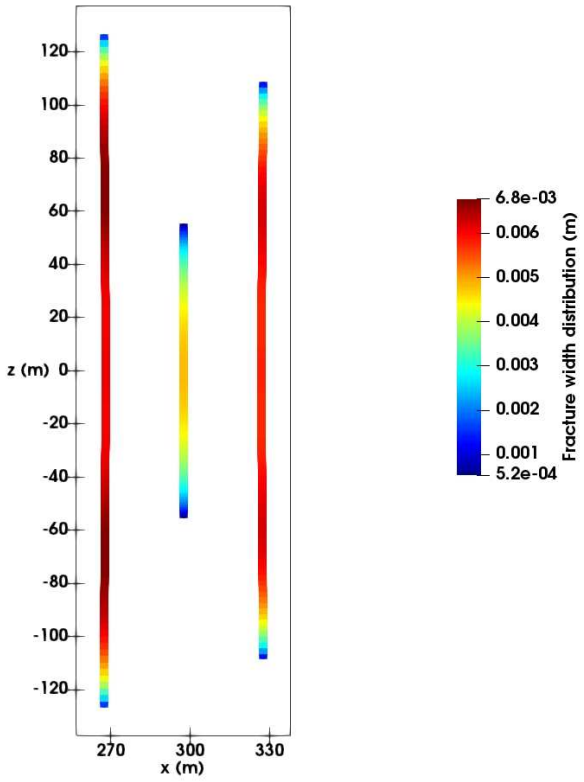

Figure 5.6: Fracture length and width distributions obtained at the end of pumping for the base case.

pressure drop due to wellbore friction and perforation friction, we developed an integrated ROM which was used in the proposed design technique. In the formulation, Eq. (5.11), the fracturing fluid's pumping schedule was divided into 12 pumping stages; the duration of each pumping stage was $\Delta = 300$ s and the total treatment time was $t_f = 3600$ s.

The pressure drop due to perforation friction in a perforation cluster, Eq. (5.6), increases with decreasing the diameter of perforations to the fourth power and with decreasing the number of perforations in a cluster to the second power. Therefore, use of a small diameter and number of perforations in a cluster can greatly increase the pressure drop due to perforation friction. [126] observed that increasing the pressure drop through perforations will result in more uniform distribution of fracturing fluids among multiple fractures which will lead to a uniform length of multiple fractures. A large pressure drop through perforations counteracts stress-shadow effects to ensure uniform distribution of fracturing fluids among multiple fractures [9]. In consistent with this obser-

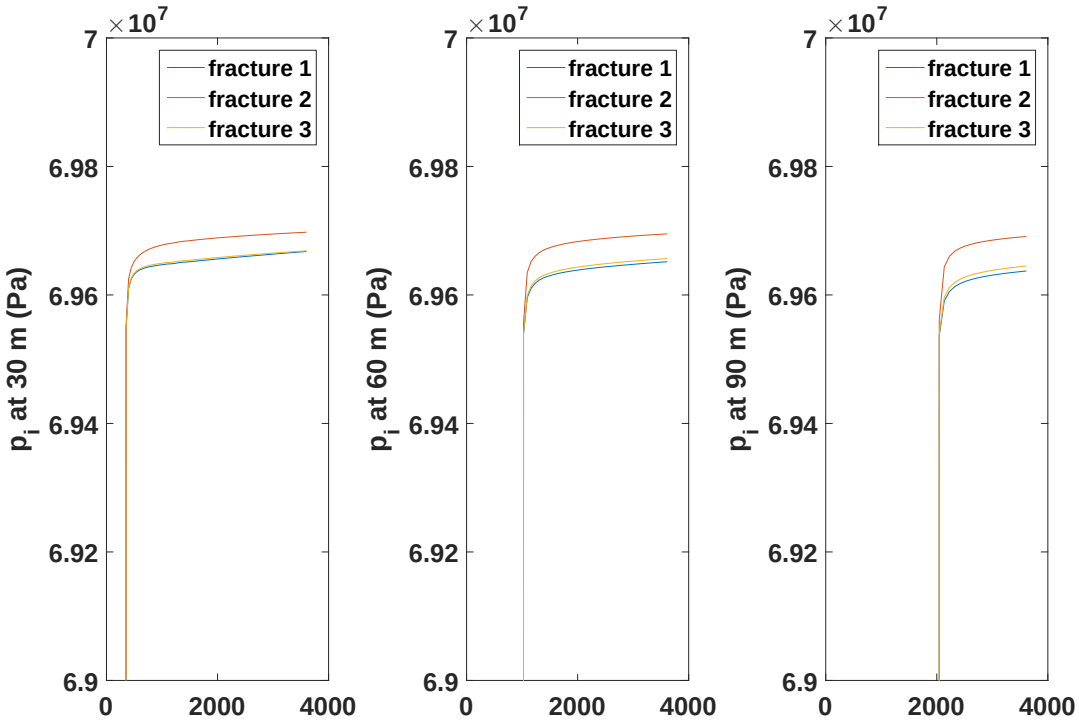

Figure 5.7: The pressure at three different locations in multiple fractures during the hydraulic fracturing process for the base case with a constant flow rate.

vation, the optimal number of perforations and the diameter of perforations in a cluster computed using the proposed design technique are $n_p = 12$ and $d_p = 0.011$ m, respectively, which are close to lower bounds and implies more pressure drop due to perforation friction, and the computed pumping schedule of fracturing fluids is shown in Fig. 5.9. Then, we applied the optimal pumping schedule of fracturing fluids and optimal perforation conditions to the high-fidelity model of a hydraulic fracturing process. The pressures at three different locations in multiple fractures during the hydraulic fracturing operation are presented in Fig. 5.10, where it is shown that the pressures at the same location in multiple fractures are uniform.

Regulating the pressures at the three different locations in multiple fractures promoted the equal distribution of fracturing fluids into multiple fractures resulting in a uniform fracture length at the end of pumping, as shown in Fig. 5.11. The difference between the longest and shorted fracture lengths is less than 1% as shown in Table 5.2. Fig. 5.12 compares the distribution of fracturing fluids into multiple fractures between the base case and the proposed method, where

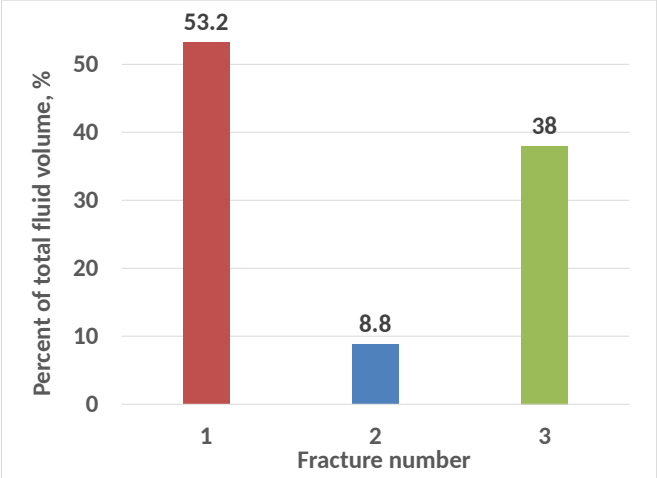

Figure 5.8: Percentage of the total fracturing fluid volume distributed into each fracture at the end of pumping for the base case.

more fracturing fluids were distributed into the interior fracture by manipulating the perforation conditions and flow rate as described in the proposed model-based design technique.

In hydraulic fracturing treatments, fracturing fluids are typically injected at a constant rate. To take into account this common practice in the field, we have performed an additional test with a constant flow rate of fracturing fluids. In Table 5.3, the obtained fracture length and average fracture width are presented for a constant flow rate of $0.18\ \mathrm{m}^3/\mathrm{s}$ and the perforation conditions of $n_p = 12$ and $d_p = 0.011\ \mathrm{m}$. By comparing with Tables 5.2 and 5.3, it was observed that the maximum deviation between the fracture lengths from the constant flow rate case (1.38%) is slightly greater than that of the time-varying flow rate case (0.94%); which shows that the effect of varying flow rate of fracturing fluids on uniform growth is not significant. On the other hand, changing the perforation conditions has a major influence on uniform growth.

Then, we studied the effect of model uncertainty by considering plant-model mismatch in the Young's modulus, E. Specifically, we applied the optimal pumping schedule (fracturing fluid flow rate) and optimal perforation conditions to the high-fidelity model by varying the Young's modulus +/-10% from its nominal value. Table 5.4 shows that the maximum deviation between the fracture lengths is slightly greater when there is plant-model mismatch. In this work, we solved the pro-

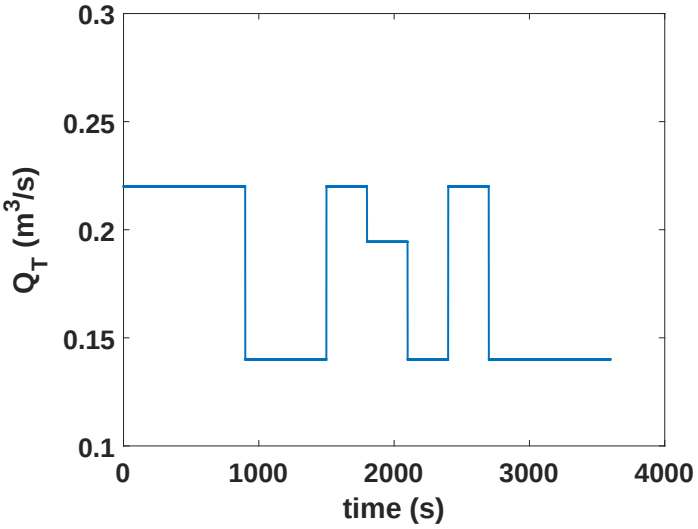

Figure 5.9: Pumping schedule of fracturing fluids using the proposed model-based design technique to achieve uniform pressure at different locations in multiple fractures with time.

Fracture number	Fracture length, m	Fracture average width, m
1	239.8	0.0050
2	238.5	0.0046
3	237.5	0.0050

Table 5.2: Fracture length and average width at the end of pumping using the proposed model-based design technique.

posed model-based design technique once and offline by utilizing the integrated ROM and limited entry design technique to compute the fracturing fluid flow rate and the perforation conditions. In the future, we can consider a closed-loop operation of simultaneously growing multiple fractures. Specifically, in hydraulic fracturing, the available real-time measurements are the fracture width near the wellbore and fracture length. In practice, the plant-model mismatch and the uncertainties in process model parameters can be handled through the design of a feedback control system by utilizing these available real-time measurements as a feedback from the system.

5.5 Conclusions

In this work, we developed a model-based design technique that computes the flow rate of fracturing fluids and perforation conditions to achieve uniform growth of simultaneously propagating multiple fractures. First, we presented a dynamic model of hydraulic fractures to describe

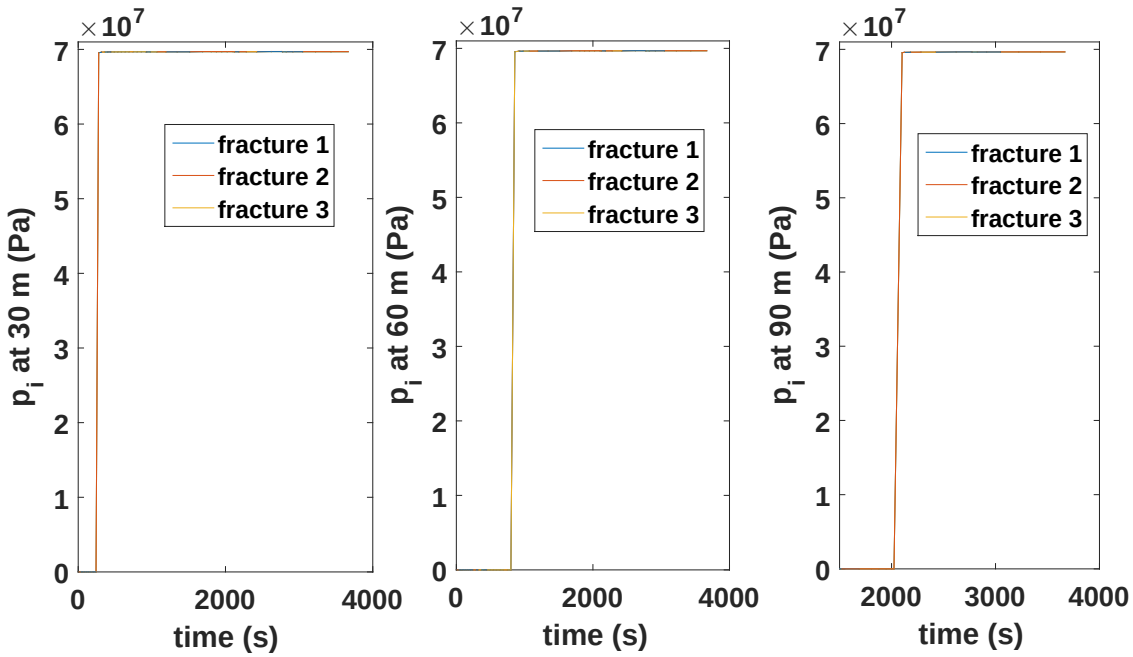

Figure 5.10: The pressures at three different locations in multiple fractures during the hydraulic fracturing process after applying the flow rate of fracturing fluids and perforation conditions using the proposed model-based design technique.

Fracture number	Fracture length, m	Fracture average width, m
1	239.4	0.0054
2	237.8	0.0049
3	236.5	0.0054

Table 5.3: Fracture length and average width at the end of pumping for a constant flow rate using the proposed model-based design technique.

the stress-shadow effects in simultaneously propagating multiple fractures. Second, we developed a new model order-reduction technique for simultaneously propagating multiple fractures by integrating the analytical models to calculate the pressure drop due to perforation friction and wellbore friction and a data-based ROM, using the data generated from the high-fidelity process model, to describe the pressure drop due to stress-shadow effects. Lastly, we proposed a model-based design technique by utilizing the integrated ROM and the limited entry design technique to compute the flow rate of fracturing fluids and the perforation conditions which promote equal distribution of fracturing fluids to achieve uniform growth of multiple fractures while mitigating the undesired stress-shadow effects. Simulation results demonstrated that the proposed design technique was

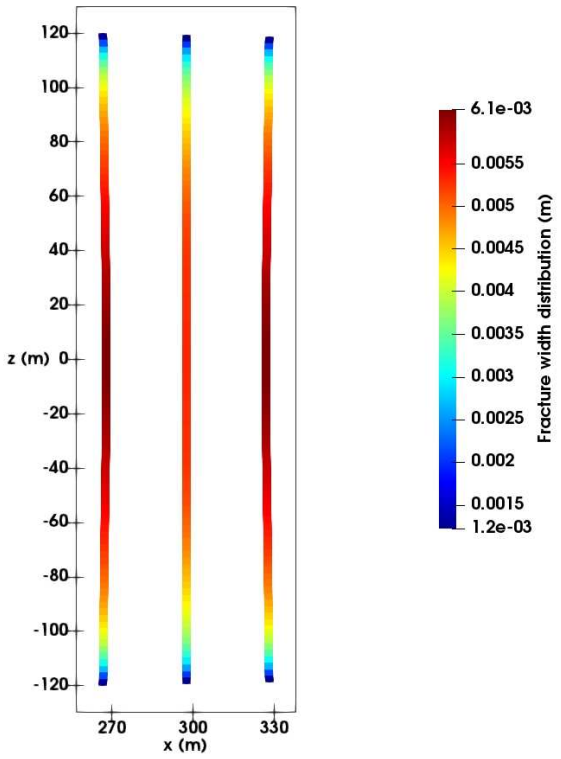

Figure 5.11: Fracture length and width distributions obtained at the end of pumping using the proposed model-based design technique.

Mismatch in E	% of deviation between the fracture lengths
-10%	1.03
0%	0.94
10%	1

Table 5.4: Maximum deviation between the fracture lengths when there is plant-model mismatch in the Young's modulus.

able to outperform the base case with respect to achieving uniform fracture growth, by explicitly handling stress-shadow effects, and changing the perforation conditions has a dominant effect on uniform growth compared to varying flow rate of fracturing fluids.

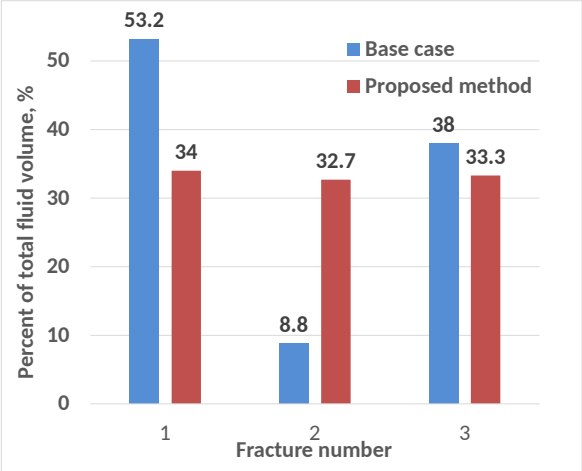

Figure 5.12: Percentage of the total fracturing fluid volume distributed into each fracture at the end of pumping for the base case and for the one with the proposed model-based design technique.

6. MODELING AND CONTROL OF PROPPANT DISTRIBUTION OF MULTI-STAGE HYDRAULIC FRACTURING IN HORIZONTAL WELLS*

6.1 Introduction

In chapter 5, we developed a model-based design technique that computes the flow rate of fracturing fluids and perforation conditions to achieve uniform growth of simultaneously propagating multiple fractures. However, we only described simultaneously propagating multiple fractures under stress shadow effect without incorporating proppant transport mechanisms.

The proppant transport takes place along the horizontal direction by the fracturing fluid and the vertical direction due to the gravitational force. Specifically, the proppant transport in the horizontal direction is mainly governed by three mechanisms. First, the proppant particles may transport in suspension in a fracturing fluid due to advection. Second, the proppant particles may roll over the surface of a proppant bank. Lastly, the proppant particles on the surface of a proppant bank may lift off due to shear force, and then travel in the horizontal direction before landing on other proppant bank. In addition to these three mechanisms, the use of slick water may lead to fast proppant settling and significant proppant bank formation.

In hydraulic fracturing, proppant transport is simulated using two kinds of numerical methods: Eulerian-Lagrangian method and Eulerian-Eulerian method. For the Eulerian-Lagrangian method, the fracturing fluid flow is solved in Eulerian grids and the proppant transport is solved using a Lagrangian method [63, 136, 137, 138]. This approach is computationally very expensive to be incorporated into the simultaneously propagating multiple fractures model. Therefore, Eulerian-Eulerian method was developed to quickly solve the proppant transport in the fracture in which both the fracturing fluid and proppant are solved in Eulerian grids. The following models were built using the Eulerian-Eulerian method to simulate the proppant transport. Schols and Visser [139] proposed a model to calculate the proppant bank formation in a vertical fracture by neglect-

*Reprinted with permission from "Modeling and Control of Proppant Distribution of Multistage Hydraulic Fracturing in Horizontal Shale Wells" by Siddhamshetty et al., 2019. *Industrial & Engineering Chemistry Research*, 58, 3159-3169, Copyright 2019 by American Chemical Society.

ing the fracturing fluid loss. Based on this model, Gu and Hoo [43] developed a model to calculate the proppant transport with a high-viscosity fracturing fluid. However, they did not consider the proppant resuspending. Recently, Hu et al. [140] developed a new model that describes proppant transport in a single vertical fracture. These proppant transport models focused on simple fracture geometry, i.e., a single, planar fracture. While some efforts have been made to describe simultaneously propagating multiple fractures under stress shadow effect, they did not incorporate proppant transport mechanisms [9, 122, 124]. Motivated by these considerations, in this chapter we will develop a new model that accounts for proppant transport as well as simultaneously propagating multiple fractures.

One of the important challenge in simultaneously propagating multiple fractures with close spacing is that they often induce non-uniform fracture development due to stress-shadow effects. In Chapter 5, we proposed an optimization-based limited entry design technique to determine the perforation conditions to achieve uniform growth of multiple fractures.

The hydrocarbon production rate through multiple fracture networks is strongly dependent on the proppant distribution within the fractures at the end of pumping, because they will create conductive channels for oil and gas transport [141]. In certain oil reservoirs, 10% difference in the fracture length from the desired value may cause 50% less oil production rate [65, 142]. Motivated by this, in this chapter, we will focus on introducing a new model-based control algorithm by utilizing the new high-fidelity model to compute online fracturing fluid pumping schedules for uniform proppant distribution in simultaneously propagating multiple fractures.

This chapter is organized as follows: First, a dynamic model of simultaneously propagating multiple fractures including proppant transport and proppant resuspending is presented by coupling fluid flow, rock mechanics and proppant transport. Next, a data-based linear approximate model is constructed using the high-fidelity simulation data to design a Kalman filter that estimates unmeasurable states. Lastly, a model-based feedback controller is developed to achieve a uniform proppant bank height in simultaneously propagating multiple fractures at the end of pumping by handling the undesired stress-shadow effects.

6.2 Dynamic modeling of simultaneously propagating multiple fractures

In this work, a dynamic model of simultaneously propagating multiple fractures consists of following three sub-processes: (1) fracture propagation, (2) proppant transport, and (3) proppant settling and proppant resuspending.

The fracture propagation model is presented in Section 5.2.

6.2.1 Modeling of proppant transport

The proppant volume concentration, C_i, is given by [140]:

$$\frac{\partial(C_i W_i)}{\partial t} + \nabla \cdot (W_i C_i V_{p,i}) = 0 \tag{6.1}$$

where subscript i denotes the fracture number, and ∇ is the vector differential operator. The net velocity of proppant particles, $V_{p,i}$, is obtained by describing the proppant transport along the horizontal and vertical directions by the slurry velocity, $V_{hz,i}$, and the settling velocity, $V_{s,i}$, respectively, in the form presented below [79, 142]:

$$V_{p,i} = V_{hz,i} + V_{s,i} \tag{6.2}$$

The gravity-induced proppant settling velocity of the fracturing fluid, $V_{s,i}$, is computed by [60]:

$$V_{s,i} = \frac{(1 - C_i)^2}{10^{1.82 C_i}} \frac{(\rho_p - \rho_f)\, g D_p^2}{18\mu} \tag{6.3}$$

where μ is the fracturing fluid viscosity, ρ_p is the proppant particle density, ρ_f is the pure fluid density, D_p is the proppant diameter, and g is the gravitational acceleration constant. The relationship between the fracturing fluid viscosity, μ, and the suspended proppant concentration, C_i, can be described through the following empirical model [70]:

$$\mu(C_i) = \mu_0 \left(1 - \frac{C_i}{C_{\max}}\right)^{-\beta} \tag{6.4}$$

where the μ_0 is the effective Newtonian viscosity of clean fluid, and β is a constant obtained from experiments, ranging between 1 and 3 [69].

6.2.2 Modeling of proppant settling and proppant resuspending

In unconventional reservoirs, due to the use of low-viscosity fracturing fluids, the amount of proppant settling during hydraulic fracturing is significant. The settled proppant forms a proppant bank and its height is dynamically determined by two factors: the rates of proppant bank formation and proppant resuspending. The proppant bank formation due to the proppant settling can lead to an increase in proppant bank height, and the proppant resuspending due to the shear force can contribute to a decrease in proppant bank height. Therefore, the overall evolution of proppant bank height, $H_{bank,i}$, is described by [140]:

$$H_{bank,i} = \int_0^t \left(\frac{dH_{b,i}}{dt} - \frac{dH_{w,i}}{dt} \right) dt \tag{6.5}$$

where $\frac{dH_{b,i}}{dt}$ is the rate of proppant bank formation, and $\frac{dH_{w,i}}{dt}$ is the rate of proppant resuspending. The rate of proppant bank formation via proppant settling is described by:

$$\frac{dH_{b,i}}{dt} = \frac{C_i V_{s,i}}{C_{max}} \tag{6.6}$$

where $C_{\max}$ is the theoretical maximum concentration in the proppant bank. The rate of proppant resuspending due to shear force is given by [140]:

$$\frac{dH_{w,i}}{dt} = \frac{K f_i \rho_{s,i} V_{hz,i}}{2\rho_p} \tag{6.7}$$

where K is the comprehensive experimental factor which is set as 0.8 by [140] to obtain a good match with experimental data, f_i is the friction factor of fracture i, and $V_{hz,i}$ is the slurry velocity. The following expression can be used to compute f_i [143].

$$\frac{1}{\sqrt{(2f_i)}} = -0.86 \left(\frac{(D_p/D_{h,i})}{3.7} - \frac{2.51}{Re_i \sqrt{(2f_i)}} \right) \tag{6.8}$$

where Re_i is Reynolds number, and $D_{h,i}$ is the hydraulic diameter given by:

$$D_{h,i} = \frac{2W_i H_{f,i}}{(W_i + H_{f,i})} \tag{6.9}$$

where $H_{f,i}$ is the height of the free cross-sectional area, which is the distance between the fracture height and the proppant bank height, ($H_{f,i} = H - H_{bank,i}$). Then, Re_i and $\rho_{s,i}$ are obtained by the following equations:

$$Re_i = \frac{\rho_{s,i} V_{s,i} D_{h,i}}{\mu} \tag{6.10a}$$

$$\rho_{s,i} = (1 - C_i)\rho_f + C_i \rho_p \tag{6.10b}$$

6.3 Optimal fracture geometry in unconventional reservoirs

We used the section-based optimization method presented Section 4.4.1 for determining the optimum number of wells n_c, number of fractures per well n_r, and fracture half-length x_f, at which the productivity of a stimulated well is maximized subject to a fixed amount of fracturing resources like proppant [113].

In this work, we assumed the total amount of proppant available to stimulate a section is $M_{prop} = 3.96 \times 10^7$ kg. Using the method developed by Liu and Valkó [113] for the above amount of proppant, the optimal values that maximize the productivity from a section are found to be: $n_c = 6$, $n_r = 55$, $x_f = 120$ m, $I_x = 0.895$.

Fig. 4.1 illustrates the growth and propagation of proppant bank height during hydraulic fracturing. Because of predominantly low-viscosity fracturing fluids used in unconventional reservoirs, the proppant settles quickly. The settled proppant forms a bank, which will grow to an equilibrium height, h_{eq}, at which the rate of proppant bank formation via proppant settling is equal to that of the proppant wash-out due to the shear force. The main objective of hydraulic fracturing is to achieve a proppant bank with a height of h_{eq} and a fracture length of x_f. The above-mentioned objective

can be translated into achieving an average width of $W_{avg,target}$, which can be obtained as follows:

$$W_{avg,target} = \frac{M_{prop,frac}}{2\rho_p h_{eq} x_f (1-\phi)} \tag{6.11}$$

where the amount of proppant to be injected into each fracture is $M_{prop,frac} = 72,000$ kg, and the equilibrium height of proppant bank for the considered flow condition is $h_{eq} = 57$ m. In our case, the calculated target width for each fracture at the end of pumping is $W_{avg,target} = 3.74$ mm. In the following section, we focus on the development of a model-based feedback controller whose objective is to achieve a fracture length of $x_f = 120$ m, and an average fracture width of $W_{avg,target} = 3.74$ mm. In simultaneously growing multiple fractures, close spacing between neighboring fractures often induces non-uniform fracture development due to stress-shadow effects. In Chapter 5, we proposed an optimization-based limited entry design technique to determine a perforation condition to achieve uniform growth of simultaneously propagating multiple fractures [144]. We considered the same perforation conditions of $n_p = 12$ and $d_p = 0.011$ m in the following sections.

6.4 Model predictive control for hydraulic fracturing processes

In this section, we first use the multi-variable output error state-space (MOESP) algorithm to construct a linear time-invariant approximate model from the high-fidelity simulation data. The real-time measurements of fracture width at the wellbore (using the wellbore pressure data) and the length (using the microseismic data) of all the fractures are assumed to be available at every sampling time [53]. Utilizing these available measurements and the obtained linear time-invariant approximate model, we design a Kalman filter to estimate the average fracture width at each sampling time. Then, we design a model-based feedback controller that computes the optimal proppant pumping schedule (i.e., the flow rate and proppant concentration of the fracturing fluid at the wellbore) to achieve the desired average fracture width at the end of pumping, which will lead to the proppant bank height with a desired value and thereby the maximal gas production rate.

6.4.1 Development of reduced-order models

Due to the infinite-dimensional nature of the high-fidelity process model of Eqs. (6.5)–(6.10), a reduced-order model (ROM) is required for the purpose of model-based feedback controller design. First, a series of step inputs are applied to the high-fidelity process model to generate input/output data of proppant transport in simultaneously propagating multiple fractures. Then, the MOESP algorithm is used to obtain a linear time-invariant state-space model of hydraulic fracturing process, which is presented in the following form:

$$\underbrace{\begin{bmatrix} x_1(t_{k+1}) \\ \vdots \\ x_n(t_{k+1}) \end{bmatrix}}_{X(t_{k+1})} = A \underbrace{\begin{bmatrix} x_1(t_k) \\ \vdots \\ x_n(t_k) \end{bmatrix}}_{X(t_k)} + B \underbrace{\begin{bmatrix} Q_{z0}(t_k) \\ C_0(t_k) \end{bmatrix}}_{U(t_k)} \tag{6.12}$$

$$\underbrace{\begin{bmatrix} W_{avg,1}(t_k) \\ \vdots \\ W_{avg,N}(t_k) \\ W_{0,1}(t_k) \\ \vdots \\ W_{0,N}(t_k) \\ L_1(t_k) \\ \vdots \\ L_N(t_k) \end{bmatrix}}_{Y(t_k)} = C \underbrace{\begin{bmatrix} x_1(t_k) \\ \vdots \\ \vdots \\ \vdots \\ \vdots \\ \vdots \\ \vdots \\ x_n(t_k) \end{bmatrix}}_{X(t_k)} \tag{6.13}$$

where $U(t_k)$ denotes the vector of input variables, $Y(t_k)$ denotes the vector of output variables, and $X(t_k)$ represents the n-dimensional state vector. Specifically, $Q_{z0}(t_k)$ is the flow rate and $C_0(t_k)$ is the proppant concentration of the fracturing fluid at the wellbore (i.e, the manipulated input variables), $W_{avg,i}(t_k)$ is the average fracture width, $W_{0,i}(t_k)$ is the fracture width at the wellbore,

$L_i(t_k)$ is the length of fracture i, and $A \in \mathbb{R}^{\mathrm{n}\times\mathrm{n}}$, $B \in \mathbb{R}^{\mathrm{n}\times 2}$ and $C \in \mathbb{R}^{3\mathrm{N}\times\mathrm{n}}$ are the system matrices which are estimated via the MOESP algorithm utilizing the input and output data, U and Y, respectively. In practice, the available real-time measurements are limited to the fracture width near the wellbore and the lengths of simultaneously propagating multiple fractures at every sampling time. This leaves the average fracture width to be estimated through a Kalman filter at each sampling time, which will be discussed in the following section.

6.4.2 Kalman filter design

The process and measurement noise is added to the ROM presented as follows:

$$X(t_{k+1}) = AX(t_k) + BU(t_k) + w(t_k) \tag{6.14a}$$

$$Y(t_k) = CX(t_k) + v(t_k) \tag{6.14b}$$

where w is the process noise and v represents the measurement noise. Both w and v are assumed to be drawn from a zero mean Gaussian distribution with covariances Q and R, respectively, as follows:

$$w(t_k) \sim N(0, Q) \tag{6.15a}$$

$$v(t_k) \sim N(0, R) \tag{6.15b}$$

The Kalman filter is a two-step process: prediction and measurement update. Combining the prediction and measurement update steps, the Kalman filter is presented in the following form:

$$\hat{X}(t_{k+1}) = A\hat{X}(t_k) + BU(t_k) + M(t_k)(Y_m(t_k) - \hat{Y}(t_k)) \tag{6.16a}$$

$$M(t_k) = P(t_k)C^T(R(t_k) + CP(t_k)C^T)^{-1} \tag{6.16b}$$

$$P(t_{k+1}) = (I - M(t_k)C)P(t_k) \tag{6.16c}$$

where the notation $\hat{(\cdot)}$ denotes the estimated variables, $M(t_k)$ is the Kalman filter gain, $P(t_k)$ de-

notes the covariance of the state estimation error, and $Y_m(t_k) = [W_{0,1}(t_k) \dots W_{0,N}(t_k), L_1(t_k) \dots L_N(t_k)]^{\mathrm{T}}$ are the available real-time measurements, the width at the wellbore and the lengths of simultaneously propagating multiple fractures.

Fig. 6.1 shows the comparison between the estimated and the true average fracture width with time in simultaneously propagating multiple fractures. It is observed that the estimated average fracture width quickly converges to the true value obtained from the high-fidelity process model. The effect of the measurement noise, which is often found in experimental readings, is simulated by introducing white noise with a zero mean Gaussian distribution.

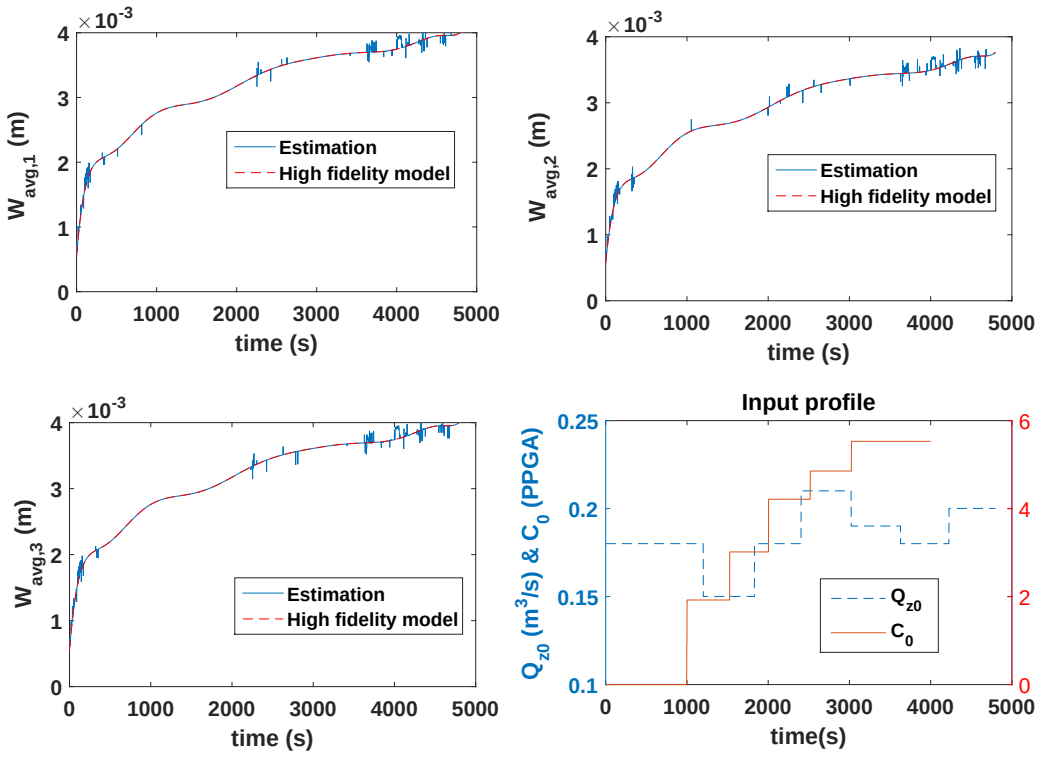

Figure 6.1: Comparison between the true values and the estimates of average width profiles of simultaneously propagating multiple fractures.

6.4.3 Model-based feedback control formulation

Within this regard, a novel model-based feedback control system is designed to minimize the sum of the squared deviation of the average fracture width at the end of pumping from its set-point

value over multiple fractures ($i = 1, ..., N$), which is formulated in the following form:

$$\min_{\substack{C_{stage,k},\ldots,C_{stage,8}\\ Q_{stage,k},\ldots,Q_{stage,8}}} \quad \sum_{i=1}^{N}(\hat{W}_{avg,i}(t_f) - W_{avg,target})^2 \tag{6.17a}$$

$$\text{s.t.} \quad \text{Kalman filter, Eq. (6.16)} \tag{6.17b}$$

$$\text{ROM, Eqs. (6.12) and (6.13)} \tag{6.17c}$$

$$\hat{W}_{0,i}(t_k) = W_{0,i}(t_k), \qquad \hat{L}_i(t_k) = L_i(t_k) \tag{6.17d}$$

$$C_{stage,k-1+m} \leq C_{stage,k+m} \leq 5 \text{ PPGA} \tag{6.17e}$$

$$Q_{min} \leq Q_{stage,k+m} \leq Q_{max} \tag{6.17f}$$

$$m = 1, \ldots, 8-k \tag{6.17g}$$

$$\Delta\left(\sum_{k=1}^{8} 2Q_{stage,k}C_{stage,k}\right) = NM_{prop,frac} \tag{6.17h}$$

where N is the total number of simultaneously propagating fractures considered, $W_{avg,target}$ is the desired average fracture width at the end of pumping, $\hat{W}_{avg,i}(t_k)$ is the predicted average width of fracture i obtained via Eq. (6.16), t_f is the total operation time of hydraulic fracturing, Δ is the sampling time, which is also the duration of each pumping stage, t_k is the current time, $W_{0,i}(t_k)$ and $L_i(t_k)$ are the two measurements available at $t = t_k$, and $C_{stage,k}$ and $Q_{stage,k}$ are the inlet proppant concentration and the inlet flow rate of the k^{th} pumping stage ($t \in [t_k, t_k + \Delta]$), respectively, which are to be determined by solving Eq. (6.17) with a shrinking prediction horizon $N_p = t_f - t_k$.

In the optimization problem of Eq. (6.17), the cost function of Eq. (6.17a) describes the sum of the squared deviation of the predicted average fracture width from the set-point value at the end of pumping over multiple fractures. The real-time measurements of the width at the wellbore and the length of all the multiple fractures are available at each sampling time, which is described by Eq. (6.17d), and are used to initialize the Kalman filter of Eq. (6.16) to predict the unmeasurable average fracture width trajectories of simultaneously propagating multiple fractures. Please note that the Kalman filter plays a role as a soft sensor to provide measurements to the model predictive control (MPC) formulation. The constraint of Eq. (6.17e) implies that the proppant concentra-

tion will be increased monotonically, and the maximum injected proppant concentration is less than $5\ \mathrm{PPGA}$. The constraint of Eq. (6.17f) imposes limits on the flow rate of fracturing fluids at the wellbore. The constraint of Eq. (6.17h) describes the amount of proppant to be injected to a horizontal well to create a N fractures. In multi-stage hydraulic fracturing, there are two challenges: 1) mitigating stress-shadow effects to achieve a uniform fracture length; 2) driving the average fracture width over multiple fractures to a set-point value, which will lead to a proppant bank height with a desired value in simultaneously propagating multiple fractures. We mitigate the stress-shadow effects by using the optimal perforation conditions obtained in Chapter 4 [144]. The remaining challenge of regulating the average fracture widths of multiple fractures will be handled by the proposed MPC scheme.

6.5 A case study for three fractures propagating simultaneously

In this section, we first studied a base case where the multiple fractures grow unevenly due to stress-shadow effects resulting in non-uniform propped fracture geometry, leading to a poor production rate of oil and gas resources from shale formations. Then, we applied the proposed model-based feedback controller for the regulation of the average fracture width in simultaneously propagating multiple fractures to achieve the optimal propped fracture geometry at the end of pumping. For all the cases, we considered three simultaneously propagating fractures. We used the parameters from a field case in the high-fidelity process model, and they are presented in Table 5.1 [3].

6.5.1 Non-uniform fracture growth (Base case)

In the base case, we considered a constant flow rate of $0.18\ \mathrm{m}^3/\mathrm{s}$ to inject fracturing fluids and an amount of $3M_{prop,frac}$ of proppant. We considered 20 perforations per cluster (n_p = 20), and the diameter of perforation was $d_p = 0.015\ \mathrm{m}$. The fracture geometry and width profile of the base case at the end of pumping are shown in Fig. 6.2. The exterior fractures were developed more at the expense of the interior fracture, while the interior fracture width was greatly restricted. The stress-shadow effects exerted additional compression on the interior fracture and increased the flow

resistance, resulting in fluid diverting into the exterior fractures. Due to the uneven distribution of fracturing fluids, the propped fracture geometry of fractures is different from the desired one obtained from the section-based optimization method as shown in Fig. 6.3.

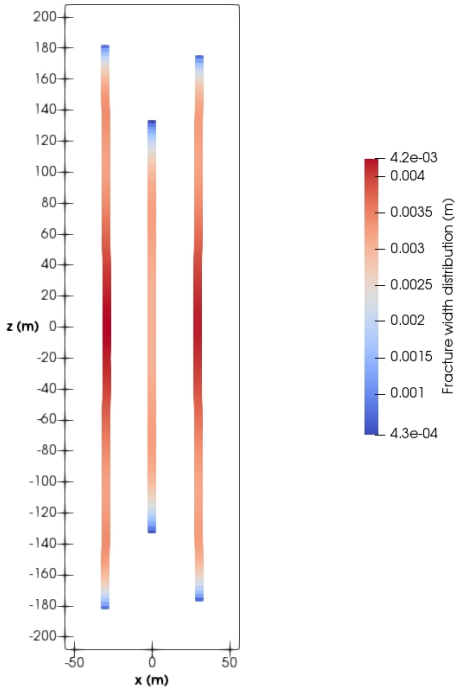

Figure 6.2: Fracture length and width distributions in multiple fractures obtained at the end of pumping for the base case.

6.5.2 Closed-loop simulation results under the proposed model-based feedback controller

In this subsection, we applied the proposed model-based feedback controller for regulation of the average fracture widths of simultaneously propagating multiple fractures to achieve the optimal propped fracture geometry at the end of pumping in unconventional reservoirs. The dynamic high-fidelity process model of simultaneously propagating multiple fractures, described earlier, was utilized to simulate a hydraulic fracturing process. The high-fidelity model was initially used to generate the input/output data of simultaneously propagating multiple fractures for develop-

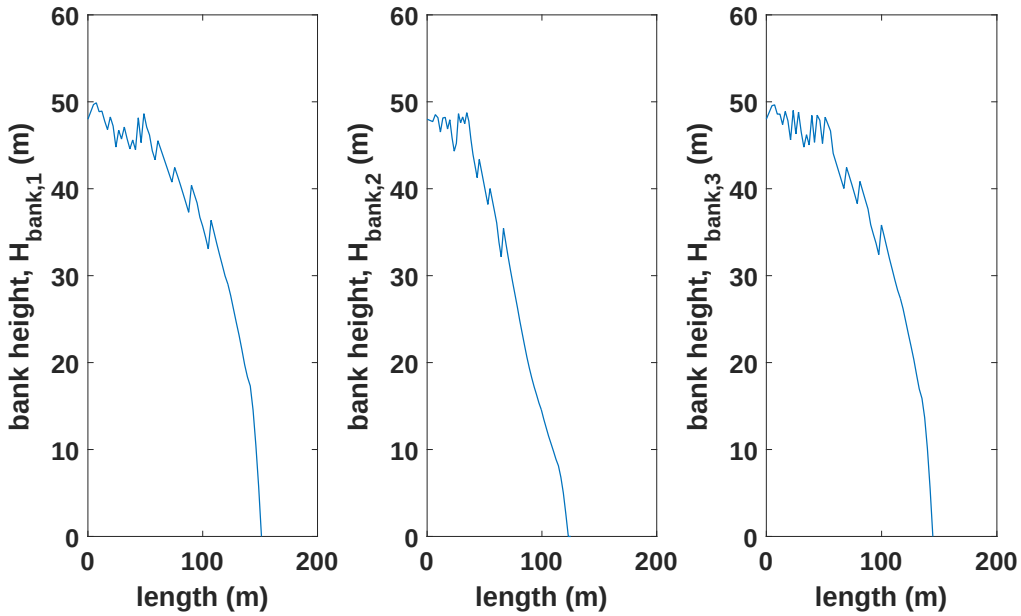

Figure 6.3: Spatial proppant bank height profiles of the simultaneously propagating three fractures obtained at the end of pumping for the base case.

ing a linear approximate model for developing a Kalman filter and model-based feedback control system. In order to achieve the uniform equilibrium proppant bank height, h_{eq}, over the optimal fracture half-length, $x_f = 120$ m, the desired average fracture width at the end of pumping was found to be $W_{avg,target} = 3.74$ mm. For the simulations, the pad time, t_p, was fixed to be 1200 s in order to avoid premature termination of the hydraulic fracturing process. The feedback control system and the Kalman filter were initialized from the beginning of hydraulic fracturing operation. In the closed-loop simulations, Δ and t_f were chosen to be 600 s and 4800 s, respectively. The pumping schedule of proppant and fracturing fluid was divided into 8 pumping stages and the duration of each pumping stage was 600 s, which was equal to the sampling time Δ. The real-time measurements of the width at the wellbore, $W_{0,i}(t_k)$, and the length, $L_i(t_k)$, of all the fractures were assumed to be available at each sampling time, which were then used to estimate the average fracture width, $\hat{W}_{avg,i}$, via the Kalman filter. The first step of solution, $C_{stage,k}$ & $Q_{stage,k}$, obtained by solving the optimization problem over a prediction horizon length of N_p was applied to the high-fidelity process model in a sample-and-hold fashion, and this procedure was repeated at every sampling time until the end of hydraulic fracturing.

One of the challenges in simultaneously propagating multiple fractures with close spacing is that they often induce non-uniform fracture development due to stress-shadow effects. In this work, we used an optimization-based limited entry design technique to determine the perforation conditions which promote equal distribution of fracturing fluids to achieve uniform growth of multiple fractures [144]. Specifically, we considered the perforation conditions of $n_p = 12$ and $d_p = 0.011$ m through which we were able to achieve almost uniform distribution of fracturing fluids into simultaneously propagating multiple fractures as shown in Fig. 6.4.

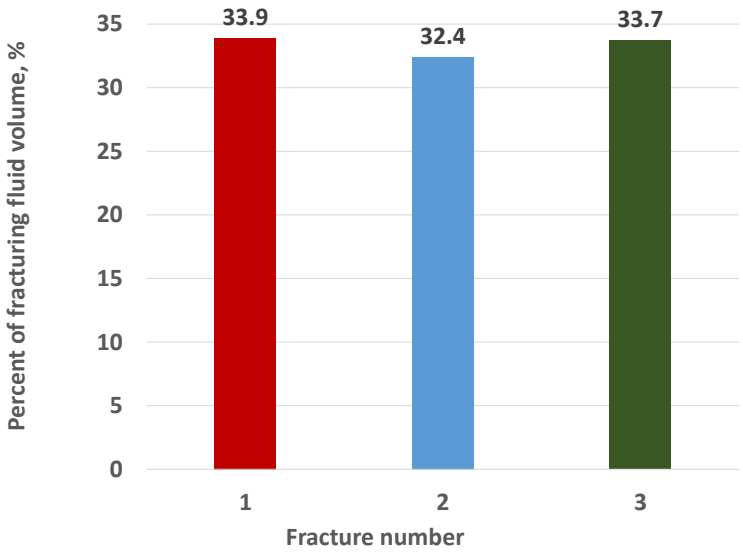

Figure 6.4: Percentage of the total fracturing fluid volume distributed into each fracture at the end of pumping under the optimal perforation conditions.

Then, we tried to achieve the set-point value of the average width for each fracture in simultaneously propagating multiple fractures by applying the proposed model-based feedback controller to the high-fidelity process model to achieve the uniform proppant bank height across the fractures, which will lead to uniform proppant bank with the equilibrium height, h_{eq}, over the optimal fracture half-length, $x_f = 120$ m. The average fracture width profiles of the three fractures are presented in Fig. 6.5, where they are very close to the set-point value. Fig. 6.6 shows the optimal

pumping schedules computed by the proposed model-based feedback controller. The corresponding proppant bank height over the optimal half-length, x_f, is uniform with the equilibrium value as shown in Fig. 6.7. At the end of pumping, some amount of proppant (2000 kg) still remains in suspension, which are assumed to quickly join the bank during the shut-in period.

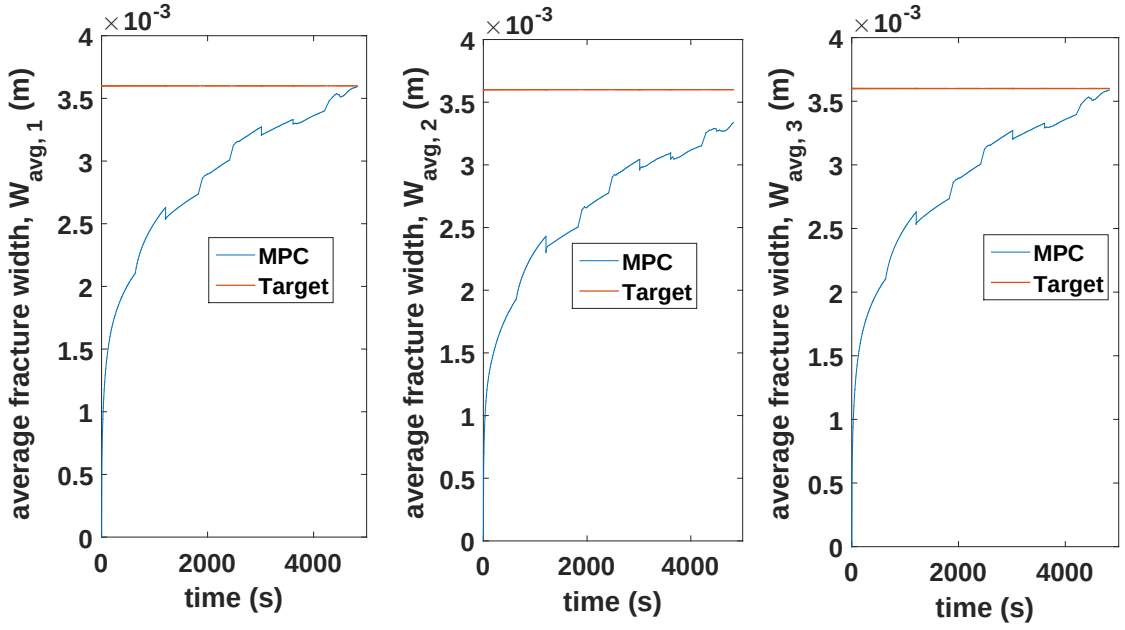

Figure 6.5: Average width profiles of simultaneously propagating multiple fractures during hydraulic fracturing under the proposed controller.

6.6 Conclusions

In this work, we developed a model-based feedback control system that computes an optimal pumping schedule to achieve the uniform proppant bank height over the optimal fracture length in simultaneously propagating multiple fractures at the end of pumping by handling the undesired stress-shadow effects. First, we developed a dynamic model of simultaneously propagating multiple fractures to describe the formation of a proppant bank including proppant settling and proppant resuspending by coupling fluid flow and rock mechanics. Second, a method called section-based optimization was employed to determine the optimal well-fracture configuration, maximizing the overall productivity achievable by a given amount of proppant to be injected. Third, using the data

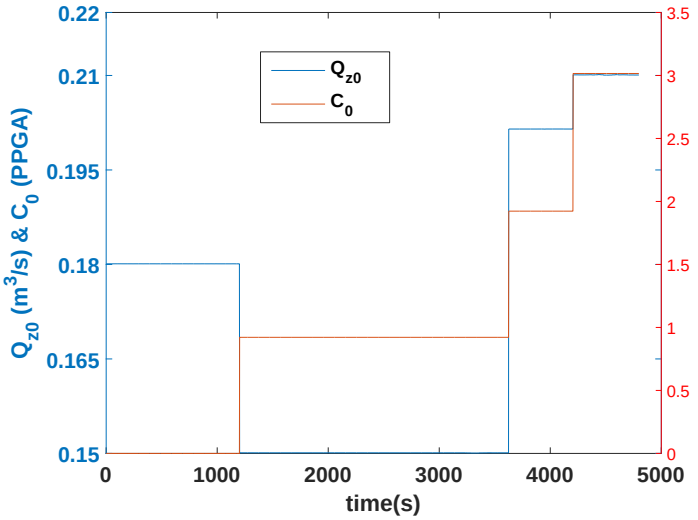

Figure 6.6: Optimal pumping schedules generated under the proposed controller.

generated from the high-fidelity process model of simultaneously propagating multiple fractures, a ROM was constructed, and a Kalman filter was designed to effectively estimate the average fracture width at each sampling time. We considered the optimal perforation conditions in the high-fidelity model which were available from Chapter 4 to mitigate the stress-shadow effects, and promote equal distribution of fracturing fluids to achieve uniform fracture growth. Lastly, the proposed MPC scheme was applied for the design of a real-time model-based feedback control system to compute online fracturing fluid pumping schedules. The proposed methodology was able to generate a uniform proppant bank height along the targeted fracture length while explicitly taking into account actuator limitations, state constraints for process safety, and economic considerations.

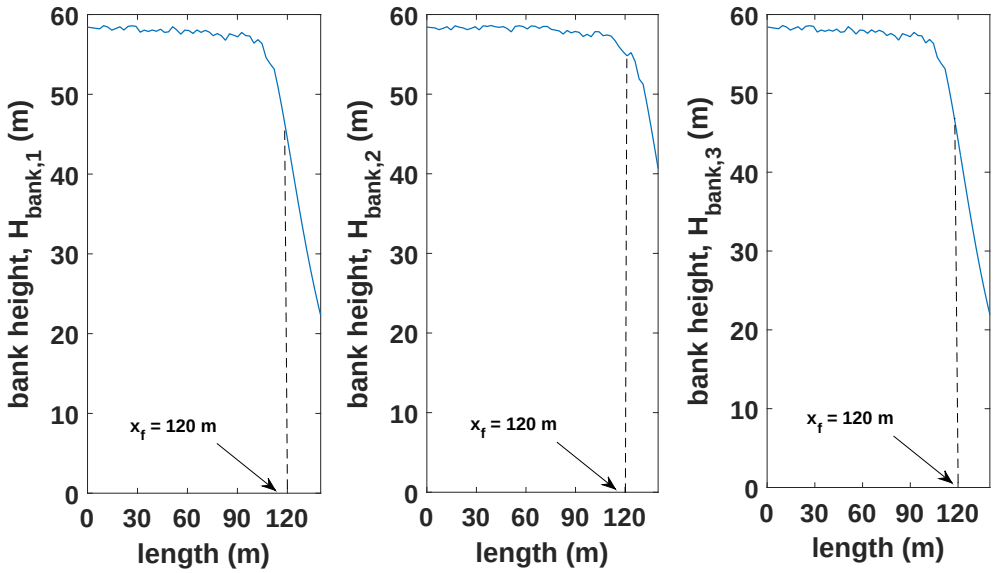

Figure 6.7: Spatial proppant bank height profiles of the simultaneously propagating three fractures obtained at the end of pumping.

7. SIMULTANEOUS MEASUREMENT UNCERTAINTY REDUCTION AND PROPPANT BANK HEIGHT CONTROL OF HYDRAULIC FRACTURING*

7.1 Introduction

In Chapter 4, we have developed a real-time feedback control systems for hydraulic fracturing to regulate proppant bank height for low-permeability reservoirs, where unmeasurable output variables (e.g., average fracture width) and states were estimated using Kalman filters for the purpose of controller design using available measurements. In hydraulic fracturing, among a variety of available measurement technologies, microseismic monitoring (MSM) is the most commonly used one to determine the geometry and location of created hydraulic fractures because it provides the most comprehensive picture of hydraulic fracture growth [53, 54, 55].

The principle of MSM is as follows: energy is released due to the cracks propagated in a shale rock formation. This microseismic energy will travel away from the cracks in the form of seismic waves through the surrounding rock formation as shown in Fig. 7.1 [145]. These seismic waves will temporarily deform the surrounding rock formation when they travel and can be classified into two types: primary (P-) waves, which are the fast propagating waves and secondary (S-) waves, which are the relatively slow propagating shear waves. These microseismic events are then picked up by arrays of accelerometers or three-component geophones which are placed at a nearby monitoring well. Then, the distance between the microseismic event location and the geophone is determined based on the difference in arrival times between primary and secondary waves and a previously calibrated seismic-wave velocity model. Using three or more geophones to detect the same microseismic event location will allow us to determine the location of created fractures in the three-dimensional (3D) space. In general, the measurement uncertainty associated with geophones is very high due to the remote nature of hydraulic fracturing taking place in an underground environment, placing multiple sensors and drilling monitoring wells are required,

*Reprinted with permission from "Simultaneous measurement uncertainty reduction and proppant bank height control of hydraulic fracturing" by Siddhamshetty et al., 2019. *Computers & Chemical Engineering*, 127, 272-281, Copyright 2019 by Elsevier.

which is often very expensive.

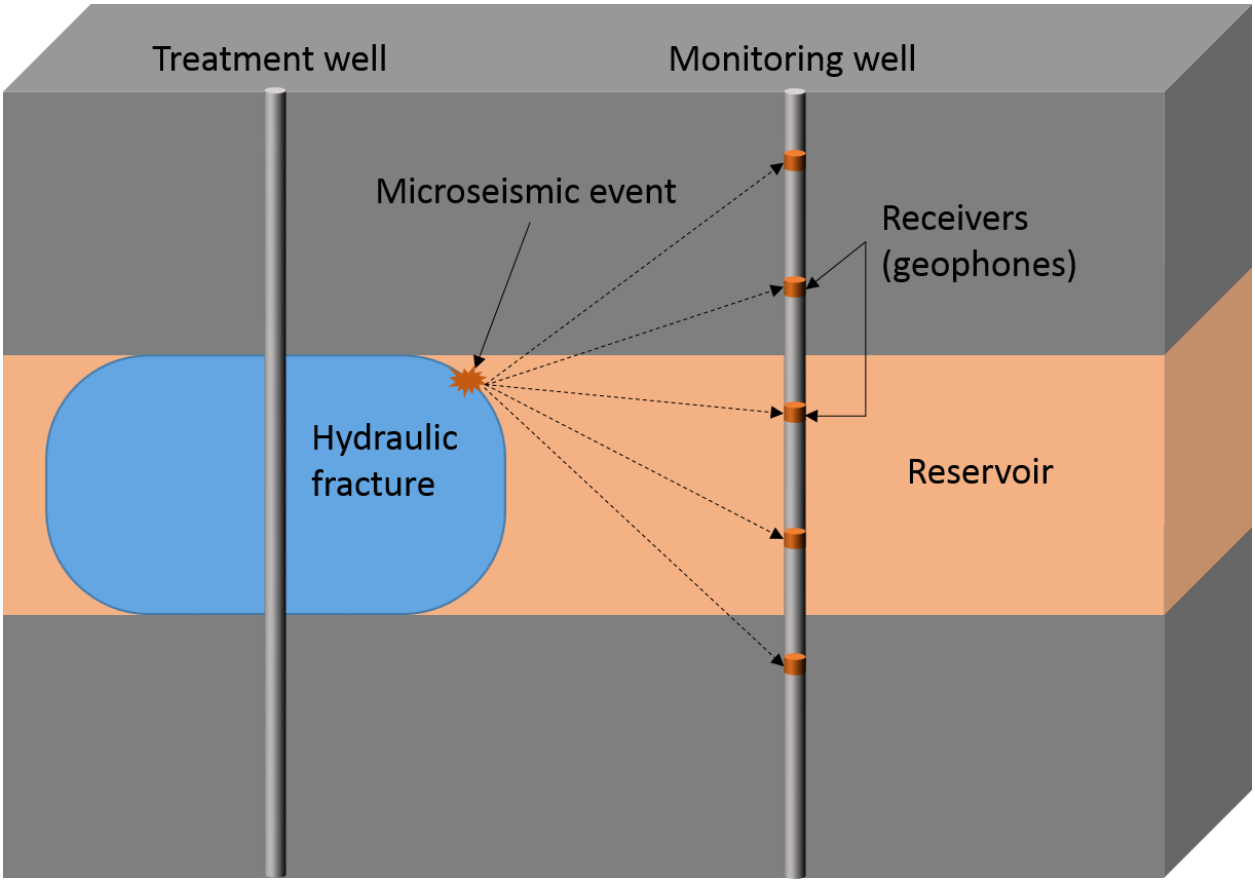

Figure 7.1: Schematic of how MSM works.

However, unlike other industrial applications, in hydraulic fracturing the occurrence of measurement depends on the fracturing fluid injection rate at the wellbore [53]. More microseismic events can take place due to increased stress triggered by higher fracturing fluid injection rates. Therefore, creating more microseismic events can reduce measurement errors using MSM. Based on this, Sun et al. [146] proposed an idea of reducing measurement uncertainty for state and output estimation by manipulating the fracturing fluid injection rate. However, they did not consider regulating the optimal fracture geometry, which can be done by manipulating the same variable. Motivated by this, we propose to develop a model-based feedback control system to reduce the

measurement uncertainty while at the same time accomplishing the original control task of achieving the desired fracture geometry at the end of hydraulic fracturing. In this regard, a controller is formulated to minimize the estimation error covariance (uncertainty reduction) as well as the deviation of fracture geometry from its target (set-point tracking) [147].

This paper is organized as follows: in Section 7.2, we explain the problem statement, and describe the Kalman filter and the relationship between the manipulated input and measurement error covariance. A dynamic model of hydraulic fracturing is described in Section 7.3. In Section 7.4, we present the section-based optimization method to obtain the optimal configuration of fractures and wells, and the optimal fracture geometry in unconventional oil and gas reservoirs. In Section 7.5, we present the development of a reduced-order model (ROM) using the simulation data generated from the dynamic model of hydraulic fracturing, which is then used to develop a Kalman filter for state and output estimation. Next, we introduce a novel real-time model-based feedback control system. The paper concludes with closed-loop simulation results to analyze the performance of the proposed control scheme for simultaneous measurement uncertainty reduction and set-point tracking.

7.2 Problem statement

In hydraulic fracturing, it is important to achieve a uniform proppant bank height across the optimal fracture length at the end of the process, which will maximize the oil and gas production rates from shale rock formations. In order to obtain the optimal fracture geometry, we propose to design a model-based feedback control system. In the controller, we can estimate unmeasurable states through state estimators such as Kalman filter by utilizing the measurement data available from MSM.

Consider the following state-space representation of a discrete time linear model:

$$x(t_{k+1}) = Ax(t_k) + Bu(t_k) + w(t_k) \tag{7.1a}$$

$$y(t_k) = Hx(t_k) + v(t_k) \tag{7.1b}$$

where the input, state, and output variables are represented using $u(t_k)$, $x(t_k)$, and $y(t_k)$, respectively. The random process noise, $w(t_k)$, and measurement noise, $v(t_k)$, are assumed to be derived from a Gaussian distribution with zero mean and covariances Q and R, respectively.

$$w(t_k) \sim N(0, Q) \tag{7.2a}$$

$$v(t_k) \sim N(0, R) \tag{7.2b}$$

A Kalman filter consists of two steps: prediction and measurement update steps. Combining these two steps, the formulations for a Kalman filter are presented as follows:

$$\hat{x}(t_{k+1}) = A\hat{x}(t_k) + Bu(t_k) + M(t_k)(y_m(t_k) - \hat{y}(t_k)) \tag{7.3a}$$

$$M(t_k) = P(t_k)H^T(R(t_k) + HP(t_k)H^T)^{-1} \tag{7.3b}$$

$$P(t_{k+1}) = (I - M(t_k)H)P(t_k) \tag{7.3c}$$

$$E(t_k) = HP(t_k)H^T + R \tag{7.3d}$$

where the notation $\hat{(\cdot)}$ denotes the estimated variables, $M(t_k)$ is the Kalman filter gain, $P(t_k)$ and $E(t_k)$ denote the covariances of the state and output estimation errors, respectively, and the available measurement from the system is denoted using $y_m(t_k)$.

In general, the process and measurement noise information within a Kalman filter is assumed to be known a priori. However, in some systems like hydraulic fracturing, the noise covariance matrices depend on the manipulated input as follows:

$$Q(t_k) = f_w(u(t_k)) \tag{7.4a}$$

$$R(t_k) = f_v(u(t_k)) \tag{7.4b}$$

where the nonlinear functions $f_w(\cdot)$ and $f_v(\cdot)$ capture the dependences of covariance matrices on the manipulated input.

In hydraulic fracturing, the occurrence of measurements (i.e., microseismic events) depends on the fracturing fluid injection rate at the wellbore which is an input to the process [53]. More microseismic events will be generated simultaneously due to increased stress and pore pressure triggered by higher fracturing fluid injection rates. The measurement error covariance of simultaneously generated microseismic events can be determined by $R(t_k) = R_{single}/N(t_k)$ where R_{single} is the error covariance of individual measurement and N is the total number of microseismic events per a unit time period. Since N depends on the fracturing fluid injection rate, the measurement error covariance depends on fracturing fluid injection rate at the wellbore which is also the input to the hydraulic fracturing process. Therefore, we have an extra degree of freedom to reduce the measurement uncertainty associated with MSM; otherwise, a high measurement error may lead to incorrect state and output estimation and thereby to a poor controller performance. Therefore, by utilizing this unique dependence of the MSM measurement error on the manipulated input, it is desirable to design a controller to achieve uncertainty reduction as well as set-point tracking.

7.3 Modeling of hydraulic fracturing

The hydraulic fracturing process model considers fracture propagation, proppant transport, and proppant bank formation. The fracture propagation model is presented in Section 2.1.1 which considers Perkins, Kern, and Nordgren model to describe the propagation of a fracture. Proppant transport and proppant bank formation models are presented in Section 4.2.2 and 4.2.3. Essentially, we can obtain the spatio-temporal profiles of fracture width, $W(x,t)$, length, $L(t)$, suspended proppant concentration, $C(x,t)$, and proppant bank height, $\delta(x,t)$ using these models.

7.4 Optimal configuration of fractures and wells in unconventional oil and gas reservoirs

We use the section-based optimization method presented in Section 4.4.1 to determine the optimal number of wells, n_c, number of fractures per each well, n_r, and half-length of fracture, x_f, as this configuration will maximize the productivity of unconventional shale formations for given amounts of fracturing resources [113] . In this work, we fixed the total amount of proppant available for injection as $M_{prop} = 2.38 \times 10^7$ kg, and the resultant optimal values obtained by the section-based optimization method were $n_c = 6$, $n_r = 55$, and $x_f = 120$ m.

In unconventional reservoirs, because of the use of slickwater which is a low-viscosity fracturing fluid, the proppant settles quickly forming a proppant bank, which will eventually reach an equilibrium height, h_{eq}. It is very important to achieve this equilibrium height over the required fracture half-length, x_f, which can be translated into achieving the following average fracture width at the end of the hydraulic fracturing process:

$$W_{avg,target} = \frac{M_{prop,frac}}{2\rho_p h_{eq} x_f (1-\phi)} \tag{7.5}$$

where the total amount of proppant injected to create one fracture is $M_{prop,frac} = 72000$ kg, the proppant particle density is $\rho_p = 2650$ kg/m^3, the porosity of proppant bank is $\phi = 0.61$, the equilibrium height is $h_{eq} = 54$ m for the considered fracturing fluid flow conditions, and the calculated average fracture width at the end of the hydraulic fracturing process is $W_{avg,target} = 5.37$ mm. It is very important to achieve this target average fracture width (set-point for controller design) as it will lead to the optimal fracture geometry for the maximum oil and gas production. However, the measurement of average fracture width is not directly available. Thus, we have to utilize the available measurement of fracture length to estimate the average fracture width using a Kalman filter. In the following section, we will develop a model-based feedback controller to obtain the desired average fracture width at the end of the hydraulic fracturing process and simultaneously reduce the estimation error of average fracture width.

7.5 Model-based control systems for simultaneous uncertainty reduction and set-point tracking in hydraulic fracturing

In this section, we first construct a ROM of hydraulic fracturing process using the simulation data from the high-fidelity model described in Section 7.3. MSM is the only reliable measurement technique available during the hydraulic fracturing process, through which we can obtain the real-time measurement of fracture length [53]. Utilizing this available measurement of fracture length and the ROM, we will develop a Kalman filter to predict the average fracture width. As mentioned earlier, the estimation error depends on the measurement noise which is a function of the fracturing fluid injection rate. Based on this, we develop a model predictive controller (MPC) to compute the optimal pumping schedule that will allow us to achieve the desired average fracture width at the end of the hydraulic fracturing process and simultaneously reduce the estimation error associated with the average fracture width.

7.5.1 Development of ROM

Due to the infinite-dimensional nature of the high-fidelity model, multi-variable output error state-space (MOESP) algorithm is used to obtain a discrete time state-space model describing fracture propagation and proppant transport phenomena in hydraulic fracturing, which is represented in the following form:

$$x(t_{k+1}) = Ax(t_k) + Bu(t_k) \tag{7.6a}$$

$$y(t_k) = Hx(t_k) \tag{7.6b}$$

where the manipulated input variables, $u(t_k) = [Q_{x0}(t_k), C_0(t_k)]^{\mathrm{T}}$, are the injected fracturing fluid flow rate and proppant concentration into the fracture at the wellbore, the output variables, $y(t_k) = [W_{avg}(t_k), L(t_k)]^{\mathrm{T}}$, are the average fracture width and length, and $x(t_k)$ represents the system states. In this work we used a 3^{rd} order state-space model, and the obtained A, B, and H matrices using MOESP algorithm are given in Eq. (7.7). We have used the open-loop simulation

data generated from the high-fidelity process model to obtain a linear time-invariant state-space model of the hydraulic fracturing process. The training input was designed by taking into account the ranges of allowed input profile (i.e., the minimum and maximum allowable flow rate and proppant concentration). Fig. 7.2 shows the comparison between the estimated and the actual average fracture width and fracture length with time. It is observed that the estimated average fracture width and fracture length quickly converge to the true values obtained from the high-fidelity process model.

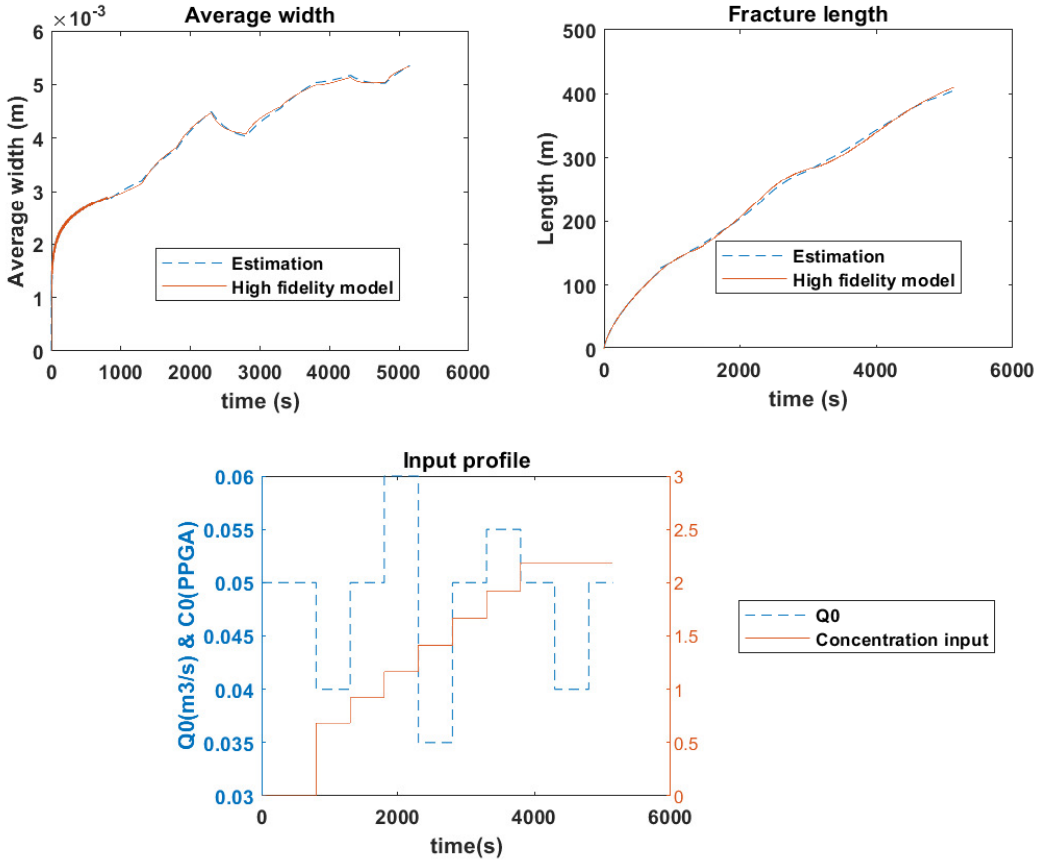

Figure 7.2: Comparison between the true values and the estimates of average fracture width and fracture length.

$$A = \begin{bmatrix} 0.9996 & 1.2434e-04 & -2.3447e-04 \\ 2.010e-04 & 0.9998 & 1.8187e-04 \\ -6.0175e-04 & 2.8465e-04 & 0.9996 \end{bmatrix} \tag{7.7a}$$

$$B = \begin{bmatrix} 8.4973e-04 & -2.0869e-05 \\ -7.2948e-04 & 3.1820e-05 \\ 0.0011 & 3.6069e-05 \end{bmatrix} \tag{7.7b}$$

$$H = \begin{bmatrix} 344.8 & -89.7 & 1.1 \\ 1288.5 & -549.1 & -1759.7 \end{bmatrix} \tag{7.7c}$$

Remark 12. *We can also use closed-loop identification methods to obtain a reduced order model as described in [148], and [149].*

Remark 13. *In practice, the only reliable measurement during the hydraulic fracturing process is the fracture length. Using this measurement (i.e., $y_m(t_k) = [L(t_k)]$), the average fracture width is estimated through a Kalman filter as described in Section 7.2.*

7.5.2 Uncertainty reduction

In hydraulic fracturing due to the use of MSM technology, the occurrence of measurement depends on the fracturing fluid injection rate at the wellbore. Higher flow rates are likely to trigger more simultaneous microseismic events because of increased stress and pore pressure resulting from higher fracturing fluid injection rates. The total number of microseismic events per a unit time period, N, is given below:

$$N(t_k) = f_N(Q_{x0}(t_k)) \tag{7.8}$$

In this work, we assume that two consecutive microseismic events may occur at the same location and time with a same measurement uncertainty [146]. The measurement error covariance

of simultaneously generated microseismic events can be determined by:

$$R(t_k) = R_{single}/N(t_k) \tag{7.9}$$

where R_{single} is the error covariance of individual measurement. In practice, R_{single} is the error band of single microseismic event uncertainty. By combining Eqs. (7.8) and (7.9), the relationship between the fracturing fluid flow rate, $Q_{x0}(t_k)$, and measurement error covariance, $R(t_k)$, is given below:

$$f_v(Q_{x0}(t_k)) = R_{single}/f_N(Q_{x0}(t_k)) \tag{7.10}$$

Because the covariance of a vector sequence is a matrix, we use the trace (the sum of eigenvalues) of a covariance matrix to evaluate the degree of measurement uncertainty.

7.5.3 MPC formulations

As indicated by Eqs. (7.8)-(7.10), by manipulating the fracturing fluid injection rate, the measurement covariance error and thereby output estimation error can be adjusted as shown in Section 7.2. Within this regard, a novel MPC is developed to minimize the squared deviation of the average fracture width at the end of the hydraulic fracturing process from its set-point, and the trace value of the covariance of output estimation error from its desired value, which is given below:

$$\min_{\substack{C_{stage,k},\ldots,C_{stage,9}\\ Q_{stage,k},\ldots,Q_{stage,9}}} \quad (\hat{W}_{avg}(t_f) - W_{avg,target})^2 + Q_c \sum_{i=k}^{9} (tr(E(t_k)) - E_{sp})^2 \tag{7.11a}$$

$$\text{s.t.} \quad \hat{L}(t_k) = L(t_k) \tag{7.11b}$$

$$\text{Kalman filter, Eq. (7.3)} \tag{7.11c}$$

$$C_{stage,k-1+m} \leq C_{stage,k+m} \leq 2 \text{ PPGA} \tag{7.11d}$$

$$Q_{min} \leq Q_{stage,k+m} \leq Q_{max} \tag{7.11e}$$

$$R_{single}(t_k) = 10000 + 5000sin(2/(20\pi t_k)) \tag{7.11f}$$

$$f_N(Q_{x0}(t_k)) = N_0 + 10(Q_{stage,k} - q_0)/q_0 \tag{7.11g}$$

$$R(t_k) = f_v(Q_{x0}(t_k)) = R_{single}(t_k)/f_N(Q_{x0}(t_k)) \tag{7.11h}$$

$$m = 1, \ldots, 9 - k \tag{7.11i}$$

$$\Delta \left(\sum_{k=1}^{9} 2Q_{stage,k}C_{stage,k} \right) = M_{prop,frac} \tag{7.11j}$$

where Q_c is the weighted norm, the target average fracture width at the end of the hydraulic fracturing process is denoted using $W_{avg,target}$, the average fracture width estimated by the Kalman filter of Eq. (7.11c) is given by $\hat{W}_{avg}(t_k)$, $tr(E(t_k))$ is the trace of the output estimation error covariance matrix, E_{sp} is the desired trace value, $N_0 = 10$ is the number of nominal microseismic events at the fracturing fluid injection rate of $q_0 = 0.035 \text{ m}^3/\text{s}$, the total process operation time is given by t_f, the period of each sampling time is Δ, the current time is denoted by t_k, the measurements available using MSM is the fracture length, $L(t_k)$, and $C_{stage,k}$ and $Q_{stage,k}$ are the manipulated input variables at the k^{th} pumping stage. The schematic diagram of the proposed MPC is presented in Fig. 7.3.

In the optimization problem, the only available measurement is the fracture length (Eq. (7.11b)) and this measurement is used within the Kalman filter to estimate the average fracture width (Eq. (7.11c)), and the constraints on proppant concentration and fracturing fluid flow rate are considered (Eqs. (7.11d)-(7.11e)). The total amount of proppant injected is constrained using

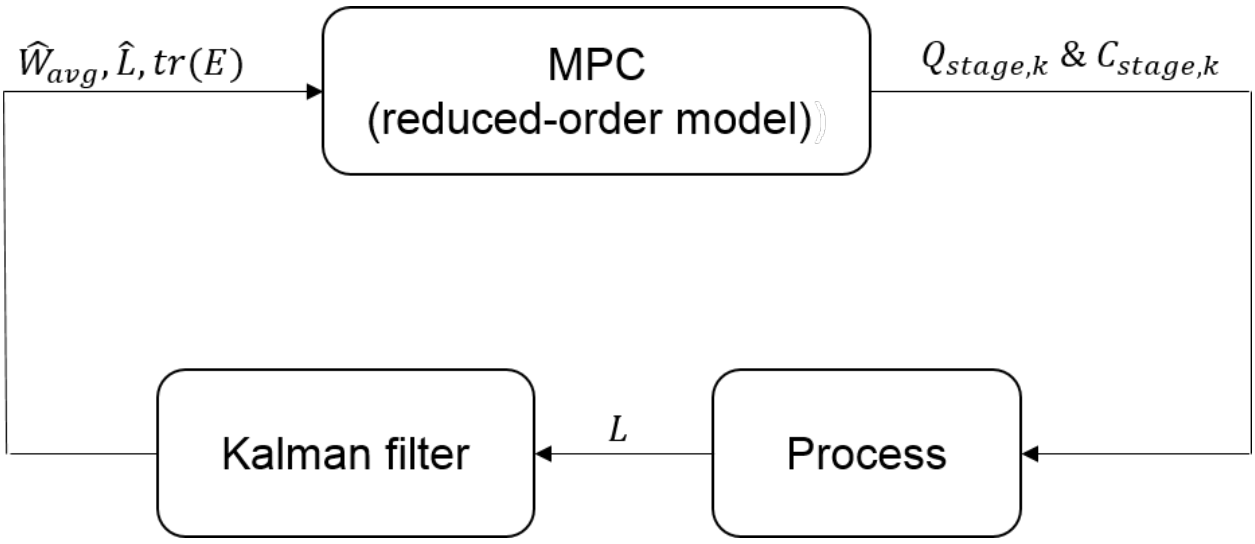

Figure 7.3: Schematic of the proposed closed-loop operation.

Eq. (7.11j). The trace of the output estimation error covariance, $tr(E(t_k))$, is given by the Kalman filter using Eq. (7.3).

Remark 14. *The proposed method can be easily extended to account for system nonlinearities by adopting extended Kalman filter techniques, which uses linearized models. By using the input dependent measurement error covariance relationship and extended Kalman filter, we can use the proposed MPC framework for measurement uncertainty reduction while achieving the original control task for nonlinear systems.*

Remark 15. *There is no desired threshold value on output estimation error covariance and further reducing the error covariance is always beneficial to achieve a better control performance.*

7.6 Closed-loop simulation results under the proposed MPC

In this section, the closed-loop simulation results are presented to demonstrate the performance of the proposed MPC. The high-fidelity model presented in Section 7.3 was utilized to simulate a hydraulic fracturing process, and the input/output data generated from this model was used to develop a ROM of the process. This ROM was then used to design a Kalman filter for state and output estimation, and subsequently a MPC was designed. In Table 4.2, the parameter values

considered in the high-fidelity process model are provided. The desired average fracture width was $W_{avg,target} = 5.37\ \mathrm{mm}$. The pad time of $t_p = 800\ \mathrm{s}$ was used. The proposed MPC and the Kalman filter were initialized at $t = t_p$. In the proposed MPC, Δ and t_f values were chosen to be $500\ \mathrm{s}$ and $5300\ \mathrm{s}$, respectively, implying that the fracturing fluid pumping schedule consists of 9 stages with the duration of $500\ \mathrm{s}$ for each pumping stage. We assumed that the measurement of fracture length, $L(t_k)$, was available at the beginning of each pumping stage (Eq. (7.11b)). This real-time measurement was then used to predict the unmeasurable state, average fracture width $\hat{W}_{avg}$, via the Kalman filter; then, the output error covariance was predicted. The MPC computed the control input to reduce the measurement uncertainty and simultaneously drive the average fracture width to a desired value at the end of the hydraulic fracturing process.

In this study we examined two cases, where in the first case we considered a fixed fracturing fluid pumping schedule with a constant flow rate and pre-defined proppant concentration profile, and in the second case, the flow rate and proppant concentration were manipulated using the proposed MPC. With the pumping schedule used in the first case (Fig. 7.4), a discrepancy between the predicted and actual average fracture widths was observed (Fig. 7.5). The trace of output error covariance, $tr(E)$, is presented in Fig. 7.6. As shown in Fig. 7.7, we were not able to achieve the required average fracture width using the fixed fracturing fluid pumping schedule.

In Fig. 7.8, on the other hand, the average fracture width estimated by the proposed MPC is close to the true value. The pumping schedule obtained by the proposed MPC is shown in Fig. 7.9. In Fig. 7.10, it is observed that the proposed MPC can effectively reduce the trace of output error covariance, $tr(E)$. In unconventional reservoirs, because of the use of slickwater which is a low-viscosity fracturing fluid, the proppant settles quickly forming a proppant bank, which will eventually reach an equilibrium height, h_{eq}. With the amounts of resources (e.g., water, proppant and so on) considered in this work, it is very important to achieve this equilibrium height over the required fracture half-length, $x_f = 120$ m, and the desired average fracture width, $W_{avg,target} = 5.37$ mm, at the end of hydraulic fracturing process. Using a fixed fracturing fluid pumping schedule, we were not able to achieve the required average fracture width as shown in

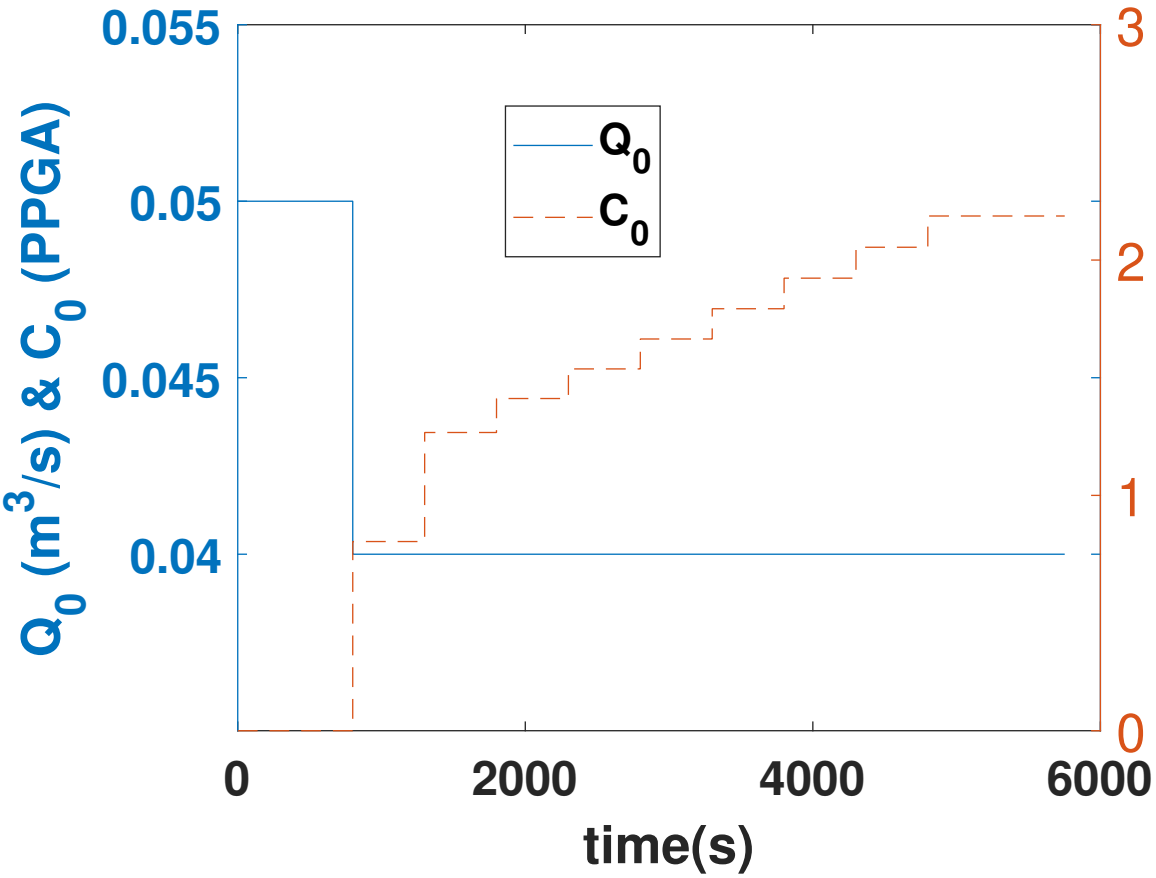

Figure 7.4: The fixed pumping schedule used in the first case.

Fig. 7.7, and the proppant bank height is uniform only for the first 87 m of fracture length as shown in Fig. 7.11 which is less than the optimal fracture length, and thus, it affects the overall production rate. However, using the proposed MPC, we were able to achieve the desired average fracture width at the end of the process as shown in Fig. 7.12, and the resultant proppant bank height is uniform across the optimal fracture length, $x_f = 120$ m, as shown in Fig. 7.13; we have marked the point in Fig. 7.13 to represent the fracture length covered with the uniform proppant bank height. The fluctuations in Fig. 7.12 under the proposed MPC is due to the variation in the injected fracturing fluid flow rate as shown in Fig. 7.9. The growth of average fracture width depends on the interplay between the injected fracturing fluid flow rate and the fracturing fluid leak-off rate into the surrounding porous rock formation. When the fracturing fluid flow rate is dominant

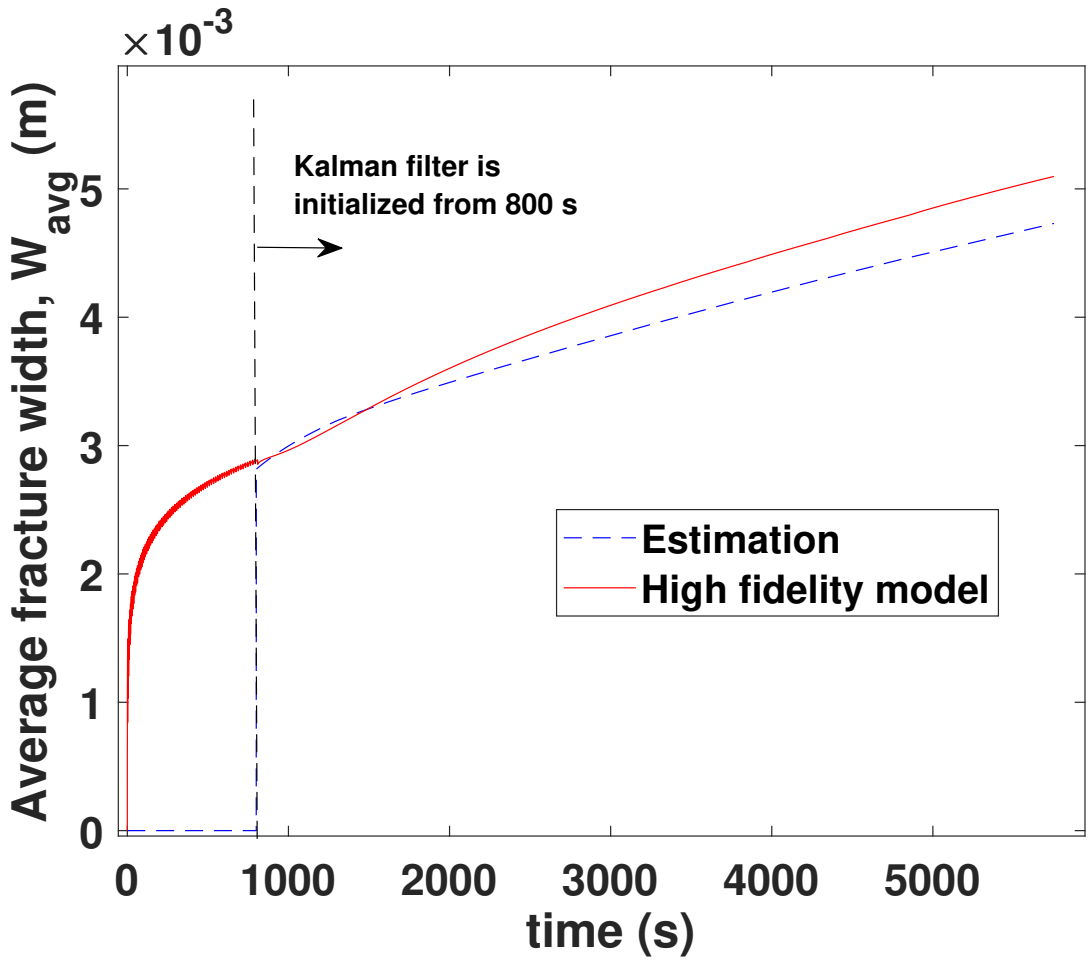

Figure 7.5: Average fracture width profile under the fixed pumping schedule.

it will lead to an increase in the average fracture width; otherwise, it will lead to a decrease in the average fracture width if the fracturing fluid flow rate is less dominant. To demonstrate the proposed MPC's performance, we further extended the total simulation time from 5300 s to 6300 s. Since the output already reached the set-point value, the proposed MPC system tried to maintain the flow rate at its lower bound to decrease the variation in the average fracture width from its set-point value. Because of the constant flow rate in the last three stages (from 4800 s to 6300 s) as shown in Fig. 7.14, we did not observe any fluctuations in the average fracture width (Fig. 7.15), which is similar to the case with fixed pumping schedule (Fig. 7.16).

We studied the effect of a plant-model mismatch in the Young's modulus, E, by performing the

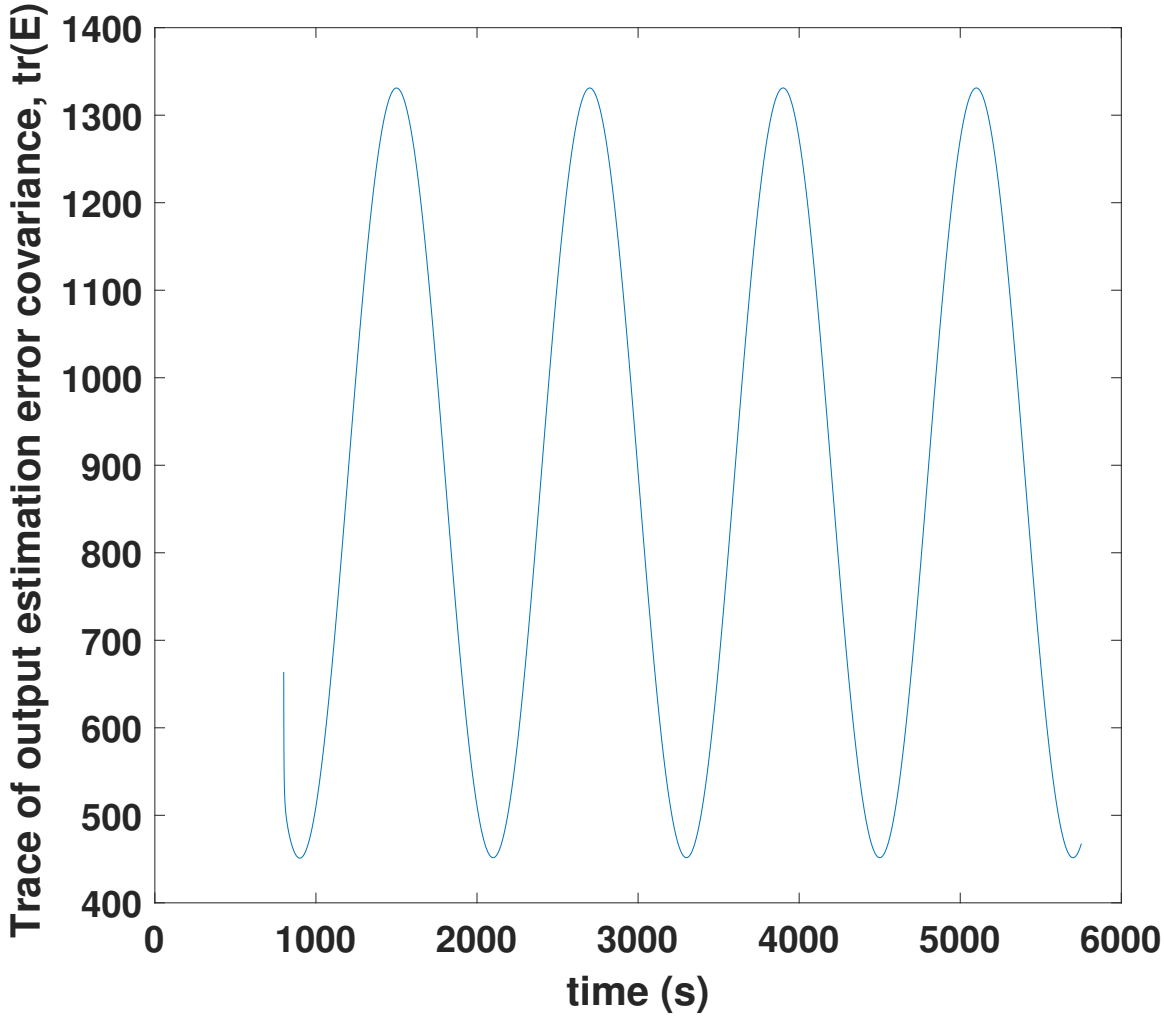

Figure 7.6: Trace of output error covariance under the fixed pumping schedule.

closed-loop simulations by varying the Young's modulus +/-10% from its nominal value. Using the proposed MPC, the average fracture width at the end of the process is close to the desired value as shown in Fig. 7.17 even when there is a mismatch in E. The performance of the closed-loop system can be further improved when there is a plant-model mismatch by considering offset-free approaches [150].

Comparing the above simulation results for the two cases, it is evident that using the proposed MPC, the output estimation error associated with the average fracture width can be greatly reduced by taking advantage of the relationship between the fracturing fluid injection rate and the

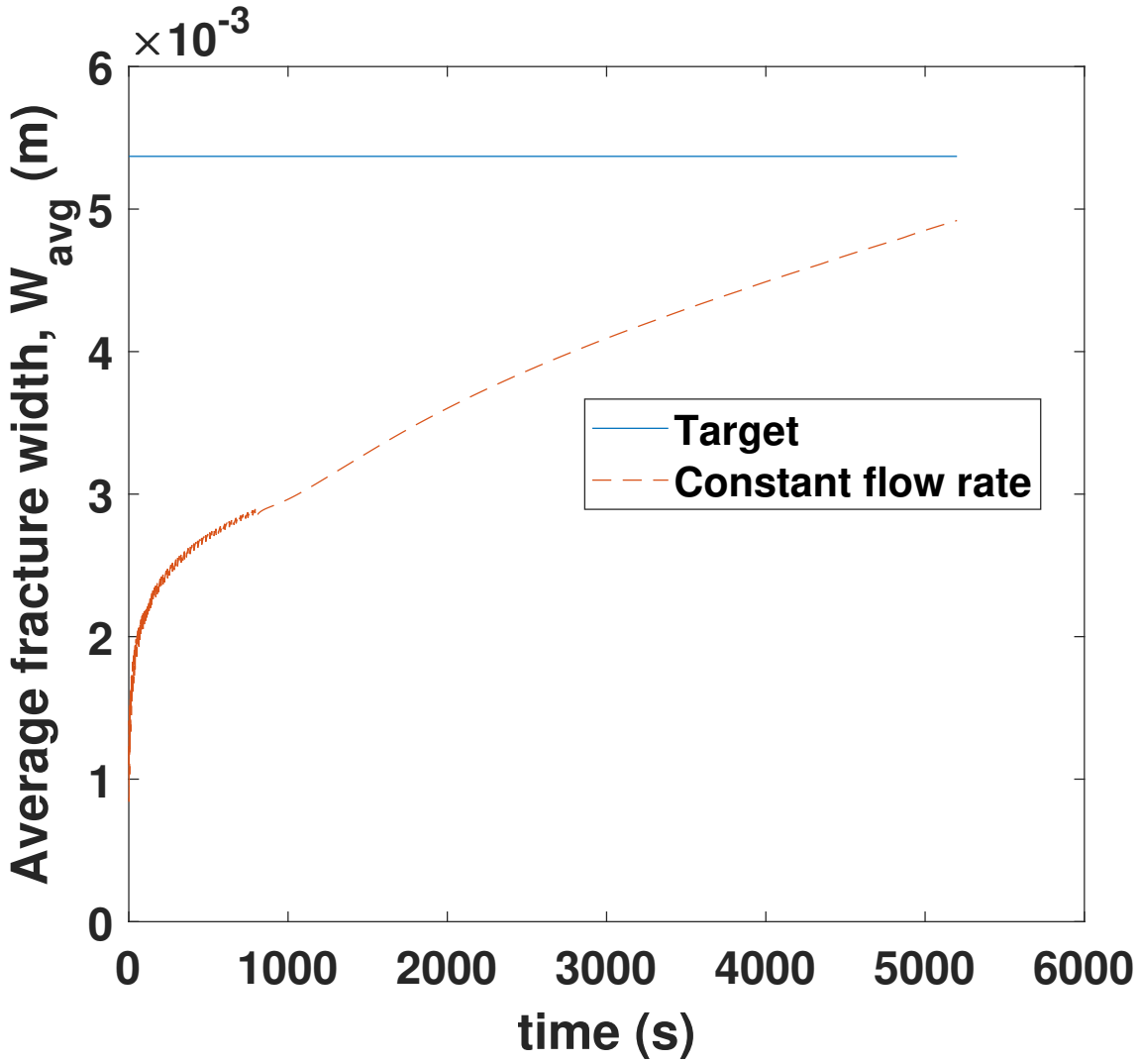

Figure 7.7: Average fracture width profile under the fixed pumping schedule compared to its target.

frequency of microseismic events; as a result of the accurate estimation of the average fracture width, the desired fracture geometry was also achieved by the proposed MPC. Considering the inaccurate nature of the microseismic sensors, it is very important to accurately estimate states and unmeasurable output variables during the hydraulic fracturing process.

7.7 Conclusions

In this work, we designed a novel MPC framework to simultaneously reduce the measurement uncertainty in hydraulic fracturing and to achieve the desired average fracture width at the end of

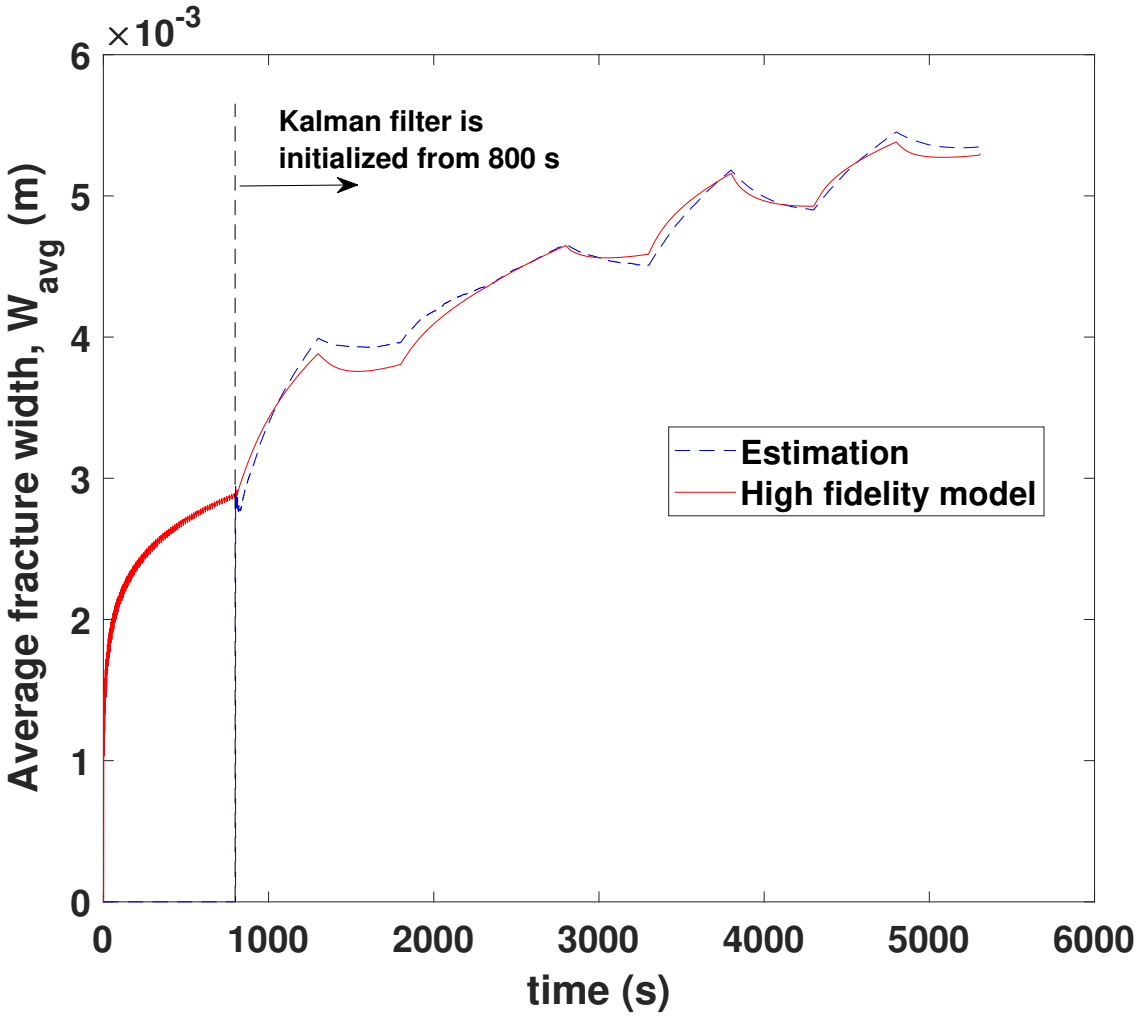

Figure 7.8: Average fracture width profile under the proposed MPC.

the process. The proposed MPC was designed by taking advantage of the relationship between the fracturing fluid injection rate and measurement noise covariance in MSM technique; the most widely used measurement technique for a comprehensive understanding of fracture geometry. To this end, we initially constructed a ROM using the simulation data generated from the high-fidelity process model, which was then used to develop a Kalman filter for state and output estimation. Utilizing the ROM and Kalman filter, we developed a real-time MPC system to compute the pumping schedule that reduces the measurement uncertainty while at the same time accomplishing the orig-

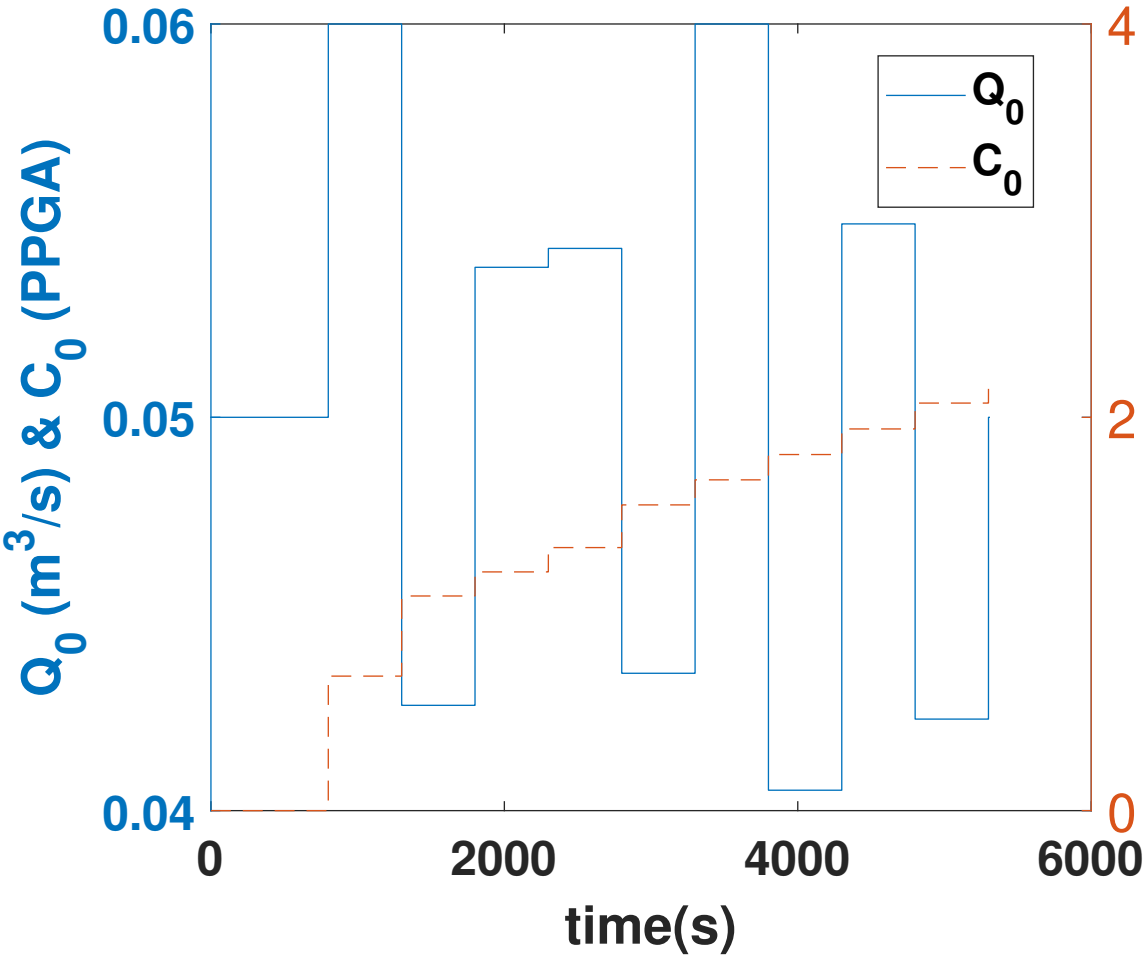

Figure 7.9: Pumping schedule computed by the proposed MPC.

inal task of achieving the desired average fracture width, which will lead to the optimal fracture geometry at the end of the process in unconventional oil and gas reservoirs.

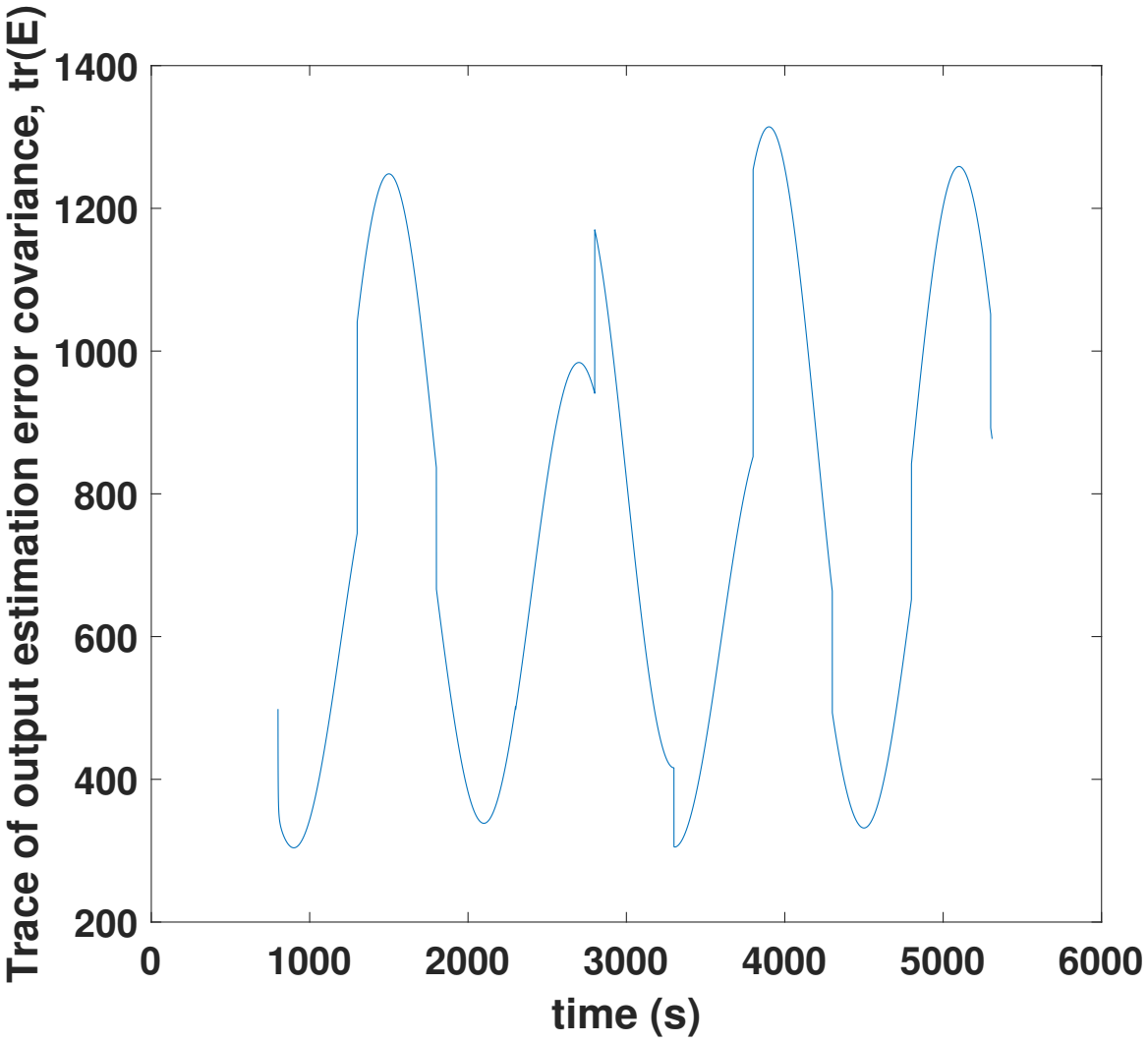

Figure 7.10: Trace of output error covariance under the proposed MPC.

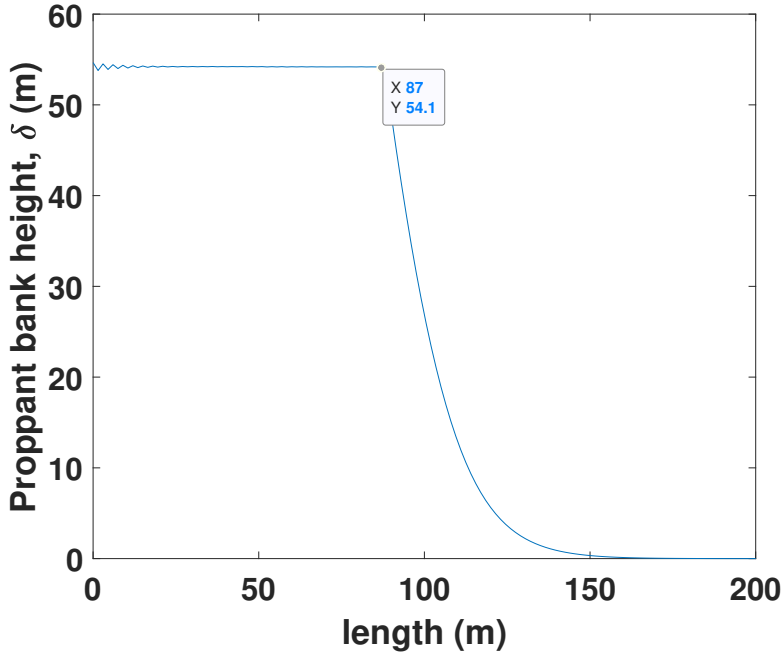

Figure 7.11: Proppant bank height at the end of the hydraulic fracturing process under the fixed pumping schedule.

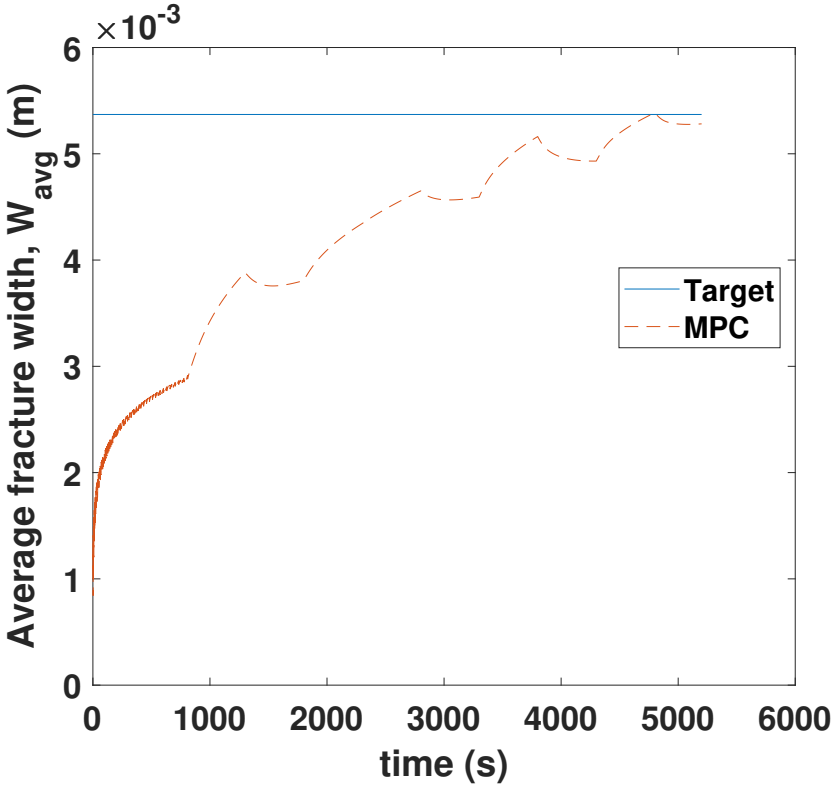

Figure 7.12: Average fracture width profile under the proposed MPC compared to its target.

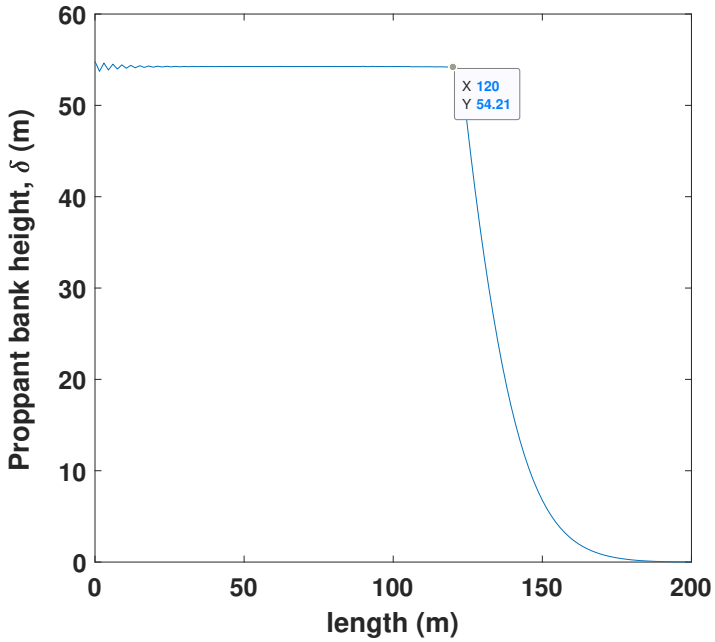

Figure 7.13: Proppant bank height at the end of the hydraulic fracturing process under the proposed MPC.

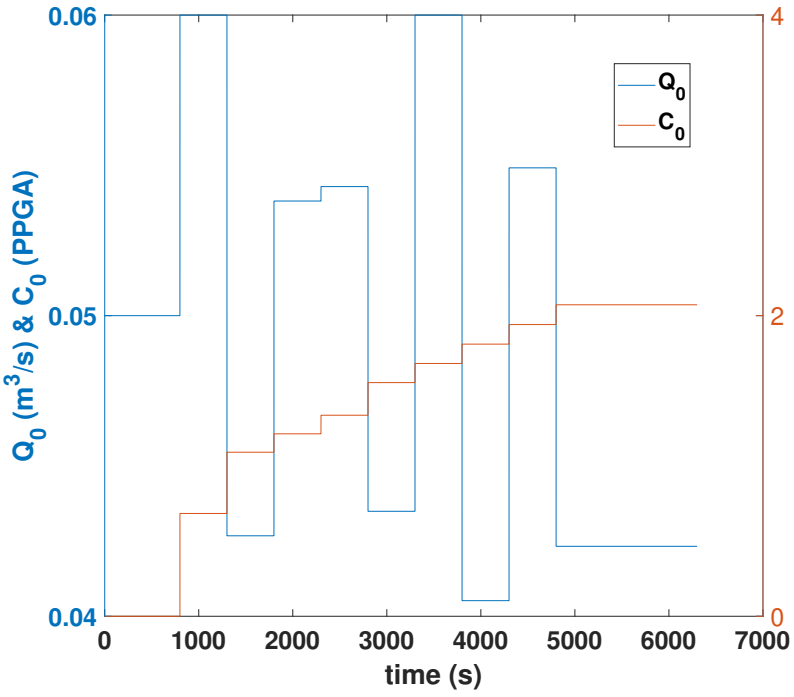

Figure 7.14: Pumping schedule computed by the proposed MPC after extending simulation time.

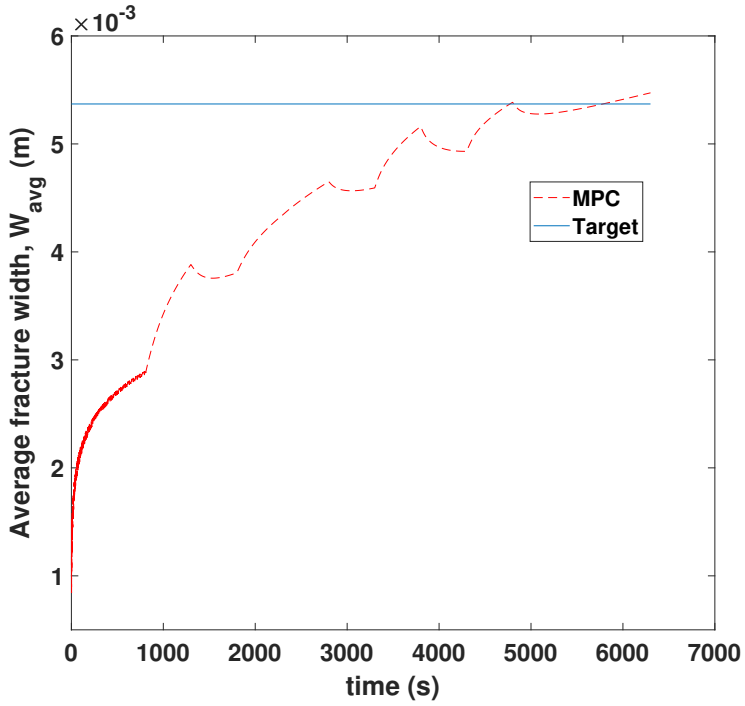

Figure 7.15: Average fracture width profile under the proposed MPC after extending simulation time.

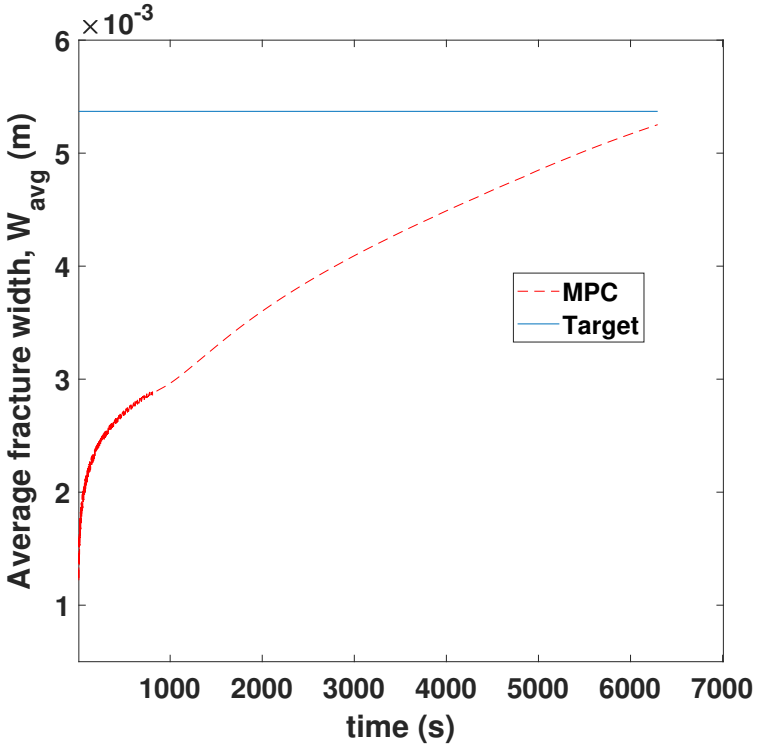

Figure 7.16: Average fracture width profile under the fixed pumping schedule after extending simulation time.

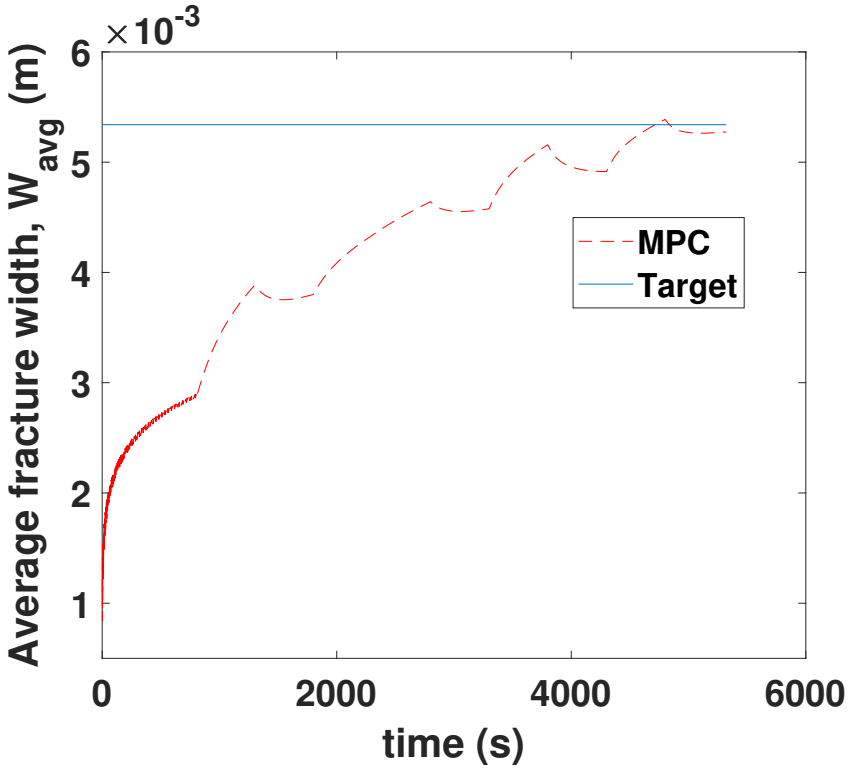

Figure 7.17: Average fracture width profile under the proposed MPC when there is a plant-model mismatch in the Young's modulus with 110% of its nominal value.

8. ENHANCING TOTAL FRACTURE SURFACE AREA IN NATURALLY FRACTURED UNCONVENTIONAL RESERVOIRS VIA MODEL PREDICTIVE CONTROL*

8.1 Introduction

In hydraulic fracturing, achieving an optimal fracture geometry is important as it will maximize the oil production rate from unconventional reservoirs [142]. In Chapter 3, 4 and 6, we computed the fracturing fluid pumping schedule by developing real-time model-based feedback control strategies and to achieve an optimal fracture geometry for conventional and unconventional reservoirs. However, we did not consider natural fractures, which may result in a complex fracture geometry [151]. Because of this complex fracture growth behavior, the ultimate goal of hydraulic fracturing in naturally fractured unconventional reservoirs should be changed from achieving a desired fracture geometry to maximizing the total fracture surface area (TFSA) for given fracturing resources such as water, proppant, viscosifying agent, etc. This will increase the drainage area, thereby enhancing the overall oil production rate in naturally fractured unconventional reservoirs [152]. Therefore, the previous pumping schedules cannot be directly applied to naturally fractured unconventional reservoirs. Motivated by this, in this chapter, we develop a model-based pumping schedule to maximize the TFSA by utilizing Mangrove to describe complex fracture growth in naturally fractured unconventional reservoirs.

Natural fractures (discontinuities in shale rock formations) are commonly observed in most of the unconventional reservoirs using advanced fracture diagnostic techniques such as microseismic monitoring, core samples and outcrops [56, 57, 153, 154]. These natural fractures will interact with hydraulic fractures, divert fracture propagation and result in a complex fracture geometry [58, 59]. The resulting complex fracture geometry in naturally fractured unconventional reservoirs plays a major role in recovering oil, subsequently determining the performance of the well. Therefore, it is very important to consider the interaction between hydraulic fractures and natural fractures to

*Reprinted with permission from "Enhancing total fracture surface area in naturally fractured unconventional reservoirs via model predictive control" by Siddhamshetty et al., 2020. *Journal of Petroleum Science and Engineering*, 184, 106525, Copyright 2020 by Elsevier.

optimize hydraulic fracturing treatments in naturally fractured unconventional reservoirs.

The three possible scenarios when a propagating hydraulic fracture interacts with a natural fracture are shown in Fig. 8.1 [58]. First, the hydraulic fracture will continue to propagate like a planar fracture in the same direction by crossing the natural fracture (Fig. 8.1a). Second, the hydraulic fracture will divert into the natural fracture and will re-initiate its propagation at the natural fracture's tip (Fig. 8.1b). Third, the diverted hydraulic fracture will re-initiate at some weak point along the natural fracture (Fig. 8.1c).

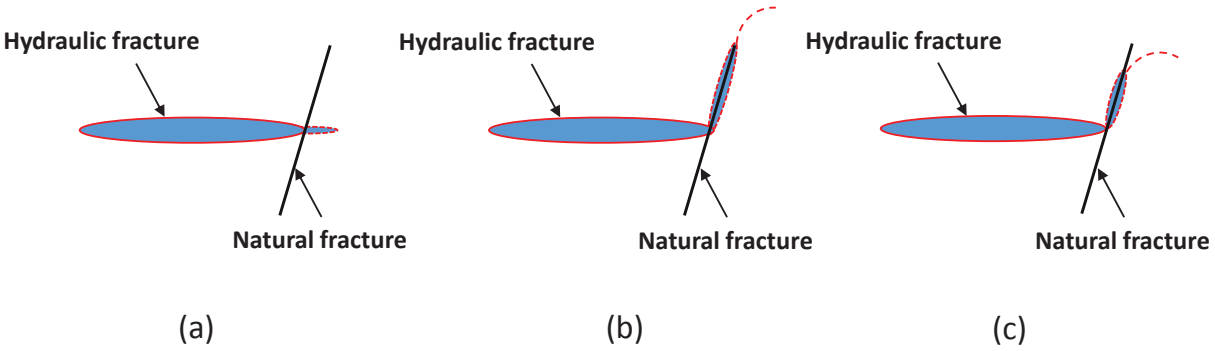

Figure 8.1: Possible scenarios when a hydraulic fracture interacts with a natural fracture.

The interaction between hydraulic fractures and natural fractures has been studied experimentally and numerically by many researchers [155, 156, 157, 158, 159]. To analyze complex fracture networks, the wire-mesh model [160, 161] and the discrete-fracture-network model [52] are generally used, in which a complex fracture geometry is approximated by the orthogonal grid pattern of hydraulic fractures. However, these approaches ignore the mechanisms of how natural and hydraulic fractures interact. Olson and Taleghani [162] developed a model to describe multiple, nonplanar, pseudo-3-dimensional (P3D) fracture propagation in naturally fractured unconventional reservoirs, but the model did not consider pressure drops in fractures due to fluid flow. Budyn et al. [163] and Keshavarzi et al. [164] modeled the hydraulic fracture propagation using an extended-

finite-element-method (XFEM) model to analyze the natural and hydraulic fracture interaction. However, both of these XFEM models are two-dimensional (2D) and do not consider the three-dimensional (3D) effects such as the evolution of fracture height. Recently, Wu and Olson [165] developed a complex hydraulic fracturing model by employing the 3D displacement discontinuity method, which was computationally efficient. In this model, the hydraulic fracture propagation direction during its interaction with natural fractures was determined using a crossing criterion by modifying the extended Renshaw and Pollard criterian [157, 166]. However, this model did not consider the proppant transport in naturally fractured unconventional reservoirs. Recently, Weng et al. [167] developed an unconventional fracture model (UFM) by considering height growth, fracture deformation, fluid flow and proppant transport in naturally fractured unconventional reservoirs to simulate complex fracture network. Based on the UFM, Schlumberger developed a hydraulic fracture simulator called Mangrove which is an engineered stimulation package available in Schlumberger Petrel platform. In this work, we have used Mangrove to simulate the complex fracture growth in naturally fractured unconventional reservoirs.

This chapter is organized as follows: High-fidelity model formulation using Mangrove is described in Section 8.2. In Section 8.3, we present a sensitivity analysis to show the importance of maximizing the TFSA in naturally fractured unconventional reservoirs. In Section 8.4, we present existing pumping schedule design techniques and their drawbacks. In Section 8.5, we construct a reduced-order model (ROM) that describes the relationship between the manipulated input variables (i.e., flow rate of fracturing fluid and proppant concentration at the wellbore) and output variable (i.e., TFSA) using the data generated from Mangrove. Next, we design a Kalman filter utilizing the available measurement to estimate unmeasurable ROM states. In Section 8.6, we present a model-based feedback control framework to compute the fracturing fluid pumping schedule that maximizes TFSA with given resources. In Section 8.7, we present the closed-loop simulation results to demonstrate that the obtained TFSA can lead to an enhanced oil production rate from naturally fractured unconventional reservoirs.

8.2 High-fidelity model formulation using Mangrove

In this section, we will discuss the UFM developed by Weng et al. [167], which considers the complex fracture growth in naturally fractured unconventional reservoirs.

8.2.1 Overview of the UFM

The UFM introduced by Weng et al. [167] has assumptions and equations very similar to that of P3D model, but solves a problem where fluid flow and rock deformation are coupled in a complex fracture network where natural fractures have to be considered. A key advantage of the UFM is that it is able to simulate the interaction of hydraulic fractures with pre-existing natural fractures. In particular, it determines whether (a) a hydraulic fracture propagates like a planar fracture in the same direction by crossing a natural fracture, (b) a hydraulic fracture is arrested when it interacts with a natural fracture, or (c) a hydraulic fracture diverts into a natural fracture and subsequently propagates along a natural fracture. In addition to the interaction between hydraulic fractures and natural fractures, the UFM also considers the interaction between adjacent fractures (i.e., the stress-shadow effect). The UFM solves a system of governing equations describing fluid flow in the fracture network, mass conversation, fracture deformation, height growth, proppant transport and fracture interaction to simulate the propagation of a complex fracture network that consists of many intersecting fractures, which are described below.

8.2.1.1 Fluid Flow equations

The local mass conservation equation at any location in the complex fracture network is given as:

$$\frac{\partial q}{\partial s} + \frac{\partial (H_{fl}\overline{w})}{\partial t} + q_L = 0 \tag{8.1}$$

$$q_L = 2h_L u_L \tag{8.2}$$

where H_{fl} is the height of a fracture at position s and time t, q denotes the local fracturing fluid flow rate, $\overline{w}$ is the average width of a fracture at position $s = s(x, y)$, and q_L is the leak-off volume rate through the hydraulic fracture wall (leak-off velocity, u_L, times leak-off fracture height, h_L),

which is computed using Carter's leak-off model.

The pressure drop along a fracture branch in a complex fracture network for laminar flow of power-law fluid can be expressed using Poiseuille law:

$$\frac{\partial p}{\partial s} = -\alpha_0 \frac{1}{\overline{w}^{2n'+1}} \frac{q}{H_{fl}} \left| \frac{q}{H_{fl}} \right|^{n'-1} \tag{8.3a}$$

and for turbulent fracturing fluid flow:

$$\frac{\partial p}{\partial s} = -\frac{f\rho}{\overline{w}^3} \frac{q}{H_{fl}} \left| \frac{q}{H_{fl}} \right| \tag{8.3b}$$

where

$$\alpha_0 = \frac{2k'}{\phi(n')^{n'}} \cdot \left(\frac{4n'+2}{n'} \right)^{n'} ; \phi(n') = \frac{1}{H_{fl}} \int_{H_{fl}} \left(\frac{w(z)}{\overline{w}} \right)^{\frac{2n'+1}{n'}} dz \tag{8.4}$$

where p is the fluid pressure, $w(z)$ denotes the fracture width as a function of depth z, f represents the fanning factor, ρ is the density of slurry, and n' and k' are the fracturing fluid power-law index and consistency index, respectively.

The fracture height and width profiles in a multi-layered formation depends on the fluid pressure, fracture toughness, in-situ stresses, layer thickness and elastic modulus of each layer. The fracture height is calculated by matching the fracture toughness to the stress intensity factors at fracture tips. Stress intensity factors K_{1u}, K_{1l} and width profile are given as follows [134]:

$$K_{1u} = \sqrt{\frac{\pi h}{2}}\left[p_{cp} - \sigma_n + \rho_f g\left(h_{cp} - \frac{3h}{4}\right)\right] + \sqrt{\frac{2}{\pi h}}\sum_{i=1}^{n-1}(\sigma_{i+1} - \sigma_i) \times \left[\frac{h}{2}\arccos\left(\frac{h-2h_i}{h}\right) - \sqrt{h_i(h-h_i)}\right] \tag{8.5a}$$

$$K_{1l} = \sqrt{\frac{\pi h}{2}}\left[p_{cp} - \sigma_n + \rho_f g\left(h_{cp} - \frac{h}{4}\right)\right] + \sqrt{\frac{2}{\pi h}}\sum_{i=1}^{n-1}(\sigma_{i+1} - \sigma_i) \times \left[\frac{h}{2}\arccos\left(\frac{h-2h_i}{h}\right) + \sqrt{h_i(h-h_i)}\right] \tag{8.5b}$$

$$w(z) = \frac{4}{E'}\left[p_{cp} - \sigma_n + \rho_f g\left(h_{cp} - \frac{h}{4} - \frac{z}{2}\right)\right]\sqrt{z(h-z)} + \frac{4}{\pi E'}\sum_{i=1}^{n-1}(\sigma_{i+1} - \sigma_i) \left[(h_i - z)\,\mathrm{arcCosh}\,\frac{z\left(\frac{h-2h_i}{h}\right) + h_i}{|z-h_i|} + \sqrt{z(h-z)}\arccos\left(\frac{h-2h_i}{h}\right)\right] \tag{8.5c}$$

where K_{1u} and K_{1l} are the stress intensity factors at the top and bottom of fracture tips, respectively, h is the fracture height, p_{cp} is fracturing fluid pressure at height h_{cp} measured from the bottom tip of the reference fracture, σ_n and σ_i are the in-situ stresses at the top and the i^{th} layer, respectively, h_i is the distance between the fracture bottom tip and top of i^{th} layer, ρ_f is the fluid density and $E' = E/(1-\nu^2)$ where E is Young's modulus, ν is Poisson's ratio.

In addition to the above equations, the following global volume balance must be satisfied at each time:

$$\int_0^t Q(t)dt = \int_0^{L(t)} h(s,t)\overline{w}(s,t)ds + \int_{H_L}\int_0^t\int_0^{L(t)} 2u_L ds dt dh_L \tag{8.6}$$

where t is the current time, $L(t)$ is the total fracture length in the hydraulic fracture network at time t and $Q(t)$ is the fracturing fluid flow rate at the wellbore. The global volume balance equation essentially signifies that the total volume of injected fracturing fluid is equal to the volumes of fracturing fluid present in the fracture network and leak-off fluid to the surrounding formation.

These equations, along with the boundary conditions stating that the fracture tip's width, net pressure and flow rate are zero, describe the fluid flow through a complex fracture network.

8.2.1.2 *Hydraulic and natural fractures interaction*

The interaction between propagating hydraulic fractures and pre-existing natural fractures is a very complex phenomenon. The modeling of this system requires consideration of various rock properties like Young's modulus, tensile strength, poisson's ratio, toughness, permeability and cohesion. It should also incorporate various fracturing fluid properties like viscosity, density and pressure. In addition to this, mechanical properties like cluster spacing and relative angle between hydraulic fractures and natural fractures also govern whether a hydraulic fracture will cross a natural fracture, dilate a natural fracture, or be arrested at a natural fracture as explained by Wu and Olson [152]. The average opening width of a fracture [129] and average pressure of a fracturing fluid in the natural fracture [168] are governed by the following equations:

$$\overline{w} = 2.53 \left[\frac{Q\mu L^2}{E'H} \right]^{1/4} \qquad p_{NF}(t) = p_f \tanh \left(\sqrt{\frac{2kp_f}{\mu b_s^2}} t \right) \tag{8.7}$$

where μ is the slurry viscosity, p_f is the fracture tip's fluid pressure, p_{NF} is the fluid pressure within a natural fracture, k is the permeability of natural fracture, t is the contact time and b_s is the boundary of sliding zone as a result of contact between a natural fracture and hydraulic fracture.

8.2.1.3 *Stress shadow effects*

Stress shadow effects refer to alteration in the growth pattern of a hydraulic fracture due the presence of neighboring fractures. The disturbance from nearby fractures leads to a significant perturbation in the propagating hydraulic fracture. In this work, 2D Displacement Discontinuity Method (DDM) described by Crouch et al. [131] is used to quantify the normal and shear stresses on a fracture element due to opening and shearing displacement discontinuities. It is defined as follows:

$$\sigma_n^i = \sum_{j=1}^{N} A^{ij} C_{ns}^{ij} D_s^j + \sum_{j=1}^{N} A^{ij} C_{nn}^{ij} D_n^j \tag{8.8a}$$

$$\sigma_s^i = \sum_{j=1}^{N} A^{ij} C_{ss}^{ij} D_s^j + \sum_{j=1}^{N} A^{ij} C_{sn}^{ij} D_n^j \tag{8.8b}$$

where σ_n and σ_s are the normal and shear stresses, respectively, D_n and D_s are the opening and shearing displacement discontinuities, respectively, C^{ij} are the 2D plane-strain elastic influence coefficients and A^{ij} are the 3D correction factors introduced by Olson [169] to account for the 3D effect caused by finite fracture height.

Based on this UFM, Schlumberger developed a hydraulic fracture simulator called Mangrove which is an engineered stimulation package available in Schlumberger Petrel platform. In this work, we have used Mangrove to simulate complex fracture growth in naturally fractured unconventional reservoirs.

Remark 16. *The parameters required to set up the Mangrove simulator for a specific rock formation are reservoir thickness, Young's modulus, Poisson ratio, minimum and maximum horizontal stresses, and natural fracture properties such as length, orientation and spacing between natural fractures. The minimum horizontal stress of rock formation can be obtained from minifrac or extended leak-off test, and maximum horizontal stress is available from wellbore failure image and modeling. Rock properties such as Young's modulus and Poisson ratio can be obtained from well logs. Microseismic measurements can be used to partially predict the distribution of natural fractures by comparing the effective stimulated volume for a given distribution of natural fractures.*

8.2.2 Reservoir Simulator

Apart from simulating complex fracture networks, Mangrove can model the oil production through proppant-propped complex fractured networks. Specifically, the output from the UFM is fed as an input to the automated grid generator [170]. After establishing the production grid including a complex fracture geometry, we simulate production from an oil well in a naturally

fractured unconventional reservoir using Mangrove. Then the Net Present Value (NPV) of the oil produced from the well is calculated using the following equation:

$$NPV = \int_0^T Q_{oil} r_{oil} (1+I)^{-ct} dt \tag{8.9}$$

where Q_{oil} is the oil production rate from the well, t is the elapsed time since the oil production was initiated, T is the total oil production time, r_{oil} is the oil market price, c is the time constant, and I is the money discount rate. In this work, c and I are taken as 0.1 and 1/365 (1/day), respectively.

8.3 Sensitivity analysis of complex fracture growth in naturally fractured reservoirs

During hydraulic fracture propagation in naturally fractured reservoirs, the complex fracture growth depends on in-situ stresses, rock mechanical properties, natural fracture properties and hydraulic fracture treatment parameters (e.g., fracturing fluid properties and pumping schedules). In this section, we performed sensitivity analysis on the effect of natural fracture distribution (e.g., length, orientation and spacing between natural fractures) and fracturing fluid pumping schedule (e.g., flow rate and proppant concentration injected at the wellbore) on TFSA for given rock properties (e.g., Young's modulus, Poisson ratio and in-situ stresses).

8.3.1 Effect of natural fracture distribution on TFSA

For all the simulations, we considered a single-stage hydraulic fracturing operation with three simultaneously propagating multiple fractures from the three clusters with a fracture spacing of 100 ft. We considered a total of 487200 lb proppant available for injection per stage. All the other parameters used in the simulations are given in Table 8.1.

8.3.1.1 Effect of natural fracture orientation on TFSA

The orientation of natural fractures, which is defined by the relative angle (β in Fig. 8.2) between hydraulic fractures and natural fractures, is one of the important factors affecting the final fracture geometry. As the relative angle decreases, the tendency of hydraulic fractures to cross natural fractures decreases [171]. Consequently, hydraulic fracture propagation will divert into natural

Parameter	Value
Fracturing fluid flow rate	$60\ \mathrm{bbl/min}$
Stage length	$200\ \mathrm{ft}$
Reservoir thickness	$500\ \mathrm{ft}$
Young's modulus	$1.57\ \mathrm{Mpsi}$
Poisson ratio	0.35
Proppant particle density	$2640\ \mathrm{kg/m^3}$
Slick-water density	$1000\ \mathrm{kg/m^3}$
Viscosity	$0.64\ \mathrm{cp}$
Minimum horizontal stress	$4450\ \mathrm{psi}$
Maximum horizontal stress	$4650\ \mathrm{psi}$
Perforations in each cluster	12
Diameter of each perforation	$0.42\ \mathrm{in}$
Proppant mesh size	$80/100$
Diameter of proppant	$0.00647\ \mathrm{in}$
Friction coefficient	0.6

Table 8.1: Model parameters used for sensitivity studies.

fractures leading to a complex fracture geometry. In this sensitivity analysis, we considered four different relative angles (0°, 30°, 45° and 90°) with a differential stress (i.e., the difference between the maximum and minimum horizontal stresses) of 200 psi and all other parameters were kept as same of those given in Table 8.1. The total number of natural fractures, their lengths, and inter-fracture spacing were generated assuming they will follow normal distributions [172]. The statistical parameters used to generate natural fractures with different relative angles are given in Table 8.2 and the corresponding 2D traces of fracture networks are shown in Fig. 8.3.

	Length (ft)	Spacing (ft)	Friction coefficient	Relative angles			
Average	100	50	0.6	0°	30°	45°	90°
Standard deviation	50	5	0	0°	0°	0°	0°

Table 8.2: Natural fracture distribution with different relative angles.

We observed that hydraulic fractures are unable to cross natural fractures for the four relative

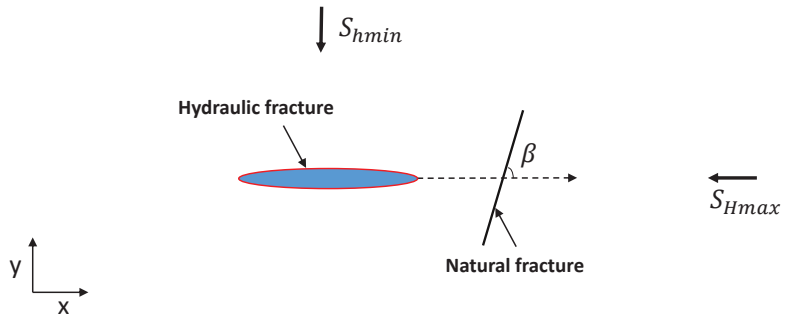

Figure 8.2: Schematic showing a hydraulic fracture approaching a natural fracture.

angles considered in this work. Instead, they diverted into natural fractures leading to a complex fracture geometry as shown in Fig. 8.3. Mangrove uses the crossing criterion developed by Chuprakov et al. [168] to predict the interaction between hydraulic fractures and natural fractures; the criterion was developed by considering the effect of in-situ stress ratio, friction coefficient, relative angle, flow rate and viscosity. As per this criterion, a fracturing fluid will leak into natural fractures and divert the hydraulic fracturing propagation when the product of fracturing fluid flow rate, Q, and viscosity, μ, is small (i.e., $Q\mu$ is a small value); otherwise, when the product value is large, hydraulic fractures tend to cross natural fractures and propagate in the same direction, like planar fractures. We considered a slick water for hydraulic fracturing which is of very-low viscosity (0.64 cp), and thus, hydraulic fractures diverted into natural fractures for the four relative angles resulting in a complex fracture geometry (Fig. 8.3). In addition, the TFSA is also affected by the relative angles as shown in Fig. 8.4. When the relative angle is 0°, hydraulic fractures will propagate in the direction of the maximum horizontal stress after diverting into natural fractures (Fig. 8.2). In this case, the compressional stress acting perpendicular to the surface of hydraulic fractures is the minimum horizontal stress. As the relative angle increases, the compressional stress acting on hydraulic fractures after diverting into natural fractures increases. Eventually, at 90° the

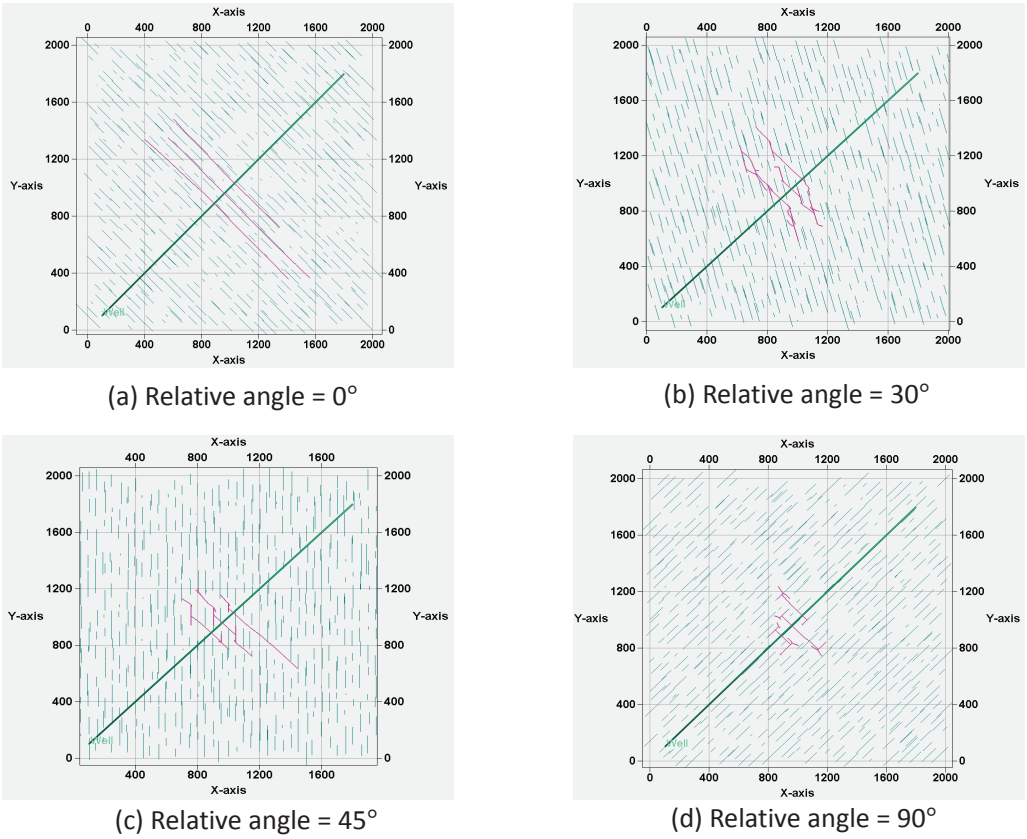

Figure 8.3: Fracture network at the end of hydraulic fracturing operation for four different relative angles between hydraulic fractures and natural fractures.

compressional stress acting on hydraulic fractures is the maximum horizontal stress. In summary, the fracture growth becomes more restricted with relative angle (Fig. 8.3). Therefore, as can be seen from Fig. 8.4, a smaller relative angle generates a higher TFSA.

8.3.1.2 Effect of natural fracture length on TFSA

As observed from the data obtained from Barnett shale [172], the length of natural fractures in naturally fractured reservoirs is not constant. Generally, natural fractures with different lengths are generated using a normal distribution to replicate the field case. In this sensitivity analysis, we considered two different distributions of natural fracture length as given in Table 8.3 with a fixed relative angle of 45°. All other parameters were used as described in Table 8.1. The 2D trace of natural fracture network and final complex fracture network obtained at the end of hydraulic

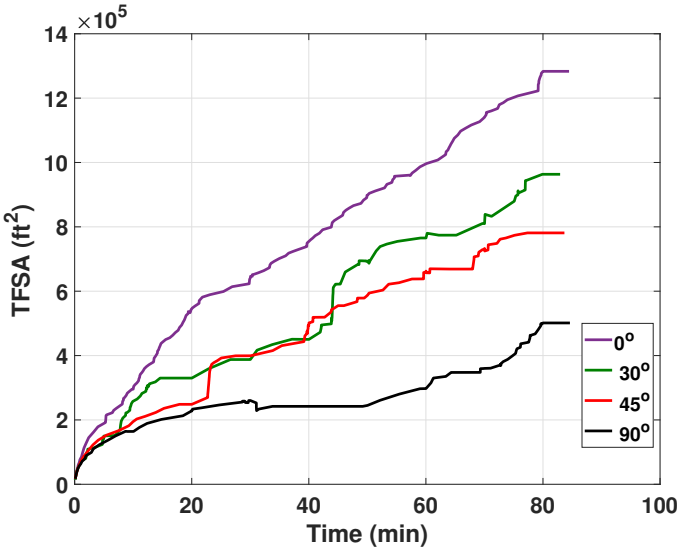

Figure 8.4: Comparison of TFSA for four different relative angles between hydraulic fractures and natural fractures.

fracturing operation for these two cases are shown in Fig. 8.5. It is observed that the hydraulic fracture propagation pattern depends on the length of natural fractures. Hydraulic fractures tend to propagate in the direction of natural fractures when the length of natural fractures is long; whereas in the case of short natural fracture length, they tend to propagate in the original hydraulic fracture propagation direction. In addition, TFSA is also affected by natural fractures length, as shown in Fig. 8.6. Until a hydraulic fracture diverts into a natural fracture, the compressional stress acting perpendicular to the fracture surface area is the minimum horizontal stress. However, after it diverts, the compressional stress becomes greater than the minimum horizontal stress. This happens due to a change in the fracture orientation until the fracture grows out of a natural fracture. For longer natural fracture lengths, the high compressional strength will act for a longer time period which further restricts fracture growth and generates a less TFSA compared to those of shorter natural fracture lengths.

8.3.1.3 Effect of natural fracture spacing on TFSA

In this sensitivity analysis, we considered two different distributions for natural fracture spacing as given in Table 8.4 with a fixed relative angle of 45°. All other parameters were kept as described

	Relative angle	Spacing (ft)	Friction coefficient	Length (ft)	
Average	45°	40	0.6	100	200
Standard deviation	0°	5	0	50	50

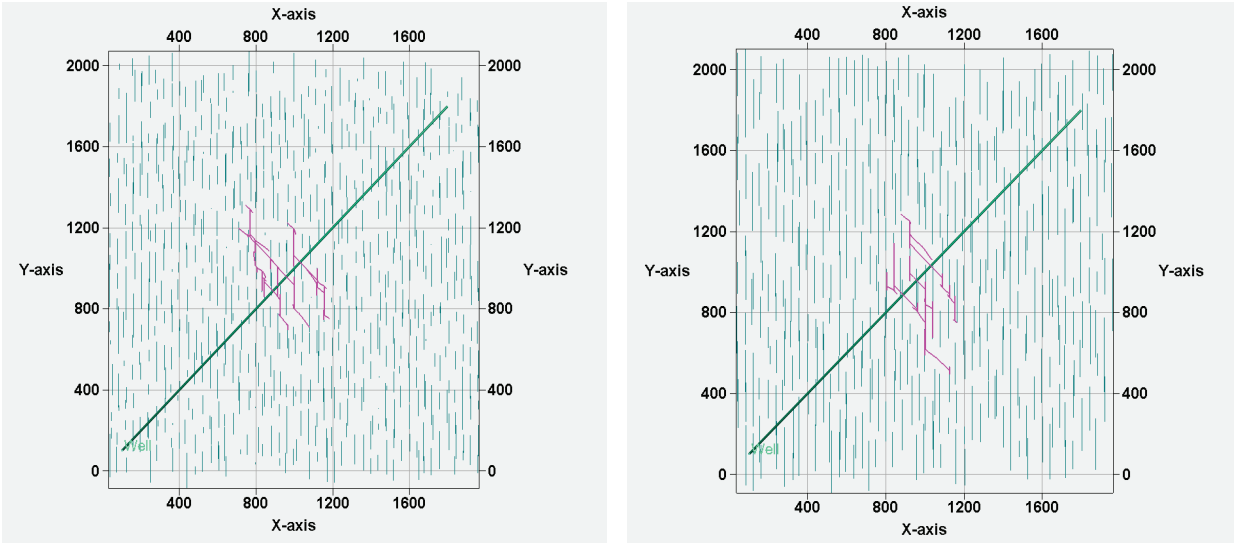

(a) Average length = 100 ft

(b) Average length = 200 ft

Figure 8.5: Fracture network at the end of hydraulic fracturing operation for two different natural fracture length distributions.

in Table 8.1. The 2D trace of natural fracture network and final complex fracture network obtained at the end of hydraulic fracturing operation for these two cases are shown in Fig. 8.7. It is observed that a decrease in natural fracture spacing leads to a more complex fracture geometry, as more natural fractures are likely to be encountered by hydraulic fractures. Because of this complex interaction of hydraulic fractures with multiple closely-spaced natural fractures, TFSA decreases with natural fracturing spacing as shown in Fig. 8.8.

Based on the sensitivity analysis presented above, we can observe that natural fracture attributes (e.g., spacing, length and orientation) have a major impact on complex fracture growth

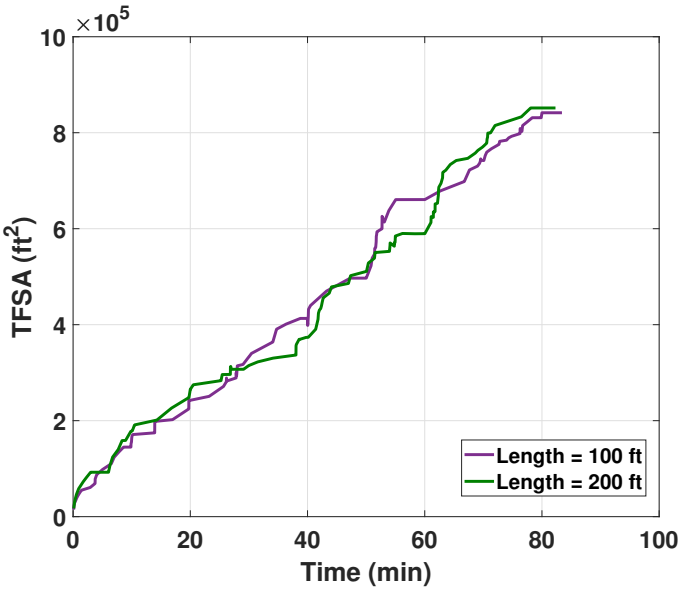

Figure 8.6: Comparison of TFSA for two different natural fracture length distributions.

	Relative angle	Length (ft)	Friction coefficient	Spacing (ft)	
Average	45°	100	0.6	20	60
Standard deviation	0°	50	0	5	5

Table 8.4: Natural fracture distribution with different spacing values.

during hydraulic fracturing in naturally fractured unconventional reservoirs. Therefore, it is very important to consider the interaction between hydraulic fractures and natural fractures to optimize the hydraulic fracturing treatment in naturally fractured unconventional reservoirs. In practice, microseismic measurements can be used to partially predict the distribution of natural fractures by comparing the effective stimulated volume for a given distribution of natural fractures. In this work, we assume that the natural fracture distribution is available, which is used as a feedback to design a model-based feedback control framework to compute the pumping schedule by maximizing the TFSA for given fracturing resources.

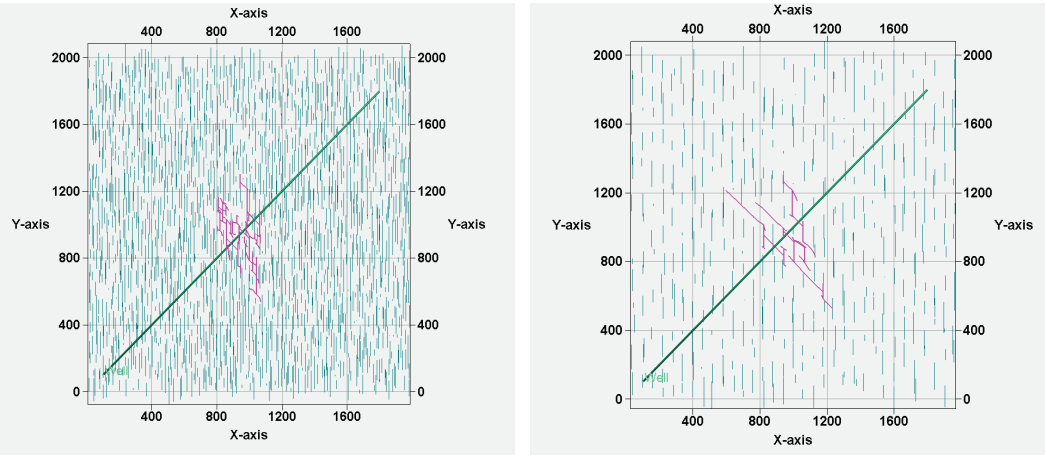

(a) Spacing= 20 ft

(b) Spacing = 60 ft

Figure 8.7: Fracture network at the end of hydraulic fracturing operation for two different natural fracture spacing distributions.

8.3.2 Effect of pumping schedule on TFSA

In this subsection, we performed a sensitivity analysis to find the effect of fracturing fluid pumping schedule (i.e., flow rate and proppant concentration at the wellbore) on the TFSA at the end of pumping for given rock properties (e.g., Young's modulus, Poisson ratio and in-situ stresses), natural fracture distribution (length, orientation and spacing between natural fractures) and amount of proppant. The statistical parameters used to generate the natural fracture distribution are given in Table 8.7. We considered a total amount of $M_{prop} = 487200\,\text{lb}$ proppant to be injected for creating fractures in a stage. All the other parameters used in the simulations are given in Table 8.1. We generated three fractures in a single stage with a fixed fracture spacing. For the purpose of sensitivity studies, we considered three cases with three different pumping schedules. The pumping schedule used in each case and the evolution of TFSA with time are shown in Fig. 8.9 and Fig. 8.10, respectively. We can clearly see that the TFSA depends on pumping schedules.

Thereafter, we simulated the corresponding oil production for 30 years in each case using the reservoir properties given in Table 8.5 and the generated complex fracture geometry at the end of

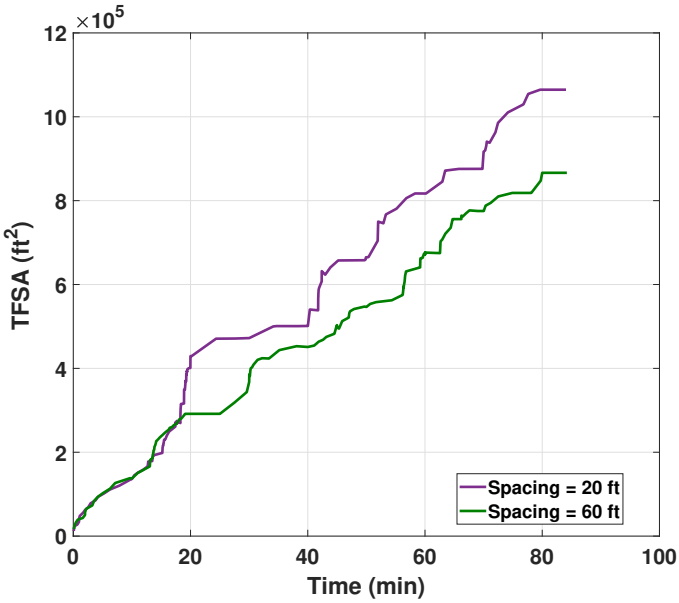

Figure 8.8: Comparison of TFSA for two different natural fracture spacing distributions.

hydraulic fracturing operation. The cumulative oil production is shown in Fig. 8.11, where it can be observed that the oil production rate is proportional to the TFSA at the end of pumping. This can also be seen from the results presented in Table 8.6, where it is observed that a reduction of 18% in the TFSA at the end of pumping leads to a reduction of around 60% in the cumulative oil production at the end of 30 years. This is mainly due to the fact that the drainage area for hydrocarbon recovery is directly related to TFSA, and achieving a greater TFSA will lead to a greater oil production rate in naturally fractured unconventional reservoirs. Therefore, because of complex fracture growth, the main goal of hydraulic fracturing in naturally fractured unconventional reservoirs should be to maximize the TFSA by manipulating the fracturing fluid pumping schedule for given resources as it will lead to more oil recovery.

Parameters	Value
Reservoir rock type	Consolidated sandstone
Permeability	$0.0001 - 0.0005$ mD
Porosity	0.08
Reservoir pressure	5000 psi
Unpropped fracture conductivity	10^{-3} mD.ft
Production time	30 years

Table 8.5: Reservoir properties used for the oil production simulation.

Case	TFSA (ft^2)	% Change in TFSA compared to case A	Cumulative oil production (STB)	% Change in production compared to case A
Case A	1769942	0	501542	0
Case B	1664617	- 5.9	483678	- 3.6
Case C	1445647	- 18.3	192969	- 61.5

Table 8.6: TFSA and cumulative oil production for three cases with different pumping schedules.

8.4 Background on pumping schedule design techniques

In this section, we present currently available pumping schedule design techniques. Nolte [28] developed a power-law type proppant concentration schedule, $C_0(t)$, which is given below:

$$C_0(t) = \begin{cases} C_{target}\left(\frac{t-t_p}{t_e-t_p}\right)^{\epsilon} & \text{for } t \geq t_p \\ 0 & \text{for } t < t_p \end{cases} \tag{8.10}$$

where the desired proppant concentration at the end of hydraulic fracturing operation is denoted using C_{target}, ϵ is an exponent which depends on fracturing fluid efficiency η, the total time for pumping is denoted using t_e, and $t_p = \epsilon t_e$ is the pad time at which injection of proppant is started. Because of its easy-to-implement nature, Nolte's pumping schedule has been widely used, however it has the following practical limitations: (1) both proppant settling due to gravity and practical constraints are not considered; (2) because of the predefined form if there is a plant-model mismatch, it will lead to early termination of hydraulic fracturing by creating a shorter propped fracture length;

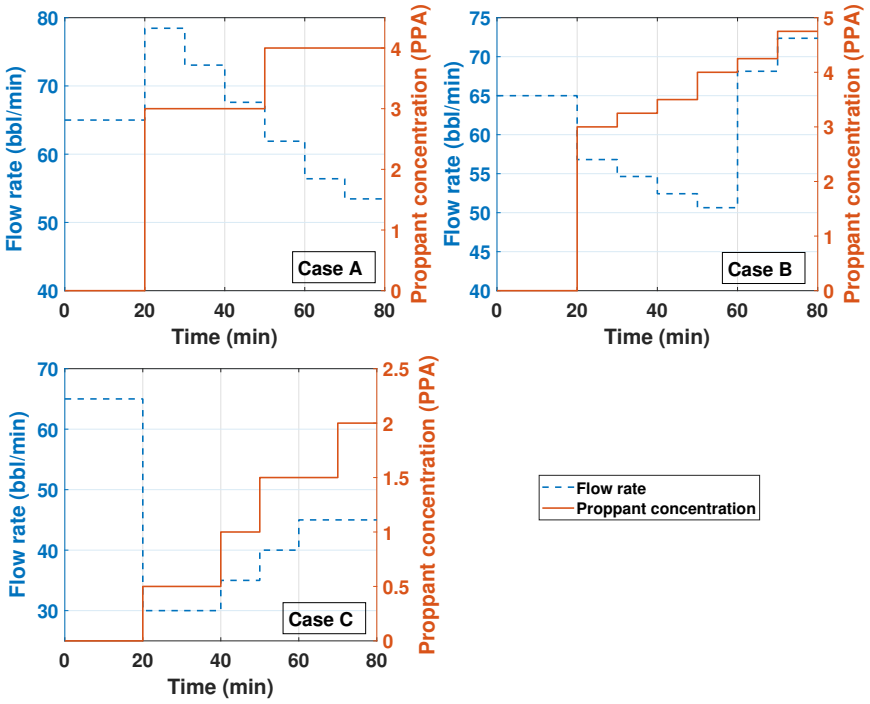

Figure 8.9: Pumping Schedules used for sensitivity analysis.

(3) the pumping schedule is designed offline and applied in an open-loop manner to a hydraulic fracturing process; (4) focused only on a single hydraulic fracture; and (5) interaction between hydraulic fractures and natural fractures is not considered.

In Chapter 6, to overcome the limitations of Nolte's pumping schedule, a new model-based control system was developed to compute fracturing fluid pumping schedules online to achieve a uniform proppant distribution and optimal fracture geometry in simultaneously growing multiple fractures by Siddhamshetty et al. [5]. Specifically, we considered a dynamic model of simultaneously propagating multiple fractures including fracture propagation, stress shadow effect and proppant transport. However, we did not consider the interaction between hydraulic fractures and natural fractures, which resulted in fractures with a planar shape.

As shown from the sensitivity analysis presented in Section 8.3, hydraulic fracturing operation in naturally fractured unconventional reservoirs may result in a complex fracture geometry and it is very important to maximize the TFSA at the end of pumping as it is directly related to oil produc-

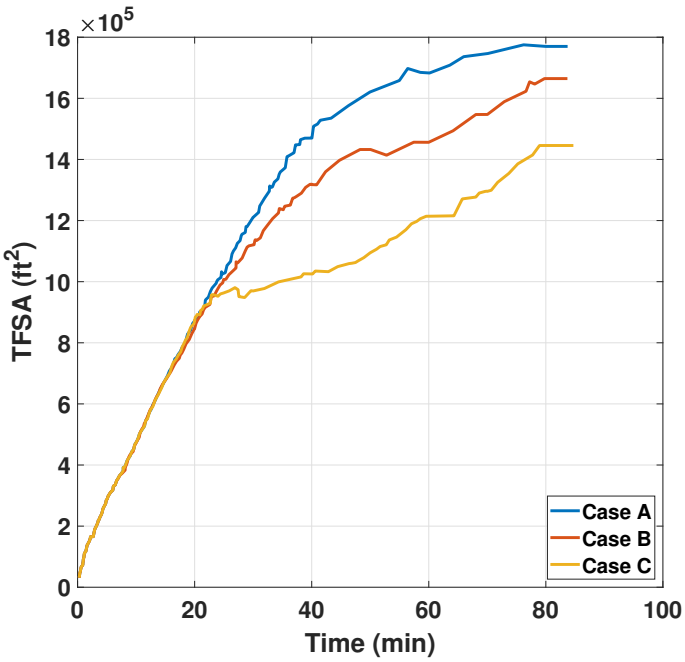

Figure 8.10: Comparison of TFSA for three cases with different pumping schedules.

tion rate. Pumping schedule design techniques mentioned above, which were developed to achieve a specific fracture geometry (length, width and height), may not result in the maximum TFSA when directly applied to naturally fractured unconventional reservoirs. Therefore, in the following section, a model predictive controller (MPC) is developed to compute a pumping schedule that will maximize the TFSA in naturally fractured unconventional reservoirs by utilizing Mangrove, which will eventually lead to an enhanced oil production rate.

8.5 Handling computational requirement in control of hydraulic fracturing processes

The UFM described using Eqs. (8.1)–(8.8) is computationally very expensive to be used directly for the design of MPC. In this work, we developed a ROM using MOESP algorithm to describe hydraulic fracture propagation and proppant transport phenomena in naturally fractured

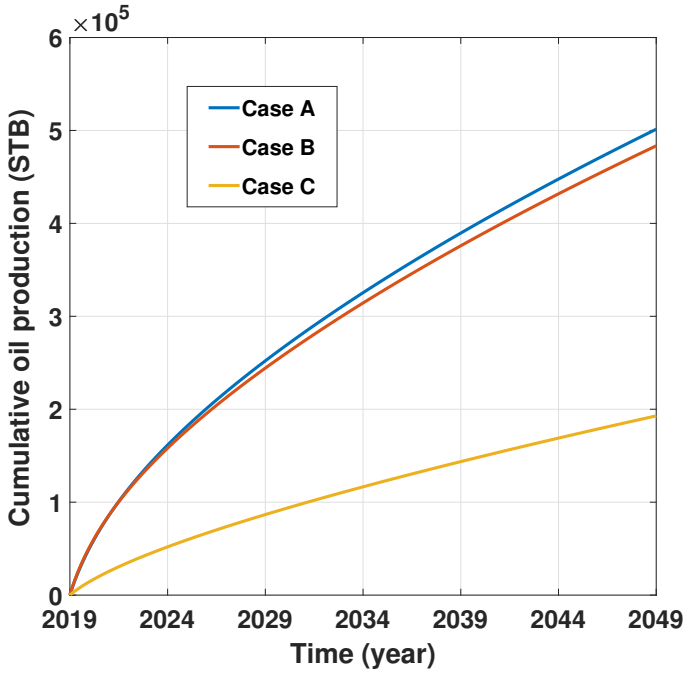

Figure 8.11: Cumulative oil production over time for three cases with different pumping schedules.

unconventional reservoirs, which is given below:

$$x(t_{k+1}) = Ax(t_k) + Bu(t_k) \tag{8.11a}$$

$$y(t_k) = Cx(t_k) \tag{8.11b}$$

where $u(t_k) = [Q_{x0}(t_k), C_0(t_k)]^{\mathrm{T}}$ are the input variables, $Q_{x0}(t_k)$ and $C_0(t_k)$ are the fracturing fluid flow rate and proppant concentration injected at the wellbore, respectively, the output variable, $y(t_k) = [A_{frac}(t_k)]$ is the TFSA, and the ROM states are represented using $x(t_k)$. For a system with a given order, the model parameters to be determined include the matrices A, B, and C, and the initial state estimate, $x(0)$, using a training data set.

For training, we used an open-loop simulation data obtained using Mangrove to obtain a 3^{rd} order linear time-invariant state-space model. The training input is chosen by considering the minimum and maximum allowable fracturing flow rate and proppant concentration. Fig. 8.12 shows the comparison between the estimated and true TFSA with time. It is observed that the estimated

TFSA from the ROM quickly converges to the true value obtained from the high-fidelity process model. The computational requirement to solve Eq. (8.11) is a small fraction relative to that of solving the UFM, Eqs. (8.1)–(8.8). We have validated the ROM by comparing its performance with the high fidelity model by considering a different pumping schedule within the limits of minimum and maximum fracturing flow rate and proppant concentration considered while developing ROM. Fig. 8.13 shows that TFSA obtained from the ROM is close to the high fidelity model.

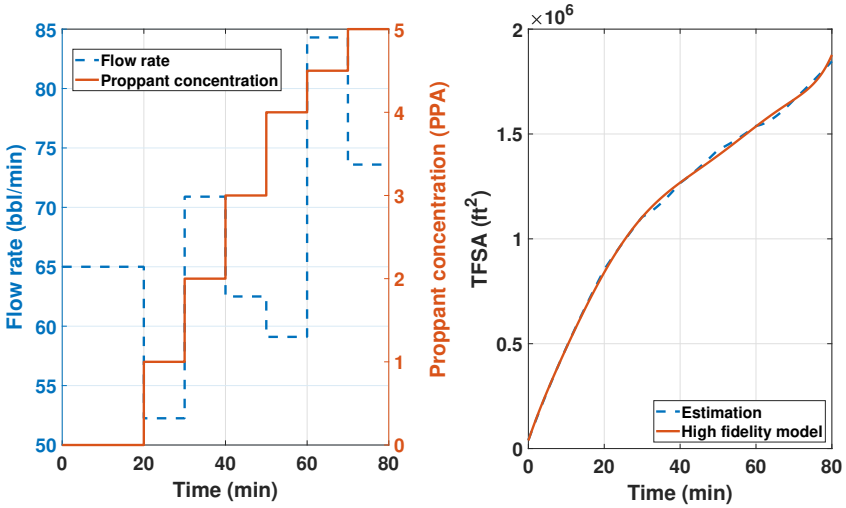

Figure 8.12: Comparison between the true values and the estimates of TFSA for a given pumping schedule.

In the present work, we assumed that TFSA is measurable, which is then used for estimation of the ROM states at time $t = t_k$, $x(t_k)$, using a Kalman filter, which is given in the following form:

$$\hat{x}(t_{k+1}) = A\hat{x}(t_k) + Bu(t_k) + M(t_k)(y_m(t_k) - \hat{y}(t_k)) \tag{8.12a}$$

$$M(t_k) = P(t_k)C^T(R(t_k) + CP(t_k)C^T)^{-1} \tag{8.12b}$$

$$P(t_{k+1}) = (I - M(t_k)C)P(t_k) \tag{8.12c}$$

where the variables estimated by the Kalman filter are denoted using $\hat{(\cdot)}$, $y_m(t_k) = [A_{frac}(t_k)]$ is the TFSA, the process and measurement noise covariance matrices are denoted using Q and R,

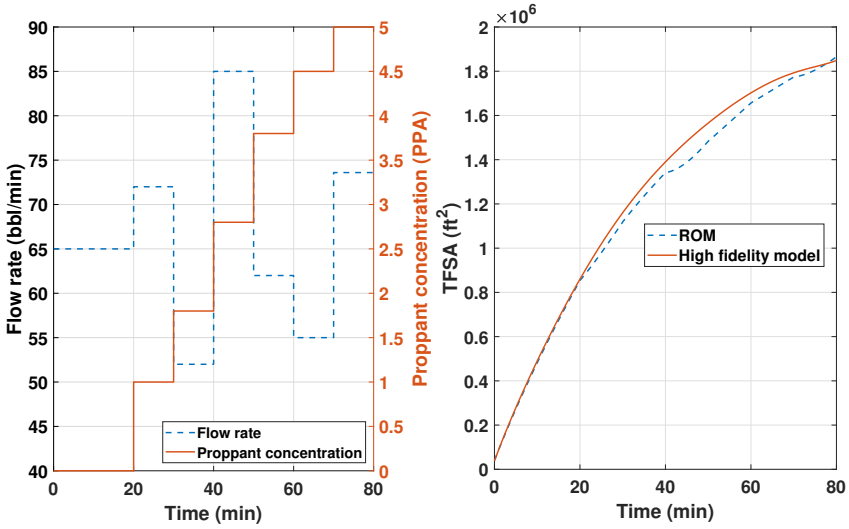

Figure 8.13: Validation of ROM by comparing it with high fidelity model for a given pumping schedule.

respectively, $M(t_k)$ is the gain of Kalman filter, and $P(t_k)$ denotes the state estimation error covariance. In this work, a Kalman filter is used for state estimation. However, other state estimators such as Luenberger observer or moving horizon estimator can be readily used.

Remark 17. *In this work, Kalman filter is used to estimate the ROM states which will also handle any plant-model mismatch by considering the real-time measurement of TFSA. Furthermore, due to the nature of closed-loop operation based on the proposed controller design technique, model-plant mismatch would be handled.*

Remark 18. *Please note that it is not practical to measure TFSA in real-time. However, TFSA can be estimated from other available measurements using state estimators such as Kalman filter or moving horizon estimator. In practice, we have very limited access to real-time measurements such as the fracture width at the wellbore. Real-time measurement of fracture width at the wellbore can be obtained using the wellbore pressure data and the elasticity equation relating the fracture width at the wellbore and the wellbore pressure [43, 44, 146, 173, 174, 175]. Previously, we have used this available measurement to estimate unmeasurable variables such as proppant concentration across the fracture and average fracture width using a Kalman filter [142, 144, 176]. Similarly, we*

can estimate TFSA by using a Kalman filter and the available real-time measurement of fracture width at the wellbore.

8.6 Model-based feedback control system for enhancing TFSA in naturally fractured unconventional reservoirs

This section presents a MPC formulation to compute an optimal pumping schedule that maximizes the TFSA in naturally fractured unconventional reservoirs at the end of hydraulic fracturing process. The following MPC optimization problem is solved utilizing the ROM and Kalman filter to compute the optimal pumping schedule:

$$\max_{\substack{C_{stage,k},\ldots,C_{stage,8}\\ Q_{stage,k},\ldots,Q_{stage,8}}} \quad A_{frac}(t_f) \tag{8.13a}$$

$$\text{s.t.} \quad y_m(t_k) = A_{frac}(t_k) \tag{8.13b}$$

$$\text{ROM, Eq. (8.11)} \tag{8.13c}$$

$$\text{Kalman filter, Eq. (8.12)} \tag{8.13d}$$

$$C_{stage,k-1+m} \leq C_{stage,k+m} \leq 5 \text{ PPA} \tag{8.13e}$$

$$Q_{min} \leq Q_{stage,k+m} \leq Q_{max} \tag{8.13f}$$

$$m = 1, \ldots, 8-k \tag{8.13g}$$

$$\Delta \left(\sum_{k=1}^{8} Q_{stage,k} C_{stage,k} \right) = M_{prop} \tag{8.13h}$$

where the duration of each sampling is given by Δ, t_k is the time of k^{th} sample, $y_m(t_k)$ is the TFSA measured at $t = t_k$, t_f is the hydraulic fracturing total operation time, and the manipulated input variables, $C_{stage,k}$ and $Q_{stage,k}$, are obtained by solving Eq. (8.13) with a shrinking prediction horizon $N_p = t_f - t_k$.

In the optimization problem of Eq. (8.13), a Kalman filter, Eq. (8.13d), is used to estimate unmeasurable ROM states and it is initialized at every sampling time utilizing the TFSA measured in real-time, which is described by Eq. (8.13b). Eqs. (8.13e)-(8.13f) are the constraints on the

manipulated input variables (e.g., proppant concentration and fracturing fluid flow rate injected at the wellbore). The units of fracturing fluid flow rate and proppant concentration are $\mathrm{bbl/min}$ and PPA (1 pound of the proppant added to one gallon of fracturing fluid), respectively. The total amount of proppant injected is constrained using Eq. (8.13h).

8.7 Closed-loop simulation results under the proposed MPC

In this section, we present the closed-loop simulation results to signify the performance of our proposed MPC scheme. For all the cases, we considered a single stage hydraulic fracturing operation to generate three simultaneously propagating multiple fractures for a given natural fracture distribution. The statistical parameters used to generate the natural fracture distribution are given in Table 8.7 and the generated natural fracture distribution is shown in Fig. 8.14. The total proppant amount considered is $M_{prop} = 487200$ lb. All the other parameters used in the simulations are given in Table 8.1. The high fidelity model of Mangrove described in Section 8.2 was utilized to simulate a hydraulic fracturing operation in naturally fractured unconventional reservoirs. This model is initially used with a given training input for generating the input/output data which was used to develop a ROM of the process. We then designed a Kalman filter for state estimation using this ROM, which eventually helped us in developing the complete MPC scheme. The Kalman filter and the proposed MPC were initialized at the beginning of hydraulic fracturing operation. In the proposed MPC, Δ and t_f values were chosen to be 10 min and 80 min, respectively. This implies that the fracturing fluid pumping schedule consists of 8 stages, each with a duration of 10 min. We assumed that the measurement of TFSA, $A_{frac}(t_k)$, was available at the beginning of each pumping stage (Eq. (8.13b)). The unmeasurable ROM states were then predicted with the help of real-time measurement via the Kalman filter. Using these estimated states, the proposed MPC computed the control input over a prediction horizon length of N_p to maximize the TFSA at the end of hydraulic fracturing operation, which will lead to an enhanced oil production rate due to a higher drainage area available for hydrocarbon recovery. We applied the first step of solution, $C_{stage,k}$ & $Q_{stage,k}$, to the high-fidelity model of Mangrove in a sample-and-hold fashion and this procedure was repeated at every sampling time until the end of the process.

	Length (ft)	Spacing (ft)	Orientation	Friction coefficient
Average	500	100	15	0.5
Standard deviation	250	50	15	0

Table 8.7: Natural fracture distribution used in the closed-loop simulation.

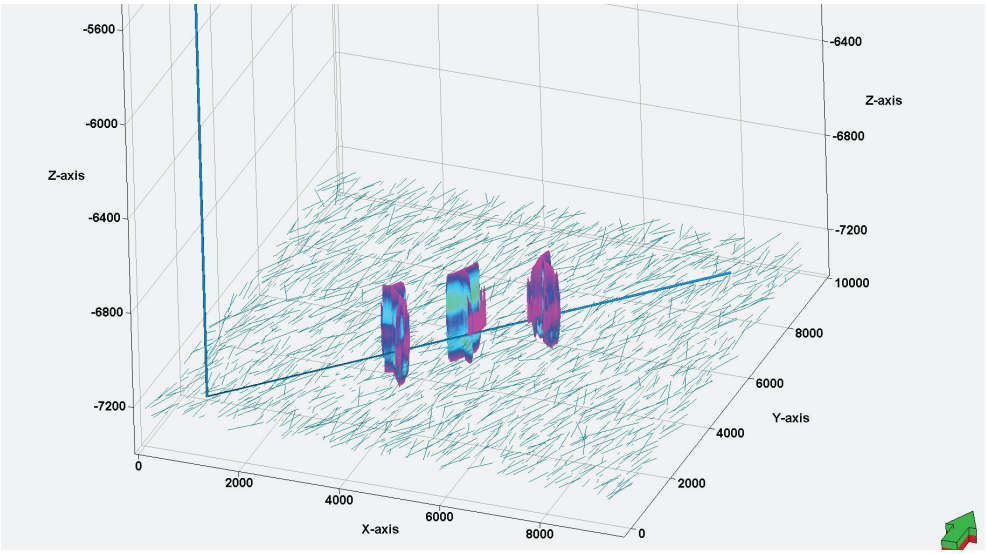

Figure 8.14: Fracture geometry at the end of hydraulic fracturing operation under the proposed MPC.

The pumping schedule obtained under the proposed MPC scheme (Fig. 8.15) is then fed as an input to Mangrove. The obtained fracture geometry at the end of hydraulic fracturing operation under the proposed MPC is presented in Fig. 8.14. For given rock properties and natural fracture distributions, hydraulic fractures divert into natural fractures resulting in a complex fracture geometry. We then compared the performance of the pumping schedule computed by the proposed MPC with existing pumping schedules such as Nolte (Fig. 8.16) and the one introduced in Chapter 6 by Siddhamshetty et al. [5] (Fig.8.17), which were developed without considering natural fractures. All the other parameters such as Young's modulus, Poisson ratio, and proppant amount are kept same in all the cases. Fig. 8.18 compares the evolution of the TFSA for the three cases. Fig. 8.19 and Fig. 8.20 show the comparison of the cumulative oil production and oil production

rates for the three cases. We can see clearly from the figures that the pumping schedule under the proposed MPC maximizes the TFSA, which subsequently leads to the maximum oil production rate and maximum cumulative oil production compared to other pumping schedules. We reported the NPV of oil produced for these three cases in Table 8.8. Using the proposed MPC will result in an revenue that is \$0.74 millions and \$0.4 millions more than those obtained by the pumping schedule in Chapter 6 by Siddhamshetty et al. [5] and Nolte [28], respectively.

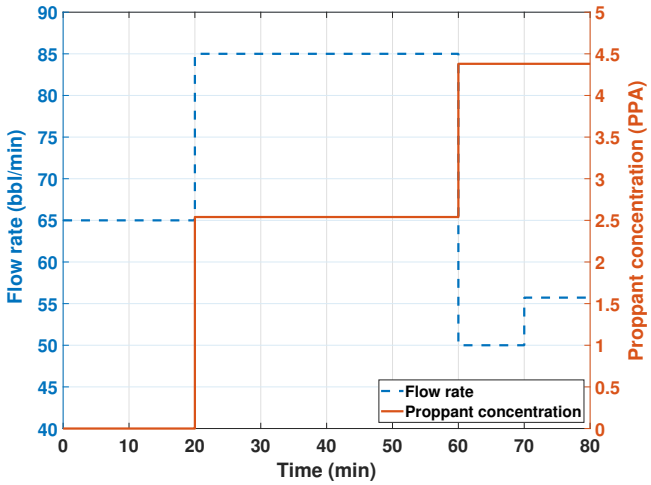

Figure 8.15: Pumping schedule obtained under the proposed MPC.

	TFSA (ft^2)	Cumulative oil production (STB)	NPV (M\$)
MPC	1979450	512707	13.36
Nolte	1793945	487310	12.96
Siddhamshetty et al. [5]	1755249	473338	12.62

Table 8.8: TFSA, cumulative oil production and NPV of oil produced under the proposed MPC, Nolte's and Siddhamshetty et al. [5] pumping schedules.

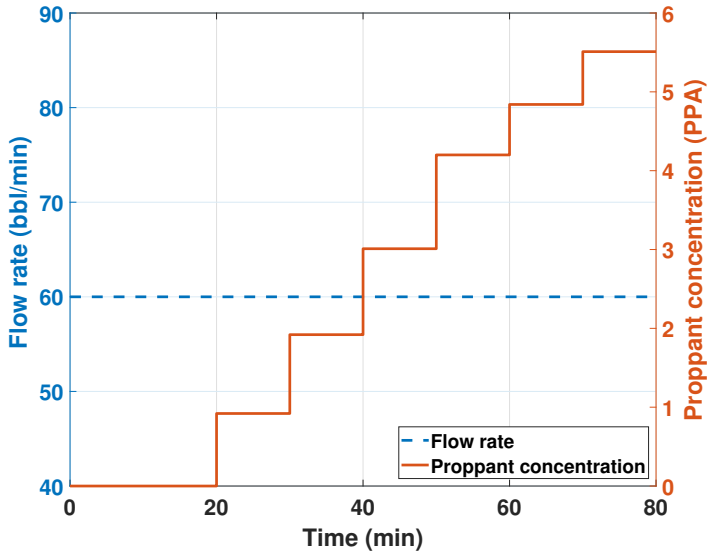

Figure 8.16: Nolte's pumping schedule with input constraints being considered.

Because linear ROMs were used to solve this problem, we achieved a significant reduction in the computational requirement. The time required to solve the optimization problem, Eq. (8.13), at every sampling time instant is given in Table 8.9. Since the problem was solved using a shrinking horizon approach, we can see that the computational time with every iteration has a tendency to decrease. Please note that all calculations were performed using MATLAB on a Dell workstation, powered by Intel(R) Core(TM) i7-4790 CPU@3.60GHz, running the Windows 8 operating system.

Pumping stage number	Computational time (s)
1	4.93
2	0.70
3	0.56
4	0.36
5	0.30
6	0.14
7	0.19
8	0.05

Table 8.9: Computational time required to solve the optimization problem, Eq. (8.13), at each pumping stage.

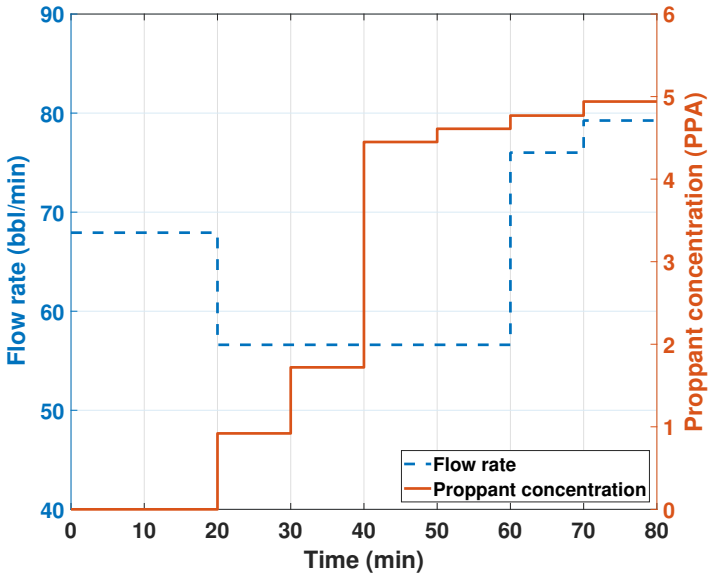

Figure 8.17: Pumping schedule obtained by the method proposed by Siddhamshetty et al. [5].

Natural fractures are present in most of unconventional reservoirs and affect hydraulic fracture propagation. Therefore, we cannot ignore the interaction of hydraulic fractures with natural fractures when we design pumping schedules to inject given fracturing resources. We have to utilize these interaction to achieve an even greater TFSA, which would not have been possible to achieve without considering natural fractures. Drainage area for hydrocarbon recovery is directly related to TFSA. Therefore, achieving a greater TFSA will lead to an increased oil production rate in naturally fractured unconventional reservoirs. The model-based pumping schedule design technique developed in this work considers the interaction of hydraulic fractures with natural fractures. Therefore, we were able to achieve a TFSA greater than those of the existing pumping schedules which were developed without considering natural fractures.

8.8 Conclusions

In this work, it was observed from the sensitivity analysis that the cumulative oil production from a well is proportional to TFSA, which in-turn depends on the fracturing fluid pumping schedule for given fracturing resources and natural fracture distributions. Therefore, we developed a novel MPC framework to compute the fracturing fluid pumping schedule that maximizes the TFSA

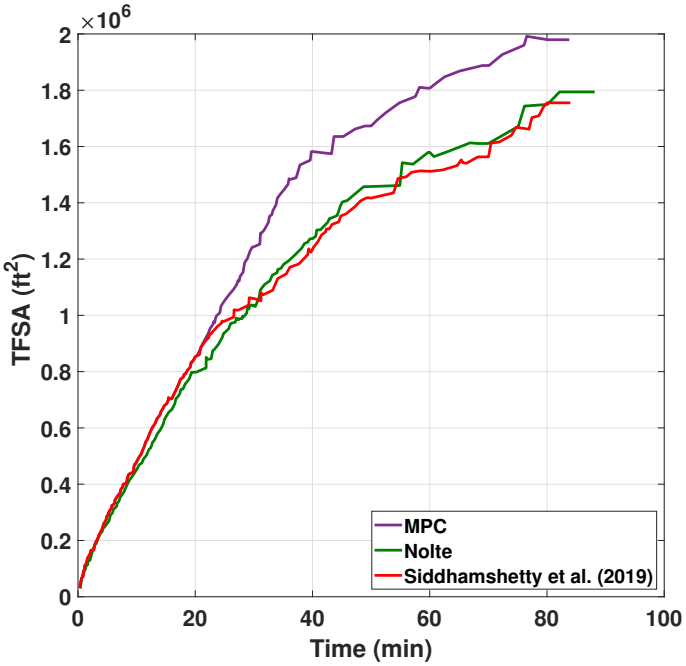

Figure 8.18: Comparison of TFSA under the proposed MPC, Nolte's and Siddhamshetty et al. [5] pumping schedules.

in naturally fractured unconventional reservoirs. Initially, we constructed a ROM using the simulation data generated from Mangrove by considering the complex fracture growth in naturally fractured unconventional reservoirs. Then, the developed ROM was used for state estimation using a Kalman filter and available measurements. Next, a real-time MPC framework was developed utilizing the ROM and Kalman filter to compute the pumping schedule that maximizes the TFSA. Simulation results presented in this work show that the maximum TFSA will lead to an oil production rate greater than those of the existing pumping schedules which were developed without considering natural fractures.

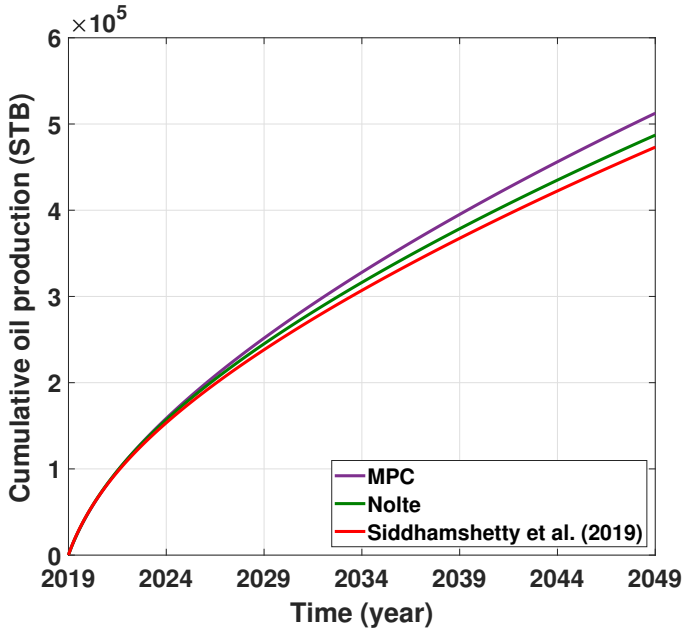

Figure 8.19: Comparison of cumulative oil production under the proposed MPC, Nolte's and Siddhamshetty et al. [5] pumping schedules.

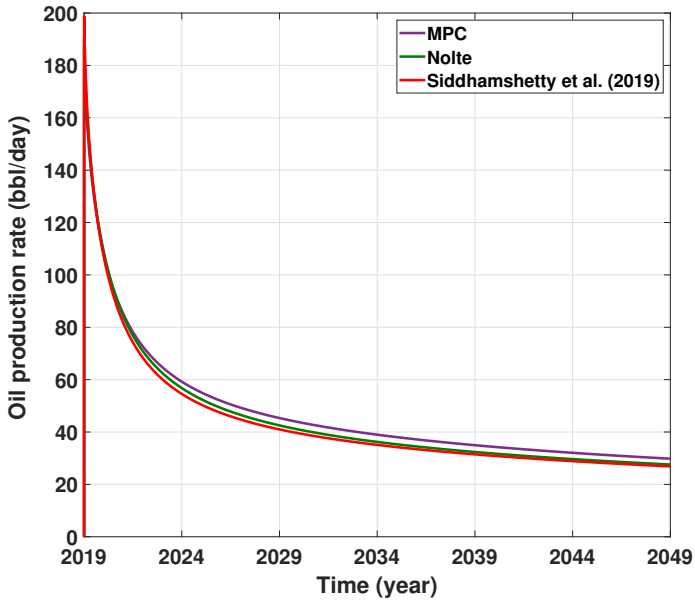

Figure 8.20: Comparison of oil production rates under the proposed MPC, Nolte's and Siddhamshetty et al. [5] pumping schedules.

9. SUMMARY AND FUTURE WORK

9.1 Summary

The combination of directional drilling and hydraulic fracturing has transformed the paradigm of energy markets by enabling the extraction process of unconventional gas resources to become more economical, eventually leading to the shale revolution. In practice, the ultimate goal of hydraulic fracturing is to increase the productivity of a stimulated (i.e., fractured) well by producing fractures with a desired geometry and achieve a uniform proppant concentration at the end of pumping which it is directly related to the overall efficiency of the hydraulic fracture process. The current status of hydraulic fracturing is primarily an open-loop approach where the pumping schedules are designed based on the properties obtained from a mini-frac test. Over the last ten years, the oil and gas production industries have applied model predictive control (MPC) theory to drilling processes to enhance pressure control flexibility and process safety; however, its application to hydraulic fracturing, particularly in the context of regulating the proppant distribution across the fracture, has not received much attention because of the following reasons: (1) limited access to real-time measurements, (2) presence of uncertainties in the measurement data, and (3) large computational requirements due to dynamic simulation of multiple highly-coupled PDEs defined over a time-dependent spatial domain.

Novel sensor types such as microseismic monitoring are becoming increasingly powerful tools for real-time underground measurements which enable the design of real-time control strategies for the hydraulic fracturing process. Here, we proposed a new methodological framework for the design of an optimal and practical proppant pumping schedule to achieve an optimal fracture geometry at the end of hydraulic fracturing process using the available real-time measurements. Initially, we focused on developing a model-predictive control framework for conventional reservoirs, where high-viscosity fracturing fluids are typically used to ensure that the most of the proppant remains in suspension during the treatment and the closure process. Thus, it is sufficient to regulate

the suspended proppant concentration along the fracture at the end of pumping. Initially, we developed a first-principles model for the hydraulic fracturing process considering a single propagating fracture. Second, a novel numerical scheme was developed to deal with the high computational requirement caused by coupling multiple PDEs defined over a time-dependent spatial domain. Third, a reduced-order model was constructed by using these simulation results, and a Kalman filter was designed to effectively estimate important variables that are not measurable in real-time. Lastly, MPC theory was applied for the design of the feedback control system to achieve uniform proppant concentration across the fracture at the end of pumping. The generated pumping schedule using the proposed control scheme was able to produce uniform concentration at the end of pumping, which was closer to the target concentration than that of Nolte's pumping schedule which is one of the most commonly used pumping schedules. Furthermore, the proposed methodology was able to generate an online pumping schedule with a reasonable computational requirement while explicitly taking into account practical, safety, and optimality considerations.

Then, we extended this approach to unconventional reservoirs, where predominantly low-viscosity ("slick-water") fluids are used and the proppant settles quickly forming a proppant bank. The proppant bank will continue to grow until it reaches the equilibrium height; a state when the rate of proppant washout on top of proppant banks due to the shear force is equal to the rate of bank formation via proppant settling. We improved the high-fidelity process model of hydraulic fracturing processes to describe the formation of a proppant bank with the equilibrium height. A section-based optimization method was employed to determine the optimal well-fracture configuration, maximizing the overall productivity for a given amount of proppant to be injected. Then, MPC theory was applied for the design of a real-time model-based feedback control system. The proposed methodology was able to generate an online pumping schedule leading to a uniform proppant bank height along the targeted length while explicitly taking into account actuator limitations, state constraints for process safety, and economical considerations. We further improved our control framework to reduce the measurement uncertainty by taking advantage of the relationship between the fracturing fluid injection rate and measurement noise covariance in a microseismic

monitoring technique, which is the most widely used measurement technique for a comprehensive understanding of fracture geometry.

Subsequently, we aimed to consider multi-stage hydraulic fracturing where multiple fractures are generated simultaneously. In multi-stage hydraulic fracturing treatments, simultaneously propagating multiple fractures with close spacing often induce non-uniform fracture development due to stress-shadow effects, resulting in one or two dominant fractures due to the uneven distribution of fracturing fluids. We initially developed a new high-fidelity model for simultaneously growing multiple fractures to describe the fracture propagation by explicitly accounting for stress shadow effects as well as the proppant transport. Then, we proposed a model-based design technique to compute the perforation conditions which promote an equal distribution of fracturing fluids to achieve a uniform growth of multiple fractures while mitigating the undesired stress-shadow effects. Lastly, the proposed MPC scheme was applied to compute online fracturing fluid pumping schedules. The proposed methodology was able to generate a uniform proppant bank height along the targeted fracture length while simultaneously incorporating the limitations of actuators, process operational safety and economic considerations.

We further considered the interaction of hydralic fractures with natural fractures in naturally fractured unconventional reservoirs. It was observed from the sensitivity analysis that the cumulative oil production from a well is proportional to total fracture surface area (TFSA), which in turn depends on the fracturing fluid pumping schedule for given fracturing resources and natural fracture distributions. Therefore, we developed a novel MPC framework to compute the fracturing fluid pumping schedule that maximizes the TFSA in naturally fractured unconventional reservoirs.

9.2 Future work

This study laid the foundations for the design of a model-predictive control framework to compute pumping schedules for hydraulic fracturing process to achieve an optimal fracture geometry. In what follows a list of potential improvements currently under consideration in the lab is provided:

1. Although the hydraulic fracturing process enhances the recovery of hydrocarbons in unconventional reservoirs, it is heavily dependent on water resources. In the five largest shale oil and gas reserves in the U.S., the average water usage per well ranges from 71,000-155,000 BBL [100, 177]. Thus, understanding the life cycle of water consumption associated with shale oil and gas production is imperative [178, 179, 180]. During the hydraulic fracturing process, the water cycle consists of five key sub-stages: water acquisition, chemical mixing, well injection, flowback and produced water, wastewater treatment and wastewater disposal. In the first 3-4 weeks after completion of the well injection, 15-40% of the injected water, depending on the specific region, flows back to the surface as highly contaminated water, which is called flowback water [99]. Generally, deep well injection has been the primary method for wastewater disposal. However, in some areas where shale gas production is abundant, this disposal option is either unavailable near the drilling site or restricted due to indications of seismic activity because of the higher injection pressure. In this regard, in the future, Dr. Kwon's lab aim to develop environmentally sustainable and economically feasible water management and treatment options.

2. Various types of fracturing fluids are used depending largely on the geologic structure and formation and formation pressure for a well. The main categories of fracturing fluids currently available/used include: (i) water frac, (ii) linear aqueous gels, (iii) cross-linked aqueous gels, (iv) aqueous viscoelastic surfactant-based fluids, (v) foam fluids, and (vi) gelled oil-based fluids. After hydraulic fracturing treatments, unbroken fracturing fluids may result in productivity impairment in shale gas production. This clean-up process is modeled by assuming Newtonian fluid behavior for the fracturing fluid. However, most cross-link gelled fracturing fluids are indeed non-Newtonian with yield stress. Motivated by this, Dr. Kwon's lab aim to improve the clean-up process model and incorporate it in the controller design.

REFERENCES

[1] T. K. Perkins and L. R. Kern, "Widths of hydraulic fractures," *Journal of Petroleum Technology*, vol. 13, pp. 937–949, 1961.

[2] R. Nordgren, "Propagation of a vertical hydraulic fracture," *SPE Journal*, vol. 12, pp. 306–314, 1972.

[3] K. Wu and J. E. Olson, "Simultaneous multifracture treatments: fully coupled fluid flow and fracture mechanics for horizontal wells," *SPE Journal*, vol. 20, pp. 337–346, 2015.

[4] K. Wu, *Numerical modeling of complex hydraulic fracture development in unconventional reservoirs*. PhD thesis, The university of Texas at Austin, TX, 2014.

[5] P. Siddhamshetty, K. Wu, and J. S. Kwon, "Modeling and control of proppant distribution of multi-stage hydraulic fracturing in horizontal shale wells," *Ind. & Eng. Chem. Res.*, vol. 58, pp. 3159–3169, 2019.

[6] M. Nikolaou, "Computer-aided process engineering in oil and gas production," *Computers & Chemical Engineering*, vol. 51, pp. 96–101, 2013.

[7] M. J. Economides, L. T. Watters, and S. Dunn-Normall, *Petroleum well construction*. Wiley, 1998.

[8] M. J. Economides and K. G. Nolte, *Reservoir stimulation*. John Wiley & Sons, 2000.

[9] B. Lecampion and J. Desroches, "Simultaneous initiation and growth of multiple radial hydraulic fractures from a horizontal wellbore," *Journal of the Mechanics and Physics of Solids*, vol. 82, pp. 235–258, 2015.

[10] M. J. Economides, R. E. Oligney, and P. Valko, *Unified fracture design*. Orsa Press, 2002.

[11] J. A. Daal and M. J. Economides, "Optimization of hydraulic fracture well in irregularly shape drainage areas," *SPE International Symposium and Exhibition on Formation Damage Control (SPE 98047), Lafayette, LA*, 2006.

[12] A. S. Demarchos, A. S. Chomatas, M. J. Economides, J. M. Mach, D. S. Wolcott, and Y. Wolcott, "Pushing the limits in hydraulic fracture design," *SPE International Symposium and Exhibition on Formation Damage Control (SPE 86483), Lafayette, LA*, 2004.

[13] S. Bhattacharya, M. Nikolaou, and M. J. Economides, "Unified fracture design for very low permeability reservoirs," *J. of Natural Gas Sci. and Eng*, vol. 9, pp. 184–195, 2012.

[14] J. D. Jansen, S. D. Douma, D. R. Brouwer, P. Van den Hof, O. H. Bosgra, and A. W. Heemink, "Closed-loop reservoir management," *SPE Reservoir Simulation Symposium (SPE 119098), The Woodlands, TX*, 2009.

[15] D. R. Brouwer, G. Naevdal, J. D. Jansen, E. H. Vefring, and C. P. Van Kruijsdijk, "Improved reservoir managment through optimal control and continuous model updating," *SPE Annual Technical Conference and Exhibition (SPE 90149), Houston, TX*, 2004.

[16] J. D. Jansen, O. H. Bosgra, and P. Van den Hof, "Model-based control of multiphase flow in subsurface oil reservoir," *Journal of Process Control*, vol. 18, pp. 846–855, 2008.

[17] A. S. Cullick, D. Heath, K. Narayanan, J. April, and J. Kelly, "Optimizing multiple-field scheduling and production strategy with reduced risk," *SPE Annual Technical Conference and Exhibition (SPE 84239), Denver, CO*, 2003.

[18] V. Goel and I. E. Grossmann, "A stochastic programming approach to planning of offshore gas field development under uncertainty in reserves," *Computers & Chemical Engineering*, vol. 28, pp. 1409–1429, 2004.

[19] P. Jacquard and C. Jain, "Permeability distribution from field pressure data," *SPE Journal*, vol. 5, pp. 281–294, 1965.

[20] B. Yeten, L. J. Durlofsky, and K. Aziz, "Optimization of nonconventional well type, location and trajectory," *SPE Journal*, vol. 8, pp. 200–210, 2002.

[21] Z. Fathi and W. Ramirez, "Use of optimal control theory for computing optimal injection policies for enhanced oil recovery," *Automatica*, vol. 22, pp. 33–42, 1986.

[22] J. A. Holmes, T. Barkve, and O. Lund, "Application of a multi-segment well model to simulate flow in advanced wells," *European Petroleum Conference (SPE 50646), The Hague, Netherlands*, 1998.

[23] F. Nyhavn, F. Vassenden, and P. Singstad, "Reservoir drainage with downhole permanent monitoring and control systems. Real-time integration of dynamic reservoir performance data and static reservoir model improves control decisions," *SPE Annual Technical Conference and Exhibition (SPE 62937), Dallas, TX*, 2000.

[24] L. J. Durlofsky and K. Aziz, "Optimization of smart well control," *SPE International Thermal Operations and Heavy Oil Symposium and International Horizontal Well Technology Conference (SPE 79031), Calgary, Alberta, Canada*, 2002.

[25] M. Litvak, L. Hutchins, R. C. Skinner, B. Darlow, R. C. Wood, and L. J. Kuest, "Prudhoe bay e-field production optimization system based on integrated reservoir and facility simulation," *SPE Annual Technical Conference and Exhibition (SPE 77643), San Antonio, TX*, 2002.

[26] B. Sundaryanto, B.daryanto, *Optimization of displacement efficiency of oil recovery in porous media using optimal control theory*. PhD thesis, University of Southern California, 1999.

[27] B. Sundaryanto and Y. Yortsos, "Optimization of displacements in porous media using rate control," *SPE Annual Technical Conference and Exhibition (SPE 71509), New Orleans, LA*, 2001.

[28] K. G. Nolte, "Determination of proppant and fluid schedules from fracturing-pressure decline," *SPE Prod. Eng*, vol. 1, pp. 255–265, 1986.

[29] H. Gu and J. Desroches, "New pump schedule generator for hydraulic fracturing treatment design," *SPE Latin American and Caribbean Petroleum Engineering Conference (SPE 81152), Port-of-Spain, Trinidad and Tobago*, 2003.

[30] E. V. Dontsov and A. P. Peirce, "A new technique for proppant schedule design," *Hydraulic Fracturing J*, vol. 1, no. 3, pp. 1–8, 2014.

[31] D. M. Hannegan, *Managed pressure drilling*. In SPE 2006-2007 distinguished lecturer series, 2007.

[32] J. M. Godhavn, A. Pavlov, G. Kaasa, and N. Rolland, "Drilling seeking automatic control solutions," *IFAC World Congress, Milano, Italy*, 2011.

[33] ø. Breyholtz, G. Nygaard, and M. Nikolaou, "Automatic control of managed pressure drilling," *Proceedings of American Control Conference, Baltimore, MD*, pp. 442–447, 2010.

[34] ø. Breyholtz and M. Nikolaou, "Drilling automation: Presenting a framework for automated operations," *SPE Drilling & Completion*, vol. 27, pp. 118–126, 2012.

[35] Y. Breyholtz, G. Nygaard, and M. Nikolaou, "Advanced automatic pressure control for dual-gradient drilling," *SPE Annual Technical Conference and Exhibition (SPE 124631), New Orleans, LA*, 2009.

[36] J. E. Gravdal, M. Nikolaou, O. Breyholtz, and L. A. Carlsen, "Improved kick management during MPD by real-time pore-pressure estimation," *SPE Drilling and Completion*, vol. 25, pp. 577–584, 2010.

[37] R. A. Shishavan, C. Hubbell, H. D. Perez, J. D. Hedengren, D. S. Pixton, and A. P. Pink, "Multivariate control for managed-pressure-drilling systems by use of high-speed telemetry," *SPE Annual Technical Conference and Exhibition (SPE 170962), Amsterdam, Netherlands*, 2014.

[38] R. Asgharzadeh Shishavan, C. Hubbell, H. D. Perez, J. D. Hedengren, D. S. Pixton, and A. P. Pink, "Multivariate control for managed-pressure-drilling systems by use of high-speed telemetry," *SPE Journal*, vol. 21, pp. 459–470, 2015.

[39] A. N. Eaton, L. D. Beal, S. D. Thorpe, C. B. Hubbell, J. D. Hedengren, R. Nybø, and M. Aghito, "Real time model identification using multi-fidelity models in managed pressure drilling," *Computers & Chemical Engineering*, vol. 97, pp. 76–84, 2017.

[40] A. Eaton, L. Beal, S. Thorpe, E. Janis, C. Hubbell, J. Hedengren, R. Nybø, M. Aghito, K. Bjørkevoll, R. Boubsi, and J. Braaksma, "Ensemble model predictive control for robust automated managed pressure drilling.," *SPE Annual Technical Conference and Exhibition (SPE 174969), Houston, TX*, 2015.

[41] M. Bellout, D. Echeverria Ciaurri, L. Durlofsky, B. Foss, and J. Kleppe, "Joint optimization of oil well placement and controls," *Computational Geosciences*, pp. 1–19, 2012.

[42] B. Foss, "Process control in conventional oil and gas fields-challenges and opportunities," *Control Engineering Practice*, vol. 20, pp. 1058–1064, 2012.

[43] Q. Gu and K. A. Hoo, "Evaluating the performance of a fracturing treatment design," *Ind. & Eng. Chem. Res*, vol. 53, pp. 10491–10503, 2014.

[44] Q. Gu and K. A. Hoo, "Model-based closed-loop control of the hydraulic fracturing process," *Ind. & Eng. Chem. Res.*, vol. 54, pp. 1585–1594, 2015.

[45] B. Wheaton, J. Miskimins, D. Wood, T. Lowe, and R. Barree, "Integration of distributed temperature and distributed acoustic survey results with hydraulic fracture modeling: a case study in the woodford shale," *In 2015 SEG Annual Meeting. Society of Exploration Geophysicists (SEG-2015-5830237), New Orleans, LA*, 2015.

[46] K. Wu and J. E. Olson, "Mechanisms of simultaneous hydraulic-fracture propagation from multiple perforation clusters in horizontal wells," *SPE Journal*, vol. 21, pp. 1000–1008, 2016.

[47] C. K. Miller, G. A. Waters, and E. I. Rylander, "Evaluation of production log data from horizontal wells drilled in organic shales," *In North American Unconventional Gas Conference and Exhibition (SPE 144326), The Woodlands, TX*, 2011.

[48] J. D. Baihly, R. Malpani, C. Edwards, S. Yen Han, J. C. L. Kok, E. M. Tollefsen, and C. W. Wheeler, "Unlocking the shale mystery: How lateral measurements and well placement impact completions and resultant production," *In Tight Gas Completions Conference. Society of Petroleum Engineers (SPE 138427), San Antonio, TX*, 2010.

[49] C. L. Cipolla, X. Weng, H. Onda, T. Nadaraja, U. Ganguly, and R. Malpani, "New algorithms and integrated workflow for tight gas and shale completions," *SPE Annual Technical Conference and Exhibition (SPE 146872), Denver, CO*, 2011.

[50] L. N. Germanovich, D. K. Astakhov, M. J. Mayerhofer, J. Shlyapobersky, and L. M. Ring, "Hydraulic fracture with multiple segments i. observations and model formulation," *International Journal of Rock Mechanics and Mining Sciences*, vol. 34, pp. 97–e1, 1997.

[51] M. K. Fisher, J. R. Heinze, C. D. Harris, B. M. Davidson, C. A. Wright, and K. P. Dunn, "Optimizing horizontal completion techniques in the barnett shale using microseismic fracture mapping," *SPE Annual Technical Conference and Exhibition (SPE 90051), Houston, TX*, 2004.

[52] B. R. Meyer and L. W. Bazan, "A discrete fracture network model for hydraulically induced fractures-theory, parametric and case studies," *In SPE hydraulic fracturing technology conference. Society of Petroleum Engineers (SPE 140514), The Woodlands, TX*, 2011.

[53] S. C. Maxwell, J. Rutledge, R. Jones, and M. Fehler, "Petroleum reservoir characterization using downhole microseismic monitoring," *Geophysics*, vol. 75, no. 5, pp. 75A129–75A137, 2010.

[54] C. L. Cipolla, M. G. Mack, S. C. Maxwell, and R. C. Downie, "A practical guide to interpreting microseismic measurements," *In SPE North American Unconventional Gas Conference and Exhibition (SPE 144067), The Woodlands, TX*, 2011.

[55] C. L. Cipolla, S. C. Maxwell, and M. G. Mack, "Engineering guide to the application of microseismic interpretations," *In SPE Hydraulic Fracturing Technology Conference and Exhibition (SPE 152165), The Woodlands, TX*, 2012.

[56] J. Gale, R. Reed, and J. Holder, "Natural fractures in the barnett shale and their importance for hydraulic fracture treatments," *AAPG Bull*, vol. 91, pp. 603–622, 2007.

[57] J. Gale, S. Laubach, J. Olson, P. Eichhubl, and A. Fall, "Natural fractures in shale: a review and new observations," *AAPG Bull*, vol. 98, pp. 2165–2216, 2014.

[58] A. Dahi Taleghani and J. E. Olson, "How natural fractures could affect hydraulic-fracture geometry," *SPE journal*, vol. 19, pp. 161–171, 2013.

[59] R. Yang, Z. Huang, W. Yu, G. Li, W. Ren, L. Zuo, X. Tan, K. Sepehrnoori, S. Tian, and M. Sheng, "A comprehensive model for real gas transport in shale formations with complex non-planar fracture networks," *Sci. Rep.*, vol. 6, p. 36673, 2016.

[60] A. Daneshy, "Numerical solution of sand transport in hydraulic fracturing," *Journal of Petroleum Technology*, vol. 30, pp. 132–140, 1978.

[61] A. Mobbs and P. Hammond, "Computer simulations of proppant transport in a hydraulic fracture," *SPE prod. Facil.*, vol. 16(02), pp. 112–121, 2001.

[62] E. Shokir and A. Al-Quraishi, "Experimental and numerical investigation of proppant placement in hydraulic fractures," *SPE Latin American and Caribbean Petroleum Engineering Conference (SPE 107927), Buenos Aires, Argentina*, 2007.

[63] C. A. Blyton, D. P. Gala, and M. M. Sharma, "A comprehensive study of proppant transport in a hydraulic fracture," *SPE Annual Technical Conference and Exhibition (SPE 174973), Houston, TX*, 2015.

[64] S. Shiozawa and M. McClure, "Comparison of pseudo-3D and fully-3D simulations of proppant transport in hydraulic fractures, including gravitational settling, formation of proppant banks, tip-screen out, and fracture closure," *SPE Hydraulic Fracturing Technology Conference (SPE 179132), The Woodlands, TX*, 2016.

[65] C. L. Cipolla, E. P. Lolon, M. J. Mayerhofer, and N. R. Warpinski, "The effect of proppant distribution and un-propped fracture conductivity on well performance in unconventional gas reservoirs," *In SPE Hydraulic Fracturing Technology Conference (SPE 119368), The Woodlands, TX*, 2009.

[66] L. Sneddon and H. Elliot, "The opening of a griffith crack under internal pressure," *Q. Appl. Math*, vol. 4, pp. 262–267, 1946.

[67] A. Gudmundsson, "Stress estimate from the length/width ratios of fractures," *Journal of Structural Geology*, vol. 5, pp. 623–626, 1983.

[68] G. C. Howard and C. R. Fast, "Optimum fluid characteristics for fracture extension," *Driling and production practices. American Petroleum Institute*, vol. 24, pp. 261–270, 1957.

[69] J. Adachi, E. Siebrits, A. Peirce, and J. Desroches, "Computer simulation of hydraulic fractures," *International Journal of Rock Mechanics and Mining Sciences*, vol. 44, pp. 739–757, 2007.

[70] R. Barree and M. Conway, "Experimental and numerical modeling of convective proppant transport," *Journal of Petroluem Technology*, vol. 47, pp. 216–222, 1995.

[71] E. J. Novotny, "Proppant transport," *SPE Annual Fall Technical Conference and Exhibition (SPE 6813), Denver, CO*, 1977.

[72] A. Armaou and P. D. Christofides, "Nonlinear feedback control of parabolic partial differential equation systems with time-dependent spatial domains," *J. Math. Anal. Appl.*, vol. 239, pp. 124–157, 1999.

[73] A. Armaou and P. D. Christofides, "Finite-dimensional control of nonlinear parabolic pde systems with time-dependent spatial domains using empirical eigenfunctions," *Int. J. Appl. Math. Comput. Sci.*, vol. 11, pp. 287–317, 2001.

[74] A. Armaou and P. D. Christofides, "Robust control of parabolic PDE systems with time-dependent spatial domains," *Automatica*, vol. 37, pp. 61–69, 2001.

[75] J. Ng and S. Dubljevic, "Optimal boundary control of a diffusion-convection-reaction PDE model with time-dependent spatial domain: Czochralski crystal growth process," *Chem. Eng. Sci.*, vol. 67, pp. 111–119, 2012.

[76] M. Izadi, J. Abdollahi, and S. S. Dubljevic, "PDE backstepping control of one-dimensional heat equation with time-varying domain," *Automatica*, vol. 54, pp. 41–48, 2015.

[77] M. Izadi and S. Dubljevic, "Order-reduction of parabolic pdes with time-varying domain using empirical eigenfunctions," *AIChE Journal*, vol. 59, pp. 4142–4150, 2013.

[78] H. M. Bücker, B. Pollul, and A. Rasch, "On CFL evolution stratgies for implicit upwind methods in linearized euler equations," *Int. J. Numer. Meth. in Fluids*, vol. 59, pp. 1–18, 2009.

[79] S. Yang, P. Siddhamshetty, and J. S. Kwon, "Optimal pumping schedule design to achieve a uniform proppant concentration level in hydraulic fracturing," *Computers & Chemical Engineering*, vol. 101, pp. 138–147, 2017.

[80] J. Quirein, J. Grable, B. Cornish, R. Stamm, and T. Perkins, "Microseismic fracture monitoring," *SPWLA 47th Annual Logging Symposium, Veracruz, Mexico*, 2006.

[81] D. J. Romero, P. P. Valko, and M. J. Economides, "The optimization of the productivity index and the fracture geometry of a stimulated well with fracture face and choke skins," *SPE International Symposium and Exhibition on Formation Damage Control (SPE 73758), Lafayette, LA*, 2002.

[82] B. Corbett and P. Mhaskar, "Subspace identification for data-driven modeling and quality control of batch processes," *AIChE Journal*, vol. 62, pp. 1581–1601, 2016.

[83] A. Garg and P. Mhaskar, "Subspace identification-based modeling and control of batch particulate processes," *Ind. & Eng. Chem. Res.*, vol. 56, pp. 7491–7502, 2017.

[84] A. Narasingam and J. Kwon, "Development of local dynamic mode decomposition with control: Application to model predictive control of hydraulic fracturing," *Computers & Chemical Engineering*, vol. 106, pp. 501–511, 2017.

[85] D. Pourkargar and A. Armaou, "Modification to adaptive model reduction for regulation of distributed parameter systems with fast trasients," *AIChE Journal*, vol. 59, pp. 4595–4611, 2013.

[86] D. Pourkargar and A. Armaou, "APOD-based control of linear distributed parameter systems under sensor/controller communication bandwidth limitations," *AIChE Journal*, vol. 61, pp. 434–447, 2015.

[87] D. Pourkargar and A. Armaou, "Design of APOD-based switching dynamic observers and output feedback control for a class of nonlinear distributed parameter systems," *Chem. Eng. Sci.*, vol. 136, pp. 62–75, 2015.

[88] A. Narasingam, P. Siddhamshetty, and J. Kwon, "Temporal clustering for order reduction of nonlinear parabolic pde systems with time-dependent spatial domains: Application to a hydraulic fracturing process," *AIChE Journal*, vol. 63, no. 9, pp. 3818–3831, 2017.

[89] L. Kern, T. Perkins, and R. Wyant, "The mechanics of sand movement in fracturing," *Journal of Petroleum Technology*, vol. 11, pp. 55–57, 1959.

[90] N. Patankar, D. Joseph, J. Wang, R. Barree, M. Conway, and M. Asadi, "Power law correlations for sediment transport in pressure driven channel flows," *International Journal of Multiphase Flow*, vol. 28, pp. 1269–1292, 2002.

[91] J. Wang, D. Joseph, N. Patankar, M. Conway, and R. Barree, "Bi-power law correlations for sediment transport in pressure driven channel flows," *International journal of multiphase flow*, vol. 29, pp. 475–494, 2003.

[92] H. Brannon, W. Wood, and R. Wheeler, "The quest for improved proppant placement: investigation of the effects of proppant slurry component properties on transport," *In SPE Annual Technical Conference and Exhibition. Society of Petroleum Engineers (SPE 95675), Dallas, TX*, 2005.

[93] M. Mack, J. Sun, and C. Khadilkar, "Quantifying proppant transport in thin fluids: theory and experiments," *In SPE Hydraulic Fracturing Technology Conference (SPE 168637), The Woodlands, TX*, 2014.

[94] X. Ma, T. Plaksina, and E. Gildin, "Integrated horizontal well placement and hydraulic fracture stages design optimization in unconventional gas reservoirs," *In SPE Unconventional Resources Conference Canada (SPE 167246), Calgary, Alberta, Canada*, 2013.

[95] T. Plaksina and E. Gildin, "Practical handling of multiple objectives using evolutionary strategy for optimal placement of hydraulic fracture stages in unconventional gas reservoirs," *Journal of Natural Gas Science and Engineering*, vol. 27, pp. 443–451, 2015.

[96] R. R. Iyer, I. E. Grossmann, S. Vasantharajan, and A. S. Cullick, "Optimal planning and scheduling of offshore oil field infrastructure investment and operations," *Ind. & Eng. Chem. Res.*, vol. 37, pp. 1380–1397, 1998.

[97] J. Gao and F. You, "Optimization of water management in shale gas production process," *53rd IEEE conference on Decision and Control, Los Angeles, CA*, 2014.

[98] J. Gao and F. You, "Optimal design and operations of supply chain networks for water management in shale gas production: MILFP model and algorithms for the water-energy nexus," *AIChE Journal*, vol. 61, pp. 1184–1208, 2015.

[99] N. Elsayed, M. Barrufet, F. Eljack, and M. El-Halwagi, "Optimal design of thermal membrane distillation systems for the treatment of shale gas flowback water," *Int. J. Membr. Sci. Technol.*, vol. 2, pp. 1–9, 2015.

[100] L. Lira-Barragán, J. Ponce-Ortega, G. Guillén-Gosálbez, and M. El-Halwagi, "Optimal water management under uncertainty for shale gas production," *Ind. & Eng. Chem. Res.*, vol. 55, pp. 1322–1335, 2016.

[101] J. Gao and F. You, "Game theory approach to optimal design of shale gas supply chains with consideration of economics and life cycle greenhouse gas emissions," *AIChE Journal*, vol. 63, pp. 2671–2693, 2017.

[102] K. Arredondo-Ramírez, J. Ponce-Ortega, and M. El-Halwagi, "Optimal planning of infrastructure for the supply chain of shale gas," *In Advances in Energy Systems Engineering. Springer International Publishing*, pp. 3–19, 2017.

[103] H. Cheng, A. Kharghoria, H. Zhong, and A. Datta-Gupta, "Fast history matching of finite-difference models using streamline-derived sensitivities," *SPE/DOE symposium on improved oil recovery (SPE 89447), Tulsa, OK*, 2004.

[104] R. Alvaro, A. Datta-Gupta, and P. Ballin, "Assisted history matching in the presence of frequent well intervention using generalize travel time inversion," *Journal of Petroleum Science and Engineering*, vol. 78, pp. 415–430, 2011.

[105] J. Yin, H. Y. Park, A. Datta-Gupta, M. J. King, and M. K. Choudhary, "A hierarchical streamline-assisted history matching approach with global and local parameter updates," *Journal of Petroleum Science and Engineering*, vol. 80, pp. 116–130, 2011.

[106] C. Kravaris and J. Seinfeld, "Identification of spatially varying parameters in distributed parameter systems by discrete regularization," *Journal of mathematical analysis and applications*, vol. 119, pp. 128–152, 1986.

[107] T. Leo, C. Kravaria, and J. Seinfeld, "History matching by spline approximation and regularization in single-phase areal reservoirs," *SPE Reservoir Engineering*, vol. 1, pp. 521–534, 1986.

[108] B. Sundaryanto, "Optimization of displacement efficiency of oil recovery in porous media using optimal control theory.," *Ph.D. thesis. University of Southern California*, 1999.

[109] K. Wilson and L. Durlofsky, "Optimization of shale gas field development using direct search techniques and reduced-physics models," *Journal of Petroleum Science and Engineering*, vol. 108, pp. 304–315, 2013.

[110] A. Boulis, R. Jayakumar, and R. Rai, "A new approach for well spacing optimisation and its application to various shale gas resources," *In International Petroleum Technology Conference. International Petroleum Technology Conference, Beijing, China*, 2013.

[111] W. Yu and K. Sepehrnoori, "Optimization of multiple hydraulically fractured horizontal wells in unconventional gas reservoirs," *Journal of Petroleum Engineering*, 2013.

[112] X. Ma, T. Plaksina, and E. Gildin, "Optimization of placement of hydraulic fracture stages in horizontal wells drilled in shale gas reservoirs," *In Unconventional Resources Technology Conference. Society of Exploration Geophysicists. American Association of Petroleum Geologists, Denver, CO*, 2013.

[113] S. Liu and P. P. Valkó, "Optimization of spacing and penetration ratio for infinite conductivity fractures in unconventional reservoirs- a sectional based approach," *SPE Journal*, vol. 22, pp. 1877–1892, 2017.

[114] A. Gringarten, H. Ramey Jr, and R. Raghavan, "Unsteady-state pressure distributions created by a well with a single infinite-conductivity vertical fracture," *SPE Journal*, vol. 14, pp. 347–360, 1974.

[115] C. Burg and T. Erwin, "Application of richardson extrapolation to the numerical solution of partial differential equations," *Numerical Methods for Partial Differential Equations*, vol. 25, pp. 810–832, 2009.

[116] S. Morsy, J. Sheng, and M. Soliman, "Waterflooding in the eagle ford shaleformation: Experimental and simulation study," *In SPE Unconventional Resources Conference and Exhibition-Asia Pacific (SPE 167056), Brisbane, Australia*, 2013.

[117] C. W. Neuhaus and A. R. Zeynal, "Completions evaluation in the eagle ford shale," *Presented at the Unconventional Resources Technology Conference, Denver, CO*, no. 1489-1497, 2014.

[118] "Eia, trends in u.s. oil and natural gas upstream costs," 2016.

[119] D. Cook, K. Downing, S. Bayer, H. Watkins, V. Sun Chee Fore, M. Stansberry, S. Saksena, and D. Peck, "Unconventional asset development work flow in the eagle ford shale," *In SPE Unconventional Resources Conference (SPE 168973), The Woodlands, TX*, 2014.

[120] D. Agboada and M. Ahmadi, "Production decline and numerical simulation model analysis of the eagle ford shale play," *In SPE Western Regional & AAPG Pacific Section Meeting 2013 Joint Technical Conference (SPE 165315), Monterey, CA*, 2013.

[121] R. Suarez-Rivera, J. Burghardt, E. Edelman, S. Stanchits, and A. Surdi, "Geomechanics considerations for hydraulic fracture productivity," *In 47th US Rock Mechanics/Geomechanics Symposium. American Rock Mechanics Association, San Francisco, CA*, 2013.

[122] K. Wu, J. Olson, M. T. Balhoff, and W. Yu, "Numerical analysis for promoting uniform development of simultaneous multiple-fracture propagation in horizontal wells," *SPE production & operations*, vol. 32, pp. 41–50, 2016.

[123] R. L. Pigford, M. Ashraf, and Y. D. Miron, "Flow distribution in piping manifolds," *Industrial & engineering chemistry fundamentals*, vol. 22, pp. 463–471, 1983.

[124] A. Peirce and A. Bunger, "Interference fracturing: Nonuniform distributions of perforation clusters that promote simultaneous growth of multiple hydraulic fractures," *SPE Journal*, vol. 20, pp. 384–395, 2015.

[125] W. Kan, S. Anusarn, and T. Jizhou, "Numerical study of flow rate distribution for simultaneous multiple fracture propagation in horizontal wells," *In 50th US Rock Mechanics/Geomechanics Symposium. American Rock Mechanics Association (ARMA-2016-038), Houston, TX*, 2016.

[126] C. Cheng, A. P. Bunger, and A. P. Peirce, "Optimal perforation location and limited entry design for promoting simultaneous growth of multiple hydraulic fractures," *In SPE Hydraulic Fracturing Technology Conference. Society of Petroleum Engineers (SPE 179158), The Woodlands, TX*, 2016.

[127] H. S. Sidhu, A. Narasingam, P. Siddhamshetty, and J. S. I. Kwon, "Model order reduction of nonlinear parabolic pde systems with moving boundaries using sparse proper orthogonal decomposition: Application to hydraulic fracturing," *Computers & Chemical Engineering*, vol. 112, pp. 92–100, 2018.

[128] J. B. Crump and M. W. Conway, "Effects of perforation-entry friction on bottomhole treating analysis," *Journal of Petroleum Technology*, vol. 40, pp. 1–41, 1988.

[129] P. Valko and M. J. Economides, *Hydraulic fracture mechanics.* Chichester: Wiley, 1995.

[130] K. Wu and J. E. Olson, "A simplified three-dimensional displacement discontinuity method for multiple fracture simulations," *International Journal of Fracture*, vol. 193, pp. 191–204, 2015.

[131] S. L. Crouch, A. M. Starfield, and F. J. Rizzo, "Boundary element methods in solid mechanics," *Journal of Applied Mechanics*, vol. 50, p. 704, 1983.

[132] K. Shou, *A higher order three-dimensional displacement discontinuity method with application to bonded half-space problems.* PhD thesis, University of Minnesota, Minneapolis, Minnesota, 1993.

[133] H. J. Siriwardane and A. W. Layne, "Improved model for predicting multiple hydraulic fracture propagation from a horizontal well," *In SPE Eastern Regional Meeting. Society of Petroleum Engineers (SPE 23448), Lexington, KY*, 1991.

[134] M. G. Mack, J. L. Elbel, and A. R. Piggott, "Numerical representation of multilayer hydraulic fracturing," *In The 33th US Symposium on Rock Mechanics (USRMS). American Rock Mechanics Association (ARMA-92-0335), Santa Fe, NM*, 1992.

[135] J. L. Elbel, A. R. Piggott, and M. G. Mack, "Numerical modeling of multilayer fracture treatments," *In Permian Basin Oil and Gas Recovery Conference. Society of Petroleum Engineers (SPE 23982), Midland, TX*, 1992.

[136] K. Tsai, E. Fonseca, E. Lake, and S. Degaleesan, "Advanced computational modeling of proppant settling in water fractures for shale gas production," *SPE Journal*, vol. 18, pp. 50–56, 2012.

[137] J. Zeng, H. Li, and D. Zhang, "Numerical simulation of proppant transport in hydraulic fracture with the upscaling cfd-dem method," *Journal of Natural Gas Science and Engineering*, vol. 33, pp. 264–277, 2016.

[138] C. H. Wu, S. Yi, and M. M. Sharma, "Proppant distribution among multiple perforation clusters in a horizontal wellbore," *In SPE Hydraulic Fracturing Technology Conference and Exhibition (SPE 184861), The Woodlands, TX*, 2017.

[139] R. S. Schols and W. Visser, "Proppant bank buildup in a vertical fracture without fluid loss," *In SPE European Spring Meeting (SPE 4834), Amsterdam, Netherlands*, 1974.

[140] X. Hu, K. Wu, X. Song, W. Yu, J. Tang, G. Li, and Z. Shen, "A new model for simulating particle transport in a low viscosity fluid for fluid driven fracturing," *AIChE Journal*, vol. 64, pp. 3542–3552, 2018.

[141] C. L. Cipolla, M. G. Mack, and S. C. Maxwell, "Reducing exploration and appraisal risk in low-permeability reservoirs using microseismic fracture mapping," *In Canadian Unconventional Resources and International Petroleum Conference (SPE 137437), Calgary, Alberta, Canada*, 2010.

[142] P. Siddhamshetty, S. Liu, P. P. Valkó, and J. S. Kwon, "Feedback control of proppant bank heights during hydraulic fracturing for enhanced productivity in shale formations," *AIChE Journal*, vol. 64, pp. 1638–1650, 2017.

[143] Y. Televantos, C. Shook, M. Streat, and A. Carleton, "Flow of slurries of coarse particles at high solids concentrations," *The Canadian Journal of Chemical Engineering*, vol. 57, pp. 255–262, 1979.

[144] P. Siddhamshetty, K. Wu, and J. S. I. Kwon, "Optimization of simultaneously propagating multiple fractures in hydraulic fracturing to achieve uniform growth using data-based model reduction," *Chemical Engineering Research and Design*, vol. 136, pp. 675–686, 2018.

[145] C. R. Clarkson, J. L. Jensen, and S. Chipperfield, "Unconventional gas reservoir evaluation: what do we have to consider?," *Journal of Natural Gas Science and Engineering*, vol. 8, pp. 9–33, 2012.

[146] Z. Sun, Q. Gu, and J. Dykstra, "Uncertainty reduction of hydraulic fracturing process," *In American Control Conference (ACC)*, pp. 2135–2141, 2016.

[147] P. Siddhamshetty and J. S. Kwon, "Simultaneous measurement uncertainty reduction and proppant bank height control of hydraulic fracturing," *Computers & Chemical Engineering*, vol. 127, pp. 272–281, 2019.

[148] U. Forssell and L. Ljung, "Closed-loop identification revisited," *Automatica*, vol. 35, pp. 1215–1241, 1999.

[149] M. Kheradmandi and P. Mhaskar, "Model predictive control with closed-loop re-identification," *Computers & Chemical Engineering*, vol. 109, pp. 249–260, 2018.

[150] M. Wallace, S. S. Pon Kumar, and P. Mhaskar, "Offset-free model predictive control with explicit performance specification," *Ind. & Eng. Chem. Res.*, vol. 55, pp. 995–1003, 2016.

[151] P. Siddhamshetty, P. Bhandakkar, and J. S. Kwon, "Enhancing total fracture surface area in naturally fractured unconventional reservoirs via model predictive control," *Journal of Petroleum Science and Engineering*, vol. 184, p. 106525, 2020.

[152] K. Wu and J. E. Olson, "Numerical investigation of complex hydraulic-fracture development in naturally fractured reservoirs," *SPE production & operations*, vol. 31, pp. 300–309, 2016.

[153] S. C. Maxwell, T. I. Urbancic, N. Steinsberger, and R. Zinno, "Microseismic imaging of hydraulic fracture complexity in the barnett shale," *In SPE Annual Technical Conference and Exhibition (SPE 77440), San Antonio, TX*, 2002.

[154] J. L. Daniels, G. A. Waters, J. H. Le Calvez, D. Bentley, and J. T. Lassek, "Contacting more of the barnett shale through an integration of real-time microseismic monitoring, petrophysics, and hydraulic fracture design," *In SPE Annual Technical Conference and Exhibition (SPE 110562), Anaheim, CA*, 2007.

[155] T. Blanton, "Propagation of hydraulically and dynamically induced fractures in naturally fractured reservoirs," *In SPE Unconventional Gas Technology Symposium (SPE 15261), Louisville, KY*, 1986.

[156] N. Warpinski and L. Teufel, "Influence of geologic discontinuities on hydraulic fracture propagation," *Journal of Petroleum Technology*, vol. 39, pp. 209–220, 1987.

[157] C. Renshaw and D. Pollard, "An experimentally verified criterion for propagation across unbounded frictional interfaces in brittle, linear elastic materials," *Int. J. Rock Mech. Min. Sci. & Geomech. Abstr.*, vol. 32, pp. 237–249, 1995.

[158] A. Dahi-Taleghani and J. Olson, "Numerical modeling of multistranded hydraulic fracture propagation: accounting for the interaction between induced and natural fractures," *In SPE Annual Technical Conference Conference and Exhibition (SPE 124884), New Orleans, LA*, 2009.

[159] W. Wang, J. Olson, and M. Prodanovic, "Natural and hydraulic fracture interaction study based on semi-circular bending experiments," *In Unconventional Resources Technology Conference (SPE 168714/URTeC 1576910), Denver, CO*, 2013.

[160] W. Xu, J. H. Le Calvez, and M. J. Thiercelin, "Characterization of hydraulically-induced fracture network using treatment and microseismic data in a tight-gas sand formation: a geomechanical approach," *In SPE tight gas completions conference (SPE 125237), San Antonio, TX*, 2009.

[161] W. Xu, M. J. Thiercelin, U. Ganguly, X. Weng, H. Gu, H. Onda, J. Sun, and J. Le Calvez, "Wiremesh: a novel shale fracturing simulator," *In International Oil and Gas Conference and Exhibition in China (SPE 132218), Beijing, China*, 2010.

[162] J. E. Olson and A. D. Taleghani, "Modeling simultaneous growth of multiple hydraulic fractures and their interaction with natural fractures," *In SPE hydraulic fracturing technology conference (SPE 119739), The Woodlands, TX*, 2009.

[163] E. Budyn, G. Zi, N. Moes, and T. Belytschko, "A method for multiple crack growth in brittle materials without remeshing," *International journal for numerical methods in engineering*, vol. 61, pp. 1741–1770, 2004.

[164] R. Keshavarzi, S. Mohammadi, and H. Bayesteh, "Hydraulic fracture propagation in unconventional reservoirs: the role of natural fractures," *In 46th US Rock Mechanics/Geomechanics Symposium, Chicago, IL*, 2012.

[165] K. Wu and J. Olson, "Mechanics analysis of interaction between hydraulic and natural fractures in shale reservoirs," *In Unconventional Resources Technology Conference, Denver, CO*, pp. 1824–1841, 2014.

[166] H. Gu and X. Weng, "Criterion for fractures crossing frictional interfaces at non-orthogonal angles," *In 44th US Rock Mechanics Symposium and 5th U.S.-Canada Rock Mechanics Symposium, Salt Lake City, UT*, 2010.

[167] X. Weng, O. Kresse, D. Chuprakov, C. E. Cohen, R. Prioul, and U. Ganguly, "Applying complex fracture model and integrated workflow in unconventional reservoirs," *Journal of Petroleum Science and Engineering*, vol. 124, pp. 468–483, 2014.

[168] D. Chuprakov, O. Melchaeva, and R. Prioul, "Injection-sensitive mechanics of hydraulic fracture interaction with discontinuities," *Rock Mechanics and Rock Engineering*, vol. 47, pp. 1625–1640, 2014.

[169] J. E. Olson, "Multi-fracture propagation modeling: Applications to hydraulic fracturing in shales and tight gas sands," *In The 42nd US Symposium on Rock Mechanics (ARMA-08-327), San Francisco, CA*, 2008.

[170] C. L. Cipolla, T. Fitzpatrick, M. J. Williams, and U. K. Ganguly, "Seismic-to-simulation for unconventional reservoir development," *In SPE Reservoir Characterisation and Simulation Conference and Exhibition (SPE 146876), Abu Dhabi, UAE*, 2011.

[171] H. Gu, X. Weng, J. B. Lund, M. G. Mack, U. Ganguly, and R. Suarez-Rivera, "Hydraulic fracture crossing natural fracture at non-orthogonal angles, a criterion, its validation and applications," *In SPE Hydraulic Fracturing Technology Conference (SPE 139984), The Woodlands, TX*, 2011.

[172] X. Weng, O. Kresse, C. E. Cohen, R. Wu, and H. Gu, "Modeling of hydraulic fracture network propagation in a naturally fractured formation," *In SPE Hydraulic Fracturing Technology Conference (SPE 140253), The Woodlands, TX*, 2011.

[173] Y. K. Sukkar and D. Cornell, "Direct calculation of bottom-hole pressures in natural gas wells," *Society of Petroleum Engineers*, vol. 204, pp. 43–48, 1955.

[174] N. R. Warpinski, L. G. Griffin, E. J. Davis, and T. Grant, "Improving hydraulic fracture diagnostics by joint inversion of downhole microseismic and tiltmeter data," *In SPE Annual Technical Conference and Exhibition (SPE 102690), San Antonio, TX*, 2006.

[175] K. D. Scott, W. C. Chu, and R. W. Flumerfelt, "Application of real-time bottom-hole pressure to improve field development strategies in the midland basin wolfcamp shale," *In Unconventional Resources Technology Conference, San Antonio, TX*, pp. 1790–1798, 2015.

[176] P. Siddhamshetty, S. Yang, and J. S. I. Kwon, "Modeling of hydraulic fracturing and designing of online pumping schedules to achieve uniform proppant concentration in conventional oil reservoirs," *Computers & Chemical Engineering*, vol. 114, pp. 306–317, 2018.

[177] H. R. Acharya, C. Henderson, H. Matis, H. Kommepalli, B. Moore, and H. Wang, "Cost effective recovery of low-tds frac flowback water for re-use," *DOE Report DE-FE0000784*, p. 100, 2011.

[178] C. E. Clark, R. M. Horner, and C. B. Harto, "Life cycle water consumption for shale gas and conventional natural gas," *Environmental Science & Technology*, vol. 47, pp. 11829–11836, 2013.

[179] M. Jiang, C. T. Hendrickson, and J. M. VanBriesen, "Life cycle water consumption and wastewater generation impacts of a marcellus shale gas well," *Environmental Science & Technology*, vol. 48, pp. 1911–1920, 2014.

[180] K. Cao, P. Siddhamshetty, Y. Ahn, R. Mukherjee, and J. S. Kwon, "Economic model-based controller design framework for hydraulic fracturing to optimize shale gas production and water usage," *Ind. & Eng. Chem. Res.*, vol. 58, pp. 12097–12115, 2019.